ANALYSIS AND OPTIMIZATION OF LEADING EDGE TUBERCLES ON VERTICAL AXIS WIND TURBINES

ANALYSE ET OPTIMISATION DES TUBERCULES DE BORD D'ATTAQUE SUR LES ÉOLIENNES À AXE VERTICAL

A Thesis Submitted to the Division of Graduate Studies
of the Royal Military College of Canada
by

Dillon Avery Hesketh, BEng, rmc.
Captain

In Partial Fulfillment of the Requirements for the Degree of
Master of Applied Science in Aeronautical Engineering

July, 2025

"Did you read the error message?"

Acknowledgements

I would like to express my sincere appreciation to my supervisor, Dr. Ruben Perez, for his consistent guidance and support throughout this project. His genuine passion for teaching—whether during my undergraduate or graduate studies—has made this journey both rewarding and memorable. I am also grateful to Dr. Peter Jansen for his support and invaluable input, which helped shape this thesis. Many thanks as well to the other members of the research group for the countless morning coffee meetings and all the ways they've contributed along the way.

I am deeply appreciative of Brendan Freeman, Curtis Keogh, Jason Pell, Charles Sadiq, and Cory Sharpe for their hands-on support in bringing the RMC VAWT Rig to life and making the experimental campaign a reality.

I would also like to thank my friends and family for their unwavering support throughout this long journey—especially my fiancée, Maryam Salih, whose patience and belief in me have kept me motivated through the most challenging moments.

Lastly, I would like to recognize the late Dr. Mohsen Ferchichi, who generously allowed us to use his wind tunnel. He was an outstanding professor and an inspiring capstone supervisor. His dedication to student success and passion for teaching left a lasting impact. He will always be remembered and missed.

Abstract

Hesketh, Dillon Avery. M.A.Sc. Royal Military College of Canada, July 2025. *Analysis and Optimization of Leading Edge Tubercles on Vertical Axis Wind Turbines.* Supervised by Ruben E. Perez, B.Eng., M.A.Sc., Ph.D., P.Eng., Professor.

Vertical axis wind turbines (VAWT) are omnidirectional and can extract energy from the wind without requiring a yaw system. This simplifies the turbine design, making it suitable for remote areas and reduces maintenance. They also perform well in turbulent flow, allowing them to be built in dense wind farms or urban areas. With an axis of rotation perpendicular to the wind, there is an advancing and retreating blade, with a high range of angles of attack, often into the post-stall regime. The cyclic nature of VAWTs, resulting in compressive and tensile stresses throughout each rotation, presents structural fatigue as another challenge. Tubercles are bio-inspired rounded leading-edge protuberances that act as passive flow control devices. They have been shown to improve post-stall performance by delaying flow separation with a gradual loss of lift post-stall and reducing the size of the dynamic stall lift hysteresis, thereby improving aerodynamic efficiency in this region. This thesis explores the application of tubercles to the leading edge of VAWT blades. An experimental aerodynamic database of six different tubercle leading edge shapes was used with a double-multiple streamtube model (DMSTM) to determine performance improvements and their sources when applied to VAWTs compared to a baseline straight leading edge blade. This DMSTM analysis was then coupled with a multi-objective optimization algorithm to maximize wind speed probability-weighted average power output, $\bar{P}$, and a fatigue life indicator, $\overline{FLI}$, by varying rotational rate and tubercle shape along the leading edge of the blades. Design trade-offs between $\bar{P}$ and $\overline{FLI}$ are shown for a small scaled H-type VAWT application. The best-performing design yielded increases in $\bar{P}$ and $\overline{FLI}$ of 19 % and 14 %, respectively, compared to the unmodified baseline blade. An alternate design resulted in a 34 % increase in $\overline{FLI}$ without sacrificing power output. To confirm these findings, an experimental VAWT rig was developed and commissioned, and preliminary results are also presented.

Keywords: vertical axis wind turbine (VAWT), double-multiple streamtube model, applied aerodynamics, bio-inspired, leading edge tubercles, multi-objective optimization, non-dominated sorting genetic algorithm II (NSGA-II), experimental testing.

Résumé

Hesketh, Dillon Avery. M.A.Sc. Collège militaire royal du Canada, juillet 2025. *Analyse et optimisation des tubercules de bord d'attaque sur les éoliennes à axe vertical.* Thèse dirigée par Ruben E. Perez, B.Eng., M.A.Sc., Ph.D., P.Eng., Professeur.

Les éoliennes à axe vertical (EAV) sont omnidirectionnelles et peuvent extraire l'énergie du vent sans nécessiter de système d'orientation. Cela simplifie l'éolienne, la rendant adaptée aux régions isolées et réduisant les besoins en maintenance. Elles fonctionnent également bien dans les flux turbulents, ce qui permet de les installer dans des parcs éoliens denses ou des zones urbaines. Avec un axe de rotation perpendiculaire au vent, il existe un côté avançant et un côté reculant, avec une large gamme d'angles d'attaque, souvent dans le régime post-décrochage. La nature cyclique des EAV, qui entraîne des contraintes de compression et de traction à chaque rotation, présente la fatigue structurelle comme un autre défi. Les tubercules sont des protubérances arrondies inspirées de la biologie qui agissent comme des dispositifs passifs de contrôle du flux. Il a été démontré qu'elles améliorent les performances post-décrochage en retardant la séparation du flux avec une perte progressive de portance post-décrochage et en réduisant la taille de l'hystérésis de portance causée par le décrochage dynamique, améliorant ainsi l'efficacité aérodynamique dans ce régime. Cette thèse explore l'application des tubercules au bord d'attaque des pales des EAV. Une base de données aérodynamiques expérimentales de six formes différentes de tubercules sur le bord d'attaque a été utilisée avec un modèle à double tube à flux multiples (MDTFM) afin de déterminer les améliorations de performances et leurs sources lorsqu'ils sont appliqués à des EAV par rapport à une pale de référence à bord d'attaque droit. Cette analyse MDTFM a ensuite été couplée à un algorithme d'optimisation multi-objectifs afin de maximiser la puissance moyenne pondérée par la probabilité de vitesse du vent, $\bar{P}$, et un indicateur de durée de vie en fatigue, $\overline{FLI}$, en faisant varier la vitesse de rotation et la forme des tubercules le long du bord d'attaque des pales. Les compromis de conception entre $\bar{P}$ et $\overline{FLI}$ sont présentés pour une application EAV à petite échelle. Le design le plus performant a permis d'obtenir une augmentation de 19 % en $\bar{P}$ et de 14 % en $\overline{FLI}$, par rapport à la pale de référence non modifiée. Un autre design a permis d'obtenir une augmentation de 34 % en $\overline{FLI}$ sans sacrifier la puissance de sortie. Afin de confirmer ces résultats, un banc d'essai expérimental pour EAV a été développé et mis en service, et les résultats préliminaires sont également présentés.

Mots-clés: éolienne à axe vertical (EAV), modèle à double tube à flux multiples, aérodynamique appliquée, bio-inspirée, tubercules de bord d'attaque, optimisation multi-objectifs, algorithme génétique de tri non dominé II, essais expérimentaux.

Contents

Acknowledgements iii

Abstract iv

Résumé v

List of Tables x

List of Figures xiii

Nomenclature xviii

1 Introduction 1
- 1.1 Motivation for the Research . . . 1
- 1.2 Research Objectives . . . 2
- 1.3 Thesis Layout . . . 3
- 1.4 Contributions . . . 3

2 Literature Review 4
- 2.1 Background on Wind Turbines . . . 4
- 2.2 Vertical Axis Wind Turbines . . . 5
  - 2.2.1 Configurations . . . 7
  - 2.2.2 Modifications . . . 9
  - 2.2.3 Analysis Methods . . . 11
- 2.3 Background on Tubercles . . . 13
- 2.4 Tubercle Mechanisms . . . 13
  - 2.4.1 Vortex Generators . . . 14
  - 2.4.2 Induced Flow and Vortex Lift . . . 15
  - 2.4.3 Flow Compartmentalization . . . 16
- 2.5 Tubercles Applied to VAWTs . . . 17
- 2.6 VAWT Design, Analysis, and Optimization . . . 19
- 2.7 Knowledge Gaps . . . 20

3 Analysis of VAWTs with Leading-edge Tubercles 21
- 3.1 Methodology . . . 21
  - 3.1.1 Double-Multiple Streamtube Model . . . 21
    - Dynamic Stall . . . 25
    - Blade Tip and Finite Aspect Ratio . . . 26
  - 3.1.2 Average Power Output . . . 27

3.1.3 Sandia 17-m VAWT . . . 28
3.1.4 Convergence Studies . . . 29
3.1.5 Sandia 17-m Validation . . . 33
3.1.6 Experimental Aerodynamic Tubercle Database . . . 34
3.2 Application of Tubercles . . . 39
3.2.1 Small-Scale H-Type VAWT . . . 39
3.2.2 Tubercle Power Contours . . . 40
3.2.3 Average Power Output Analysis . . . 44
3.2.4 Power Coefficient Contours . . . 46
3.2.5 Sources of Improvement . . . 51

4 Tubercle Shape Optimization on VAWT Blades 55
4.1 Methodology . . . 55
4.1.1 Objectives . . . 55
4.1.2 Fatigue Life Indicator . . . 56
4.1.3 Variables . . . 57
4.1.4 Optimization Problem Formulation . . . 58
4.2 Small-Scale H-Type VAWT Test Case . . . 60
4.2.1 Maximization of $\overline{FLI}$ and $\bar{P}$ . . . 60
4.2.2 Maximization of $\bar{P}_S$ and $\bar{P}_K$ . . . 63
4.3 1:7 Scale Sandia Test Case . . . 66
4.3.1 Maximization of $\overline{FLI}$ and $\bar{P}$ . . . 67
4.3.2 Maximization of $\bar{P}_S$ and $\bar{P}_K$ . . . 70
4.4 Summary . . . 72

5 Experimental Characterization of Tubercles on VAWT Blades 73
5.1 Development of RMC VAWT Rig . . . 73
5.1.1 Thesis Rig Design Objectives . . . 74
5.1.2 Thesis Rig Design Constraints . . . 75
5.1.3 Thesis Rig Design Summary . . . 75
5.1.4 Air Bearing and Braking System . . . 75
5.1.5 Main Turbine . . . 79
5.1.6 Data Acquisition and Control . . . 80
5.1.7 VAWT Rig Cart . . . 83
5.2 Methodology . . . 83
5.2.1 Experimental Objectives . . . 84
5.2.2 Data Measurements . . . 84
5.2.3 Residual Torque Measurement . . . 87
5.2.4 Spool-Up Torque Measurement . . . 89
5.2.5 Uncertainty Analysis . . . 90
5.2.6 Test Procedure . . . 90
5.2.7 Wind Tunnel . . . 91
5.2.8 Outdoor Location . . . 94
5.3 Initial Results of the RMC VAWT Rig . . . 95
5.3.1 Wind Tunnel Startup . . . 95
5.3.2 Outdoor Startup . . . 100
5.3.3 Outdoor Power Curves . . . 105

6 Conclusion and Recommendations **109**
6.1 Conclusion . . . 109
6.2 Recommendations for Future Work . . . 111

Bibliography **112**

Appendices **120**

A Experimental Tubercle Aerodynamic Database **121**
A.1 Methodology . . . 121
A.2 Uncorrected Data . . . 123
A.3 Corrected Data . . . 133

B Wind Probability Distribution of Kingston, Ontario **143**

C Additional DMSTM Results **145**
C.1 Small-Scale H-Type VAWT with Tubercles . . . 145
C.1.1 Power Contours with TSR . . . 145
C.2 1:7 Scale Sandia 17-m with Tubercles . . . 150
C.2.1 Power Contours . . . 150
C.2.2 Power Coefficient Contours . . . 155
C.2.3 Power Contours with TSR . . . 160

D Non-Dominated Sorting Genetic Algorithm II **165**
D.1 Fast Non-Dominated Sorting . . . 165
D.2 Crowding Distance . . . 165
D.3 Binary Tournament Selection and Crossover . . . 166
D.4 Validation . . . 166

E Optimization Results with Variable RPM **168**
E.1 Small Scale H-Type VAWT . . . 168
E.1.1 Maximization of $\overline{FLI}$ and $\bar{P}$ . . . 168
E.1.2 Maximization of $\bar{P}_S$ and $\bar{P}_K$ . . . 170
E.2 1:7 Scale Sandia 17-m . . . 172
E.2.1 Maximization of $\overline{FLI}$ and $\bar{P}$ . . . 172
E.2.2 Maximization of $\bar{P}_S$ and $\bar{P}_K$ . . . 174

F Experimental Uncertainty Calculations **176**
F.1 Air Density . . . 176
F.2 Wind Tunnel Velocity . . . 176
F.3 Tip Speed Ratio . . . 177
F.4 Residual Torque . . . 177
F.5 Spool Up Torque . . . 178
F.6 Torque Sensor . . . 178
F.7 Blade Torque . . . 179
F.8 Power . . . 179
F.9 Coefficient of Power . . . 179

G Additional Experimental Results **180**

G.1 Wind Tunnel Startup 180
G.2 Wind Tunnel Power Curves 188
G.3 Outdoor Startup 194

List of Tables

3.1 Forms of M_1, M_2, and γ_{max}. [3] 26
3.2 Shape and Scale Parameters of SWiFT Test Site and Kingston, ON wind speed probability distributions. 27
3.3 Geometric characteristics of the Sandia-17m wind turbine [102]. 28
3.4 Comparison of average power output for the DMSTM with experimental Sandia-17m data. 34
3.5 Summary of Leading-Edge Tubercle Geometry. 35
3.6 Geometric characteristics of the small-scale H-type VAWT 39
3.7 Location and value of maximum power output for tubercle shapes compared to the baseline. 44
3.8 Location and value of maximum wind speed probability-weighted average power output for tubercle shapes compared to the baseline. 45
3.9 Location and value of maximum power coefficient for tubercle shapes compared to the baseline. 48
3.10 Location and value of maximum wind speed probability-weighted average power coefficient for tubercle shapes compared to the baseline. 50

4.1 Summary of Discrete Values for Tubercle Shapes. 58
4.2 Summary of NSGA-II Parameters. 59
4.3 Values used for each of the optimization variables. 60
4.4 Performance characteristics of the various designs from optimizing wind probability-weighted average fatigue life indicator and power output at the SWiFT Test Site for the Small-Scale H-type VAWT with TSR as a variable. 61
4.5 Performance characteristics of the various designs from optimizing wind probability-weighted average power output at the SWiFT Test Site and Kingston, ON, for the Small-Scale H-type VAWT with TSR as a variable. 64
4.6 Geometric characteristics of the 1:7 Scale Sandia-17m wind turbine. 66
4.7 Performance characteristics of the various designs from optimizing wind probability-weighted average fatigue life indicator and power output at the SWiFT Test Site for the 1:7 Scale Sandia 17-m with TSR as a variable. 67
4.8 Performance characteristics of the various designs from optimizing wind probability-weighted average power output at the SWiFT Test Site and Kingston, ON, for the 1:7 Scale Sandia 17-m with TSR as a variable. 70

5.1 Geometric characteristics of the RMC VAWT 80
5.2 Summary of the mass moment of inertia of the individual components of the RMC VAWT Rig without the turbine and blades. 87

5.3 Summary of the mass moment of inertia of the individual components of the RMC VAWT Rig turbine. 90
5.4 Uncertainty of the various measurement devices used during the experimental campaign on the RMC VAWT Rig. 90
5.5 Wind tunnel survey results compared to wind tunnel pitot measurements. . . . 94
5.6 Summary of wind tunnel startup results of the $A03\lambda11$ blades compared to the baseline. 96

A.1 NACA 0018 Uncorrected Experimental Aerodynamic Data. 123
A.2 NACA 0018 $A02\lambda07$ Uncorrected Experimental Aerodynamic Data. 124
A.3 NACA 0018 $A02\lambda09$ Uncorrected Experimental Aerodynamic Data. 125
A.4 NACA 0018 $A03\lambda11$ Uncorrected Experimental Aerodynamic Data. 126
A.5 NACA 0018 $A04\lambda18$ Uncorrected Experimental Aerodynamic Data. 127
A.6 NACA 0018 $A05\lambda13$ Uncorrected Experimental Aerodynamic Data. 128
A.7 NACA 0018 $A06\lambda21$ Uncorrected Experimental Aerodynamic Data. 129
A.8 NACA 0018 Corrected Experimental Aerodynamic Data. 133
A.9 NACA 0018 $A02\lambda07$ Corrected Experimental Aerodynamic Data. 134
A.10 NACA 0018 $A02\lambda09$ Corrected Experimental Aerodynamic Data. 135
A.11 NACA 0018 $A03\lambda11$ Corrected Experimental Aerodynamic Data. 136
A.12 NACA 0018 $A04\lambda18$ Corrected Experimental Aerodynamic Data. 137
A.13 NACA 0018 $A05\lambda13$ Corrected Experimental Aerodynamic Data. 138
A.14 NACA 0018 $A06\lambda21$ Corrected Experimental Aerodynamic Data. 139

C.1 Location and value of maximum wind speed probability-weighted average power with constant TSR for tubercle shapes compared to the baseline. 145
C.2 Location and value of maximum power output for tubercle shapes compared to the baseline when applied to the 1:7 Scale Sandia 17-m. 150
C.3 Location and value of maximum wind probability-weighted average power output with constant RPM for tubercle shapes compared to the baseline when applied to the 1:7 Scale Sandia 17-m. 150
C.4 Location and value of maximum power coefficient for tubercle shapes compared to the baseline when applied to the 1:7 Scale Sandia 17-m. 155
C.5 Location and value of maximum wind probability-weighted average power coefficient with constant RPM for tubercle shapes compared to the baseline when applied to the 1:7 Scale Sandia 17-m. 155
C.6 Location and value of maximum wind probability-weighted average power output with constant TSR for tubercle shapes compared to the baseline when applied to the 1:7 Scale Sandia 17-m. 160

D.1 Summary of NSGA-II Parameters. 167

E.1 Performance characteristics of the various designs from optimizing wind probability-weighted average fatigue life indicator and power output at the SWiFT Test Site for the Small Scale H-type VAWT with RPM as a variable. 168
E.2 Performance characteristics of the various designs from optimizing wind probability-weighted average power output at the SWiFT Test Site and Kingston, ON, for the Small Scale H-type VAWT with RPM as a variable. 170

E.3 Performance characteristics of the various designs from optimizing probability-weighted average fatigue life indicator and power output at the SWiFT Test Site for the 1:7 Scale Sandia 17-m with RPM as a variable. 172
E.4 Performance characteristics of the various designs from optimizing probability-weighted average power output at the SWiFT Test Site and Kingston, ON, for the 1:7 Scale Sandia 17-m with RPM as a variable.. 174

List of Figures

2.1 Blyths VAWT 5
2.2 Diagram of lift-type VAWT aerodynamic characteristics throughout rotation at a TSR above 1.0. 6
2.3 Éole VAWT in Quebec, Canada [25]. 7
2.4 Examples of VAWTs. 8
2.5 Photograph of a humpback whale that shows the tubercles on the whale's pectoral fin [58]. 13
2.6 Counter-rotating stream-wise vortices produced by leading-edge tubercles in a 3D View (a) and as viewed at the trailing edge looking upstream (b). [72]. . . . 16

3.1 DMSTM Flow Chart. 23
3.2 Double Multiple Streamtube Model Symbols and Dimensions [3]. 24
3.3 Wind speed probability Weibull distributions of the SWiFT Test Site and Kingston, ON. 28
3.4 Details of the Sandia-17m VAWT. 29
3.5 Convergence study of azimuthal streamtubes when applied to the Sandia 17-m at 48.4 RPM. 30
3.6 Convergence study of vertical streamtubes when applied to the Sandia 17-m at 48.4 RPM. 31
3.7 Convergence study of velocity discretization when applied to the Sandia 17-m at 48.4 RPM. 32
3.8 Validation of the presented DMSTM code against Sandia 17-m experimental data [3]. 33
3.9 Tubercle representation with a 2D sine wave. 35
3.10 Suction surface view of all tubercle geometries studied [77]. 35
3.11 Uncorrected experimental lift and drag curves of the tubercle shapes at $Re = 150\,000$. 37
3.12 Corrected experimental lift and drag curves of the tubercle shapes at $Re = 150\,000$. 38
3.13 Rotor Radius as a function of local turbine height of the Small-Scale H-type VAWT. 40
3.14 Power contours, in watts, of various tubercle shapes applied to the Small-Scale H-type VAWT. 41
3.14 Power contours, in watts, of various tubercle shapes applied to the Small-Scale H-type VAWT. 42
3.15 Change in power contours compared to the baseline, measured in watts, of various tubercle shapes applied to the Small-Scale H-type VAWT. 43
3.16 Wind speed probability-weighted average power output for the Small-Scale H-type VAWT with various tubercle shapes. 45

3.17 Power coefficient contours of various tubercle shapes applied to the Small-Scale H-type VAWT. . . . 47
3.17 Power coefficient contours of various tubercle shapes applied to the Small-Scale H-type VAWT. . . . 48
3.18 Change in power coefficient contours compared to the baseline of various tubercle shapes applied to the Small-Scale H-type VAWT. . . . 49
3.19 Wind speed probability-weighted average power coefficient for the Small-Scale H-type VAWT with various tubercle shapes. . . . 50
3.20 Power curves of various tubercle shapes including the difference in power output compared to the baseline when applied to the Small-Scale H-type VAWT at 500 RPM. . . . 51
3.21 Local aerodynamic characteristics of the Small-Scale H-type VAWT at 500 RPM and 13 m/s (TSR of 2.0) with various tubercle shapes. . . . 52
3.21 Local aerodynamic characteristics of the Small-Scale H-type VAWT at 500 RPM and 13 m/s at the turbine equator with various tubercle shapes. . . . 53

4.1 All solutions explored by NSGA-II optimizing wind probability-weighted average fatigue life indicator and power output at the SWiFT Test Site for the Small-Scale H-type VAWT with TSR as a variable. . . . 62
4.2 Select half-blade designs from optimizing wind probability-weighted average fatigue life indicator and power output at the SWiFT Test Site for the Small-Scale H-type VAWT with TSR as a variable. . . . 63
4.3 All solutions explored by NSGA-II optimizing wind probability-weighted average power output at the SWiFT Test Site and Kingston, ON, for the Small-Scale H-type VAWT with TSR as a variable. . . . 65
4.4 Rotor Radius as a function of local turbine height of the 1:7 Scale Sandia-17m VAWT. . . . 66
4.5 All solutions explored by NSGA-II optimizing wind probability-weighted average fatigue life indicator and power output at the SWiFT Test Site for the 1:7 Scale Sandia 17-m with TSR as a variable. . . . 68
4.6 Select half-blade designs from optimizing wind probability-weighted average fatigue life indicator and power output at the SWiFT Test Site for the 1:7 Scale Sandia 17-m with TSR as a variable. . . . 69
4.7 All solutions explored by NSGA-II optimizing wind probability-weighted average power output at the SWiFT Test Site and Kingston, ON, for the 1:7 Scale Sandia 17-m with TSR as a variable. . . . 71

5.1 RMC VAWT setup during outdoor testing at the point of the RMC peninsula. 74
5.2 The air bearing used on the RMC VAWT rig and its cross-section. . . . 76
5.3 *MAXIMUM* one gallon air compressor used on the RMC VAWT rig. . . . 76
5.4 Air preparation filters and desiccant used for the air bearing on the RMC VAWT rig. . . . 77
5.5 *Magtrol* HB-450 magnetic hysteresis brake on the RMC VAWT Rig. . . . 78
5.6 Torque hysteresis curve of the *Magtrol* HB-450 hysteresis brake. . . . 78
5.7 *Magtrol* 5210-2 power supply for the hysteresis brake. . . . 79
5.8 Cross-section of the 3D printed turbine blades used on the RMC VAWT. . . . 80
5.9 *Burster* 8656-5020 rotary precision torque sensor mounted in the RMC VAWT rig. . . . 81

5.10 Schematic diagram of the RMC VAWT rig. 82
5.11 RMC VAWT Rig cart during outdoor testing at the point of the RMC peninsula. 83
5.12 Sample histograms of data measurements during wind tunnel testing of the baseline blade with the wind tunnel motor at 40 Hz. 85
5.13 Power spectral density of torque measurements during wind tunnel testing of the baseline blade with the wind tunnel motor at 40 Hz. 86
5.14 Power spectral density of all wind speed measurements during outdoor testing. 86
5.15 RPM and residual torque of the driven system on the RMC VAWT Rig with the turbine and blades removed during spool-down testing. 88
5.16 RMC Open Jet Wind Tunnel. 92
5.17 Survey of the flow at five turbine radii (2.5 m) from the exit of the RMC Open Jet Wind Tunnel. 93
5.18 Map detailing location of RMC VAWT Rig during outdoor testing. 94
5.19 Startup and spool-up power coefficient curves of the $A03\lambda11$ blades compared to the baseline in the wind tunnel at a motor frequency of 32.5 Hz. 97
5.20 Startup and spool-up power coefficient curves of the $A03\lambda11$ blades compared to the baseline in the wind tunnel at a motor frequency of 45.0 Hz. 99
5.21 Outdoor startup TSR and wind speed of the $A02\lambda09$ blades compared to the baseline at an average wind speed of 7.2 and 6.4 m/s, respectively. 101
5.22 Outdoor startup TSR and wind speed of the $A02\lambda09$ blades compared to the baseline at an average wind speed of 5.0 and 4.9 m/s, respectively. 103
5.23 Outdoor power and power coefficient curves $A02\lambda09$ blades compared to the baseline using the spool-up technique. 104
5.24 Outdoor power and power coefficient curves $A02\lambda09$ blades compared to the baseline using torque sensor measurements. 106
5.25 Rotational rate and TSR of the $A02\lambda09$ blades compared to the baseline using during torque measurements. 107

A.1 RMC Large Subsonic Wind Tunnel [113]. 121
A.2 Experimental Setup in Wind Tunnel. 122
A.3 Uncorrected experimental lift and drag curves of the tubercle shapes at $Re = 75\,000$. 130
A.4 Uncorrected experimental lift and drag curves of the tubercle shapes at $Re = 150\,000$. 131
A.5 Uncorrected experimental lift and drag curves of the tubercle shapes at $Re = 300\,000$. 132
A.6 Corrected experimental lift and drag curves of the tubercle shapes at $Re = 75\,000$. 140
A.7 Corrected experimental lift and drag curves of the tubercle shapes at $Re = 150\,000$. 141
A.8 Corrected experimental lift and drag curves of the tubercle shapes at $Re = 300\,000$. 142

B.1 Weibull plot of wind speeds recorded at the Kingston, ON, Airport from October 2014 to April 2024. 143
B.2 Weibull distribution of wind speeds recorded at the Kingston, ON, Airport from October 2014 to April 2024, compared to the wind speed probability by method of bins. 144

C.1 Power contours, in watts, with TSR of various tubercle shapes applied to the Small-Scale H-type VAWT. 146

C.1 Power contours, in watts, with TSR of various tubercle shapes applied to the Small-Scale H-type VAWT. . . . 147
C.2 Change in power contours compared to the baseline, in watts, with TSR of various tubercle shapes applied to the Small-Scale H-type VAWT. . . . 148
C.3 Wind speed probability-weighted average power with constant TSR for the Small-Scale H-type VAWT with various tubercle shapes. . . . 149
C.4 Power contours, in watts, of various tubercle shapes applied to the 1:7 Scale Sandia 17-m. . . . 151
C.4 Power contours, in watts, of various tubercle shapes applied to the 1:7 Scale Sandia 17-m. . . . 152
C.5 Change in power contours compared to the baseline, in watts, of various tubercle shapes applied to the 1:7 Scale Sandia 17-m. . . . 153
C.6 Wind probability-weighted average power output for the 1:7 Scale Sandia 17-m with constant RPM for various tubercle shapes. . . . 154
C.7 Power coefficient contours of various tubercle shapes applied to the 1:7 Scale Sandia 17-m. . . . 156
C.7 Power coefficient contours of various tubercle shapes applied to the 1:7 Scale Sandia 17-m. . . . 157
C.8 Change in power coefficient contours compared to the baseline of various tubercle shapes applied to the 1:7 Scale Sandia 17-m. . . . 158
C.9 Wind probability-weighted average power coefficient for the 1:7 Scale Sandia 17-m with constant RPM for various tubercle shapes. . . . 159
C.10 Power contours, in watts, of various tubercle shapes applied to the 1:7 Scale Sandia 17-m. . . . 161
C.10 Power contours, in watts, of various tubercle shapes applied to the 1:7 Scale Sandia 17-m. . . . 162
C.11 Change in power contours compared to the baseline, in watts, of various tubercle shapes applied to the 1:7 Scale Sandia 17-m. . . . 163
C.12 Wind probability-weighted average power for the 1:7 Scale Sandia 17-m with constant TSR for various tubercle shapes. . . . 164

D.1 Validation of the NSGA-II code solution of the KUR problem. . . . 167

E.1 All solutions explored by NSGA-II optimizing wind probability-weighted average fatigue life indicator and power output at the SWiFT Test Site for the Small Scale H-type VAWT with RPM as a variable. . . . 169
E.2 Select half-blade designs from optimizing wind probability-weighted average fatigue life indicator and power output at the SWiFT Test Site for the Small Scale H-type VAWT with RPM as a variable. . . . 170
E.3 All solutions explored by NSGA-II optimizing wind probability-weighted average power output at the SWiFT Test Site and Kingston, ON, for the Small Scale H-type VAWT with RPM as a variable. . . . 171
E.4 All solutions explored by NSGA-II optimizing wind probability-weighted average fatigue life indicator and power output at the SWiFT Test Site for the 1:7 Scale Sandia 17-m with RPM as a variable. . . . 173
E.5 Select half-blade designs from optimizing probability-weighted average fatigue life indicator and power output at the SWiFT Test Site for the 1:7 Scale Sandia 17-m with RPM as a variable. . . . 174

E.6 All solutions explored by NSGA-II optimizing probability-weighted average power output at the SWiFT Test Site and Kingston, ON, for the 1:7 Scale Sandia 17-m with RPM as a variable. 175

G.1 Startup and spool up power coefficient curves of the $A03\lambda11$ blades compared to the baseline in the wind tunnel at a motor frequency of 27.5 Hz. 181
G.2 Startup and spool up power coefficient curves of the $A03\lambda11$ blades compared to the baseline in the wind tunnel at a motor frequency of 30.0 Hz. 182
G.3 Startup and spool up power coefficient curves of the $A03\lambda11$ blades compared to the baseline in the wind tunnel at a motor frequency of 32.5 Hz. 183
G.4 Startup and spool up power coefficient curves of the $A03\lambda11$ blades compared to the baseline in the wind tunnel at a motor frequency of 37.5 Hz. 184
G.5 Startup and spool up power coefficient curves of the $A03\lambda11$ blades compared to the baseline in the wind tunnel at a motor frequency of 42.5 Hz. 185
G.6 Startup and spool up power coefficient curves of the $A03\lambda11$ blades compared to the baseline in the wind tunnel at a motor frequency of 45.0 Hz. 186
G.7 Startup and spool up power coefficient curves of the $A03\lambda11$ blades compared to the baseline in the wind tunnel at a motor frequency of 47.5 Hz. 187
G.8 Power and power coefficient curves of the baseline blades in the wind tunnel at a motor frequency of 27.5 Hz using steady state torque measurements. 188
G.9 Power and power coefficient curves of the baseline blades in the wind tunnel at a motor frequency of 30.0 Hz using steady state torque measurements. 189
G.10 Power and power coefficient curves of the baseline blades in the wind tunnel at a motor frequency of 32.5 Hz using steady state torque measurements. 190
G.11 Power and power coefficient curves of the baseline blades in the wind tunnel at a motor frequency of 40.0 Hz using steady state torque measurements. 191
G.12 Power and power coefficient curves of the baseline blades in the wind tunnel at a motor frequency of 42.5 Hz using steady state torque measurements. 192
G.13 Power and power coefficient curves of the baseline blades in the wind tunnel at a motor frequency of 45.0 Hz using steady state torque measurements. 193
G.14 Outdoor startup TSR and wind speed of the Baseline blades at varying wind conditions. 194
G.15 Outdoor startup TSR and wind speed of the $A02\lambda09$ blades at varying wind conditions. 195

Nomenclature

Roman Symbols

A	Tubercle Amplitude (percentage of chord)	[-]
AR	Aspect Ratio	[-]
c	Chord	[m]
D	Drag	[N]
d	Crowding Distance	[-]
$\hat{F}$	Empirical Cumulative Distribution Function	[-]
F_a	Cyclic Force Amplitude	[N]
FLI	Fatigue Life Indicator	[min]
$\overline{FLI}$	Wind Speed Probability-Weighted Average Fatigue Life Indicator	[min]
f	Frequency	[Hz]
H	Turbine Half Height	[m]
I	Mass Moment of Inertia	[kg m^2]
k	Weibull Shape Parameter	[-]
L	Lift	[N]
M	Mach Number	[-]
N	Number of Blades	[-]
N_f	Number of Cycles to Failure	[-]
P	Power	[W]
$\bar{P}$	Wind Speed Probability-Weighted Average Power	[W]
Pr	Wind Speed Probability Density Function	[-]
p	Pressure	[Pa]
R	Rotor Radius	[m]

R_{air}	Specific Gas Constant of Dry Air	[J/kg K]
Re	Reynolds Number	[-]
Re_b	Local Blade Reynolds Number	[-]
r	Local Turbine Radius	[m]
S	Rotor Swept Area	[m^2]
T	Temperature	[K]
TK_0	Temperature Effect on Zero Point	[Nm/K]
TK_s	Temperature Effect on Sensitivity	[Nm/K]
t	Time	[s]
t/c	Thickness to Chord Ratio	[-]
U_{hys}	Relative Hysteresis	[Nm]
U_{lin}	Relative Non-linearity	[Nm]
U_s	Tolerance of Sensitivity	[Nm]
u	Upwind Interference Factor	[-]
u'	Downwind Interference Factor	[-]
V	Upwind Induced Velocity	[m/s]
V'	Downwind Induced Velocity	[m/s]
V_e	Induced Equilibrium Velocity	[m/s]
V_∞	Freestream Velocity (Wind Speed)	[m/s]
W	Local Blade Relative Velocity	[m/s]
z	Local Rotor Height	[m]

Greek Symbols

α	Angle of Attack	[deg]
α_0	Zero-Lift Angle of Attack	[deg]
α_{ss}	Static Stall Angle of Attack	[deg]
$\dot{\alpha}$	Rate of Change of Angle of Attack	[deg/s]
Δp	Pressure Differential	[Pa]
δ	Local Blade Meridian Angle	[deg]
ζ	Normalized Local Height (z/H)	[-]

η	Normalized Local Radius (r/R)	[-]
θ	Azimuth Angle	[deg]
λ	Tubercle Wavelength (percentage of chord)	[-]
$\hat{\lambda}$	Tip Speed Ratio	[-]
$\tilde{\lambda}$	Weibull Scale Parameter	[m/s]
ν	Kinematic Viscosity	[m^2/s]
ξ	Instantaneous Angular Acceleration	[rad/s^2]
ρ	Density	[kg/m^3]
σ	Solidity	[-]
σ_a	Cycle Stress Amplitude	[Pa]
Ω	Rotational Rate	[1/min]
ω	Angular Velocity	[rad/s]

Dimensionless Groups

C_D	Drag Coefficient	[-]
C_d	Local Drag Coefficient	[-]
C_d^{dyn}	Local Dynamic Drag Coefficient	[-]
C_{d_0}	Local Zero-Lift Drag Coefficient	[-]
C_L	Lift Coefficient	[-]
$C_{L_{\max}}$	Maximum Lift Coefficient	[-]
C_l	Local Lift Coefficient	[-]
C_l^{dyn}	Local Dynamic Lift Coefficient	[-]
C_{l_α}	Lift Curve Slope	[1/rad]
C_l/C_d	Local Aerodynamic Efficiency	[-]
C_N	Normal Force Coefficient	[-]
C_n	Local Normal Force Coefficient	[-]
C_P	Power Coefficient	[-]
$\bar{C_P}$	Wind Speed Probability-Weighted Average Power Coefficient	[-]
C_T	Tangential Force Coefficient	[-]
C_t	Local Tangential Force Coefficient	[-]

Roman Subscripts

∞	Freestream
b	From Turbine Blades
K	Kingston, Ontario
ref	Reference
res	Residual
rig	Rig
S	SWiFT Test Site, Lubbock, Texas
turb	Turbine

Abbreviations

2D	Two-dimensional
3D	Three-dimensional
AoA	Angle of Attack
ASA	Acrylonitrile Styrene Acrylate
CFD	Computational Fluid Dynamics
CMAES	Covariance Matrix Adaptation Evolutionary Strategy
CRSWV	Counter-rotating Stream-wise Vortices
CSV	Comma-Separated Value
DES	Detached eddy simulation
DMSTM	Double-multiple Streamtube Model
FDM	Fused Deposition Modelling
HAWT	Horizontal Axis Wind Turbine
LES	Large eddy simulation
NMEA	National Marine Electronics Association
NSGA-II	Non-Dominated Sorting Genetic Algorithm II
PIV	Particle Image Velocimetry
PSD	Power Spectral Density
PWM	Pulse Width Modulation
RAM	Random Access Memory

RANS Reynolds averaged Navier-Stokes

RMC Royal Military College of Canada

RPM Revolutions per Minute

SWiFT Scaled Wind Farm Technologies

TSR Tip Speed Ratio

URANS Unsteady Reynolds averaged Navier-Stokes

VAWT Vertical Axis Wind Turbine

1 Introduction

1.1 Motivation for the Research

With the ongoing climate crisis, wind is considered a promising alternative energy source to fossil fuels. As of 2019, renewable sources account for approximately 11.4% of all energy produced, including in transportation, heating, and electricity [1]. To reduce the emissions of greenhouse gases, the main contributor to climate change, there is a need for a significant increase in renewable energy production. Wind is primarily caused by the uneven heating of the Earth's surface by the sun. This creates regions of low and high temperature, corresponding to higher and lower pressures, respectively. Wind is also affected by vertical pressure gradient, gravitational forces, the rotation of the Earth, and friction with the Earth's surface. Local features such as mountains and buildings also affect the wind [2, 3].

A wind turbine is a machine that converts wind energy into electricity. They are categorized into two groups, based on the axis of rotation. The most common group, Horizontal Axis Wind Turbines (HAWTs), have an axis of rotation parallel to the wind. The other group, Vertical Axis Wind Turbines (VAWTs), have an axis of rotation perpendicular to the wind. VAWTs are further classified by how they derive their power, whether through lift or drag [2,3]. Similar to modern HAWTs, lift-type VAWTs, such as the Darrieus rotor, generate power through a net positive torque between the tangential components of lift and drag. Drag-type VAWTs, on the other hand, such as the Savonius rotor or cup anemometers, generate power through a difference in drag between the advancing and retreating sides of the rotor [3]. Due to the irregularity of wind and its variation with location, there is no single wind turbine solution in terms of type, shape, size, or configuration.

HAWTs are generally preferred due to their high efficiencies and power outputs. To achieve this, however, they need clean, undisturbed flow for the best performance. This requires them to be built high above the ground and spaced far apart so that they are not affected by each other's wakes. HAWTs must also be oriented to face the wind, which necessitates a yaw setting system. These challenges are not an issue for VAWTs since they are omnidirectional. They can extract energy from wind coming from any direction and perform well with highly turbulent flow [3]. This makes VAWTs a promising clean energy solution to be employed in urban areas and on rooftops. With a lack of a yaw system, their simplicity and portability make them suitable for remote communities as well. These advantages, however, come at the cost of lower efficiencies and power outputs than HAWTs. Since VAWT blades rotate with an axis perpendicular to the wind, the angle of attack changes cyclically as it rotates, often resulting in angles of attack in the post-stall regime each rotation. For traditional airfoils, this means decreased performance after stall and during flow reattachment later in the cycle as a consequence of dynamic stall. The decreased efficiencies and power

outputs of VAWTs have been attributed to this phenomenon by several studies [4, 5]. Due to the cyclic nature of VAWTs, structural fatigue presents itself as another major problem with tensile and compressive stresses experienced by the blades during each rotation [3].

Tubercles are bio-inspired modifications of a wing leading edge that provide passive flow control [6]. At low angles of attack, tubercles behave similarly to conventional wings. However, at high angles of attack, they have been shown to improve the lift and drag characteristics post-stall. This improvement is attributed to counter-rotating stream-wise vortices that reattach the boundary layer. The result is a more gradual stall but with a reduced maximum lift coefficient [7–13]. Recent research has also shown that tubercles reduce the size of the dynamic stall hysteresis, minimizing the negative effects of dynamic stall [14, 15]. With improved post-stall characteristics, VAWTs would benefit from the higher aerodynamic efficiency, resulting in greater torque and consequently a higher power output compared to a straight leading-edge blade. The reduction in maximum lift coefficient may further benefit VAWTs by decreasing the range of tensile and compressive stresses experienced during each rotation. To date, most research applying tubercles to VAWT blades has been limited to Computational Fluid Dynamics (CFD) studies on fixed tubercle configurations. Thus, this thesis aims to analyze the effect of tubercles on VAWTs using methods that enable rapid evaluation and design optimization of various tubercle shapes for different wind environments and to confirm these findings using experimental means.

1.2 Research Objectives

This research aims to investigate the effect on the performance of various tubercle shapes when applied to the leading edge of VAWT blades. The optimal configuration of tubercles and turbine rotational rate in various wind environments is also explored. Specifically, the objectives are:

i. Develop and validate a Double-Multiple Streamtube Model (DMSTM) for rapid analysis and optimization of tubercles applied to VAWT blades,
ii. Generate a 2D experimental aerodynamic database of local lift and drag coefficients for different tubercle shapes for a range of Reynolds numbers to be used in the DMSTM,
iii. Evaluate the performance of various tubercle geometries in terms of power output and power coefficient using the DMSTM for a range of rotational rates and wind speeds compared to a baseline straight leading edge turbine,
iv. Create a multi-objective design optimization code to determine the ideal rotational rate and configuration of leading-edge tubercles along the blade span to maximize power output and fatigue life for a given wind environment,
v. Construct and run an experimental VAWT rig to validate the findings of the DMSTM, and
vi. Experimentally compare the startup performance of tubercle shapes compared to the baseline.

1.3 Thesis Layout

This thesis is organized into six chapters. Following the introduction, Chapter 2 will present a literature review of VAWT development, tubercles and their applications, and VAWT analysis methods. Studies investigating the application of leading-edge tubercles to lifting surfaces and VAWTs will also be discussed. Chapter 3 introduces the DMSTM, the initial experimental tubercle aerodynamic database used, and the effect of applying tubercles to VAWT blades. Chapter 4 explains the development of the multi-objective optimization routine and its results in various wind environments. Chapter 5 covers the development and results of the experimental VAWT campaign, showing the performance of tubercles on VAWT blades compared to a straight leading edge for various rotational rates. Finally, Chapter 6 completes the thesis with concluding remarks and recommendations for future research on this topic.

1.4 Contributions

The contributions of this thesis include:

i. The first analytical investigation of the effect that various leading-edge tubercle shapes have on the performance of VAWTs using the DMSTM,
ii. The development of a 2D aerodynamic database of various tubercle shapes from experimental data for use with the DMSTM,
iii. The first numerical optimization of leading-edge tubercles on VAWT blades in the current body of knowledge using the DMSTM and the first multi-objective optimization applying tubercles to VAWT blades,
iv. The design, construction, and commissioning of the Royal Military College VAWT Rig, and
v. An experimental study of different leading-edge tubercle shapes on VAWT blades and their effect on power output and startup characteristics.

2 Literature Review

This section presents research to date on vertical axis wind turbines (VAWTs) and leading-edge tubercles relevant to this thesis. This includes a historical review of wind turbines and current design considerations/methods, followed by current research on VAWTs. Subsequently, the background information on tubercles will be given, along with their effect on lifting surfaces and current research applying tubercles to VAWTs. Finally, methods of VAWT optimization and knowledge gaps aimed to be filled by this thesis will be described.

2.1 Background on Wind Turbines

The earliest recorded windmills were simple vertical axis drag-type mills from around the seventh century BC. It was not until around 1000 AD that the commonly known horizontal-axis windmills were used. Historical documents relating to these early mills were found in Persia, Tibet, and China [16]. The world's first electricity-generating wind turbine was built by James Blyth in July 1887 with a conventional horizontal axis European windmill design with cloth sails. This required him to turn the turbine into the wind manually and also furl the cloth to control the speed in high winds. To work around this, he built a vertical axis turbine in 1891, similar to the Robinson cup anemometer, because it was self-limited (lower efficiency at high wind speeds) and did not need to be rotated into the wind. This was also the first electricity-producing VAWT. Blyth went by three rules when it came to harnessing the wind: it must (i) be always ready to go, (ii) go without attendance for lengthened periods, and (iii) go through the wildest gale and be able to take full advantage of it [17]. His wind turbine can be seen in Figure 2.1. For size reference, there is a woman standing in front of the shed that was used to hold the batteries. Blyth used this turbine to light his home for 27 years until the start of the First World War. There are no records of the turbine's performance [18, 19].

The 1919 Agricco wind turbine in Denmark was the first use of airfoils on a wind turbine, while also being the first turbine connected to an AC network. It nominally produced about 40 kW [18]. The first lift-type VAWT was patented by Georges Jean Marie Darrieus in France in 1925 [20] and the United States in 1931 [21]. Deriving its power from lift, the design aimed to reduce the adverse effect of drag on the torque/power output that limited the efficiency of previous drag-type VAWTs. With drag-type VAWTs, the tangential speed of the rotor is at most equal to the speed of the wind, whereas for the Darrieus concept, the tip speeds could be greater than the wind speed, resulting in lower angles of attack (AoA). His patent included the curved troposkein bladed turbine, often called a Φ-configuration or a Darrieus turbine, where the blades are attached directly to the centre rotating shaft. An example of a Φ-rotor is shown in Figure 2.3. His patent also included the straight-bladed

H-rotor concept, where the blades are attached to the centre shaft by cross-arms.

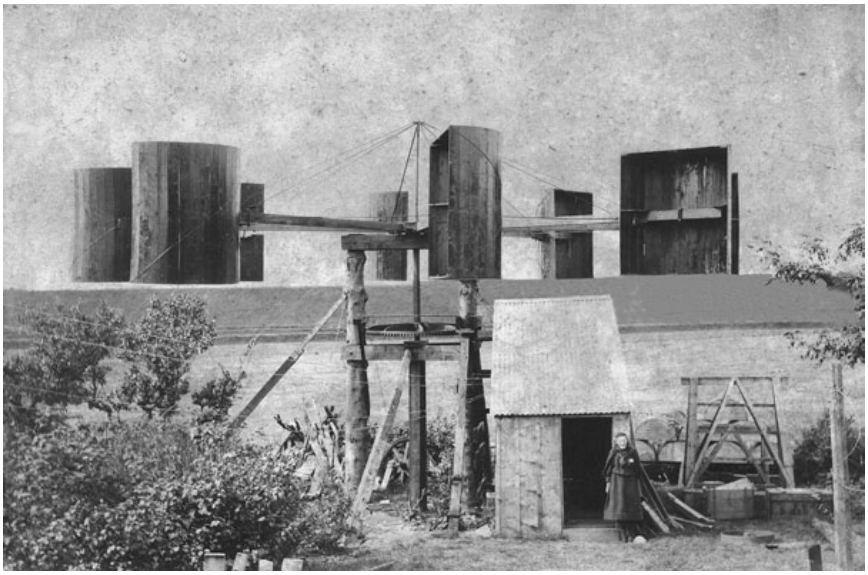

Figure 2.1: Blyth's vertical axis wind turbine [19].

2.2 Vertical Axis Wind Turbines

This section presents developments on VAWTs, specifically the lift-type, following the original patent by Darrieus. This includes the different configurations of the turbine blades, geometric and aerodynamic design considerations, flow control devices, and analysis methods.

To extract power from the wind, lift-type VAWTs require a net-positive torque resulting from the tangential component of lift, L, being greater than the tangential component of drag, D, on average throughout rotation. Therefore, to improve power output, there should be higher aerodynamic efficiencies (L/D) at higher AoAs. The range of AoAs experienced by the VAWT blades throughout rotation are influenced by the tip speed ratio (TSR), $\hat{\lambda}$, which is described by the following equation, where ω is the rotational velocity, R is the turbine radius at the equator, and V_∞ is the freestream velocity.

$$\hat{\lambda} = \frac{\omega R}{V_\infty} \tag{2.1}$$

Drag-type VAWTs, which rely on the advancing side having less drag than the retreating side, are limited to a TSR below unity, since they cannot spin faster than the wind. Lift-type VAWTs, on the other hand, can rotate faster than the wind, similar to a sail boat moving at an angle to the wind. The operating TSR varies between turbine designs, but is typically below 10.0 [3]. Figure 2.2 is a diagram of the aerodynamic forces experienced by the blades at four azimuthal stations throughout rotation. The azimuth angle, θ, is zero when the blade is upwind and perpendicular to the wind and increases in the direction of rotation. In this position, the highest positive AoA is experienced, as the induced velocity, V, is perpendicular to chord line of the airfoil. However, due to the turbine rotation, the blades also experience a tangential velocity, ωr, where r is the local turbine radius.

Combining V and ωr results in W, the local relative velocity, at an AoA, α. With a constant V_∞, increasing ω (i.e. increasing TSR), results in a lower AoA in this region. At $\theta = 180°$ in the downwind, the same is true, except it is now the position of the highest negative angle of attack. Additionally, the downwind induced velocity is dependant on the upwind induced velocity, as some energy was extracted by the blades in the upwind. The last two azimuthal positions shown are 90° and 270°, corresponding to the retreating and advancing sides, respectively. Both of these regions have an AoA of zero, resulting in only drag. However, on the advancing side, W is the sum of V and ωr, whereas the retreating side is the difference, resulting in less drag. For positions between these examples, the AoA decreases on the retreating side (0° to 180° azimuth), and increases on the advancing side (180° to 0° azimuth).

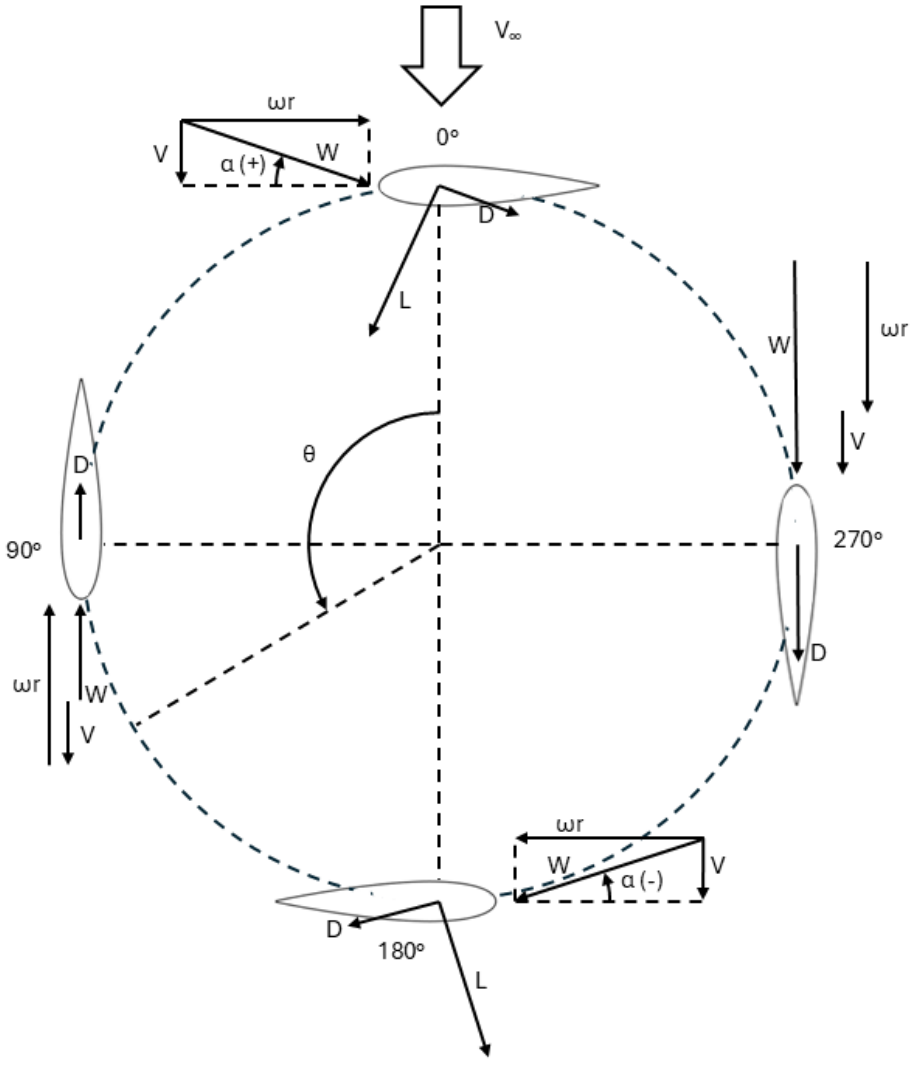

Figure 2.2: Diagram of lift-type VAWT aerodynamic characteristics throughout rotation at a TSR above 1.0.

2.2.1 Configurations

The Φ-rotor or 'Egg Beater' geometry, usually following a parabolic or troposkein shape, provides for minimum bending stresses in the blades. This allows for large-scale applications, such as the 3.8 MW Éole in Canada [22], as shown in Figure 2.3. However, it is difficult and costly to manufacture the blades, limiting commercial-scale production. On a large scale, typically above 100 kW, the blades also suffer from gravity-induced bending stresses, as opposed to the support arm on other configurations [23]. Since the diameter of the turbine reduces towards the tips of the blades, it also experiences lower starting torque, reducing the ability to self-start [24].

Figure 2.3: Éole VAWT in Quebec, Canada [25].

The straight-bladed H-rotor configuration is simple to construct compared to the Φ-rotor. It has enhanced starting characteristics since all the blades are at the furthest distance from the axis of rotation. An example of a straight-bladed H-type is shown in Figure 2.4 (a). The simple design also allows for active blade pitch control during rotation, such as a giromill, which can further enhance starting torque [24]. Although active pitch control provides greater power production than a fixed pitch Darrieus VAWT, the complex pitch-change system, support structures, and maintenance required have made it not economically viable, preventing it from being used on a large scale. Fixed pitch rotors, on the other hand, are known for fewer moving parts, leading to better availability, reliability, and lower maintenance costs than conventional wind turbines [23].

A few other variations of the H-rotor include the helical H-rotor, as shown in Figure 2.4 (b), where the blades are twisted along the perimeter of the rotor uniformly. This reduces the fluctuation of rotor torque during rotation, reducing cyclic stress on the drive train. The design also has reduced noise and gives an elegant design, making them common in urban areas. However, the helical blades are expensive to manufacture. There are also

(a) Uppsala University 200 kW H-type [26] (b) Quietrevolution© Qr6 Helical [27]

Figure 2.4: Examples of VAWTs.

studies into articulating H-rotors, where the blades are free to oscillate or tilt about the rotor hub, similar to a helicopter. It allows for self-starting in low winds, higher torque while operating, and quicker reaction to changing winds [23].

All the previous variations focused on the performance of individual turbines. However, other research has considered the performance of multiple turbines in farms or clusters. Since HAWTs require clean and undisturbed flow for the best performance, they are typically spaced 3-5 turbine diameters laterally and 6-10 diameters downwind. For these types of wind farms, the maximum power density is only 2-3 W/m^2 [28]. When it comes to VAWTs, studies have shown that they can be placed closer together, increasing the overall maximum power density, with some configurations increasing the power output of the average turbine compared to an individual turbine due to synergistic wake interactions [29]. Furthermore, individual VAWTs can have smaller footprints compared to a similar swept area HAWT since the height and radius of the VAWT are independent. These benefits suggest that VAWTs could be used in dense wind farms, having a smaller footprint than a HAWT wind farm producing equal power.

It is clear that for VAWTs to become a prevalent source of energy, they need to be simple with minimal moving parts to reduce construction and maintenance costs. Additionally, they should be able to self-start at low wind speeds, while also being able to take full

advantage of high winds to ensure the most power extraction by increasing their efficiency to be competitive with HAWTs. Finally, cyclic stresses on the blades and drive train should be reduced to minimize fatigue while also giving strong consideration towards reducing noise for applications in populated areas.

2.2.2 Modifications

Although there has been success with applying traditional NACA airfoils to VAWTs, VAWTs operate in unsteady conditions, oscillating between positive and negative AoAs, often experiencing stall. Thus, there have been efforts to design airfoils specifically for VAWTs [23]. Since the suction and pressure sides alternate throughout rotation on VAWT blades, it is believed that symmetric airfoils would give the greatest performance. However, the upwind and downwind blades do not share the same flow characteristics. With the loss of energy in the upwind half of the rotor, resulting in reduced local velocities in the downwind half, along with unsteady shed vortices, some research has challenged the use of symmetric airfoils on VAWTs [30].

Mohamed [31] numerically compared 20 airfoils, symmetric and asymmetric, based on NACA 00XX, NACA 63XXX, S-Series, A-Series, and FX-Series profiles using a sliding mesh discretization model with unsteady RANS calculations for an H-rotor VAWT. It was found that the symmetric S-1046 provided the highest power coefficient of all airfoils studied, and also provided a relative increase in power coefficient of 26.8% compared to the standard symmetric NACA airfoils. The symmetric airfoils also had a wider operating range of TSR.

Investigations by Wang *et al.* [32] used similar unsteady RANS calculations with a 2D sliding mesh of an H-rotor VAWT. They found that increasing the camber of a NACA 63A612 airfoil decreased the power coefficient for the range of cambers and TSRs evaluated. On the other hand, Sengupta *et al.* [33] experimentally found that an asymmetric EN0005 blade exhibited a faster start from static compared to a NACA 0018, and an asymmetric S815 blade yielded a higher power coefficient than the NACA 0018 in low TSR conditions. While the research is inconclusive on whether symmetric is definitively better than asymmetric, it is clear that there is room to improve upon the traditional airplane airfoils (i.e. NACA 4 series) as they are not optimized for VAWTs.

Although it may seem that a greater maximum lift coefficient would provide the best power output, Elkhoury *et al.* [34] performed experiments and a Large Eddy Simulation of a three-blade H-type VAWT and found that thicker airfoils tended to perform better as a result of the increased leading edge radius, which provided smoother stall characteristics, allowing for greater lift on average over the range of AoAs experienced by the turbine.

When it comes to the size and number of blades on the turbine, solidity should be considered. Solidity, σ, is the ratio of the rotor blade surface area divided by the swept area that the blades pass through, as calculated by the following equation, where N is the number of blades and c is the blade chord [35]:

$$\sigma = \frac{Nc}{2\pi R} \tag{2.2}$$

Work by Li and Li [35] using a 2D computational fluid dynamics (CFD) model of combinations of two and four blades with chord lengths of either 0.05 m or 0.1 m found that static

torque increased with solidity, consequently improving the VAWT's self-starting capability. Nevertheless, increasing solidity also decreased the maximum power coefficient, which occurred at a lower TSR. Experimental work by Li *et al.* [36] is in agreement with these findings. However, solidity was increased by increasing the number of blades. Rezaeiha *et al.* [37] used a 2D unsteady RANS simulation of two-, three-, and four-blade VAWT configurations while changing the solidity by increasing the chord length. While the results were consistent with previous findings that increasing solidity decreased the TSR of maximum power coefficient, it was noted that increasing solidity through longer blade chords improved the maximum power coefficient by as much as 22.5% as a result of favourable Reynolds number effects. Therefore, to effectively design a VAWT, local chords and Reynolds numbers must be considered.

Staelens *et al.* [38] studied the effect of changing pitch angle throughout the rotation of a straight-bladed VAWT. First, they tried to change the blade pitch angle such that the blade was just before stall throughout the entire rotation. This resulted in a linear increase in power with windspeed, providing significant improvements in power output. However, it was deemed mechanically infeasible due to the sudden change in pitch angle as the blade passes from the upwind to the downwind side of the rotor. Next, they changed the blade pitch angle such that the effective AoA would be just less than stall only when the geometric AoA is greater than the static stall angle. This eliminated the discontinuities in blade pitch angle as the blades pass between the upwind and downwind halves of the rotor. While this method improved power output, there were still abrupt changes in pitch angle, making it unfeasible since it would require an instantaneous change in pitch when the effective AoA would have increased beyond the stall angle. Lastly, they examined a pitch angle that followed a sinusoidal function throughout rotation. Although it did not exhibit as much of an improvement in power as the other two methods, it is mechanically feasible and shows some power output improvement over constant pitch blades. Actively changing the pitch in this manner, however, would require mechanical adjustments based on the wind direction. This would necessitate the equivalent of a yaw system, thereby increasing complexity and undermining the advantage of the VAWT's omnidirectional design.

Instead of actively changing the pitch of the blade to ensure the flow remains attached, some studies have tried flow control to promote flow attachment [30]. One of these methods is inward dimples, where a circular cavity is placed on the suction or pressure side of the airfoil near either the leading or trailing edge. The main hypothesis is that the dimple traps the vortex created during the pitch-up motion dynamic stall, leading to a gentler lift reduction after detachment of the primary vortex [39]. Using CFD, Sobhani *et al.* [40] found that cavities of diameter 8% chord placed towards the leading edge on the pressure side of a NACA 0021 provided an increase in average efficiency of 25% for the range of TSRs examined. Other methods include a gurney flap, leading-edge micro-cylinder, trailing-edge flap, and vortex generators [30].

When it comes to the performance of VAWTs, many factors play a role and often compete with the goals of a commercially viable VAWT. Even with something as simple as the number of blades, for example. Although increasing the number of blades improves the self-starting capability, it reduces the maximum power output. The same can be said for the other design considerations, including the modifications for flow control. There is a combination of design variables that best satisfies the goals of a VAWT, but even then,

that combination will change with different wind environments. Therefore, a method for designing VAWTs should be able to efficiently consider these various design variables for a solution in different environments.

2.2.3 Analysis Methods

Analysis of VAWTs is typically accomplished using a Momentum model, Vortex model, Cascade model, or CFD [3, 41–44]. Each method will be briefly discussed, including the advantages, drawbacks, and data gathered.

Momentum models, also called Blade Element Momentum models, determine the induced velocity of the turbine by calculating the streamwise aerodynamic forces on the blade with the rate of change of momentum of the fluid [41]. The main limitation of these models occurs at high TSRs and solidities, where the momentum equations are insufficient [3]. The first momentum model for VAWTs was the single streamtube model, proposed by Templin in 1974 [45]. With this model, a single streamtube is analyzed across the entire turbine, so the induced velocity is assumed to be constant throughout both the upwind and downwind sides of the rotor. The influence of airfoil properties and rotor geometry, such as solidity and size, is accounted for. While this is the simplest momentum model, it can only determine the overall performance of the turbine, including the torque and power coefficient. It was found by Paraschivoiu to over-predict the power output at certain TSRs and is unable to account for a wind velocity distribution across the rotor that would be caused by the boundary layer from the Earth's surface [3].

The Multiple Streamtube Model, introduced by Strickland [46], was built to address the drawbacks of the single streamtube model by dividing the rotor into a series of streamtubes, each having its own induced velocity through the rotor. Once again, using the streamwise momentum equation, the streamwise aerodynamic forces can be calculated with the changing momentum of the fluid. This allows for localized changes to geometry and free stream conditions, such as blade taper and wind shear/boundary layer, to be accounted for. While it provides more insight into where the torque and power contributions occur, it cannot consider local blade effects such as Reynolds number and dynamic stall [3].

The most recent form of the momentum model applied to VAWTs, the Double-Multiple Streamtube Model (DMSTM), was developed by Paraschivoiu in 1981 [47]. This model splits the streamtubes of the Multiple Streamtube model in half, one for the upwind and the other for the downwind portion of the turbine. With this improvement, the induced velocities vary between the upwind and downwind half of the rotor, accounting for the energy extracted, and consequently, the decreased velocity of the flow from the upwind half of the rotor. The influence of airfoil properties, Reynolds number, dynamic stall, the centre rotating tower, and struts could be properly accounted for. Not only does this model provide the overall power and torque coefficients, but it also gives the local aerodynamic characteristics throughout the rotation of the turbine, providing insight into the sources of positive or unfavourable performance. The cost of this model's simplicity is that it tends to over-predict power output for high solidity turbines, and has difficulties converging on the downwind side for high TSRs [41]. All the momentum models also require a 2D aerodynamic database of an airfoil's lift and drag with the AoA and Reynolds number to solve

for the induced velocities through iteration.

The vortex model was first used on a cyclogiro by Larsen in 1975 [48]. It uses a potential flow model that calculates the velocity field throughout the turbine using the influence of the vorticity in the wake of the turbine blades. The blades are represented by lifting-line vortices with strengths that are found in an aerodynamic database and the local flow velocity and AoA. The significant disadvantage of this model is the computational time, especially considering the simplifications, such as potential flow is assumed in the turbine wake, and experimental data is required to account for viscosity on blade aerodynamics [41].

The cascade model, typically used for turbomachinery, was first proposed for use on VAWTs in 1987 by Hirsch and Mandal [49]. Once the local flow velocity and AoA are determined, the turbine is put into the cascade configuration about a reference blade. The remaining blades are assumed to be on the same plane, with the distance between them equal to the circumference of the rotor divided by the number of blades. With an aerodynamic database dependent on the local Reynolds number and AoA, the instantaneous torque and power coefficients can be determined. After averaging the results for a complete rotation into a set of azimuthal steps, the overall power and torque coefficients can be determined. Although this model does not have convergence problems at high TSRs or solidities, it requires more computational time than the DMSTM and can only provide the overall performance characteristics of the VAWT.

The final and most common method of VAWT analysis is CFD. By modelling the turbine with a mesh, in either two or three dimensions, then iteratively solving a form of the Navier-Stokes equations, the characteristics of the flow field can be determined, subsequently providing the torque and power coefficients of the turbine. The benefit of CFD is that no aerodynamic database is required, and the influence of dynamic stall, tip vortices, and wake interactions, among others, can be accounted for without depending on semi-empirical equations/models [50]. The major drawback is the intensive computational cost and time. Furthermore, these costs will increase further when higher fidelity is required for complex flow behaviours such as post-stall, wake interactions, and vortices [51]. As a result, many optimization analyses using CFD on VAWTs rely on design of experiment methods to identify promising designs, while limited to a reasonable number of evaluations to reduce computational time [52–55].

When considering different VAWT analysis methods, the DMSTM stands out as the one with a good balance between fidelity, aerodynamic interactions and phenomena included, and computational time. This makes it suitable for initial design and optimization. Unlike the earlier momentum models, the DMSTM can account for phenomena such as dynamic stall, upwind/downwind blade-wake interactions, central tower, struts, and wake expansion while also accounting for local geometric characteristics along the blade span. Furthermore, a DMSTM analysis then results in span-wise aerodynamic characteristics throughout rotation, facilitating the investigation of causes behind turbine performance changes, while also giving an idea of forces experienced by the blades throughout rotation. The remaining analysis methods require more computational time than the DMSTM, making them infeasible or computationally expensive for the initial design and numerical optimization of a VAWT, where many design variables are considered. For these reasons, the DMSTM was the chosen analysis method for this thesis.

2.3 Background on Tubercles

Tubercles are bio-inspired rounded leading-edge protuberances found on the pectoral fins of humpback whales, which can be seen in Figure 2.5. Humpback whales are the only cetaceans (aquatic animals which include whales, dolphins, and porpoises) that have tubercles [6]. They are also the only baleen whale species that relies on manoeuvrability for feeding. Typically, a baleen whale's movement is restricted while skimming the water for food. However, humpback whales are known for swimming in tight circles while bubble-net feeding to round up their prey [56]. Tubercles were first hypothesized to be functional adaptations in terms of aerodynamic performance by reducing drag by Bushnell and Moore [57]. Fish and Battle [6] suggested that tubercles delay stall by producing vortices that prevent flow separation, maintaining lift and reducing drag at high AoAs. Although there was no physical evidence of vortices at the time, Fish and Battle noted that there was a lack of barnacles in between the tubercle peaks, suggesting the presence of eddies near the tubercle peaks that provided a velocity gradient low enough for the barnacles to attach [6].

Figure 2.5: Photograph of a humpback whale that shows the tubercles on the whale's pectoral fin [58].

To study the effect of tubercles, the tubercle geometry needs to be properly characterized. While other characterizations exist, including a power law model [59], the most common representation is a sine wave. The leading edge of an airfoil with tubercles is defined using an amplitude, A, and wavelength, λ, expressed as a percentage of airfoil chord. The airfoil coordinates forward of the maximum thickness are then scaled, only in the chord-wise direction, to follow the new sinusoidal leading edge. This ensures there are no discontinuities on the surface of the airfoil [60–62].

2.4 Tubercle Mechanisms

Following Fish and Battle's [6] initial work on tubercles, Watts and Fish [10] performed an inviscid simulation of a finite wing with leading-edge tubercles using a 3D panel code at 10° AoA. They observed a reduction in induced drag of 10.9%, an increase in lift of 4.8%, and subsequently an increase of 17.5% L/D for the tubercle wing compared to the straight leading edge. Their results also show a reduction in pressure coefficient in the troughs between tubercle peaks, as well as an increased density of streamlines in this region, suggesting a

higher local flow velocity. Further research by Fish and Lauder in 2006 [63] accounted for viscous effects using an unsteady RANS simulation, provided by Paterson *et al.* [64], of a NACA 63-021 in the same condition. This simulation revealed vortices in the region behind the tubercle troughs with chord-wise vorticity.

Johari *et al.* [8] was one of the first papers to compare the effect of varying tubercle wavelength and amplitude. They conducted water tunnel testing of a NACA 63_4-021 airfoil with six variants of sinusoidal leading-edge shapes for a range of AoAs from $-6°$ to $30°$ at a Reynolds number of 1.83×10^5. This provided results similar to those of Miklosovic *et al.* [7] in terms of C_L, showing an increase of up to 50% with the sinusoidal leading edge in the post stall regime. The tubercles, however, resulted in a greater C_D in the pre-stall regime. Johari *et al.* also performed flow visualization using tufts. They found that the flow remained attached well past the stall angle for the modified leading-edge wings. Additionally, when the modified wings stalled, it was mainly at the leading edge in the troughs between tubercles [8]. The authors also noted that smaller amplitudes resulted in higher stall angles and $C_{L_{\max}}$. Although not as significant, their results also show that smaller wavelengths provide higher stall angles and $C_{L_{\max}}$ [8].

Using the same water tunnel models as Johari *et al.* [8], Custodio [65] carried out flow visualization experiments beyond the tuft visualization of Johari *et al.* to further understand tubercle's effect on the flow. This included particle image velocimetry (PIV) and dye visualization. It was found that neighbouring vortices produced by a tubercle peak are counter-rotating and the vorticity is increasing with the AoA. PIV measurements showed little effect of tubercles on the wing tip vortex. However, wings with tubercles kept the wing tip vortex intact at high AoAs [65]. This confirms Fish and Battle's [6] initial speculation of the effect of tubercles on the flow.

Following the work of Miklosovic *et al.* [7], Pedro and Kobayashi conducted a CFD simulation of their work using Detached Eddy Simulation (DES), which uses Large Eddy Simulation (LES) outside of the boundary layer and Reynolds Averaged Navier-Stokes (RANS) in the boundary layer. After validating their lift and drag results against the experimental data of Miklosovic *et al.*, the simulation showed the presence of counter-rotating streamwise vortices, energizing the boundary layer but also creating a spanwise physical barrier for stall propagation from the flipper tip to root [66].

While it was shown that tubercles produce counter-rotating streamwise vortices, the actual mechanism of aerodynamic improvement is not well understood. There are several widely accepted theories which will be discussed in the following sections. These include vortex generators, induced flow, vortex lift, and wing fences [67].

2.4.1 Vortex Generators

Miklosovic *et al.* [7] conducted wind tunnel testing with two NACA 0020 wings with planforms resembling that of a whale flipper. One of the flippers had a smooth leading edge while the other had a sinusoidal leading edge that decreased in amplitude and wavelength towards the tip, similar to that found on whales. They found that, at Reynolds numbers of just over 5×10^5, tubercles can increase the stall angle by up to 40%. They also noted an increase in maximum lift coefficient, $C_{L_{\max}}$, of 6% with the tubercle flipper. Although

the tubercle flipper has a region of higher drag pre-stall, in the post-stall regime it outperformed the smooth leading-edge model by as much as 32% in terms of drag. As a result, for AoAs between 5° and 8.5°, the tubercle flipper has a lower aerodynamic efficiency, L/D. However, for the higher AoAs, it has a higher L/D than the straight leading-edge flipper, with significant improvement in the post-stall regime.

Miklosovic *et al.* compared these improvements to vortex generators. The vortices cause momentum exchange between the low-momentum boundary layer near the surface and the high-momentum region near the free stream. This additional momentum aids in keeping the flow attached despite an adverse pressure gradient [7]. However, the height of vortex generators is typically 10% to 50% of the boundary layer thickness [68], while the amplitude and wavelength are much larger than the boundary layer thickness [69]. While true, Hansen [70] suggests that the effective height of tubercles is dependent on the AoA, by the equation, $h_{\text{eff}} = A \sin \alpha$, since the actual height experienced by the flow is the component of the amplitude perpendicular to the flow. Using this equation, the effective height is within 10% to 50% of the boundary layer thickness, as suggested by Lin [68].

Stein and Murray [71] performed tests of tubercles and vortex generators applied to a NACA 0020 section and then compared them to the unmodified airfoil. It was found that the vortex generator provided similar lift pre-stall as the unmodified airfoil with greater lift post-stall, whereas the tubercles only had similar lift up to 3° AoA, but less lift beyond that angle. Although this suggests that tubercles do not behave like vortex generators, it is important to note that the vortex generators used were optimized for that airfoil section, whereas the tubercles were not. Therefore, an optimized tubercle shape could behave like a vortex generator and potentially provide similar or greater performance improvements.

2.4.2 Induced Flow and Vortex Lift

Since each tubercle produces a pair of counter-rotating stream-wise vortices (CRSWVs), as shown in Figure 2.6, there is a region of downwash at the tubercle peaks and a region of upwash at the troughs. This causes a lower effective AoA at the peaks and a higher effective AoA at the troughs creating a periodic change in the stall angle and pressure distribution while also thinning the boundary layer behind the peaks, resulting in a more gradual stall of the entire lifting surface [67, 69].

Vortex lift is similar to induced flow. As discussed by Bolzon *et al.* [67], vortex lift is caused by strong vortices producing downwash on the suction side of a wing, causing the flow to remain attached and delaying stall. Vortex lift is typically experienced by delta wings that have sharp, swept wings, creating significant vortices. It was proposed by Custodio [65] that this is a contributor to the improvements experienced by tubercles as a result of the CRSWVs created at the peaks. However, the vortex created by a delta wing is formed along the leading edge towards the tip of the wing. Therefore, the upwash portion of the vortex is outside the wing surface and does not increase the effective AoA. Whereas, for tubercled wings, both the upwash and downwash portions of the CRSWVs affect the lifting surface, which will periodically promote flow separation. Tubercles are also on a much smaller scale compared to delta wings, resulting in much weaker vortices compared to those produced by delta wings [67]. Thus, vortex lift likely does not account for a significant portion of the performance improvements shown by leading-edge tubercles.

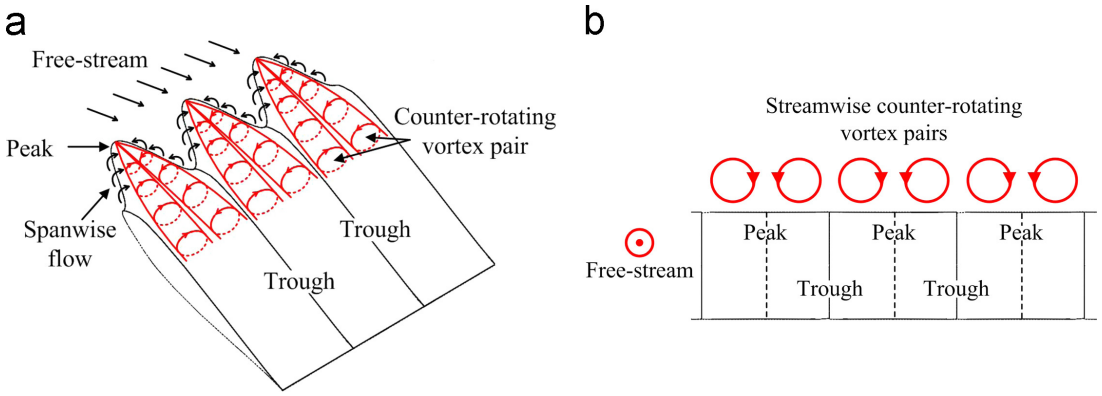

Figure 2.6: Counter-rotating stream-wise vortices produced by leading-edge tubercles in a 3D View (a) and as viewed at the trailing edge looking upstream (b). [72].

2.4.3 Flow Compartmentalization

The flow compartmentalization mechanism was first hypothesized by Watts and Fish [10], suggesting that the tubercles cause a perturbation of the span-wise flow on the wing, reducing the size of the wing tip vortex, which minimizes induced drag. If the CRSWVs affected the flow in a similar manner to wing fences, the stalled flow could be compartmentalized with further propagation inhibited, allowing other portions of the wing to create lift [73]. This could also explain the gradual stall onset [67].

To confirm that tubercles compartmentalize the flow, Cai *et al.* [74] performed a comparison between a fenced airfoil and a tubercle airfoil using an unsteady Reynolds-Averaged Navier-Stokes (URANS) solver. It was found that the fenced airfoil produced similar flow characteristics as the tubercle airfoil under various conditions. This confirmed the presence of a compartmentalization effect resulting from leading-edge tubercles.

The actual mechanism of tubercles is unlikely to be a single one, but rather a combination of these, each giving a specific effect, with vortex generation likely being the largest contributor. With tubercles typically providing enhanced lift and reduced drag in the post-stall regime at the expense of reduced characteristics during pre-stall, as well as yielding a gentler and delayed stall, promising applications would be where high AoAs are expected. Enhanced dynamic stall characteristics and noise reduction also open up more possible applications of tubercles [15, 67]. Some of these applications include propellers [75, 76], tilt-wing vehicles [77], rotorcraft [78, 79], and transonic wings [80], among others. The benefits of tubercles fit well into the requirements of the commercially viable VAWT. With a gentler and delayed stall, more power can be produced at low rotational rates, improving self-starting characteristics, while also increasing the overall torque since they provide a higher aerodynamic efficiency at a wider range of AoAs. Additionally, at low rotational rates where dynamic stall is present, tubercles could reduce the size of aerodynamic hystereses [15], further improving the power output. The reduction in maximum lift would benefit the VAWT due to the reduction in overall tensile and compressive stresses experienced by the blades, potentially improving fatigue life, which would reduce required maintenance. This modification is also a simple passive method, not increasing the mechanical complexity of the VAWT, with the potential of reducing overall noise.

2.5 Tubercles Applied to VAWTs

The first reported and accessible application of tubercles on a VAWT was performed by Chan [81] in 2014 as part of their Master's thesis. Using an open jet wind tunnel, various VAWT blade configurations on a mini-turbine were examined. A NACA 0015 straight leading-edge blade of 6 cm was compared to an $A12\lambda50$ blade. They found that the tubercle blade had a significantly lower power coefficient compared to the straight blade for TSRs down to stall at a wind speed of 6 m/s. Since TSRs were not low enough to result in AoAs beyond stall, the enhancement of aerodynamic efficiency post-stall was not captured. Additionally, this study only examined a single tubercle configuration and a single wind speed. Notably, with large amplitude tubercles, aerodynamic efficiency is significantly lower, especially in the pre-stall regime, as determined by Hansen [70]. To properly assess the applicability of tubercles to VAWTs, a wider range of wind speeds and tubercle configurations would need to be examined.

During their PhD Thesis in 2015, Du [82] compared tubercles to a NACA 0018 using the DMSTM. Using the aerodynamic database produced by Sheldahl and Klimas [83], Du modified the lift curves to provide similar characteristics provided by tubercles by reducing the pre-stall lift and increasing the post-stall lift to provide a more gradual stall. The results using the modified and original database showed that the 'tubercle' geometry yields a higher power coefficient at TSRs below four. While this shows that tubercles should provide improved performance at low TSRs, it does not use an actual tubercle aerodynamic database. Furthermore, the effect of tubercles was only assumed to change the lift curves post-stall, and the drag only differed around the point of stall, despite post-stall drag being improved by tubercles as well. Du also performed an experimental comparison between an unmodified NACA 0021 and an $A03\lambda11$ NACA 0021. The results showed significantly improved self-starting capabilities of the tubercle blades but did not provide a comparison in terms of power output with the unmodified blade, since it failed to self-start. While later work by Du *et al.* [84] includes a new unmodified blade with an aspect ratio of seven that self-starts and shows an improved peak power coefficient compared to the original tubercle blade, the results should not be directly compared because the original tubercle blade has an aspect ratio of six.

In 2015, Bai *et al.* [85] performed a URANS simulation of tubercle blades with varying amplitudes and wavelengths. The model consisted of a single tubercle wavelength with periodic boundary conditions at the tubercle peaks, ignoring tip vortices that would be generated spanwise. They found that all tubercle shapes reduced the average thrust by 1%-10% at a TSR of 1.6, providing AoAs between 0° and 40°, while increasing tubercle amplitude reduced the average thrust. Although this study solidifies the trends of improved aerodynamic efficiency with decreased tubercle amplitude, it does not capture the effect of flow compartmentalization or tip vortices due to the simulation using periodic boundary conditions at the tubercle peaks. Additionally, only one TSR is examined, so tubercles may outperform the straight leading edge at different TSRs.

Sridhar *et al.* [86] conducted a 3D unsteady RANS CFD simulation of a two-bladed H-type VAWT for three tubercle shapes at six different TSRs. It was found that all tubercle shapes studied outperformed the straight leading edge baseline, with the greatest improvement being a 28.1% increase in power coefficient at a TSR of 2.5. During dynamic stall,

the tubercles showed an increase in maximum lift coefficient of 14.4% while maintaining a 28% lower drag coefficient. By analyzing the streamlines in the tubercle peak and troughs throughout the turbine rotation, it was apparent that the baseline blade showed complete flow separation during dynamic stall, whereas the flow over the peak section of the best-performing tubercle shape remained attached, while partial separation and flow circulation were present in the troughs. The simulation also revealed a reduction in noise by 20% and 12% in the mid-plane and tip-plane of the blade, respectively. While this study provides an excellent amount of information, giving insight into the effects of tubercles on dynamic stall, noise, and overall power production, it is computationally expensive. Although the computer used is not described, it took 8.2 days to solve their medium-scale mesh of 6.1 million elements. This would make it infeasible for large-scale design optimization without making considerable trade-offs, such as limiting the number of design variables or using a design of experiments method.

In 2022, Gonçalves *et al.* [87] tested a three-bladed H-type VAWT with 3D-printed blades in an open jet wind tunnel. Using a brushless motor to control the braking torque or start the turbine in low wind velocity conditions, the startup and performance characteristics of a baseline straight leading edge were evaluated against an $A0.8\lambda17$ leading edge tubercle blade. The modified blade not only was able to start at a 20% lower wind speed but also only required 50% of the time to reach the nominal rotational speed compared to the baseline. In addition to improved starting characteristics, the modified blade produced 46% to 20% more power compared to the baseline, with the improvement diminishing as wind speed increased. While this paper provided performance data determined through CFD of multiple tubercle amplitudes and wavelengths, only the best-performing $A0.8\lambda17$ was tested experimentally.

Although many studies show the improvements that leading-edge tubercles provide to VAWTs, the majority of them use CFD [85, 88–93]. While this aids in detailing the mechanisms of improvement that the tubercles provide, it limits the number of configurations, tubercle shapes, and data points that can be analyzed as a result of the significant computational cost. Other studies have used experimental methods to examine the effects of tubercles, but have typically used a single tubercle shape or did not examine a complete range of TSRs or wind speeds [81, 82, 84, 87, 90, 94, 95]. Du's PhD thesis [82] was the only work to explore the use of the DMSTM with tubercles as a fast analysis alternative. However, the tubercle aerodynamic data used in the DMSTM was derived from straight leading edge NACA 0018 data with modifications to smooth out the lift curve past the critical AoA, and the increasing drag about the critical region. This does not account for the decrease in lift pre-stall nor the improved drag characteristics post-stall. Therefore, this domain of tubercle research is lacking a sufficient set of experimental data for a variety of tubercle shapes, and a range of wind speeds and TSRs, along with a DMSTM analysis of a diverse set of tubercle shapes using an experimental aerodynamic database. This thesis aims to fill these deficiencies in the current body of knowledge.

2.6 VAWT Design, Analysis, and Optimization

Chen *et al.* [96] combined the DMSTM with a Covariance Matrix Adaptation Evolutionary Strategy (CMAES) to determine the optimal equatorial radius, the ratio of radius over half-height, and the number of blades of a Φ-shape VAWT for a given range of wind speeds. The resulting geometry provided a 12.5% higher efficiency compared to the baseline two-blade Sandia 5m turbine. A CFD simulation of the resultant geometry provided good agreement with the DMSTM result, while also providing wake and vortex insight. For comparison, the entire optimization using the DMSTM-CMAES framework performed 150 evaluations in less than one hour, while a single instance for validation using their CFD model took 200 hours.

In 2018, Wang *et al.* [55] used CFD paired with the Taguchi method to find the best combination of helical twist, tubercle amplitude, and wavelength of a three-bladed VAWT. For each of these design variables, there were three potential values. After analyzing 9 of the 27 potential combinations at a single TSR using CFD, an additive model was used to estimate the performance of the remaining combinations. The combination with the best-estimated performance was then analyzed at the same TSR in CFD. However, it yielded a lower performance than the best performing of the original nine combinations. A different additive model was used, however, the resulting combination was the best performer in the original nine. So, it was concluded that the best combination is an $A2.5\lambda17$ leading edge tubercle blade with a helical twist of 60° at a TSR of 2.0, which improved the power output by 18.3%. While this shows that the Taguchi method can be used to reduce the computational time of optimization, it was only done at a single TSR and would get significantly more computationally expensive with increased design variables, such as tubercle shape variation along the blade, or if a more accurate optimal amplitude, wavelength, or helical twist is desired, as more combinations would be required.

In 2023, ul Hassan *et al.* [54] used a hybrid design of experiments approach with response surface methodology paired with CFD to evaluate 14 different combinations of tubercle amplitude and wavelengths for a fixed turbine geometry at the baseline on-design TSR of 2.1 and an off-design TSR of 3.7. At on-design conditions, the tubercles result in a degradation in moment coefficient by approximately 14%, while providing at most a 55% improvement during off-design conditions. While this studied more combinations of tubercle amplitude and wavelengths compared to Wang *et al.* [55], the tubercle shape on the blade was not varied along the blade and the turbine geometry was fixed. Interestingly, the worst-performing tubercle shape during the off-design condition was also the best-performing shape when on-design for the baseline blade. Since only two TSRs were considered, it is unknown which tubercle shapes would perform best for the widest range of TSRs. To further emphasize the computational cost of CFD, each of their evaluations took a 32-core, 2.1 GHz processor, with 128 GB of random access memory (RAM), two weeks to compute the 10.46 million element medium mesh [54]. Multiplying the time per task by the number of cores and the clock speed gives approximately 8.1×10^{16} clock cycles per task, assuming the algorithm is perfectly parallelized and not RAM limited.

To study the effect of partially applying tubercles to a VAWT blade, Butt *et al.* [53] used CFD on five configurations of $A10\lambda25$ varying from 0 to 100% of the blade leading edge of a two-bladed helical marine turbine. It was found that covering only 25% of the span,

starting from the blade tips, provided the greatest improvement of 14.48% in the average torque at a TSR of one. Using the determined optimal coverage, four different combinations of tubercle amplitude and wavelengths were simulated at the same TSR. The $A20\lambda25$ shape covering only 25% of the span was found to produce an average torque 15.2% higher than the baseline straight leading edge. Just like the previous CFD optimizations of tubercles, this was only done at a single TSR. It also does not consider that other tubercle geometries may provide more improvement with a different percentage of the span, nor does it apply multiple tubercle shapes in the same configuration. For example, one shape may provide the greatest benefit at the blade tips, while another could further improve the configuration if placed at the centre of the blade simultaneously.

Overall, current research aiming to optimize tubercles applied to VAWT blades is mainly compensating for the increased computational time of CFD by using the design of experiments, which limits the design space/configurations and does not completely search the design space with sufficient resolution. Other research reduces the problem to a specific TSR, which fails to get the full picture of the turbines' performance. Instead of limiting the optimization to ensure a high fidelity result, there should be more effort to use faster methods of medium fidelity, such as DMSTM, to better search the design space. Then, one can use a higher fidelity method, such as CFD, to get a more accurate understanding of the performance and flow characteristics of that optimized configuration, as was done by Chen *et al.* [96].

2.7 Knowledge Gaps

Current research on applying tubercles to VAWTs is primarily focused on understanding the sources of improvements through the use of CFD, which is computationally expensive. To date, there has been one attempt at analyzing tubercles using the DMSTM, performed by Du [82]. However, a modified aerodynamic database was used, instead of a proper tubercle database. This analysis also examined only a single representative shape, despite evidence showing that the tubercle shape has a significant impact on VAWT performance. When it comes to the optimization of tubercles on VAWT blades, all research has used CFD to analyze while limiting the design space and variables, and also reducing the resolution that they are searching with, to compensate for the increased computational time of CFD. This is typically done by limiting the study to a single TSR while analyzing a limited number of designs or by limiting the optimization to a single variable. There has been no optimization of tubercles on VAWT blades using a medium-fidelity method, such as the DMSTM, nor one that properly optimizes a turbine for use in a real-world environment, including structural considerations such as fatigue life. Furthermore, there has been no investigation analyzing and optimizing the tubercles applied to VAWT blades, which includes an experimental validation of the results. While there have been experimental investigations of tubercles on VAWTs, they are typically limited to a single tubercle shape or examine a narrow range of TSRs or wind speeds. This thesis aims to fill these knowledge gaps in a comprehensive investigation using the DMSTM in a large-scale design optimization supplemented with experimental validation to further demonstrate how tubercles can be applied to VAWTs to improve their performance and fulfill the goals of a commercially viable VAWT.

3 Analysis of VAWTs with Leading-edge Tubercles

The literature review revealed a lack of research using computationally efficient methods to analyze leading-edge tubercles applied to the blades of vertical axis wind turbines (VAWTs). This chapter aims to fill this knowledge gap by developing the first Double-Multiple Streamtube Model (DMSTM) paired with an experimental tubercle airfoil aerodynamic database. This includes convergence studies, validation, and the creation of the experimental aerodynamic tubercle database. The performance of tubercles applied to a small-scale H-type VAWT was then characterized through power contours, showing the effect of wind speed and tip speed ratio (TSR) on the overall performance compared to a straight leading-edge turbine blade. These contours were then used to show the average power output for a given wind environment with varying TSR. The physical sources of improvement given by tubercles were also explored.

3.1 Methodology

As described in Chapter 2, there are a variety of methods for analyzing VAWTs. The DMSTM was chosen for its minimal computational cost, while still considering more aerodynamic phenomena than other momentum models, such as dynamic stall, upwind/downwind blade-wake interaction, and local geometric characteristics, among others. These benefits also make the DMSTM a viable analysis method for optimization routines. This section describes the development of the DMSTM code used throughout this thesis. The creation of the experimental tubercle database is described, followed by a way of characterizing the performance of a turbine design for a given wind environment.

3.1.1 Double-Multiple Streamtube Model

To determine the effects on performance that various tubercle shapes have when applied to VAWT blades, the DMSTM, introduced by Paraschivoiu [3], was used. This numerical approach is based on the conservation of momentum and uses the aerodynamic forces on the turbine blades to determine changes in stream-wise momentum by discretizing the rotor into several streamtubes. These streamtubes are located by an azimuth angle, θ, and local rotor height, z, such that the entire turbine cross-section is represented by a set number of streamtubes in the azimuthal and height directions. Unlike previous streamtube models, such as single or multiple streamtube, the DMSTM splits each rotor element into two actuator disks in tandem, accounting for the upwind and downwind halves of the turbine. It uses an iterative approach that is briefly described in the flow chart shown in Figure 3.1. Figure 3.2 is a visual of the geometric variables used in the DMSTM. While this subsection

covers equations used in the code, the derivations can be found in detail in Chapter 6 of Paraschivoiu's textbook [3].

For each streamtube, the upwind induced velocity, V, is given by [3]:

$$V = uV_\infty \tag{3.1}$$

where u is the upwind interference factor and V_∞ is the local wind velocity, which could be a function of height above the ground and/or azimuth to account for phenomena such as boundary layer in the wind. u is initially assumed to be unity. However, it is recalculated each iteration and is used to determine convergence. The local blade Reynolds number, Re_b, and the local angle of attack (AoA), α, are then determined by the following equations where W is the local blade relative velocity [3].

$$Re_b = \frac{cW}{\nu_\infty} \tag{3.2}$$

$$\alpha = \sin^{-1}\left(\frac{V\cos\theta\cos\delta}{W}\right) \tag{3.3}$$

$$W = V\sqrt{\left(\frac{r\omega}{V} - \sin\theta\right)^2 + \cos^2\theta\cos^2\delta} \tag{3.4}$$

where c is the local blade chord, ν_∞ is the freestream kinematic viscosity, r is the local turbine radius, ω is the angular velocity of the turbine, θ is the azimuthal position of the centre of the streamtube on the turbine radius, and δ is the local meridian angle of the blade, shown in Figure 3.2. The local normal and tangential coefficients, C_n and C_t, respectively, are determined through interpolation of an airfoil aerodynamic database. This allows verification of the initially assumed interference factor through the following equations [3].

$$u(\theta) = \frac{KK_0\eta}{KK_0\eta + \displaystyle\int_{\theta-\Delta\theta/2}^{\theta+\Delta\theta/2}\left(\frac{W}{V}\right)^2\left(C_n\cos\theta + C_t\frac{\sin\theta}{\cos\theta}\right)d\theta} \tag{3.5}$$

$$K = \frac{8\pi r}{Nc} \tag{3.6}$$

$$K_0 = \sin(\theta + \Delta\theta/2) - \sin(\theta - \Delta\theta/2) \tag{3.7}$$

where N is the number of blades, and η is the normalized local radius (r/R). This process is repeated for each upstream streamtube until the convergence of their respective interference factors. The same is performed for the downstream half of the turbine, except now the induced velocity is a function of the upstream and downstream interference factors, where the prime variables denote the downstream [3].

$$V' = u'(2u - 1)V_\infty \tag{3.8}$$

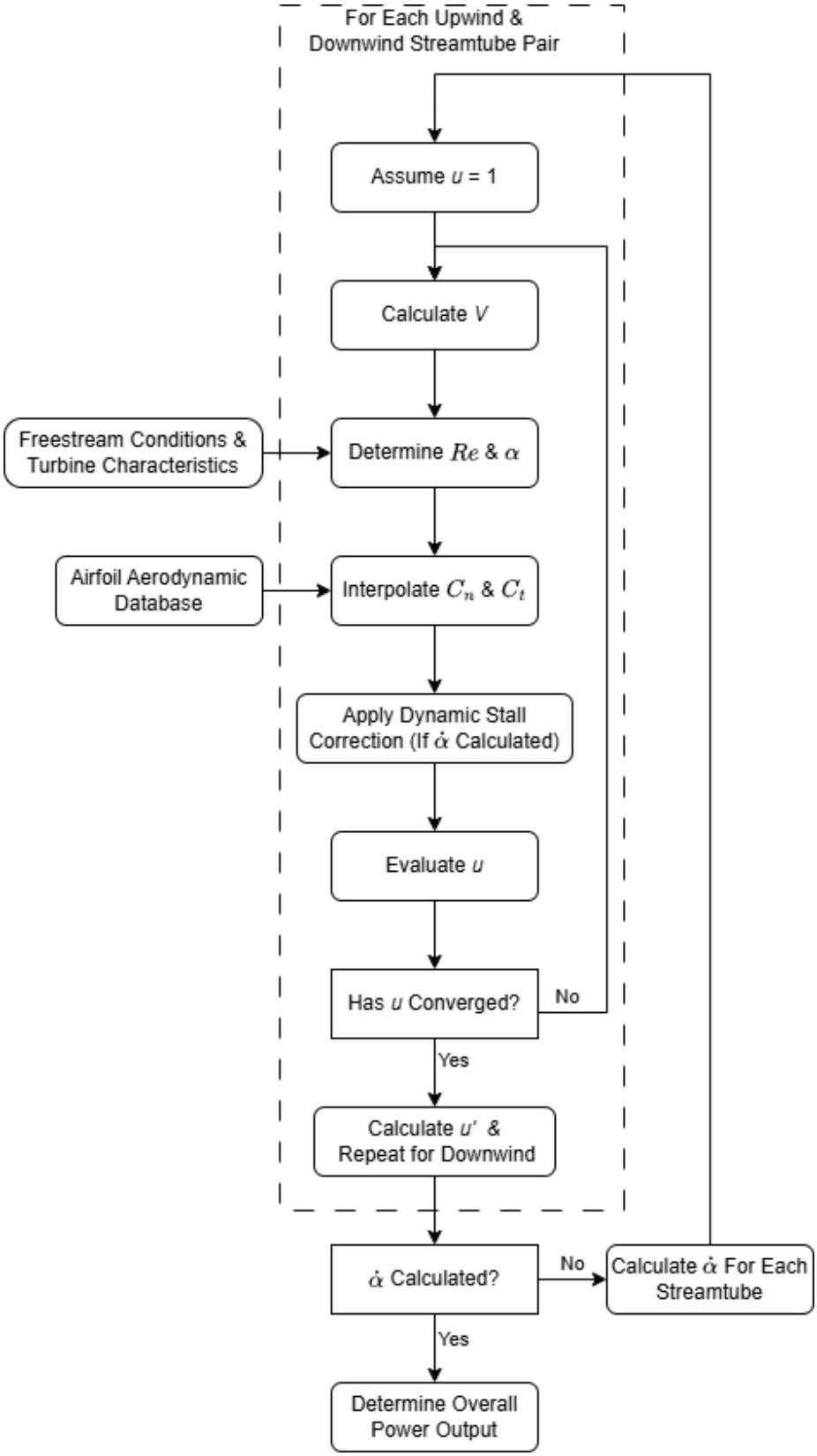

Figure 3.1: DMSTM Flow Chart. Steps contained within the dashed box are performed for each streamtube upwind/downwind pair before continuing to the items outside the dashed box.

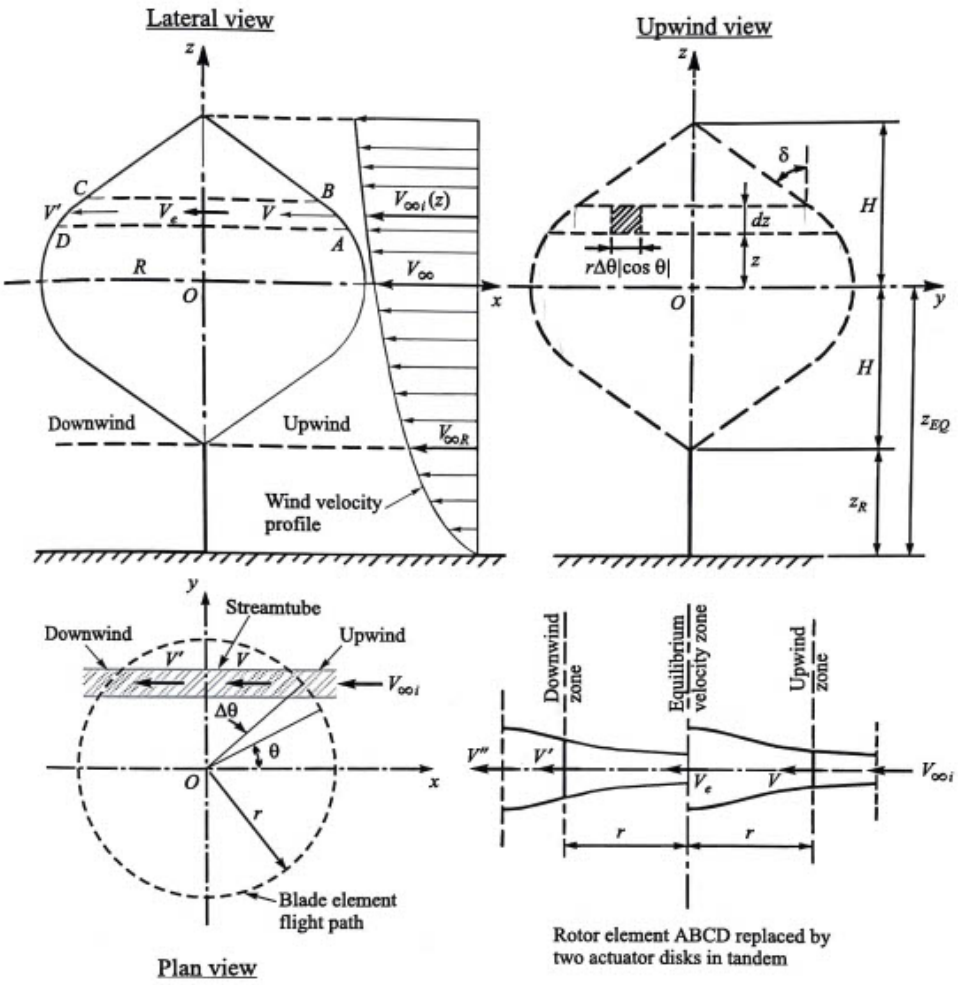

Figure 3.2: Double Multiple Streamtube Model Symbols and Dimensions [3].

With the upstream and downstream interference factors of each streamtube solved, along with their corresponding local aerodynamic characteristics, the normal and torque coefficients produced by a full blade as a function of azimuthal position can be determined by [3]:

$$C_N = \frac{cH}{S} \int_{-1}^{1} C_n \left(\frac{W}{V_\infty}\right)^2 \left(\frac{\eta}{\cos\delta}\right) d\zeta \tag{3.9}$$

$$C_T = \frac{cH}{S} \int_{-1}^{1} C_t \left(\frac{W}{V_\infty}\right)^2 \left(\frac{\eta}{\cos\delta}\right) d\zeta \tag{3.10}$$

where H is the rotor half-height, S is the rotor swept area, and ζ is the normalized local height (z/H), ranging from -1 to 1 with the rotor equator at 0. Finally, the overall power coefficient, C_P, and power, P, of the turbine are determined by [3]:

$$C_P = \frac{R\omega N}{2\pi V_\infty} \left(\int_{-\pi/2}^{\pi/2} C_T \, d\theta + \int_{\pi/2}^{3\pi/2} C'_T \, d\theta \right) \tag{3.11}$$

$$P = \frac{1}{2}\rho S V_\infty^3 C_P \tag{3.12}$$

where R is the rotor radius at the equator and ρ is the freestream density.

Dynamic Stall

Dynamic stall is an aerodynamic phenomenon resulting from the rate of change of AoA, creating a vortex that starts at the leading edge and is later shed at the trailing edge [3]. This causes a delay in flow separation while increasing AoA, and delays flow reattachment as AoA decreases. With VAWT blades rotating on an axis perpendicular to the wind, the AoA experienced by the blades is constantly changing throughout rotation, often into the post-stall regime. To account for these effects of dynamic stall, an adaptation of Berg's model was used [3]. First, all streamtubes are solved using the static aerodynamic characteristics. Then, the entire turbine is solved again using the dynamic stall model, with $\dot{\alpha}$ at each streamtube determined by a central finite difference of the adjacent streamtubes' α, solved statically. In the adaptation, the dynamic stall characteristics are only used in regions of low turbulence, not affected by the shed vortex of the upwind half of the rotor. So, for azimuth angles between 15° and 135°, static aerodynamic characteristics were used. [3]

Berg's model [97] is a modification of Gormont's dynamic stall model [98], which introduces a reference AoA, α_{ref}, to model the dynamic stall hysteresis depending on the rate of change of AoA, $\dot{\alpha}$, the local relative velocity, W, the local blade chord, c, the blade thickness to chord ratio, t/c, and the Mach number, M. K_1 was altered to be a function of the sign of α, $\operatorname{sgn}(\alpha)$, so that α_{ref} would decrease if α and $\dot{\alpha}$ have the same sign, and increase if not. This ensured the correct application of the model in the downwind half of the rotor, where α is negative.

$$\alpha_{\text{ref}} = \alpha - K_1 \Delta\alpha \tag{3.13}$$

$$\begin{aligned} K_1 &= \begin{cases} \operatorname{sgn}(\alpha) & \dot{\alpha}\operatorname{sgn}(\alpha) \geq 0 \\ -0.5\operatorname{sgn}(\alpha) & \dot{\alpha}\operatorname{sgn}(\alpha) < 0 \end{cases} \\ \Delta\alpha &= \begin{cases} \gamma_1 S & S \leq S_c \\ \gamma_1 S_c + \gamma_2 (S - S_c) & S > S_c \end{cases} \end{aligned} \tag{3.14}$$

$$S = \sqrt{\left|\frac{c\dot{\alpha}}{2W}\right|} \qquad S_c = 0.06 + 1.5\left(0.06 - \frac{t}{c}\right) \tag{3.15}$$

$$\begin{aligned} \gamma_1 &= \begin{cases} \dfrac{\gamma_2}{2} & \text{for lift characteristic} \\ 0 & \text{for drag characteristic} \end{cases} \\ \gamma_2 &= \gamma_{\max} \max\left\{0, \min\left[1, \frac{M - M_2}{M_1 - M_2}\right]\right\} \end{aligned} \tag{3.16}$$

With α_{ref} determined, the local dynamic lift and drag coefficients, C_l^{dyn} and C_d^{dyn}, respectively, are calculated by the following equations. The local lift and drag coefficients shown in the equations are determined through interpolation of the aerodynamic database for the

Table 3.1: Forms of M_1, M_2, and $\gamma_{\max}$. [3]

	Lift Characteristic	Drag Characteristic
M_1	$0.4 + 5.0(0.06 - t/c)$	0.2
M_2	$0.9 + 2.5(0.06 - t/c)$	$0.7 + 2.5(0.6 - t/c)$
$\gamma_{\max}$	$1.4 - 6.0(0.06 - t/c)$	$1.0 - 2.5(0.06 - t/c)$

given angle and local *Re*. Note that C_l^{dyn} is a function of the lowest C_{l_α} to either the static stall angle, α_{ss}, or α_{ref}. Thus, an α_{ref} below α_{ss} would delay stall onset, while a higher α_{ref} would give an unfavourable C_{l_α}, modelling the delay in flow reattachment. In the following equation, α_0 is the zero-lift angle of attack.

$$C_l^{\text{dyn}} = C_l(\alpha_0) + \min\left[\frac{C_l(\alpha_{\text{ref}}) - C_l(\alpha_0)}{\alpha_{\text{ref}} - \alpha_0}, \frac{C_l(\alpha_{ss}) - C_l(\alpha_0)}{\alpha_{ss} - \alpha_0}\right](\alpha - \alpha_0) \tag{3.17}$$

$$C_d^{\text{dyn}} = C_d(\alpha_{\text{ref}}) \tag{3.18}$$

With the dynamic lift and drag determined through Gormont's model, Berg's modification is applied through the following equations, interpolating between the static and dynamic lift coefficients. Although these equations were originally used by Massé [99], who used $A_M = 1.8$, an empirical constant. For Berg's adaptation, $A_M = 6$ was used, while also using the definition of α_{ss} as the angle at which lift coefficients depart from linear behaviour, not the static stall angle [97]. Also, note that the absolute value of α was used to ensure the proper application of the model in the downwind half of the turbine.

$$C_l^{\text{mod}} = \begin{cases} C_l + \left[\dfrac{A_M\alpha_{ss} - |\alpha|}{A_M\alpha_{ss} - \alpha_{ss}}\right](C_l^{\text{dyn}} - C_l), & |\alpha| \leq A_M\alpha_{ss} \\ C_l, & |\alpha| > A_M\alpha_{ss} \end{cases} \tag{3.19}$$

$$C_d^{\text{mod}} = \begin{cases} C_d + \left[\dfrac{A_M\alpha_{ss} - |\alpha|}{A_M\alpha_{ss} - \alpha_{ss}}\right](C_d^{\text{dyn}} - C_d), & |\alpha| \leq A_M\alpha_{ss} \\ C_d, & |\alpha| > A_M\alpha_{ss} \end{cases} \tag{3.20}$$

The dynamic stall corrections were applied within the iterative loop of the DMSTM for each streamtube. After correcting the interpolated aerodynamic characteristics from the experimental database, the process was repeated until convergence of the interference factor by Equation 3.5. The final overall torque can be calculated while also providing the local lift and drag of the rotor through each streamtube.

Blade Tip and Finite Aspect Ratio

To account for finite aspect ratio and tip effects on the turbine blades, Willmer's modified version of Prandtl's method for these effects is applied by modifying W of Equation 3.4 to be a function of a factor, F [100]:

$$W = V\sqrt{\left(\frac{r\omega}{V} - \sin\theta\right)^2 + F^2\cos^2\theta\cos^2\delta} \tag{3.21}$$

$$F = \frac{\cos^{-1}\left[\exp\left(\frac{-N\omega(H-|z|)}{V_e}\right)\right]}{\cos^{-1}\left[\exp\left(\frac{-N\omega H}{V_e}\right)\right]} \tag{3.22}$$

V_e is the induced equilibrium velocity, which is located at the connection between the upstream and downstream streamtubes. It is calculated by:

$$V_e = (2u - 1)V_\infty \tag{3.23}$$

3.1.2 Average Power Output

Since wind turbines are not always going to be operating at their ideal or maximum power output condition due to the variability of wind, the probability-weighted average power output, $\bar{P}$, was used to characterize the performance of each tubercle shape. For a given wind environment probability density function, $Pr(V)$, the average power output for a range of wind speeds is given by [2]:

$$\bar{P} = \int_0^\infty P(V)Pr(V)\,dV \tag{3.24}$$

where the power was calculated for a range of wind speeds using the DMSTM. For this comparison, the wind speed probability density function will be modelled using a two-parameter Weibull distribution, represented by the following equation [101].

$$Pr(V) = \frac{k}{\tilde{\lambda}}\left(\frac{V}{\tilde{\lambda}}\right)^{k-1} e^{-(V/\tilde{\lambda})^k} \tag{3.25}$$

The shape parameter, k, and scale parameter, $\tilde{\lambda}$, are determined experimentally, typically by recording wind speeds throughout the year at a specific site. This thesis uses two distributions, one using data from the Scaled Wind Farm Technologies (SWiFT) Test Site in Lubbock, Texas [101], while the other was determined for Kingston, Ontario, using publicly available data, as described in Appendix B. The SWiFT Test Site distribution is used in Chapter 3, while the distribution for Kingston is used in Chapter 4 alongside the SWiFT test site to provide a lower probable wind speed distribution. The shape and scale parameters are given in Table 3.2, and the resultant wind speed probability distributions are shown in Figure 3.3. The SWiFT Test Site has a higher most probable wind speed of about 6.5 m/s, with near zero probability of wind speeds above 15 m/s, while Kingston, ON, has a peak probability around 3 m/s.

Table 3.2: Shape and Scale Parameters of SWiFT Test Site and Kingston, ON wind speed probability distributions.

Location	Shape Parameter, k	Scale Parameter, $\tilde{\lambda}$ (m/s)
SWiFT Test Site [101]	2.773	7.499
Kingston, ON	1.767	4.936

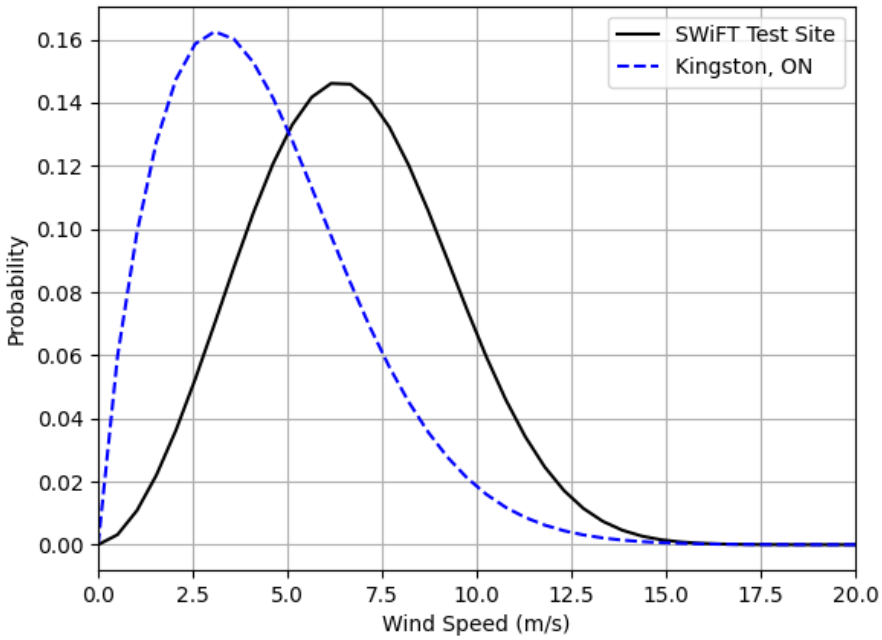

Figure 3.3: Wind speed probability Weibull distributions of the SWiFT Test Site and Kingston, ON.

3.1.3 Sandia 17-m VAWT

For the convergence studies and validation of the DMSTM code, the Sandia 17-m geometry and experimental results were used. The turbine, shown in Figure 3.4, has a straight-circular-straight blade shape, with geometric characteristics shown in Table 3.3. For the validation and convergence studies, the Sandia NACA 0015 aerodynamic database from Sheldahl and Klimas [83] was used since it has data up to a Reynolds number of 10^7, amply covering the range of Reynolds numbers experienced by the Sandia-17m turbine.

Table 3.3: Geometric characteristics of the Sandia-17m wind turbine [102].

Characteristic	Value
Height (m)	17
Equatorial Radius (m)	8.367
Chord (m)	0.533
Number of Blades	2
Swept Area, S (m^2)	187.107
Blade Length (m)	24.079
Blade Shape	NACA 0015

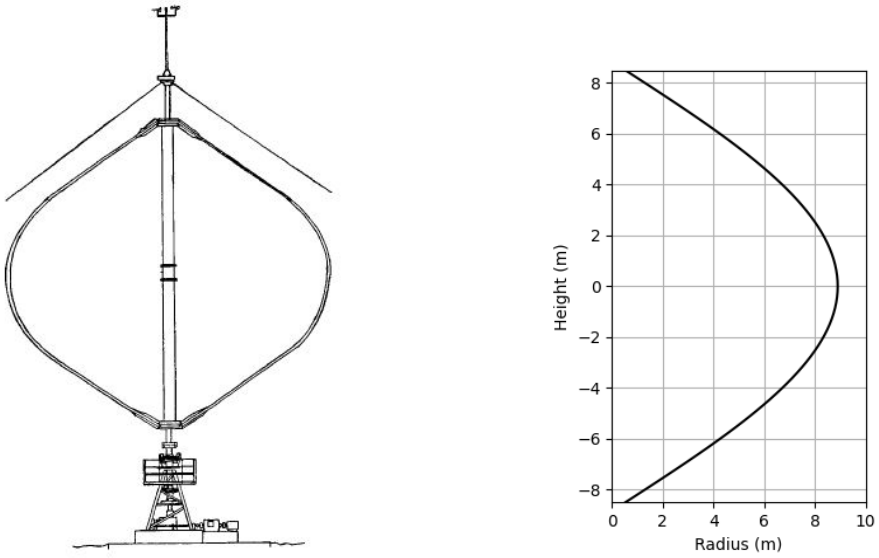

(a) Sandia-17m Drawing [102]. (b) Rotor Radius as a function of local turbine height.

Figure 3.4: Details of the Sandia-17m VAWT.

3.1.4 Convergence Studies

In addition to the geometric and aerodynamic database inputs required for the DMSTM, the number of streamtubes used to model the turbine can be changed. This includes the number of streamtubes in the vertical and azimuthal directions. If there are changes in the vertical direction, such as the straight-circular-straight blades of the Sandia-17m, it would be beneficial to increase the number of streamtubes vertically to fully capture the geometry's effect on performance. The same can be said for the number of streamtubes in the azimuthal direction to capture the variation in AoA throughout rotation and its effects on the local aerodynamics. While it would be ideal to maximize the number of streamtubes for accuracy, a compromise must be made to reduce computational time when applying the method to an optimization routine, which will be presented in Chapter 4.

First, the number of azimuthal streamtubes was varied while keeping the number of vertical streamtubes at 11. For each, the average and maximum power output of the Sandia 17-m VAWT was evaluated over 50 wind speed increments linearly spaced between 4 and 25 m/s, inclusively at a rotational speed of 48.4 RPM. These conditions were selected to align with one of the experimental data sets available for the Sandia 17-m [3]. The time to evaluate the entire power curve for the range of wind speeds was also recorded. For reference, the convergence studies were performed on a single core of an *AMD* 7900X 12-core 4.70 GHz processor. The resulting plots are shown in Figure 3.5. From the plots, both average and maximum power output converge at about 10 azimuthal streamtubes. The time per evaluation increases linearly with the number of streamtubes. For these reasons, the number of azimuthal streamtubes was chosen to be 10, where the computational time is minimized. For aerodynamic characteristic plots requiring higher resolution in the azimuthal direction, more streamtubes in this direction will be used. However, this does not impact the resulting power outputs.

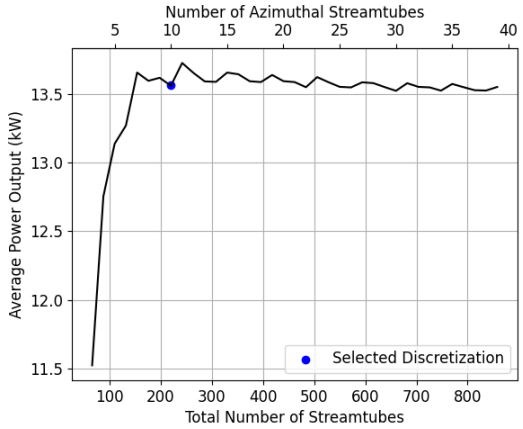

(a) Average Power Output

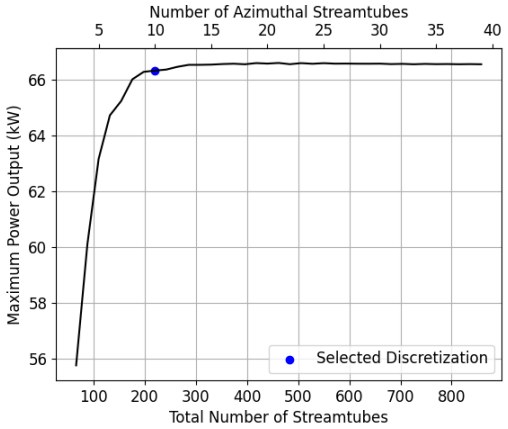

(b) Maximum Power Output

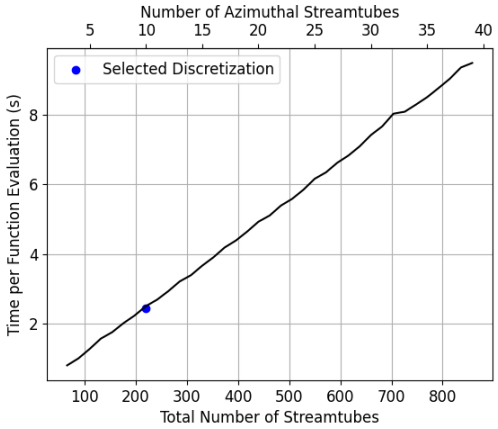

(c) Function Evaluation Time

Figure 3.5: Convergence study of azimuthal streamtubes when applied to the Sandia 17-m at 48.4 RPM.

Fixing the number of azimuthal streamtubes to 10, the convergence was then repeated for the number of vertical streamtubes using the same characteristics as the previous convergence study. The resulting plots are shown in Figure 3.6. Similar to the azimuthal streamtube convergence, the time per evaluation of the power curve is linearly increasing with the number of streamtubes. Both the average and maximum power output experience good convergence after about 10 vertical streamtubes. While 10 provides a good result, 11 was chosen to have a streamtube at the rotor equator so that aerodynamic characteristics in this region could be examined.

Lastly, with the number of azimuthal streamtubes fixed at 10, the number of velocities used to model the power curves was studied. The power curves were evaluated between 4 and 25 m/s, with 2 to 50 points per curve, resulting in Figure 3.7. Similar to the other variables, the time per evaluation varies linearly with the number of velocity points. The average power output quickly converges after about 5 points, whereas the maximum power output oscillates until about 30 points, where the difference between points consistently resolves the maximum, instead of being too far to either side and masking it.

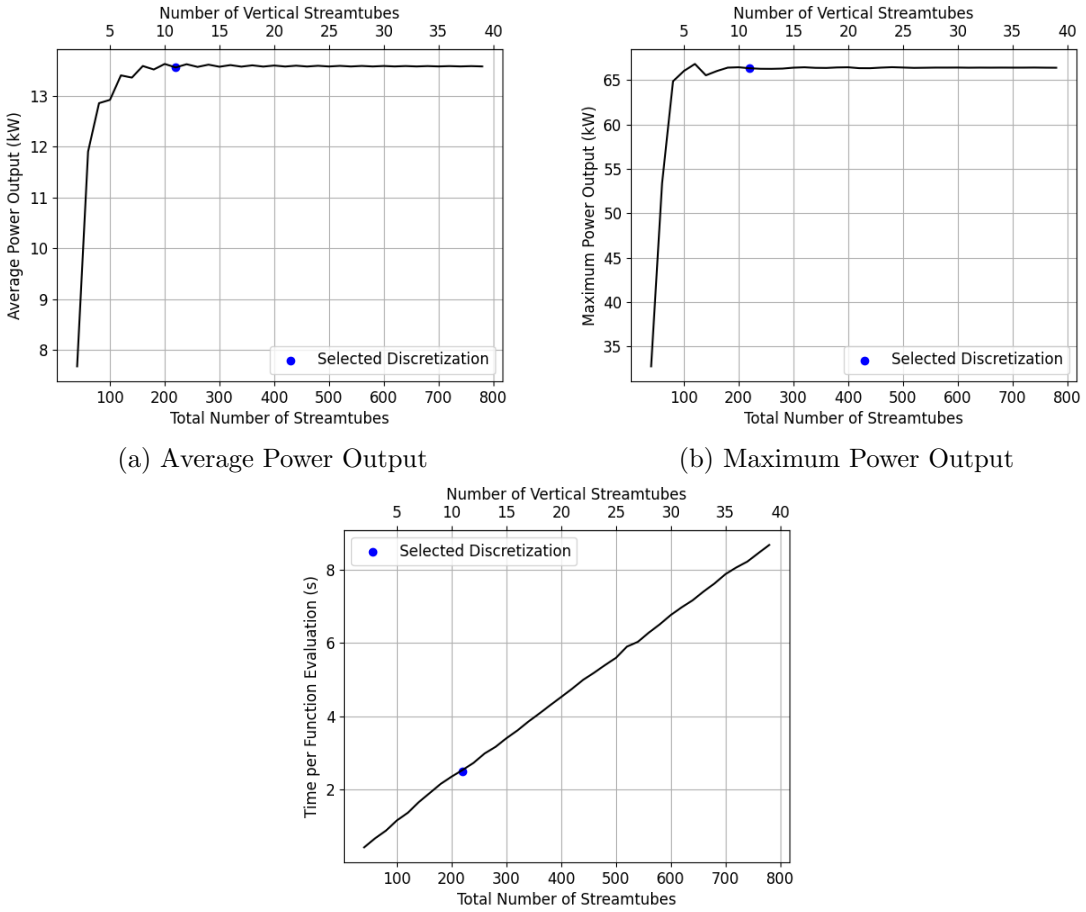

(a) Average Power Output

(b) Maximum Power Output

(c) Function Evaluation Time

Figure 3.6: Convergence study of vertical streamtubes when applied to the Sandia 17-m at 48.4 RPM.

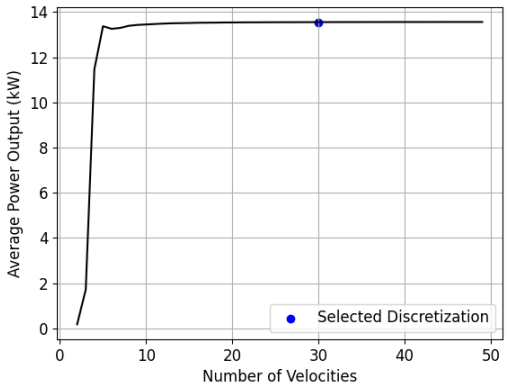

(a) Average Power Output

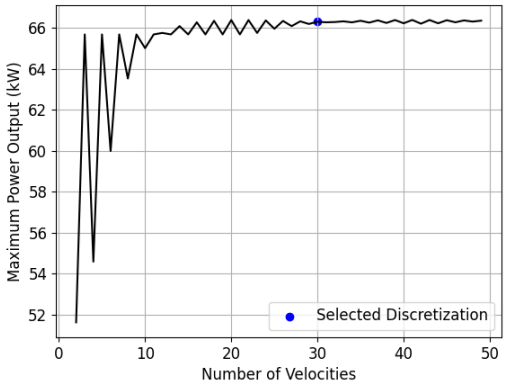

(b) Maximum Power Output

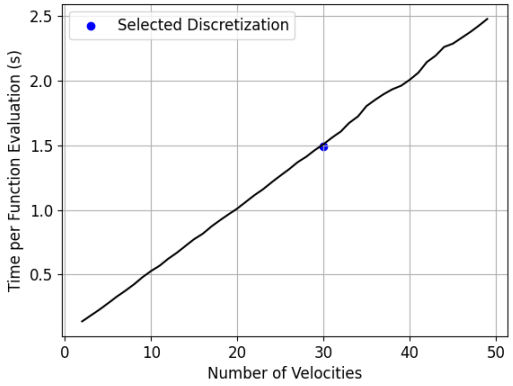

(c) Function Evaluation Time

Figure 3.7: Convergence study of velocity discretization when applied to the Sandia 17-m at 48.4 RPM.

3.1.5 Sandia 17-m Validation

Validation of the DMSTM code was done by comparison with the results of the Sandia 17-m VAWT that were presented in Section 3.1.3 for a variety of rotational rates. The power curves for 42.2, 46.6, and 50.6 RPM are shown in Figure 3.8. The DMSTM closely agrees with the experimental data [3] at high TSRs away from stall and does reasonably predict the peak power output. In all cases, however, as TSR decreases with increasing wind speed and stall is approached, the DMSTM begins to overpredict the power until the turbine stalls, where it experiences a sudden drop in power and then underpredicts power output. The experimental data, on the other hand, experience a gradual stall as the innermost segments of the blade stall sooner due to their lower TSRs compared to the outermost blade segments. This shows that the model does not accurately predict the location of turbine stall when accounting for dynamic stall and the associated post-stall performance, despite including Berg's dynamic stall model. While the performance improvements resulting from leading edge tubercles should be seen in this post-stall region, the difference in power output between the tubercle and baseline blades would still be apparent despite the poor accuracy of the DMSTM in this region.

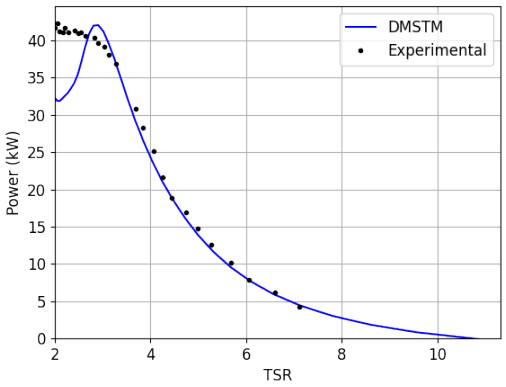

(a) 42.2 RPM

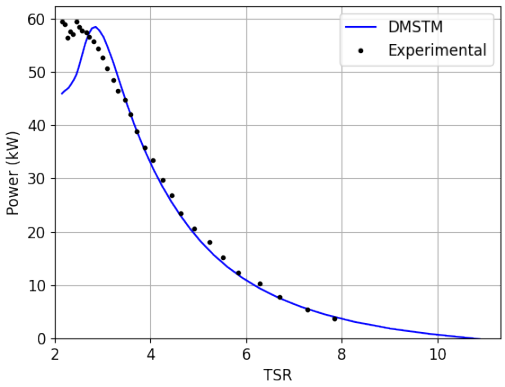

(b) 46.6 RPM

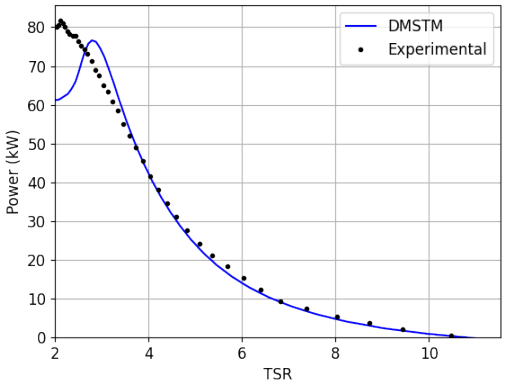

(c) 50.6 RPM

Figure 3.8: Validation of the presented DMSTM code against Sandia 17-m experimental data [3].

By comparing the average power outputs for each rotational rate in Table 3.4, it is clear that the DMSTM provides reasonable estimates of the average power output compared to the experimental data, with differences ranging from -1.15% at 42.2 RPM to 2.46% at 50.6 RPM. It is important to note that this does not mean it matches the experimental data with that much error. It is instead the wind speed probability-weighted error. This shows that the DMSTM has good agreement with the experimental data in regions of probable wind speeds.

Table 3.4: Comparison of average power output for the DMSTM with experimental Sandia-17m data.

RPM	Experimental $\bar{P}$ (kW)	DMSTM $\bar{P}$ (kW)	Difference (%)
42.2	12.60	12.81	1.63
46.6	13.42	13.57	1.15
50.6	14.29	13.94	-2.46

With the results of the validation, it can be concluded that while the DMSTM does not accurately predict the location of maximum power and power output at post-stall TSRs, it provides adequate agreement at lower TSRs and closely predicts the magnitude of maximum power output. This results in accurate predictions of the average power output, making it an excellent objective function for optimization routines. Since the deviation from the experimental results was consistent among the rotation rates, the DMSTM can also provide the difference in performance between various tubercle shapes and the baseline, although the actual performance would need to be confirmed.

3.1.6 Experimental Aerodynamic Tubercle Database

The 2D aerodynamic characteristics of various tubercle shape wings were experimentally determined using data collected in the closed-circuit wind tunnel at the Royal Military College of Canada (RMC) by Peristy *et al.* [13] and Sidhu *et al.* [62]. Details of the experiment can be found in Appendix A.

The tubercles replace the straight leading edge of the reference turbine blade forward of the maximum thickness with a sinusoidal tubercle shape that smoothly merges with the reference airfoil shape aft of the maximum thickness. The sinusoidal tubercle shape is parameterized using amplitude, A, and wavelength, λ, both expressed as a percent of the airfoil chord defined by the equation below and visualized in Figure 3.9. The airfoil coordinates forward of maximum thickness are then scaled only in the chord-wise direction to match the sinusoidal shape and to ensure no discontinuities on the airfoil surface at the location of maximum thickness.

$$x(y) = A \sin\left(\frac{2\pi y}{\lambda}\right) \tag{3.26}$$

To determine the effect of tubercle shape parameters on the performance of VAWTs, different tubercle geometries were studied, as shown in Table 3.5 and Figure 3.10. They cover a range of amplitude and wavelengths and have been studied by Peristy *et al.* [13] and Sidhu *et al.* [62]. A NACA 0018 airfoil profile was selected as it is widely used in wind-turbines [3].

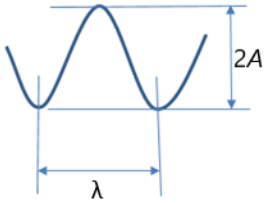

Figure 3.9: Tubercle representation with a 2D sine wave.

Table 3.5: Summary of Leading-Edge Tubercle Geometry.

Representation	Amplitude, A (% chord)	Wavelength, λ (% chord)
Baseline	-	-
$A02\lambda07$	2	7
$A02\lambda09$	2	9
$A03\lambda11$	3	11
$A04\lambda18$	4	18
$A05\lambda13$	5	13
$A06\lambda21$	6	21

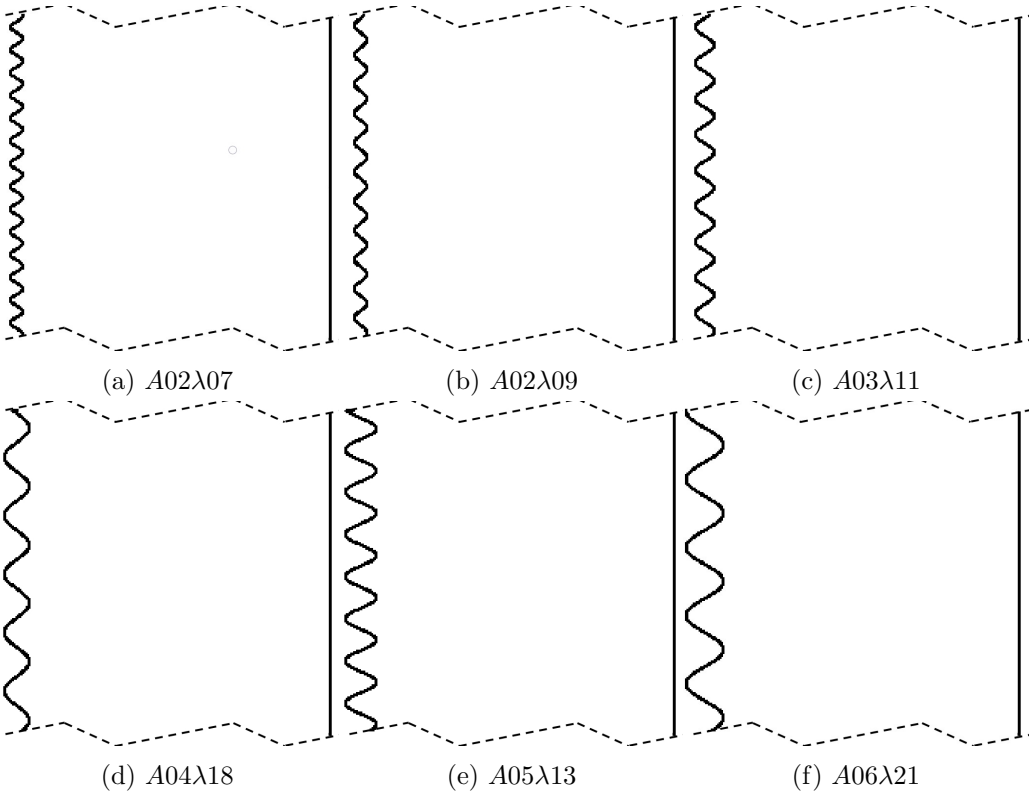

(a) $A02\lambda07$ (b) $A02\lambda09$ (c) $A03\lambda11$

(d) $A04\lambda18$ (e) $A05\lambda13$ (f) $A06\lambda21$

Figure 3.10: Suction surface view of all tubercle geometries studied [77].

Using a *Scanivalve* ZOC22b/32Px to measure the pressure along the upper and lower surfaces of the wings, the quasi-2D aerodynamic characteristics were determined for the tubercle peaks and valleys. For Reynolds Numbers of 75 000, 150 000, and 300 000, local lift and drag coefficients were determined for angles up to 30°, where they were then shown to follow flat plate characteristics. Averaging the aerodynamic characteristics of the tubercle peaks and valleys yielded Figure 3.11, showing the lift and drag curves of each tubercle shape at $Re = 150\,000$.

The leading-edge suction peak and stagnation point were not captured at low AoA due to the lack of leading-edge pressure taps, resulting in underpredicted lift and drag at these angles. Furthermore, the pressure taps only resolve pressure drag, not viscous drag, resulting in a further reduction in drag. So, a correction was added to the experimental lift and drag data to ensure a reasonable zero AoA crossing point on the lift and drag polars. This correction was determined by taking the difference between the experimental NACA 0018 and Sandia NACA 0018 data, from Sheldahl and Klimas [83], at the same Reynolds number for both the lift and drag polars. The correction was only applied for angles below the critical angle of the baseline NACA 0018. If C_d was determined to be below C_{d_0} of the Sandia data, it was assumed to be equal to that C_{d_0}. Although the NACA 0018 data from Sheldahl and Klimas [83] is not tubercle data, this correction was only added to pre-stall angles, where tubercles would not have an improvement. From Figure 3.12, it is clear that the tubercle blades do not experience the sudden drop in lift at post-stall AoAs that the baseline blade does. Although there are some tubercle shapes with notably higher drag than the baseline, namely the larger amplitude shapes, there are some shapes with similar drag in the post-stall regime. This would offer higher aerodynamic efficiencies at these post-stall angles. For VAWTs, since the tangential force comprises a larger component of lift at higher AoA, an improved aerodynamic efficiency at these AoAs would result in greater tangential forces than the same aerodynamic efficiency at a lower AoA, improving power output.

A current drawback of this database is the limited range of Re available. While the NACA airfoil data from Sheldahl and Klimas [83] has data up to a Re of 10 million, the tubercle aerodynamic performance database only goes up to 300 000. To resolve this, the interpolation in the DMSTM was not allowed to extrapolate Re outside the database, which could exaggerate its effect on the aerodynamic characteristics. For example, if Re is above 300 000, then an Re of 300 000 is assumed, and the corresponding aerodynamic characteristics from the database are used. With C_l generally increasing with Re, especially at low Re, this assumption results in an under prediction in turbine performance, making it a conservative estimate. Furthermore, a small-scale VAWT was used to analyze tubercles, minimizing Re and reducing the size of the regime requiring this constraint.

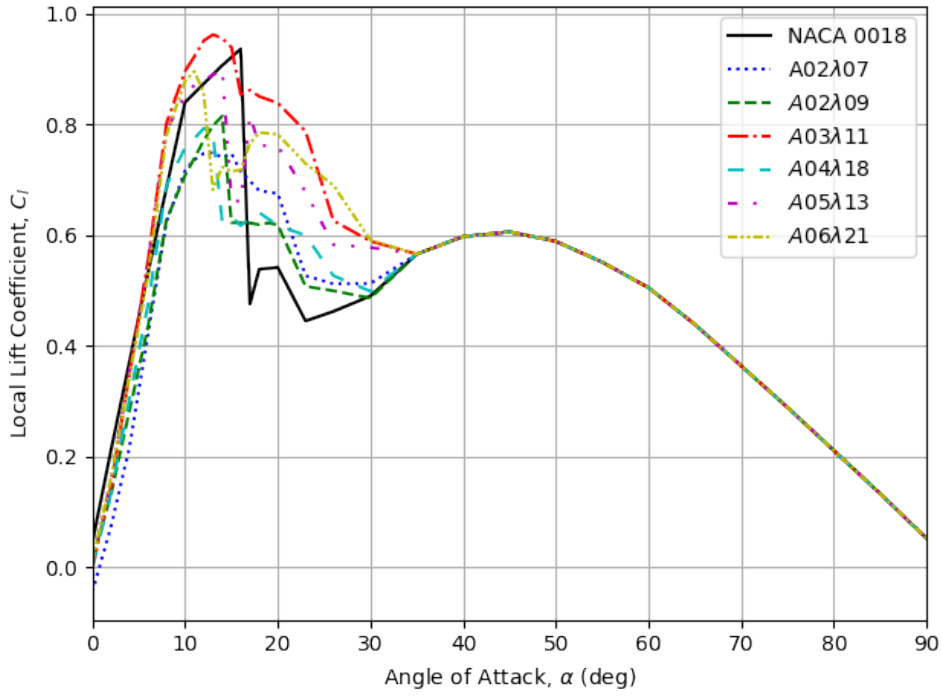

(a) C_l

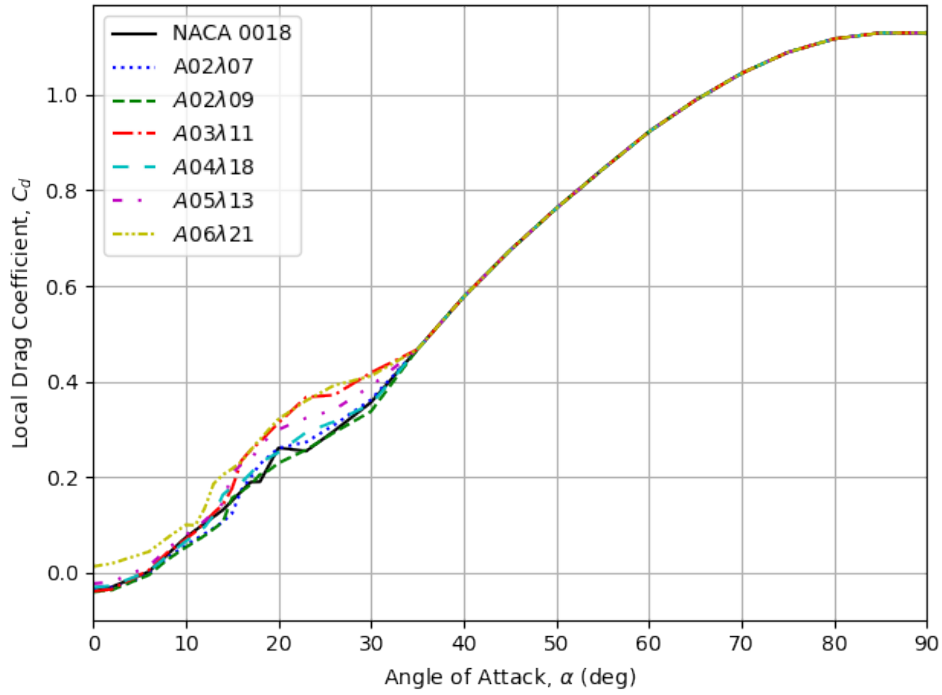

(b) C_d

Figure 3.11: Uncorrected experimental lift and drag curves of the tubercle shapes at $Re = 150\,000$.

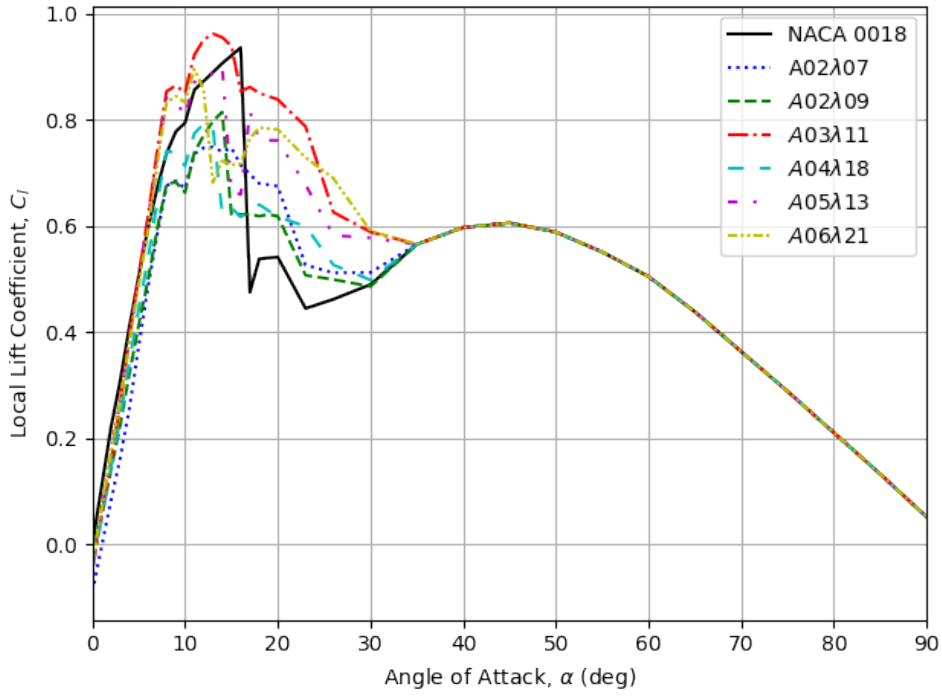

(a) C_l

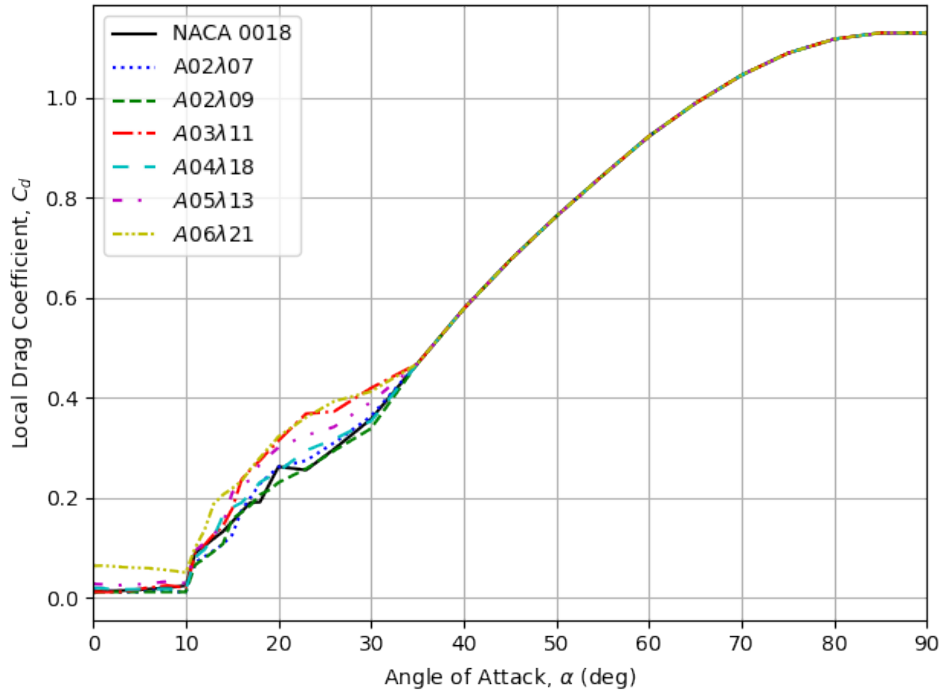

(b) C_d

Figure 3.12: Corrected experimental lift and drag curves of the tubercle shapes at $Re = 150\,000$.

3.2 Application of Tubercles

This section presents the results of the DMSTM using the tubercle experimental aerodynamic database when applied to a small H-type VAWT. The power contours were determined, providing a full-scope analysis of which rotational rates and wind speeds yield performance gains with tubercles. These contours also provide the optimal RPM for each wind speed. So, the turbine could have an RPM schedule to ensure maximum power extraction. These contours were then averaged by weight according to the wind speed probability distributions described in Section 3.1.2, which provides the ideal RPM if only a single value could be chosen, or no feedback system is available for wind speed. This was repeated for the power coefficient with wind speed and TSR. The sources of improvement are then explored through azimuthal aerodynamic characteristic plots. Additional contour plots and results for power output of the small H-type VAWT with constant TSR instead of RPM can be found in Appendix C. Similar results but applied to a 1:7 Scale Sandia 17m can also be found in Appendix C.

3.2.1 Small-Scale H-Type VAWT

With the limited experimental data available for tubercle airfoils at high Reynolds numbers, a small-scale VAWT was used to analyze the effect of tubercles, reducing the range of Re experienced. This rotor design was also used during the experimental phase of this thesis, found in Chapter 5. For this small turbine, an H-type rotor is used, which has straight blades parallel to the axis of rotation. Details on the turbine geometry can be found in Table 3.6 and Figure 3.13.

Table 3.6: Geometric characteristics of the small-scale H-type VAWT

Characteristic	Value
Height (m)	0.75
Radius (m)	0.5
Chord (m)	0.1524
Number of Blades	3
Swept Area, S (m^2)	1.5
Solidity, σ	0.146
Blade Shape	NACA 0018

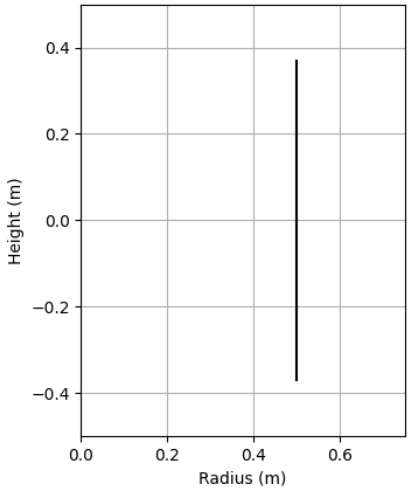

Figure 3.13: Rotor Radius as a function of local turbine height of the Small-Scale H-type VAWT.

3.2.2 Tubercle Power Contours

Using the DMSTM, power contours were produced by varying the freestream wind speed and RPM. The contours for the tubercle shapes are composed of 128 power curves at rotational rates between 6.25 and 800 RPM, each using 101 wind speeds between zero and 20 m/s. Although this fine of a discretization was not necessary to come to an adequate solution, it provided a smooth contour without the need for interpolation of the results, and only took approximately four hours to compute all the contours on a single core of an AMD 7900X 4.7 GHz processor. Multiplying the time per task by the number of cores and the clock speed gives approximately 6.8×10^{13} clock cycles per task, assuming the algorithm is not RAM-limited. Compared to the CFD analysis discussed in Chapter 2, this method is three orders of magnitude less computationally expensive. Furthermore, this is comparing the time to compute all seven contours, as opposed to a single point with the CFD analysis. The resulting contours are shown in Figure 3.14. Power outputs less than or equal to zero are not plotted and are indicated by white regions to show where the net torque is less than zero.

The contours in Figure 3.14 show in general that higher power outputs are attained at both higher wind speeds and, accordingly, higher rotational rates. As wind speed increases, more energy in the wind is available for extraction. Higher rotational rates are needed to ensure a lower, more efficient range of AoA to maximize torque. The bottom-right edge of the plots is limited by too high of a TSR, where the range of AoA is too low to produce any meaningful contribution of lift in the tangential direction, and the tangential component of drag overpowers it. The top-left edge of the contours is due to the same effect but for the opposite reason. The TSR is too low, and the range of AoA is outside the efficient range, likely into the flat-plate regime, producing significant drag that is unable to be overcome by the lift produced at intermediate AoAs. There is minimal change in the upper TSR limit between different leading edge shapes, with slight changes in the slope of V with RPM, suggesting minor differences in the near zero AoA lift and drag coefficients. There

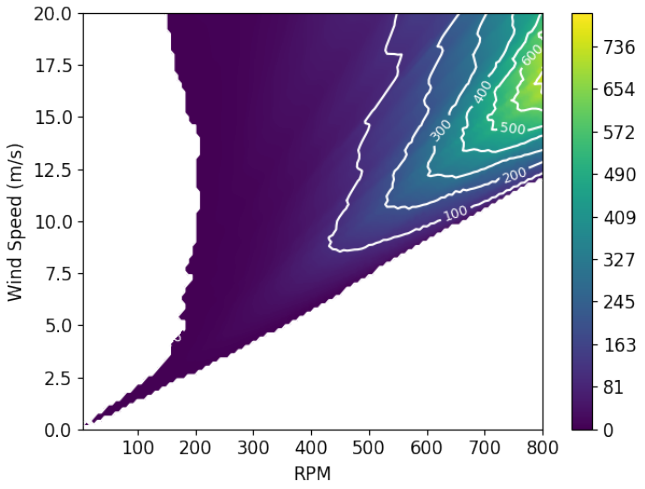

(a) Baseline

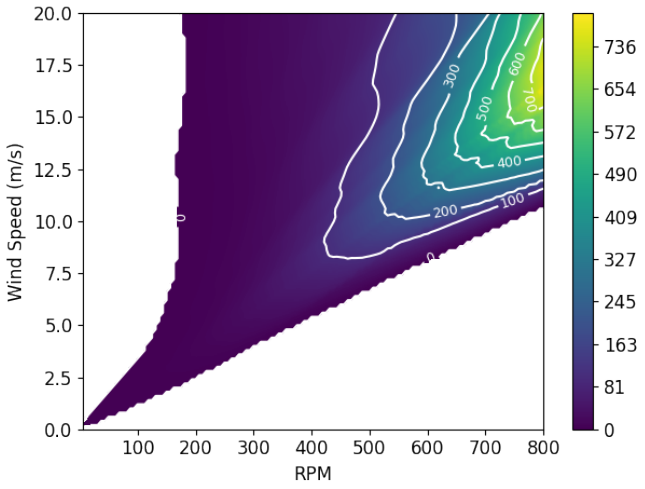

(b) $A02\lambda07$

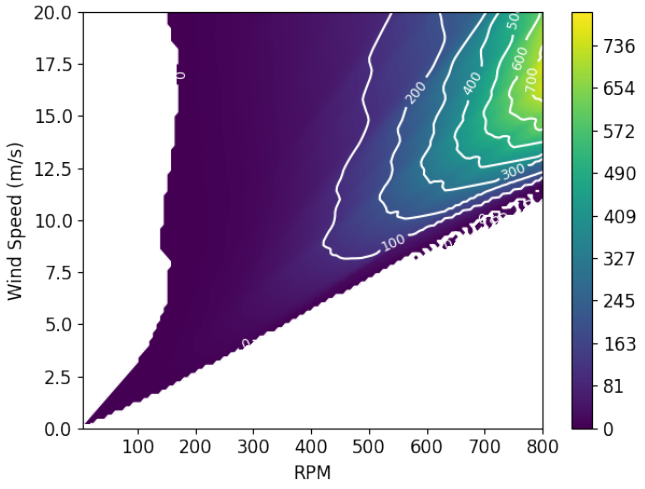

(c) $A02\lambda09$

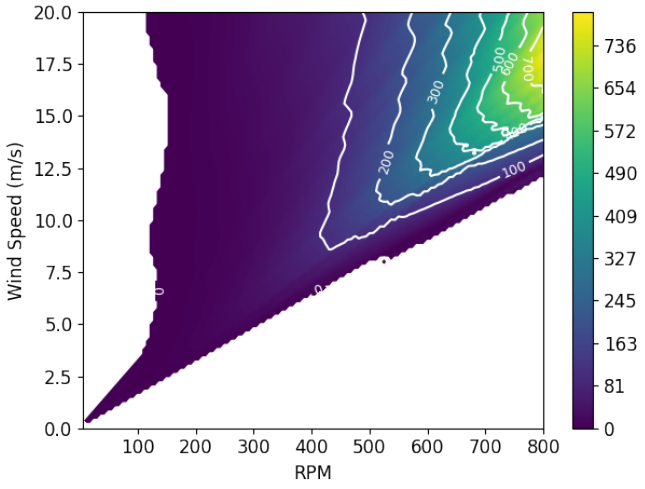

(d) $A03\lambda11$

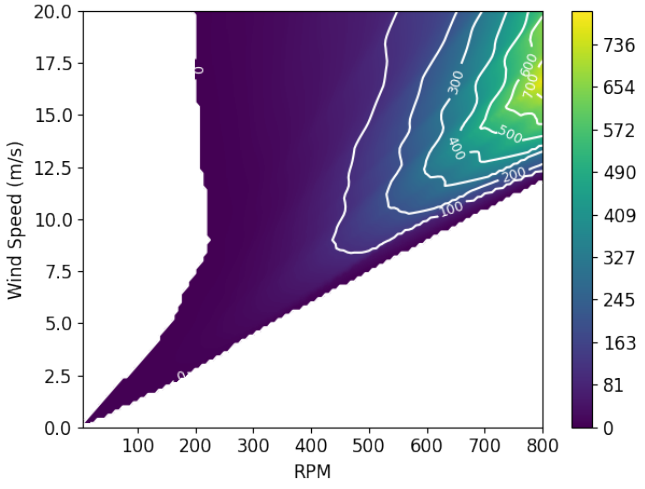

(e) $A04\lambda18$

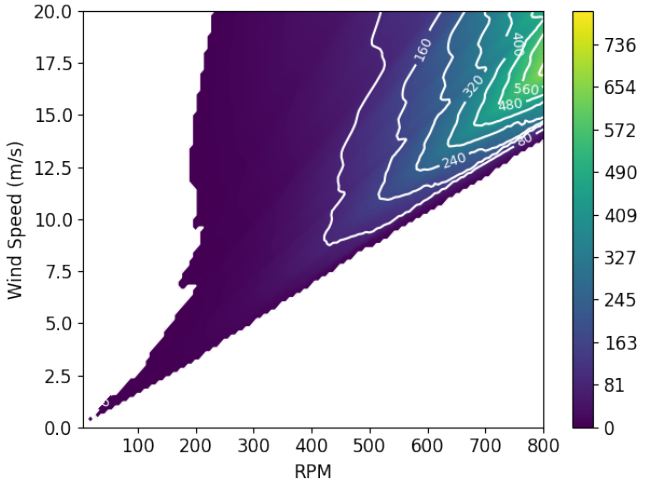

(f) $A05\lambda13$

Figure 3.14: Power contours, in watts, of various tubercle shapes applied to the Small-Scale H-type VAWT.

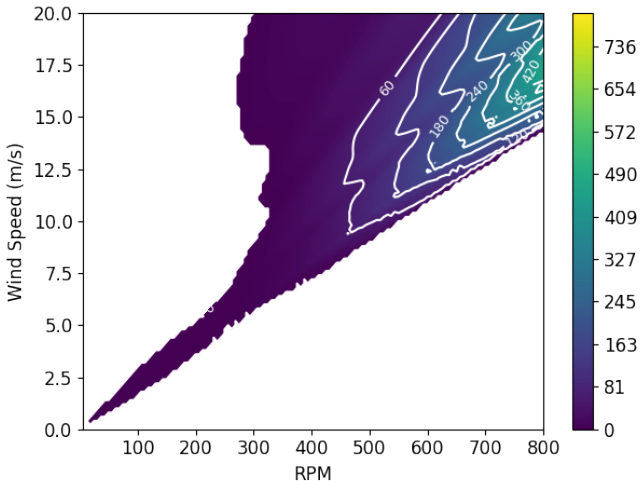

(g) $A06\lambda21$

Figure 3.14: Power contours, in watts, of various tubercle shapes applied to the Small-Scale H-type VAWT.

are significant differences between the contours at the lower TSR limit. Above 7.5 m/s, the baseline's limit varies between 150 and 200 RPM, while some of the tubercle shapes, notably the $A03\lambda11$, can go down to about 100 RPM, suggesting improved aerodynamic efficiency at lower TSRs corresponding to post-stall AoAs. This could correspond to improved self-starting capabilities as more power would be available to the turbine at a lower RPM. While this improvement is seen with the low amplitude and wavelength tubercle shapes, increasing the amplitude appears to increase the minimum RPM, with significant limitations on the contour with the $A06\lambda21$. Interestingly, the baseline shows a tightening of the contour lines after reaching peak power for a given RPM, whereas the tubercle shapes have a consistent spacing between contour lines on either side of that peak power. This indicates that the baseline blades experience a steeper stall/reduction in power as wind speed increases, whereas the tubercle shapes experience a gradual reduction in power. This would suggest improved maintenance of power in sudden gusts of wind. Additionally, to reduce structural fatigue on the turbine, the tubercle shapes could be operated at a lower RPM, without sacrificing as much power extraction.

The location and value of maximum power for each shape, presented in Table 3.7, are also a point of interest. All shapes produce their maximum power at 800 RPM but vary in wind speed. All tubercle shapes except the $A05\lambda13$ and $A06\lambda21$ have a higher maximum power output than the baseline. Most notably, the $A03\lambda11$ shows a 5.7 % increase over the baseline at 18 m/s as opposed to the baseline's 17 m/s. This suggests that the $A03\lambda11$ tubercle shape benefits from lower TSRs. While this improvement in maximum power output is minimal, there is no control over the wind to ensure the turbine is operating at peak power, so improvements in the remainder of the operating space should be examined. For this reason, the difference between each tubercle power contour and the baseline was calculated to produce the plots in Figure 3.15.

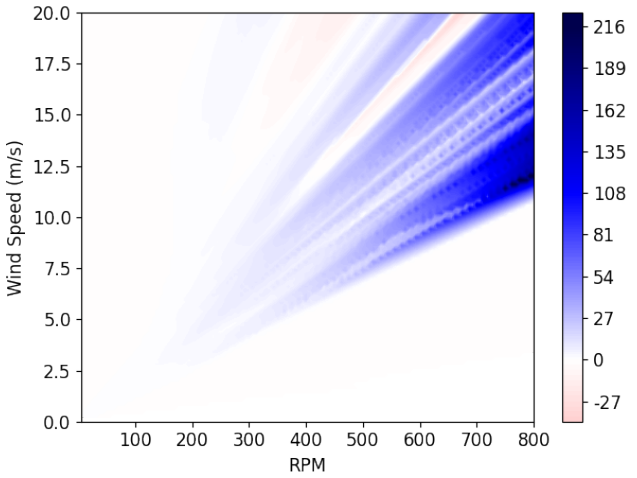

(a) $A02\lambda07$

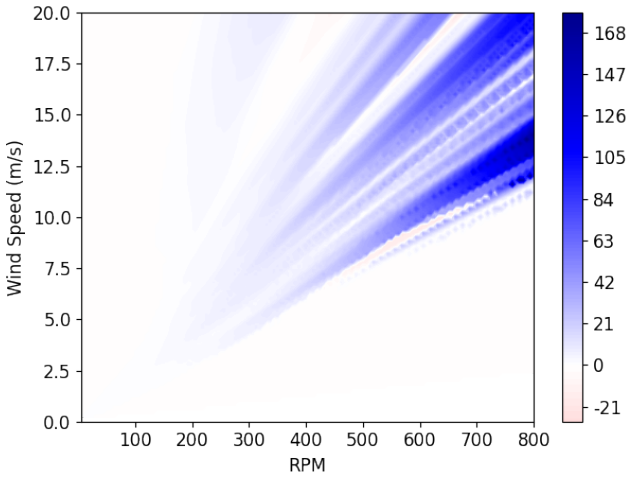

(b) $A02\lambda09$

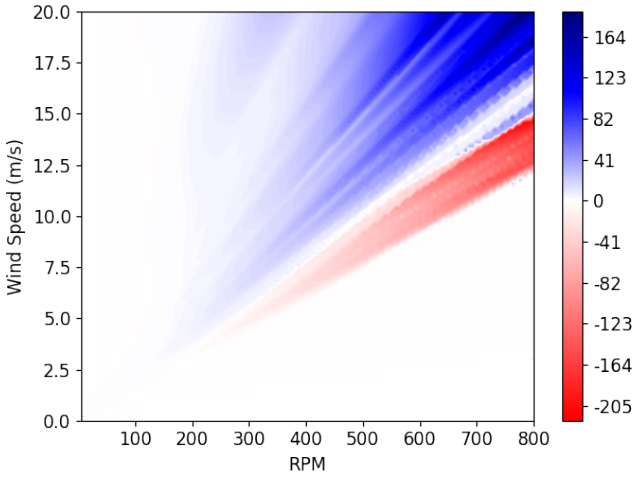

(c) $A03\lambda11$

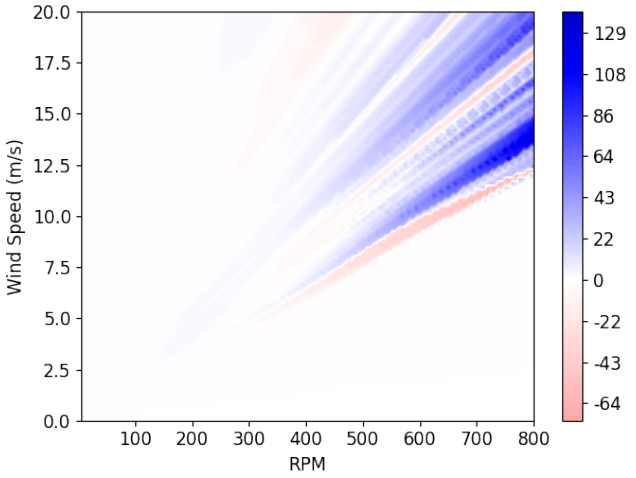

(d) $A04\lambda18$

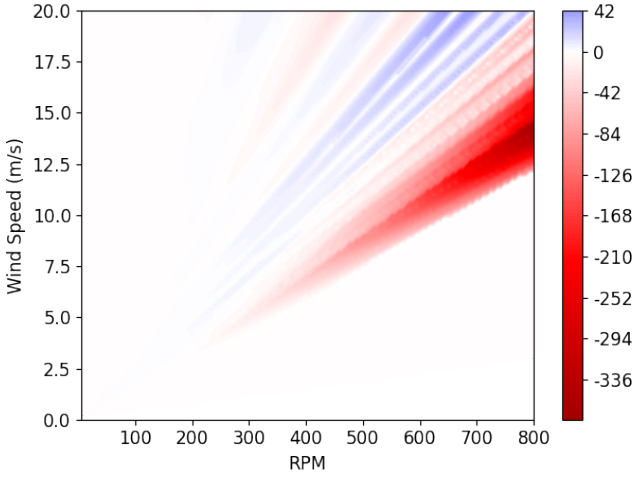

(e) $A05\lambda13$

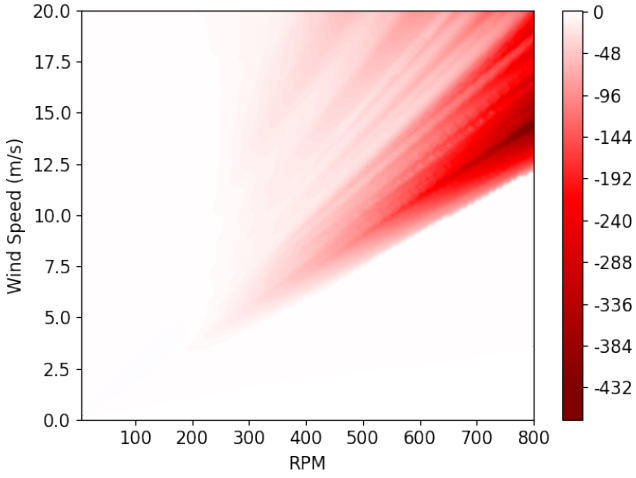

(f) $A06\lambda21$

Figure 3.15: Change in power contours compared to the baseline, measured in watts, of various tubercle shapes applied to the Small-Scale H-type VAWT.

Table 3.7: Location and value of maximum power output for tubercle shapes compared to the baseline. Note that all maximum power outputs occurred at 800 RPM.

Shape	V of Maximum P (m/s)	Maximum P (W)
Baseline	17.0	745.8
$A02\lambda07$	16.4	774.9 (+3.9%)
$A02\lambda09$	17.4	750.3 (+0.6%)
$A03\lambda11$	18.0	788.0 (+5.7%)
$A04\lambda18$	16.6	781.3 (+4.8%)
$A05\lambda13$	17.2	655.7 (−12.1%)
$A06\lambda21$	17.4	461.0 (−38.2%)

Values in parentheses denote percent difference compared to the Baseline.

From Figure 3.15, it is clear that the $A02\lambda07$ and $A02\lambda09$ yield improvement for most combinations of wind speed and RPM. However, they underperform consistently in the red strip corresponding to the region of maximum power of the baseline blade for each RPM. On the other hand, at higher V for the same RPM, these shapes consistently produce more power, while the baseline experiences a sudden decrease in power as it stalls. The $A03\lambda11$ shows a significant reduction in power output at high TSRs, corresponding to the bottom right edge of the plot, but has consistent improvement at low TSRs. Although the other tubercle shapes, notably the $A06\lambda21$, produce significantly less power than the baseline, they do perform better towards the top-left of the contours, corresponding to low TSRs and a higher range of AoA.

While these contours provide insight into the general performance of the turbines with varying wind speed and RPM, they do not account for the turbine's performance in an actual wind environment. The maximum power outputs in the contours occur between 16.6 and 18.0 m/s, which is rare for most places around the world. Furthermore, it may not be possible to adjust the operating RPM for the turbine with changing wind speeds to give the optimal power output at all times.

3.2.3 Average Power Output Analysis

By integrating the power contours along the y-axis while including the wind speed probability distribution discussed in Section 3.1.2, the average power output for each shape as a function of RPM is plotted in Figure 3.16. The location and value of the maximum average power output are shown in Table 3.8. In general, all shapes experience an increase in average power output with increasing RPM until reaching their peak, at which point average power begins to decrease. This is unlike the power contours, where the maximum power occurred at the maximum RPM evaluated. With increasing RPM, the wind speed corresponding to maximum power output increases. Eventually, at extreme RPM, the ideal wind speed is beyond the probable wind speeds for that given RPM, so its contribution to the average power output reduces.

Figure 3.16 shows that the $A02\lambda07$ and $A02\lambda09$ outperform the baseline blade for the entire range of RPM evaluated, with the $A02\lambda07$ producing as much as an 22.7 % increase in average power output, despite only having a 3.9 % higher maximum peak power output than the baseline. This shows that the performance of a VAWT is not dependent on the

maximum power it can produce, but rather on how well it can extract power from the range of wind speeds it is expected to experience. At extremely low RPM, below 225 RPM, all tubercle shapes outperform the baseline except the $A06\lambda21$. This can be explained by looking at the power contours in Figure 3.14, where at low wind speeds and RPM, the baseline has a thin region where it can produce power while the other tubercle shapes have a much wider region, allowing for more power extraction for a wider range of wind speeds.

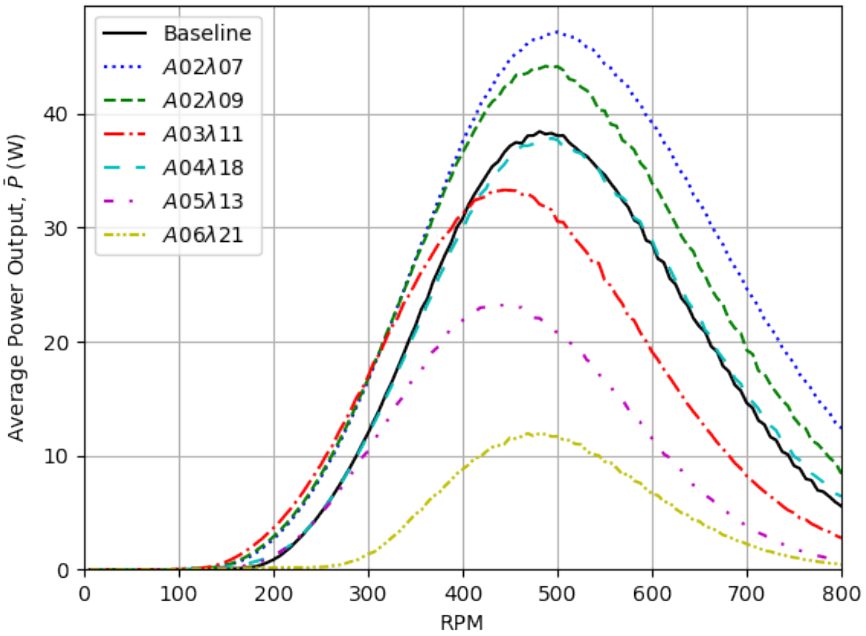

Figure 3.16: Wind speed probability-weighted average power output for the Small-Scale H-type VAWT with various tubercle shapes.

Table 3.8: Location and value of maximum wind speed probability-weighted average power output for tubercle shapes compared to the baseline.

Shape	RPM of Maximum $\bar{P}$	Maximum $\bar{P}$ (W)
Baseline	481.2	38.4
$A02\lambda07$	500.0	47.2 (+22.7%)
$A02\lambda09$	487.5	44.2 (+14.9%)
$A03\lambda11$	443.8	33.3 (−13.4%)
$A04\lambda18$	493.8	37.8 (−1.6%)
$A05\lambda13$	431.2	23.3 (−39.3%)
$A06\lambda21$	481.2	11.9 (−68.9%)

Values in parentheses denote percent difference compared to the Baseline.

While maximizing average power output is beneficial, it is not the only thing that should be considered when designing a wind turbine. Higher rotational rates cause more wear on the turbine drive train and bearings, while also increasing the frequency of cyclic stresses on the blades, posing an increased risk for material fatigue. This would require more

inspections and part replacements, ultimately increasing the cost of the turbine. For these reasons, it may be beneficial to operate the turbine at a lower RPM. For the most part, the tubercle shapes appear to have wider average power curves. With the $A03\lambda11$ having a lower maximum average power output RPM, compared to the $A02\lambda07$, $A02\lambda09$, $A04\lambda18$, and baseline. Below about 325 RPM, the $A03\lambda11$ becomes the best-performing shape due to its improved performance at low TSRs.

3.2.4 Power Coefficient Contours

Since power output is dependent on the size of the turbine and wind speed, while range of AoA is dependent on TSR, wind turbine designs are often characterized using graphs of power coefficient, C_P, with TSR to normalize the effect of wind speed and turbine area on the power output and the resulting required RPM with associated TSRs. While most studies show the variation of C_P with TSR, the following contours were produced to show the variation of C_P with both TSR and wind speed. Similar to the previous contours, C_P and the difference in C_P between the baseline for each tubercle shape were determined and are shown in Figures 3.17 and 3.18, respectively.

Similar to the power contours, the upper and lower limits in TSR are apparent. Most tubercle shapes show significant improvement at the low TSR limit, especially at low wind speeds. As wind speed increases, the lower TSR limit decreases, with some tubercle shapes, such as the $A03\lambda11$ and $A02\lambda09$ blades, reaching 0.5 at around 10 m/s, while the baseline reaches the same limit at around 15 m/s. This suggests the baseline has poorer self-starting capability, requiring higher wind speeds at the same TSR to have a net-positive torque. The $A02\lambda07$, $A02\lambda09$, $A03\lambda11$, and $A04\lambda18$ provide improvement for most TSRs at higher wind speeds, except around a TSR of 2.5, where the baseline blade reaches its maximum power output before the turbine stalls as TSR decreases further.

It is also important to point out the variation of C_P with velocity, despite being normalized. The range of operable TSRs increases, along with the magnitude of C_P. While most studies have examined the variation of C_P with just TSR, the variation of wind speed should still be included to account for Re effects on airfoil performance with increasing wind speed. Some tubercle shapes outperform the baseline at low wind speeds or have regions of improvement. However, there are significant differences as wind speed increases. So, some performance improvements would have been overlooked had V not been varied alongside TSR.

When it comes to the maximum power coefficient, shown in Table 3.9, more tubercle shapes show performance improvement, excluding the $A05\lambda13$ and $A06\lambda21$. The greatest improvement comes from the $A02\lambda07$, with a 22.3% increase. With the exception of the $A03\lambda11$, the maximum C_P decreases with increasing amplitude. Once again, averaging C_P with the wind speed probability distribution, Figure 3.19 is obtained along with the location and values of the maximum wind speed probability-weighted average in Table 3.10. The $A02\lambda07$, $A02\lambda09$, $A03\lambda11$, and $A04\lambda18$ show an improvement in average power output with as much as a 22.7% increase with the $A02\lambda07$. The $A02\lambda07$ and $A02\lambda09$ outperform the baseline for all TSRs and have a wider range of operable TSRs, while the $A03\lambda11$ and $A04\lambda18$ mainly outperform the baseline at low TSRs. All tubercle shapes excluding the $A06\lambda21$ outperform the baseline below a TSR of 2.5. An interesting characteristic of the

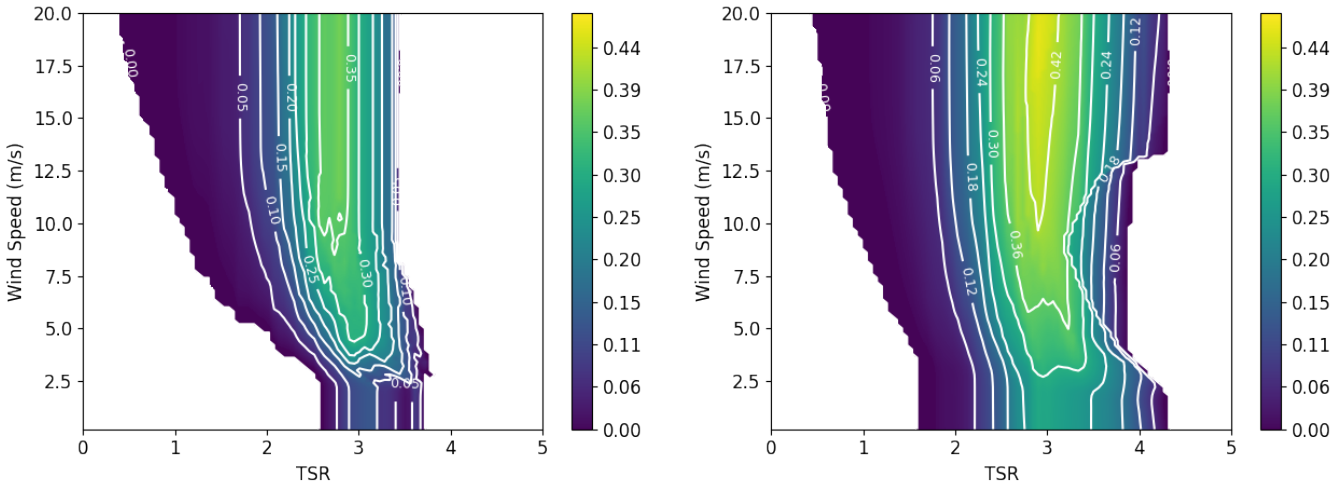

(a) Baseline

(b) $A02\lambda07$

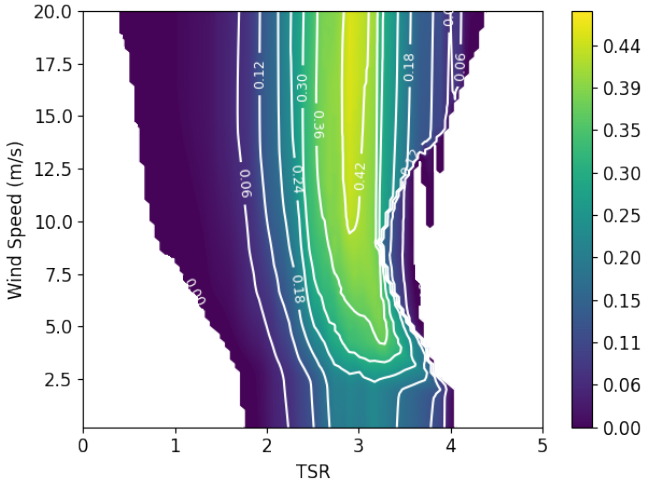

(c) $A02\lambda09$

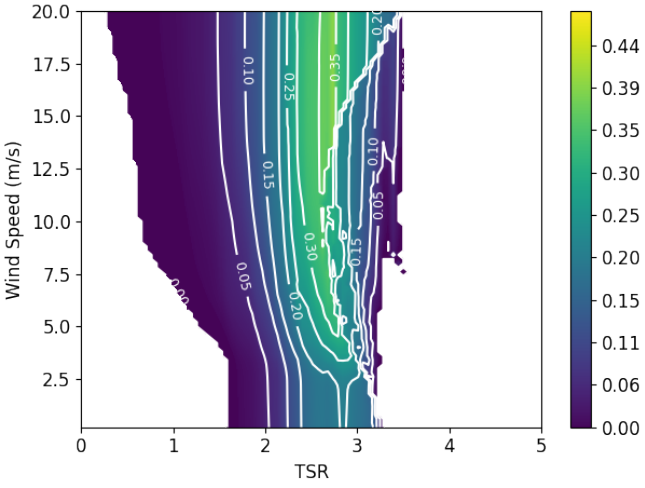

(d) $A03\lambda11$

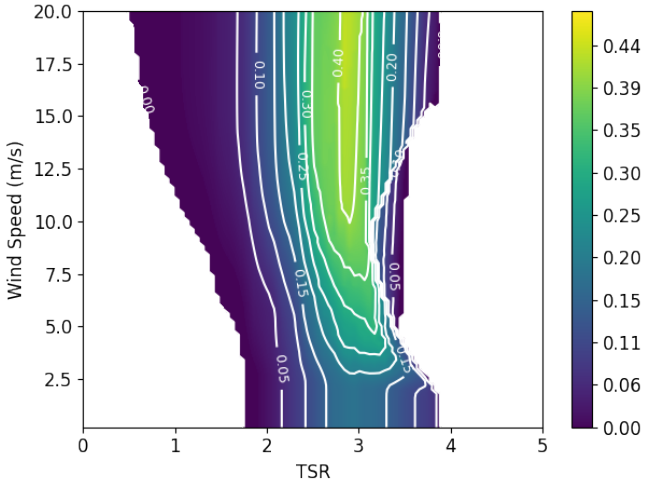

(e) $A04\lambda18$

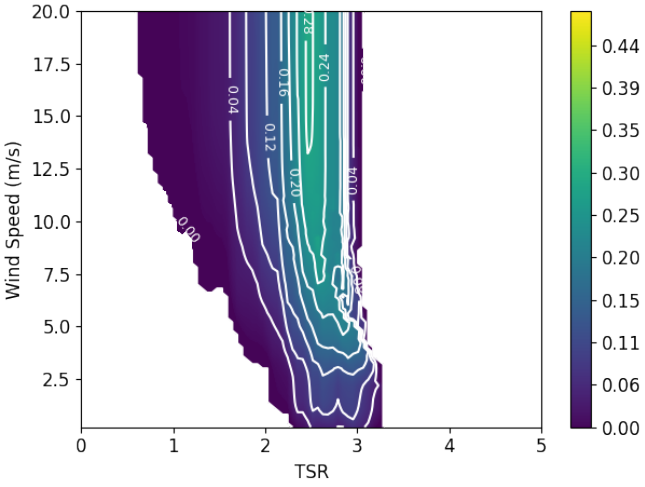

(f) $A05\lambda13$

Figure 3.17: Power coefficient contours of various tubercle shapes applied to the Small-Scale H-type VAWT.

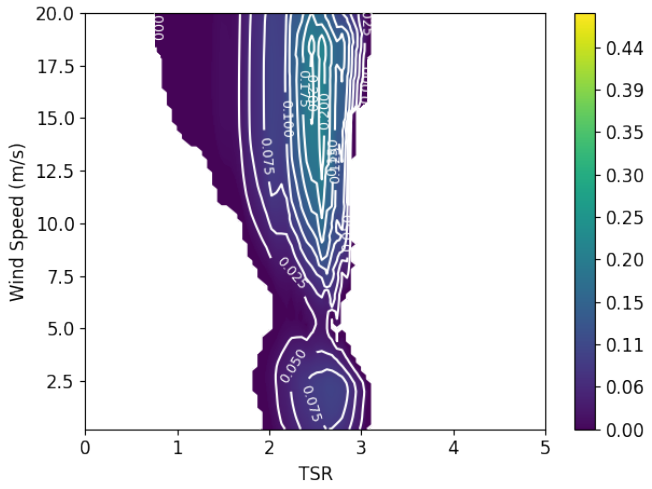

(g) $A06\lambda21$

Figure 3.17: Power coefficient contours of various tubercle shapes applied to the Small-Scale H-type VAWT.

Table 3.9: Location and value of maximum power coefficient for tubercle shapes compared to the baseline.

Shape	TSR of Maximum C_P	V of Maximum C_P (m/s)	Maximum C_P
Baseline	2.79	15.6	0.38
$A02\lambda07$	2.90	18.8	0.46 (+22.3%)
$A02\lambda09$	2.90	19.0	0.46 (+20.7%)
$A03\lambda11$	2.73	20.0	0.39 (+4.2%)
$A04\lambda18$	2.84	18.8	0.44 (+15.4%)
$A05\lambda13$	2.46	19.0	0.29 (−23.4%)
$A06\lambda21$	2.57	18.2	0.22 (−42.3%)

Values in parentheses denote percent difference compared to the Baseline.

tubercle shapes' curves is that they have a C_P 'recovery' as TSR decreases, with some shapes showing an entirely new peak or reduction in slope. This is likely due to an increase in aerodynamic efficiency post-stall, combined with a favourable component of lift and a smaller component of drag in the tangential direction as AoA increases past stall. This is not present in the baseline due to its sudden drop in lift post stall. The C_P 'recovery' peaks provide an alternative operating point that provides similar or improved efficiency at a slower, more sustainable TSR. Furthermore, the $A03\lambda11$ shows a 0.4 % improvement in average power coefficient, which occurs at 10 % lower TSR than the baseline. This would be a beneficial condition to operate at, providing slightly more power at a lower rotational rate compared to the baseline, while also outperforming the other tubercle shapes below a TSR of 2.5.

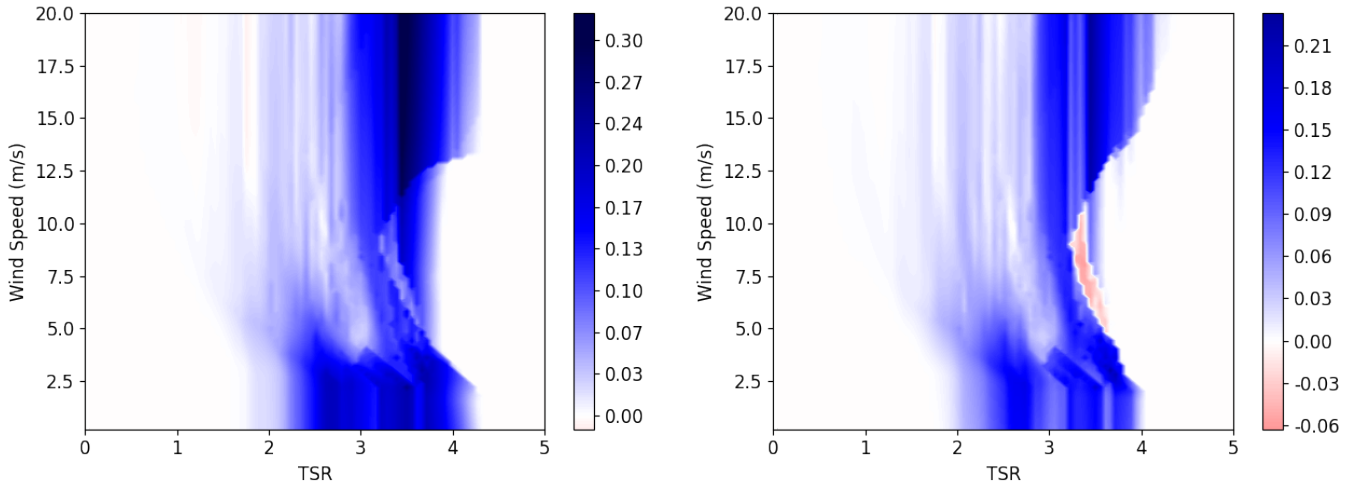

(a) $A02\lambda07$

(b) $A02\lambda09$

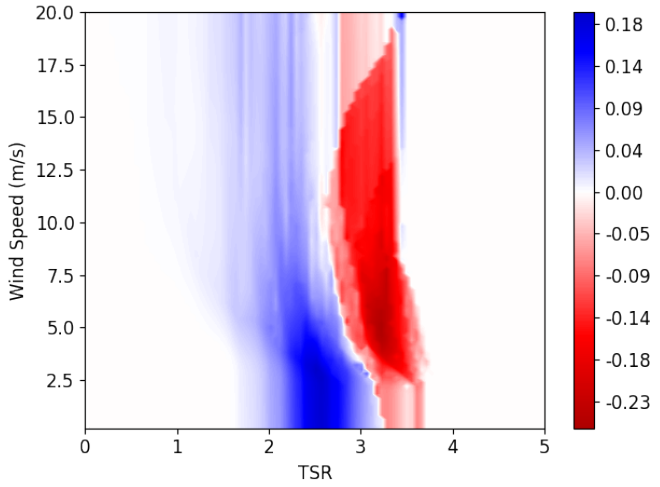

(c) $A03\lambda11$

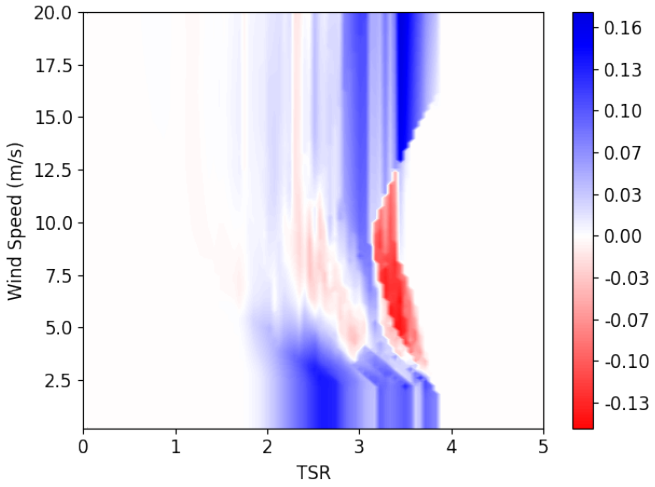

(d) $A04\lambda18$

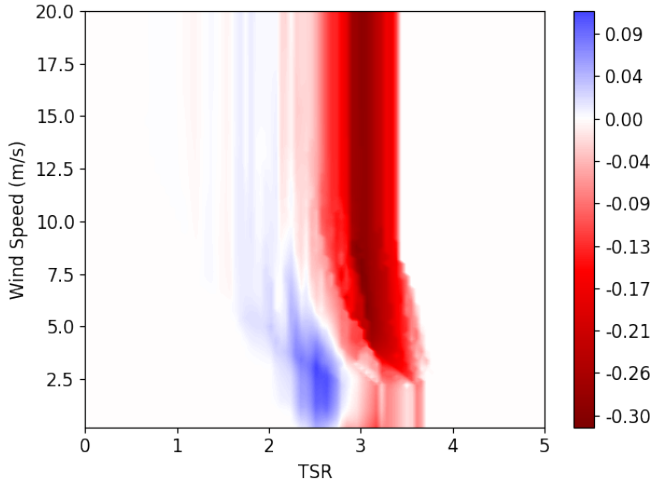

(e) $A05\lambda13$

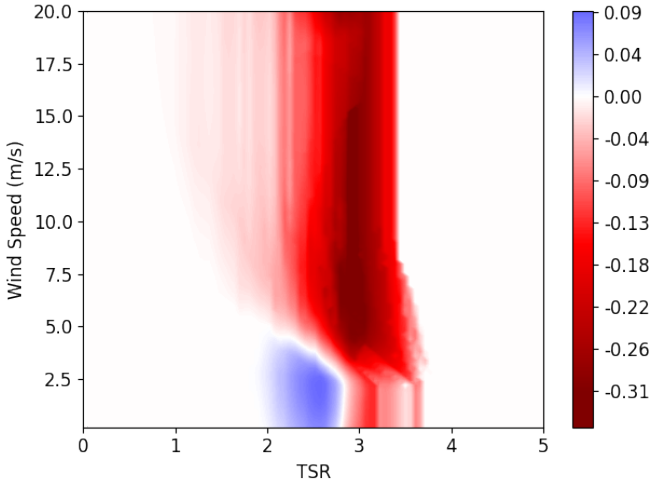

(f) $A06\lambda21$

Figure 3.18: Change in power coefficient contours compared to the baseline of various tubercle shapes applied to the Small-Scale H-type VAWT.

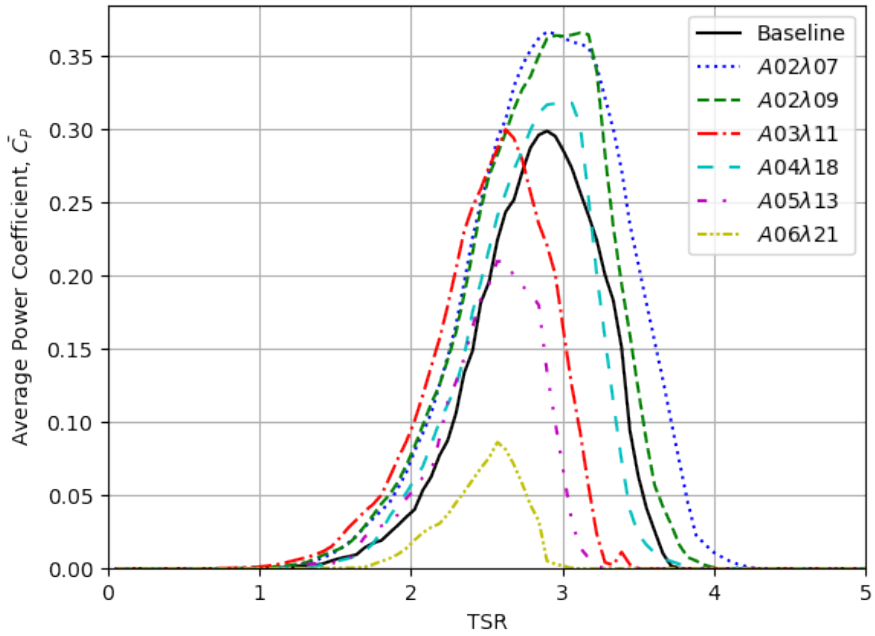

Figure 3.19: Wind speed probability-weighted average power coefficient for the Small-Scale H-type VAWT with various tubercle shapes.

Table 3.10: Location and value of maximum wind speed probability-weighted average power coefficient for tubercle shapes compared to the baseline.

Shape	TSR of Maximum $\bar{C}_P$	Maximum $\bar{C}_P$
Baseline	2.90	0.30
$A02\lambda07$	2.90	0.37 (+22.7%)
$A02\lambda09$	3.12	0.37 (+22.4%)
$A03\lambda11$	2.62	0.30 (+0.4%)
$A04\lambda18$	3.01	0.32 (+6.4%)
$A05\lambda13$	2.57	0.21 (−29.8%)
$A06\lambda21$	2.57	0.09 (−71.1%)

Values in parentheses denote percent difference compared to the Baseline.

3.2.5 Sources of Improvement

To confirm the sources of improvement that give tubercles an improvement of up to 19.2% in average power output, the power curve for all the shapes was plotted at 500 RPM, where the $A02\lambda07$ yields the most improvement over the baseline blade for the whole range of wind speed. This plot, along with the difference in power each tubercle shape provides, compared to the baseline, is shown in Figure 3.20. At low wind speeds, the $A02\lambda07$, $A02\lambda09$, and $A04\lambda18$ closely follow the baseline blade. At peak power of the baseline around 10 m/s, all shapes produce a lower or nearly equal power. After the baseline maximum power, however, is where the greatest improvement in power is seen. All tubercle shapes show a jump in relative power output due to the sudden drop in power output of the baseline at 10 m/s as the turbine stalls. The $A02\lambda07$, $A02\lambda09$, and $A03\lambda11$ all experience a higher peak power, but at a higher wind speed. After which, the tubercle blades show a gradual reduction in power output, as opposed to the baseline. It is important to note that this improvement in power output has minimal impact on the average power output at this RPM due to the low probability of wind speeds above this speed. However, this will increasingly contribute to average power output as RPM is lowered.

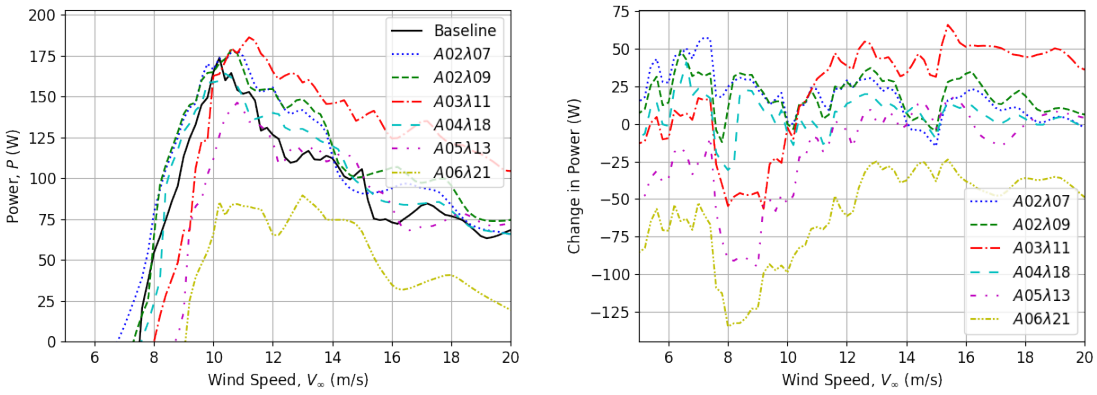

(a) Power Output

(b) Change in Power Output

Figure 3.20: Power curves of various tubercle shapes including the difference in power output compared to the baseline when applied to the Small-Scale H-type VAWT at 500 RPM.

To see why there is a sudden improvement in power output compared to the baseline blade past peak power output of the baseline, azimuthal plots were created to show the local aerodynamic characteristics of the turbine at a post turbine stall wind speed. The following plots, shown in Figure 3.21, show the local Re, α, C_l, C_d, C_n, C_t, and $C_\mathrm{l}/C_\mathrm{d}$ of the turbine equator at 13 m/s and 500 RPM. For better resolution of the plots, the number of azimuthal streamtubes was increased to 36.

As shown in Figure 3.21, the Reynolds number at this condition ranges between 130 000 and 400 000, which is outside the tubercle database limit of 300 000 from azimuth angles between 200 and 0°. However, the method does not extrapolate with Re and instead assumes a Re of 300 000 when interpolating in the database. The maximum AoA experienced is 27.5°, past the stall angle for these Reynolds numbers. The improvement in power generation is due to the tubercle blades' ability to create more lift at angles post-stall due to the presence of stream-wise counter-rotating vortices, delaying flow separation. This can be seen in Figure 3.21 (c), where the local lift coefficient for the tubercle blades is main-

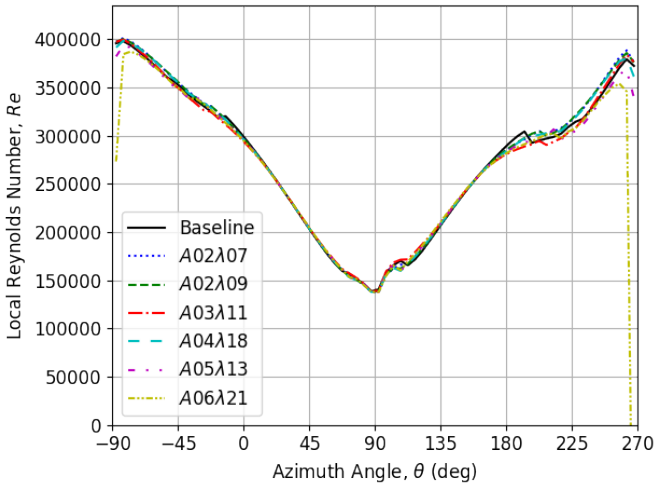

(a) Re

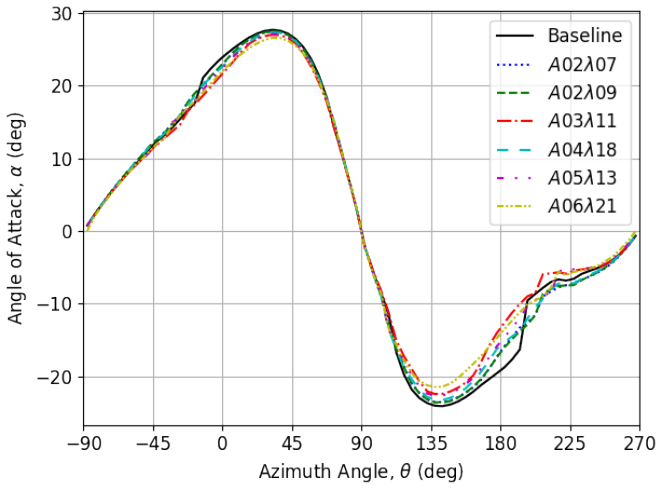

(b) α

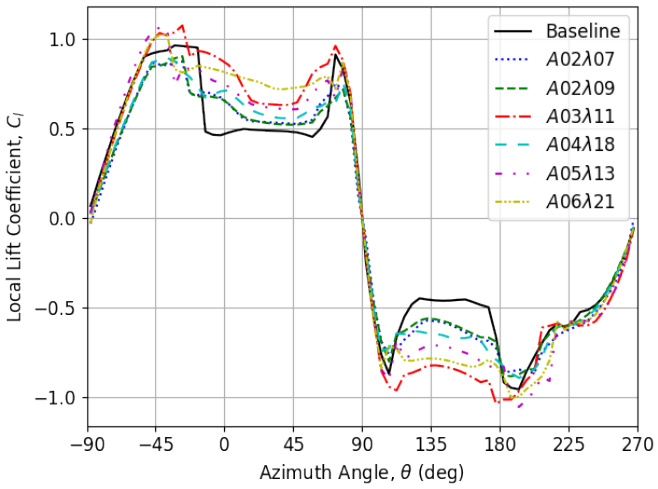

(c) C_{l}

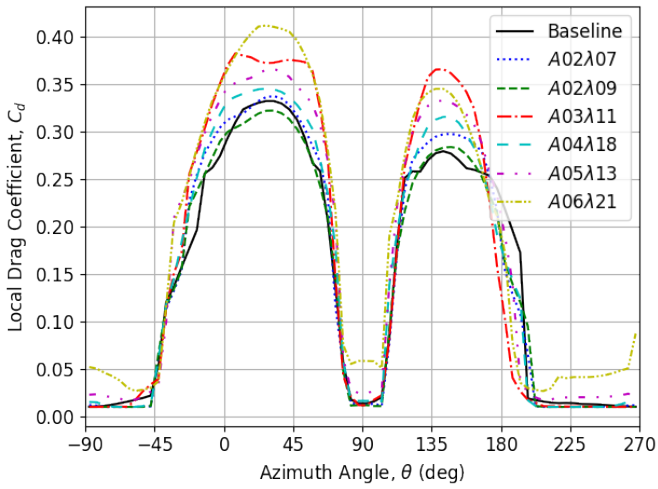

(d) C_{d}

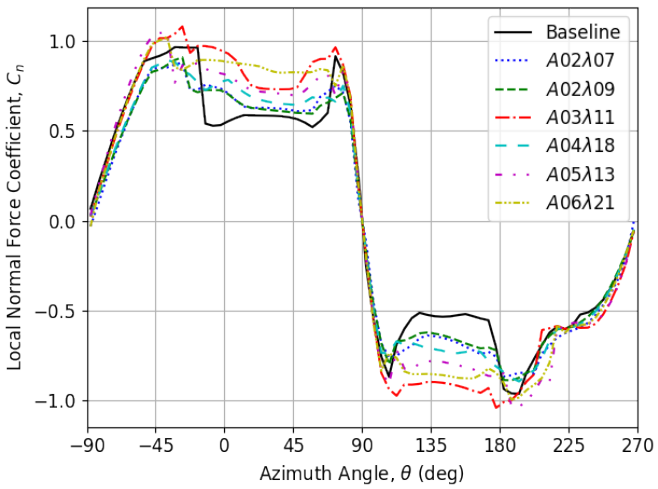

(e) C_{n}

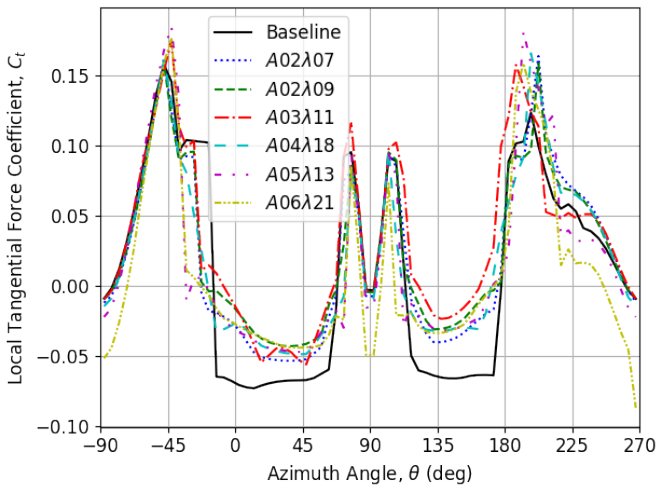

(f) C_{t}

Figure 3.21: Local aerodynamic characteristics of the Small-Scale H-type VAWT at 500 RPM and 13 m/s (TSR of 2.0) with various tubercle shapes.

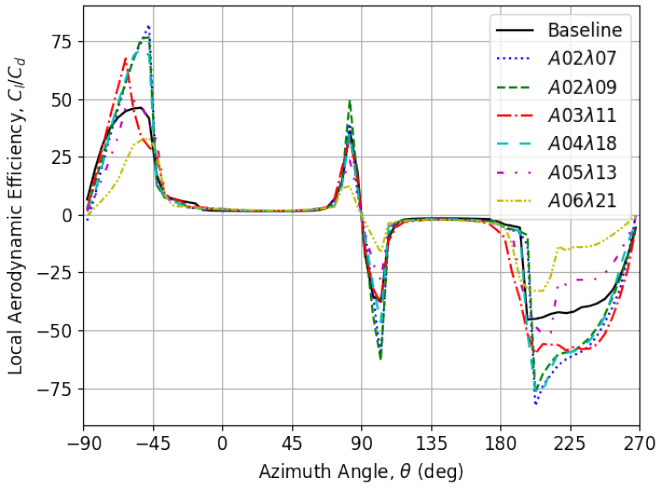

(g) C_l/C_d

Figure 3.21: Local aerodynamic characteristics of the Small-Scale H-type VAWT at 500 RPM and 13 m/s at the turbine equator with various tubercle shapes.

tained post-stall and does not have the drastic drop in lift experienced by the baseline at around θ of $-20°$ that persists until the flow reattaches around 70°. The same occurs in the downwind half of the rotor near peak α. Furthermore, the $A02\lambda09$ has a lower C_d in this post-stall region despite having a higher C_l, resulting in a higher C_t than the baseline. From Figure 3.21 (f), it can be seen that the tubercle blades produce a peak C_t similar to that of the baseline. However, most of the improvement comes from the reduction of adverse torque where α is at its greatest, into the post-stall regime. Since most tubercle shapes have a higher C_d in this regime, this improvement in C_t must be from the higher C_l due to the gradual separation of the flow over the tubercle blades and decrease in dynamic stall hysteresis.

Interestingly, since the tubercle blades extract more energy from the wind in the upwind half of the rotor, some tubercle blades experience a noticeably smaller AoA downwind than the baseline blade due to a further reduction in flow velocity, as shown in Figure 3.21 (b). This can result in pre-stall AoAs for wind speeds near the stall speed of the turbine. As a result, all tubercle shapes produce less adverse torque in the downwind stalled region, whereas the baseline maintains a similar torque to the upwind. This results in some tubercle shapes having a higher overall torque and power output.

Another characteristic of leading-edge tubercles is the reduction in $C_{l_{max}}$, which may be seen as a disadvantage in many applications. However. when used on VAWT blades, this can reduce the peak C_n in the upwind and downwind halves of the rotor, as shown in Figure 3.21 (e) for the $A02\lambda07$, $A02\lambda09$, and $A04\lambda18$ blades. This would result in a lower cyclic stress range, improving fatigue life. Since VAWT performance improvements are dependent on a higher prolonged efficiency at higher AoA, this reduction in C_l does not inhibit power production. For the $A02\lambda07$ specifically, it has an average power output improvement of 22.7%. So, applying leading-edge tubercles to VAWT blades will improve power output, while simultaneously, in some cases, improving the fatigue life of the turbine.

Overall, it is clear that the tubercle shapes provide enhanced power output for a wider range of TSRs, specifically enhancing the lower TSR limit, due to the reduction in adverse torque in the post-stall regime as a result of the counter-rotating stream-wise vortices delaying stall. Although this does not result in significant improvements in maximum power output, it does improve the wind speed probability-weighted average power output by as much as 22.7% with the $A02\lambda07$ and further suggests that tubercles would have better self-starting capabilities. With more power extracted at lower TSRs and some tubercle shapes simultaneously reducing the maximum range of C_{n}, tubercles could provide further benefit towards the cost per unit of energy of the turbine. There is also room for further improvement by varying the tubercle shape along the span of the blades. In the case of a Φ-rotor, for example, where the range of AoA along the blades increases as the blades get closer to the centre of rotation, some tubercle shapes may provide better post-stall performance in those regions, while the baseline or another shape could be used near the equator which experiences a smaller range of AoA.

4 Tubercle Shape Optimization on VAWT Blades

Results from the initial analysis of leading-edge tubercles applied to the small-scale H-type vertical axis wind turbine (VAWT) show that the wind speed probability-weighted average power output can be improved, with some tubercle shapes simultaneously reducing the ideal operating RPM of the turbine and reducing the peak forces experienced by the blades each rotation. This suggests that leading-edge tubercles can enhance power extraction while also improving fatigue life, ultimately reducing the cost per unit of energy. Since these performance improvements vary with tubercle amplitude and wavelength, there should exist an optimal combination of tubercle shape along the span of the turbine blades to capture the most improvement in average power output and fatigue life, depending on the wind environment and turbine shape. This chapter presents the first design optimization of leading-edge tubercles using the Double-Multiple Stream Tube Model (DMSTM).

4.1 Methodology

This section describes the formulation of the optimization problem and states the assumptions required to use the DMSTM. While the improvements in power output can be captured using the wind probability-weighted power output, quantifying the effect of leading-edge tubercles on fatigue life is more challenging when only using the DMSTM. This will be addressed through the use of a fatigue life indicator, FLI.

4.1.1 Objectives

The first objective considered was maximizing the wind speed probability-weighted power output, $\bar{P}$. Increasing $\bar{P}$ requires higher overall torques and rotational rates at wind speeds of high probability. Increasing torque through increased tangential force for a straight leading edge blade, however, would demand a higher RPM corresponding to the maximum lift coefficient, resulting in higher normal forces on the blades. Thus, maximizing $\bar{P}$ will negatively affect the fatigue life of the turbine. Leading-edge tubercle blades, on the other hand, can achieve higher overall torques by providing more lift at post-stall angles, reducing the adverse torque in these regions compared to the baseline. This does not require a large peak normal force nor high RPM to keep angles of attack (AoA) below stall.

This presents the next objective, which was to maximize the wind speed probability-weighted fatigue life indicator, $\overline{FLI}$. Ideally, this objective would be the actual fatigue life of the turbine. However, this would require a structural analysis to determine the maximum and minimum stresses in the turbine each cycle, which could be done, for example,

using finite element software. With a full analysis, instead of having two separate objectives, one could combine the fatigue life and $\bar{P}$ into a single objective to maximize total power output during the life of the turbine. A further improvement could come from including a cost analysis of the turbine to determine the cost per unit of power produced. However, having $\bar{P}$ and $\overline{FLI}$ both as separate objectives will provide insight into the design space of tubercle shapes applied to VAWT blades by showing which shapes provide improvements in either $\bar{P}$ and/or $\overline{FLI}$.

While the main area of interest is in the trade-offs between $\bar{P}$ and $\overline{FLI}$ with varying tubercle shapes, a second optimization case considered a different objective. Instead of $\overline{FLI}$, the other objective function is $\bar{P}$ using the wind probability-weighted average of a different geographical location. This would indicate the robustness of the VAWT design with tubercles due to the variation in probable wind speeds.

4.1.2 Fatigue Life Indicator

Without performing a structural analysis, a method for comparing the fatigue life of different tubercle configurations was created. The first step was to solve the Stress-Life equation, described by Basquin's Law (4.1), for the number of cycles until failure, N_f, where σ_a is the cycle stress amplitude, assuming a symmetric loading [103].

$$\sigma_a = \sigma'_f(2N_f)^{-b} \tag{4.1}$$

$$\ln \sigma_a = \ln(\sigma'_f(2N_f))(-b) \tag{4.2}$$

where σ'_f and b are material properties. Assuming the structural characteristics are unchanged between different turbine configurations and the stresses are within the elastic regime, σ'_f and b are unchanged, and the stress on the turbine will be proportional to the force applied to the blades.

$$-\ln(2N_f) \implies \ln F_a \tag{4.3}$$

$$N_f \implies \frac{1}{2F_a} \tag{4.4}$$

Since VAWTs experience a single cycle of tensile and compressive stresses each rotation due to normal forces, faster spinning turbines will fail sooner. To account for this, dividing N_f by the rotational rate, Ω, turns cycles until failure into minutes and gives the Fatigue Life Indicator, FLI, where F_a is the difference between the maximum and minimum forces experienced by the turbine each cycle. For this optimization, the range of forces is assumed to be the normal forces experienced by the blades, determined by integrating stream tubes at each azimuthal coordinate in the vertical direction from the DMSTM. Thus, this does not account for centrifugal forces acting on the blades. These forces, however, would decrease compressive stresses in the upwind and increase tensile stresses in the downwind equally, having minimal effect on the difference in peak stresses experienced.

$$FLI = \frac{1}{2F_a\Omega} \tag{4.5}$$

The average wind probability-weighted Fatigue Life Indicator, $\overline{FLI}$, is determined similarly to $\bar{P}$, by integrating the wind speed probability-weighted FLI for all wind speeds.

$$\overline{FLI} = \int_0^\infty FLI(V)Pr(V)\,dV \tag{4.6}$$

While $\overline{FLI}$ does not provide the fatigue life, it does allow for a quantitative comparison between turbine configurations of the same structure in the same wind environment. A turbine with a higher force amplitude or Ω will have a lower $\overline{FLI}$.

4.1.3 Variables

The possible variables for VAWT optimization using the DMSTM are the various turbine geometry parameters, the turbine rotational speed, and the airfoil shape in each streamtube, accounted for by changing the aerodynamic database used for that streamtube. Due to the limitations of $\overline{FLI}$, comparisons are only valid between turbines of the same shape and material. So, the turbine shape was fixed during optimization.

The rotational rate, Ω, can be varied. Increasing Ω increases the tip speed ratio of the turbine. For a given wind speed, this corresponds to a lower AoA range. Ideally, the turbine blades are not stalled during probable wind speeds to have higher aerodynamic efficiency, increasing $\bar{P}$. Since tubercles have higher aerodynamic efficiencies than the baseline post-stall, they may be able to operate at lower tip speed ratios, improving $\overline{FLI}$, without sacrificing $\bar{P}$. The lower limit constraint on Ω is at least above zero since the turbine should not spin in the other direction. However, since $\overline{FLI}$ approaches infinity as Ω approaches zero, the lower limit was chosen to be 200 RPM. From Figure 3.16, all leading-edge shapes show minimal $\bar{P}$ at this RPM. So, this Ω is outside the area of interest. From the same figure, all shapes have a maximum $\bar{P}$ at about 500 RPM, so the upper limit was chosen to be 800 RPM. While designing for a constant RPM is useful for applications where no feedback control with wind speed is available, designing for a constant tip speed ratio (TSR), $\hat{\lambda}$, allows the turbine to be near the ideal range of AoA, regardless of wind speed. This results in further energy extraction from the wind. Thus, another set of optimizations, where a constant TSR is chosen, was also explored. For these, the TSR was bounded between one and seven, inclusive. For clarity, designs resulting from RPM as a variable will operate at a constant RPM, while designs with TSR as a variable operate at a constant TSR.

The tubercle shape along the blade was not as straightforward to formulate. The first option considered was having sections of variable length, each with a discrete variable denoting the tubercle shape. This presents interface issues with the DMSTM since each streamtube can only have a single tubercle shape, and changing the number or spacing of streamtubes would change the validity of the results, as shown in the convergence studies in Section 3.1.4. So, it was decided to have a discrete variable, a, for each vertical set of streamtubes to denote the tubercle shape, which could be any number up to $n-1$, depending on how many different airfoils/tubercle shapes are in the aerodynamic database. For example, for the test cases presented in this thesis, the tubercle shapes and their values are shown below in Table 4.1. Since the wind boundary layer was neglected in this optimization, the blade

was assumed to be symmetric. So, six variables for airfoil shape were used instead of one for each of the 11 vertical streamtubes.

Table 4.1: Summary of Discrete Values for Tubercle Shapes.

Value	Tubercle Shape
0	Baseline
1	A02λ07
2	A02λ09
3	A03λ11
4	A04λ18
5	A05λ13
6	A06λ21

Formulating the airfoil shape along the blade in this way, however, does not ensure the tubercle wavelengths properly align. So, this optimization requires the assumption that the discontinuities on the leading edge of the blade, as a result of the improperly aligned sinusoidal shapes, do not affect the objective functions. For this to be accounted for, the size of each streamtube would need to be dependent on the tubercle wavelength, ensuring each streamtube starts and ends on the mean leading-edge value. Instead, this optimization maintains the 11 evenly spaced streamtubes in the vertical direction.

4.1.4 Optimization Problem Formulation

To summarize, the first optimization problem aims to maximize the $\bar{P}$ and $\overline{FLI}$ at a single wind speed-probability distribution environment, while varying the rotational rate and the tubercle shape along the blade span used to evaluate each vertical set of streamtubes. Thus, the formulated problem is:

$$
\begin{aligned}
\text{Maximize:} \quad & f_1(x) = \bar{P} = \int_0^\infty Pr \cdot P(x)\ dV \\
& f_2(x) = \overline{FLI} = \int_0^\infty Pr \cdot \frac{1}{2F_a(x)\Omega(x)}\ dV \\
\text{w.r.t:} \quad & x = \begin{cases} (a_1, a_2, \ldots, a_6, \Omega)^T & \text{when varying } \Omega \\ (a_1, a_2, \ldots, a_6, \hat{\lambda})^T & \text{when varying } \hat{\lambda} \end{cases} \\
\text{Subject to:} \quad & a_i \in \mathbb{Z} \cap [0, n-1] \\
& \Omega \in [\Omega_{\min}, \Omega_{\max}] \\
& \hat{\lambda} \in [\hat{\lambda}_{\min}, \hat{\lambda}_{\max}]
\end{aligned}
$$

The next optimization problem aims to maximize the $\bar{P}_1$ and $\bar{P}_2$, the wind speed-probability weighted average power at two different wind speed environments, while varying the rotational rate and the tubercle shape along the blade span in each of the 11 vertical stream tubes. This is described by:

$$
\begin{aligned}
\text{Maximize:} \quad & f_1(x) = \bar{P}_1 = \int_0^\infty Pr_1 \cdot P(x)\, dV \\
& f_2(x) = \bar{P}_2 = \int_0^\infty Pr_2 \cdot P(x)\, dV \\
\text{w.r.t:} \quad & x = \begin{cases} (a_1, a_2, \ldots, a_6, \Omega)^T & \text{when varying } \Omega \\ (a_1, a_2, \ldots, a_6, \hat{\lambda})^T & \text{when varying } \hat{\lambda} \end{cases} \\
\text{Subject to:} \quad & a_i \in \mathbb{Z} \cap [0, n-1] \\
& \Omega \in [\Omega_{\min}, \Omega_{\max}] \\
& \hat{\lambda} \in [\hat{\lambda}_{\min}, \hat{\lambda}_{\max}]
\end{aligned}
$$

Both of these optimization problems are multi-objective and have discrete variables, making Non-dominated Sorting Genetic Algorithm II (NSGA-II), developed by Deb *et al.* [104], a suitable optimization routine. It is a multi-objective evolutionary algorithm designed to handle elitism and population diversity using a fast sorting method. Instead of using a weighted-sum method with various weights to generate the Pareto Frontier, NSGA-II advances the front towards the Pareto Frontier each generation through a change in mating pool selection by introducing non-domination fronts and crowding distance. Appendix D shows an explanation and validation of the NSGA-II code created for tubercle VAWT optimization.

The genome of each member of the population comprised six permutation-encoded discrete values for the airfoil shape in each vertical set of streamtubes, symmetric about the equator. This was done because bit encoding these variables would require 2^k ($k \in \mathbb{N}$) discrete values. So, in this case, the tubercle shape could be bit-encoded if there were eight shapes instead of seven. The remainder of the genome is 16 bits for Ω to provide two decimal places of precision between 200 and 800 RPM. For optimizations with TSR as a variable, the same precision was applied. A summary of the parameters used in NSGA-II for this optimization is shown in Table 4.2. An explanation of these parameters are found in Appendix D. Since NSGA-II includes the parents in the non-dominating sorting for elitism, a relatively high mutation rate of 15% was chosen to promote random tubercle shape changes since they are permutation encoded, without the risk of losing the previous best solutions.

Table 4.2: Summary of NSGA-II Parameters.

Parameter	Value
Population Size	100
Maximum Generations	250
Crossover Rate	0.80
Mutation Rate	0.15

4.2 Small-Scale H-Type VAWT Test Case

This section presents the results of both optimization problems when applied to the Small-Scale H-type VAWT described in Section 3.2.1. The general optimization problems formulated in Section 4.1.4 are applied with the values in Table 4.3. The first optimization case, maximizing $\overline{FLI}$ and $\bar{P}$, uses the wind speed probability density of the SWiFT Test Site in Lubbock, Texas. The second optimization case maximizes $\bar{P}_K$ and $\bar{P}_S$, the wind speed probability-weighted average power output of Kingston, ON, and the SWiFT Test Site, respectively. Only results with TSR as a variable are shown in this section. Designs with RPM as a variable are presented in Appendix E.

Table 4.3: Values used for each of the optimization variables.

Characteristic	Value
n	7
Ω_{min} (RPM)	200
Ω_{max} (RPM)	800
$\hat{\lambda}_{\text{min}}$	1
$\hat{\lambda}_{\text{max}}$	7

With the results from Chapter 3, the solution for each tubercle shape, including the baseline, corresponding to maximum $\bar{P}_S$, was included in the initial population. Using the resulting streamtube and wind speed discretization from the convergence studies in Chapter 3, each optimization took approximately 40 hours to run all 250 generations on a single core of an *AMD 7900X* 4.7 GHz processor. Afterwards, the entire history of parent and child fitness values was non-dominated sorted to determine the entire Pareto frontier.

4.2.1 Maximization of $\overline{FLI}$ and $\bar{P}$

A plot of the resulting Pareto frontier of the first optimization, maximizing both $\overline{FLI}$ and $\bar{P}$, including all the solutions explored during all generations, can be seen in Figure 4.1. Overall, the Pareto frontier shows maximum $\overline{FLI}$ occurring at zero $\bar{P}$ since minimizing TSR results in the lowest RPM and range of local velocities over the blades, minimizing the range of forces experienced. If the TSR variable did not have a lower bound of 1, $\overline{FLI}$ would approach infinity as TSR goes to zero. Increasing $\bar{P}$ comes at the cost of reduced $\overline{FLI}$, up until maximum $\bar{P}$. After this point, both $\overline{FLI}$ and $\bar{P}$ decrease. This is a result of increasing TSR, which reduces the range of AoA, minimizing the component of lift in the tangential direction that can contribute to the overall torque of the turbine, while increasing the stress cycle frequency. Therefore, the best trade-off between $\overline{FLI}$ and $\bar{P}$ exists in the region bounded by the minimum TSR and the TSR of maximum $\bar{P}$. This region is characterized by a wide range of AoA either at or beyond stall, where tubercles have been shown to excel.

Figure 4.1 (b) shows a magnified view of the Pareto front, with points of interest. Details of these points are shown in Table 4.4 with drawings of the corresponding blades shown in Figure 4.2. Starting with maximum $\bar{P}$, which is a uniform $A02\lambda09$ blade operating at a TSR of 2.92, there is a 19.4 % improvement in power output while still increasing $\overline{FLI}$ by 13.6 %. This result aligns with the findings from the power coefficient contours in Chapter 3 (see Figure 3.17(c)). Since the maximum $\bar{P}$ blade operates at a 4.7 % higher TSR compared to the baseline blade, the improvement in $\overline{FLI}$ must come from the reduction in the range

of normal forces, also shown in Chapter 3 (see Figure 3.21(e)).

Table 4.4: Performance characteristics of the various designs from optimizing wind probability-weighted average fatigue life indicator and power output at the SWiFT Test Site for the Small-Scale H-type VAWT with TSR as a variable.

Design	TSR	RPM at 15 m/s	$\overline{FLI}$ (x 10^{-4})	$\bar{P}$ (W)
Baseline	2.79	799.3	2.64	68.95
Maximum $\bar{P}$	2.92 (+4.7 %)	836.5	3.00 (+13.6 %)	82.35 (+19.4 %)
Point A	2.98 (+6.8 %)	853.7	3.39 (+28.4 %)	79.94 (+15.9 %)
Equal $\bar{P}$	2.61 (−6.5 %)	747.7	3.54 (+34.1 %)	69.03 (+0.1 %)

Values in parentheses denote percent difference compared to the Baseline.

Following the Pareto front for decreasing $\bar{P}$ from the maximum $\bar{P}$ solution, the front is dominated by uniform $A02\lambda09$ blades until around 81.5 W, where $A02\lambda07$ segments are introduced. The number of segments of $A02\lambda07$ is increased until Point A, where the blade is entirely $A02\lambda07$ except for the tips, which are $A02\lambda09$. After Point A, a reduction in $\bar{P}$ gives a relatively minimal improvement in $\overline{FLI}$. While still giving a 15.9 % improvement in $\bar{P}$, it has a 28.4 % higher $\overline{FLI}$, making it a good point to trade off $\bar{P}$ for $\overline{FLI}$ instead of the maximum $\bar{P}$ design. This design also operates at a 6.8 % higher TSR than the baseline, higher than the Maximum $\bar{P}$ design. Therefore, the improvement in $\overline{FLI}$ is from a further reduction in the range of forces experienced during each rotation. From Figure 3.21 in Chapter 3, the uniform $A02\lambda07$ blade was shown to have a lower maximum and minimum normal force than the $A02\lambda09$ for a slight reduction of $\bar{P}$. Continuing to the left of Point A, the front is uniform $A02\lambda07$ blades with a slightly increasing TSR up to 3.05 until the discontinuity in the front at 78.5 W. The discontinuity corresponds to a drop in TSR down to 2.66, while still maintaining the uniform $A02\lambda07$ blades. So, the corner in the Pareto at Point A is a result of purely reducing the range of forces by replacing the $A02\lambda09$ segments with $A02\lambda07$. Beyond this, the only way to get a significant improvement in $\overline{FLI}$ is to drop TSR at the expense of $\bar{P}$. The point Equal $\bar{P}$ was chosen to show the pure improvement in $\overline{FLI}$ that tubercles can provide compared to a baseline blade operating at maximum $\bar{P}$. This blade is also purely $A02\lambda07$ but operates at a TSR of 2.61, 6.5 % lower than the baseline, and provides a 34.1 % higher $\overline{FLI}$.

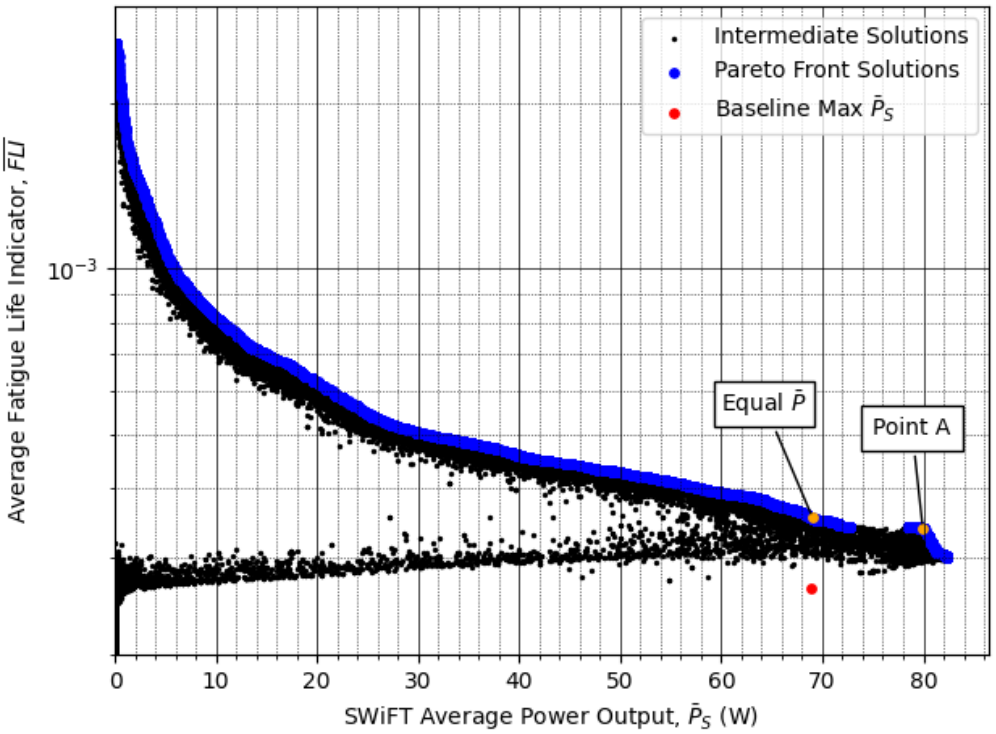

(a) All Solutions

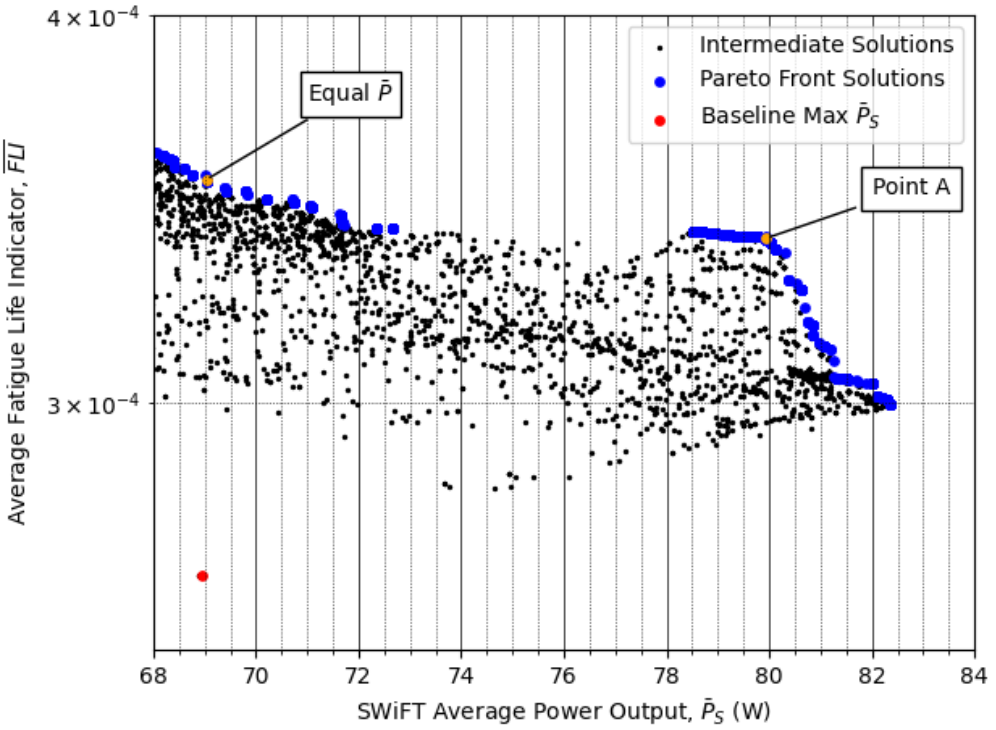

(b) Magnified View of the 68–84 W $\bar{P}_S$ Region

Figure 4.1: All solutions explored by NSGA-II optimizing wind probability-weighted average fatigue life indicator and power output at the SWiFT Test Site for the Small-Scale H-type VAWT with TSR as a variable.

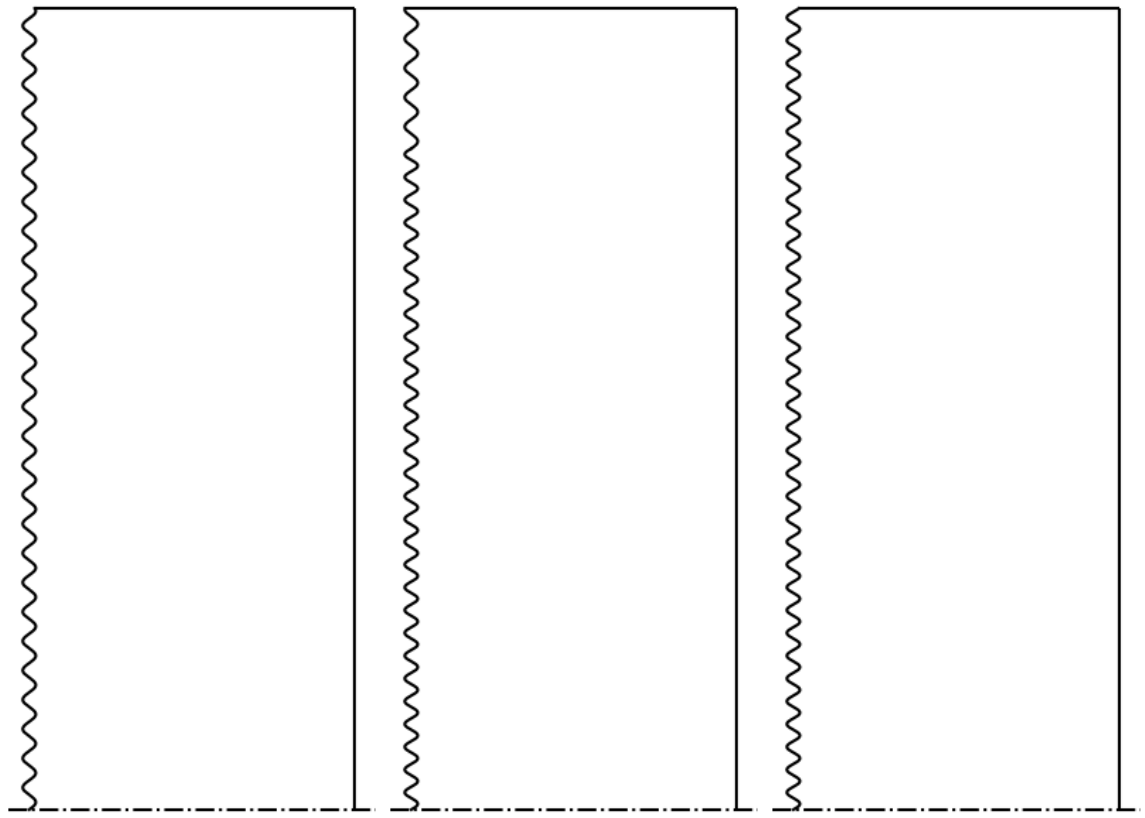

(a) Maximum $\bar{P}$ (b) Point A (c) Equal $\bar{P}$

Figure 4.2: Select half-blade designs from optimizing wind probability-weighted average fatigue life indicator and power output at the SWiFT Test Site for the Small-Scale H-type VAWT with TSR as a variable.

4.2.2 Maximization of $\bar{P}_S$ and $\bar{P}_K$

While tubercles were shown to improve both $\overline{FLI}$ and $\bar{P}$ compared to the baseline at the SWiFT Test Site in Lubbock, Texas, introducing another wind probability distribution would indicate the robustness of the design in different wind environments. For this reason, the wind probability distribution of Kingston, Ontario, was introduced, which has a most probable wind speed of 3 m/s. This is a slower wind environment compared to the SWiFT Test Site's most probable wind speed of 6.5 m/s. Using these wind environments to maximize the wind probability-weighted average power output at both the SWiFT Test Site and Kingston, ON, using NSGA-II yields the following solution, shown in Figure 4.3. Overall, designs that increase $\bar{P}_S$ also increase $\bar{P}_K$, since the turbine operates at a constant TSR. So, at slower wind speeds, the turbine will operate at a lower RPM to give the best range of AoA for maximum power output. The wind probability-weighted power output for each design in Kingston, ON is significantly lower than at the SWiFT Test Site due to the lower probable wind speeds, resulting in overall less energy in the wind on average in Kingston.

Ultimately, the solution is a single point, which is a uniform $A02\lambda09$ blade operating at a TSR of 2.92, corresponding to the maximum $\bar{P}$ solution from the previous optimization. This optimal solution, described in Table 4.5, provides a 19.4 % and 21.4 % increase in $\bar{P}_S$

and $\bar{P_K}$ compared to the baseline, respectively. This suggests that the maximum $\bar{P}$ designs are robust to different wind environments. However, further optimizations should include maximization of both $\overline{FLI}$ and $\bar{P}$ using the wind distributions of Kingston, ON, and the SWiFT test site to confirm that the other design points are robust as well.

The results using TSR as a design variable are unlike the results shown in Appendix E, where the optimization did not come to a single solution. In that case, the entire Pareto front is uniform $A02\lambda07$ blades with a lower design RPM for maximum $\bar{P_K}$. Since Kingston has a lower probable wind speed, the design is lower RPM to give a TSR closer to the optimum. It is also apparent that the constant TSR designs provide higher overall $\bar{P}$ compared to constant RPM. This is because constant TSR designs change RPM to operate at the ideal range of AoA for the current wind speed, whereas a constant RPM design will have too high of a TSR at low wind speeds but too low of a TSR at high wind speeds to operate efficiently.

Table 4.5: Performance characteristics of the various designs from optimizing wind probability-weighted average power output at the SWiFT Test Site and Kingston, ON, for the Small-Scale H-type VAWT with TSR as a variable.

Design	TSR	RPM at 15 m/s	$\bar{P_S}$ (W)	$\bar{P_K}$ (W)
Baseline	2.79	799.3	68.95	27.00
Optimal	2.92 (+4.7 %)	836.5	82.35 (+19.4 %)	32.79 (+21.4 %)

Values in parentheses denote percent difference compared to the Baseline.

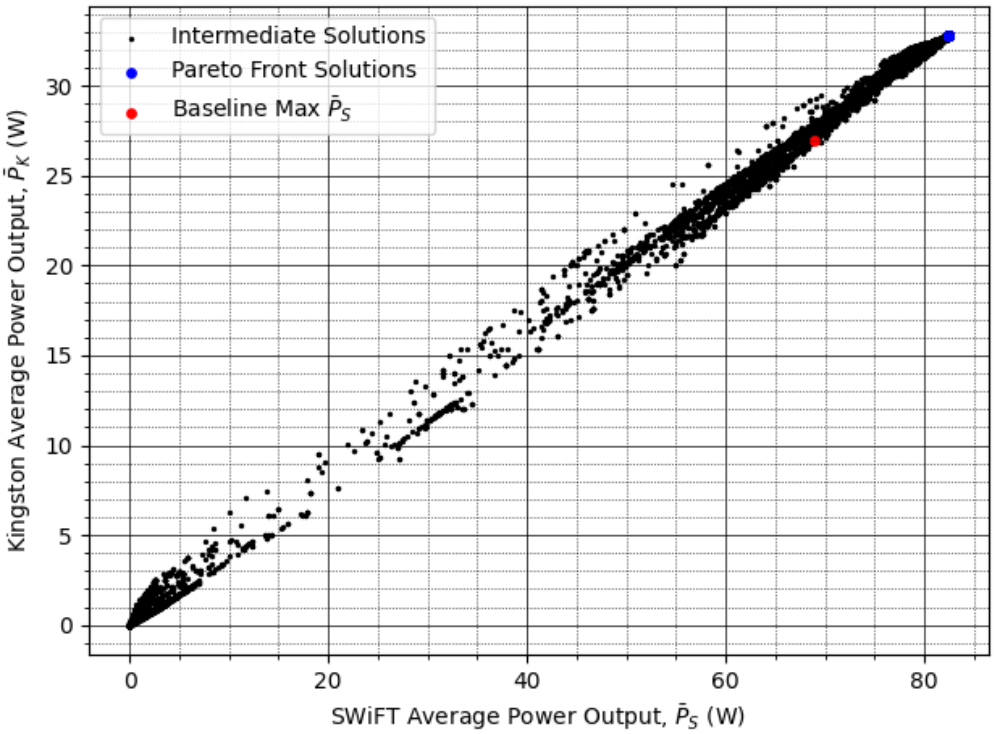

(a) All Solutions

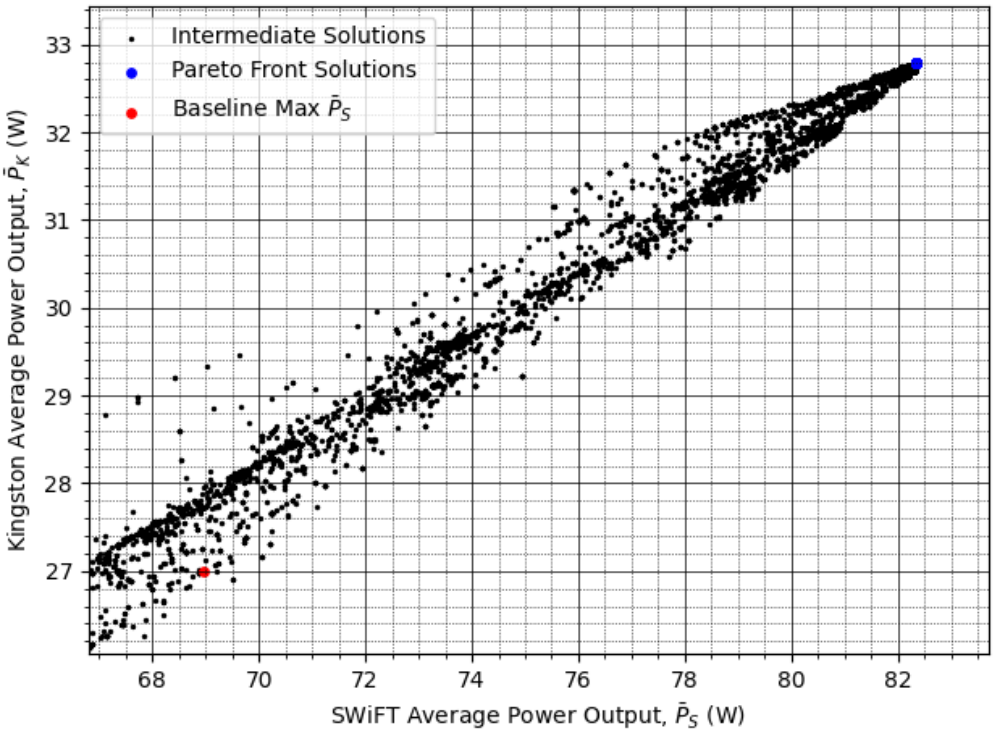

(b) Magnified View of the 67–84 W $\bar{P}_S$ Region

Figure 4.3: All solutions explored by NSGA-II optimizing wind probability-weighted average power output at the SWiFT Test Site and Kingston, ON, for the Small-Scale H-type VAWT with TSR as a variable.

4.3 1:7 Scale Sandia Test Case

Since this optimization does not change the geometry of the turbine, a small-scale Sandia 17-m Φ-rotor will also be analyzed. A scale of 1:7 was chosen, scaling the radius, height, and chord of the blades, to reduce the Re experienced while also presenting a similar-sized turbine geometry of a different shape from the small H-type. Other than the turbine geometry, all optimization parameters remain the same as those used in Section 4.2. The turbine is described in Table 4.6 and Figure 4.4.

Table 4.6: Geometric characteristics of the 1:7 Scale Sandia-17m wind turbine.

Characteristic	Value
Height (m)	2.429
Equatorial Radius (m)	1.195
Chord (m)	0.07962
Number of Blades	2
Swept Area, S (m^2)	3.913

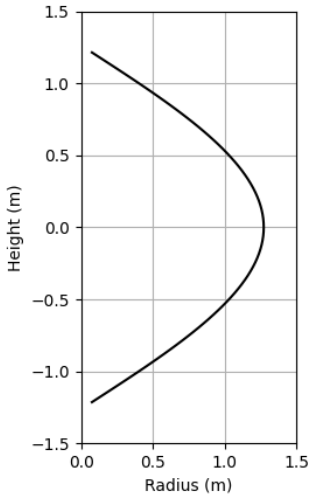

Figure 4.4: Rotor Radius as a function of local turbine height of the 1:7 Scale Sandia-17m VAWT.

Since the performance improvements from tubercles were a result of a reduction in the range of normal force throughout rotation while simultaneously being able to operate at lower TSRs due to their higher aerodynamic efficiency at a larger range of AoAs, the $\overline{FLI}$ and $\bar{P}$ improvements shown with the Small-Scale H-type VAWT should be further realized in a Φ-rotor, where the local radius of the blade decreases towards the blade tips (or root), causing a lower local TSR and wider range of AoA. The results presented in this section are with TSR as a design variable. Results with RPM as a variable are presented in Appendix E. Similar to the optimization of the Small-Scale H-type, the initial population of NSGA-II included a single genome for each maximum $\bar{P}$ uniform blade solution from the power contours of the 1:7 Scale Sandia 17-m, shown in Appendix C.

4.3.1 Maximization of $\overline{FLI}$ and $\bar{P}$

The Pareto frontier resulting from the maximization of $\overline{FLI}$ and $\bar{P}$ for the 1:7 Scale Sandia 17-m is shown in Figure 4.5. Similar to the Small-Scale H-type design space, $\overline{FLI}$ approaches infinity as TSR decreases. As $\bar{P}$ increases, $\overline{FLI}$ decreases until maximum $\bar{P}$. Afterwards, both $\overline{FLI}$ and $\bar{P}$ decrease as a result of higher TSRs, reducing the amount of lift in the tangential direction, while also increasing the stress cycle frequency. This is consistent with the H-type result, showing that the ideal designs exist in the region characterized by a TSR below the TSR for maximum $\bar{P}$, where post-stall AoAs are experienced.

Comparing the magnified view of the frontier in Figure 4.5 (b) to the Small-Scale H-type in Figure 4.1, there is no corner where a clear trade-off between $\overline{FLI}$ and $\bar{P}$ could be realized. However, there is a curvature reversal with a near-infinite slope at maximum $\bar{P}$. So, Point A was chosen as a point of interest since it could provide a greater $\overline{FLI}$ for a minimal cost in $\bar{P}$. The last design examined is the point that has an equal $\bar{P}$ of the baseline blade when operating at a TSR for maximum $\bar{P}$. These designs are shown in Figure 4.6, while their performance is quantified in Table 4.7.

Table 4.7: Performance characteristics of the various designs from optimizing wind probability-weighted average fatigue life indicator and power output at the SWiFT Test Site for the 1:7 Scale Sandia 17-m with TSR as a variable.

Design	TSR	RPM at 15 m/s	$\overline{FLI}$ (x 10^{-4})	$\bar{P}$ (W)
Baseline	5.58	669.0	1.18	263.02
Maximum $\bar{P}$	5.80 (+3.9 %)	695.4	1.12 (−5.1 %)	297.15 (+13.0 %)
Point A	5.46 (−2.2 %)	654.6	1.25 (+5.9 %)	295.36 (+12.3 %)
Equal $\bar{P}$	4.70 (−15.8 %)	563.5	1.85 (+56.8 %)	262.84 (−0.1 %)

Values in parentheses denote percent difference compared to the Baseline.

The maximum $\bar{P}$ design consists of an $A03\lambda11$ leading edge with $A02\lambda07$ at the tips at a TSR of 5.80, providing a 13 % greater $\bar{P}$ at the expense of a 5.1 % lower $\overline{FLI}$ compared to the baseline blade. Interestingly, this design outperforms the uniform $A03\lambda11$ blade shown in Appendix C, whereas the best-performing uniform blade for the H-type was also the maximum $\bar{P}$ design resulting from the optimization. While the uniform $A03\lambda11$ blade has the greatest $\bar{P}$, the $A02\lambda07$ blade has a peak $\bar{P}$ that occurs at a lower TSR, making it more ideal for the blade tips of a Φ-rotor, where the local TSR is much lower and a wider range of AoA is experienced. Although the maximum $\bar{P}$ design appears to produce 19.59 W more than the uniform $A03\lambda11$ shown in Appendix C, the results should not be compared directly since the optimization uses 30 velocity increments whereas the contours use 100. When the uniform $A03\lambda11$ is evaluated in the optimization's fitness function, it gives 297.08 W, making the maximum $\bar{P}$ design's improvement negligible. Nevertheless, it shows that non-uniform blades of varying tubercle shape, with those performing better at low TSR near the tips, can yield greater wind probability weighted power output than a similar uniform blade.

Following the Pareto to the left from maximum $\bar{P}$, the optimizer introduced another segment of $A02\lambda07$ at the tips, while simultaneously reducing TSR. This leads to Point A, which has a TSR of 5.46, 2.2 % lower than the baseline. It also has a 12.3 % higher $\bar{P}$ and

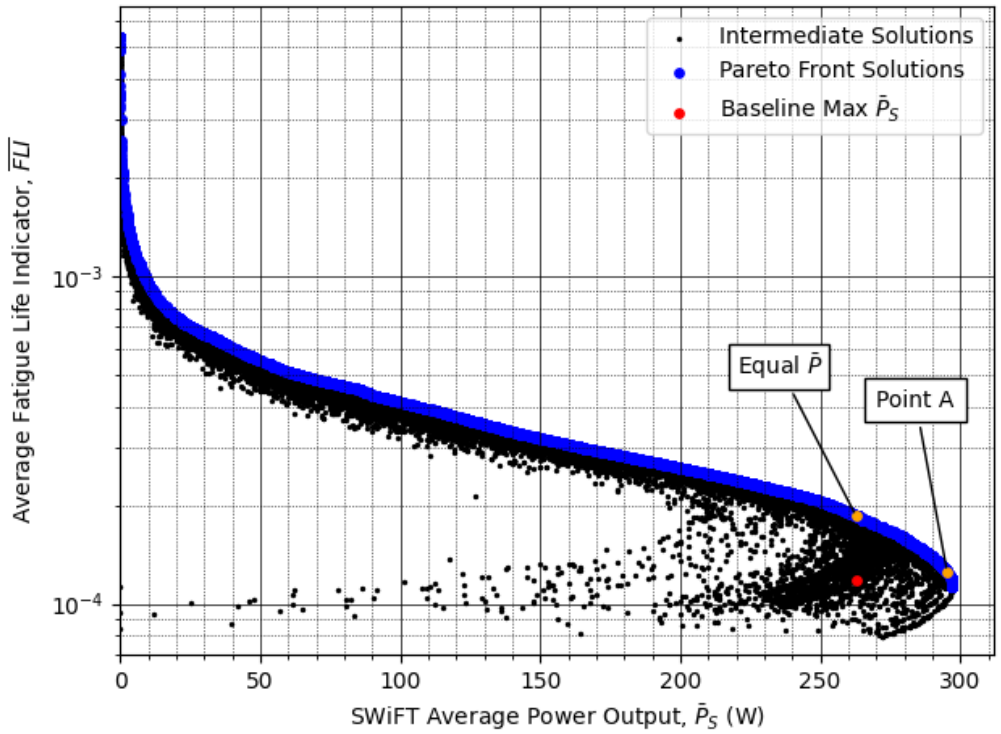

(a) All Solutions

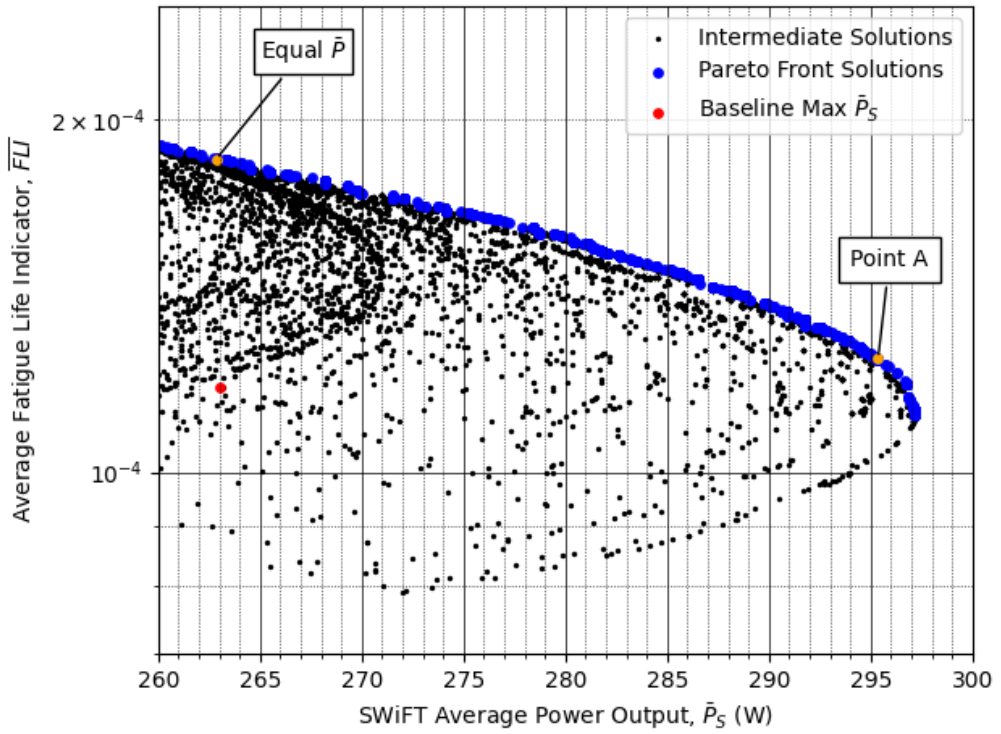

(b) Magnified View of the 260–300 W $\bar{P}_S$ Region

Figure 4.5: All solutions explored by NSGA-II optimizing wind probability-weighted average fatigue life indicator and power output at the SWiFT Test Site for the 1:7 Scale Sandia 17-m with TSR as a variable.

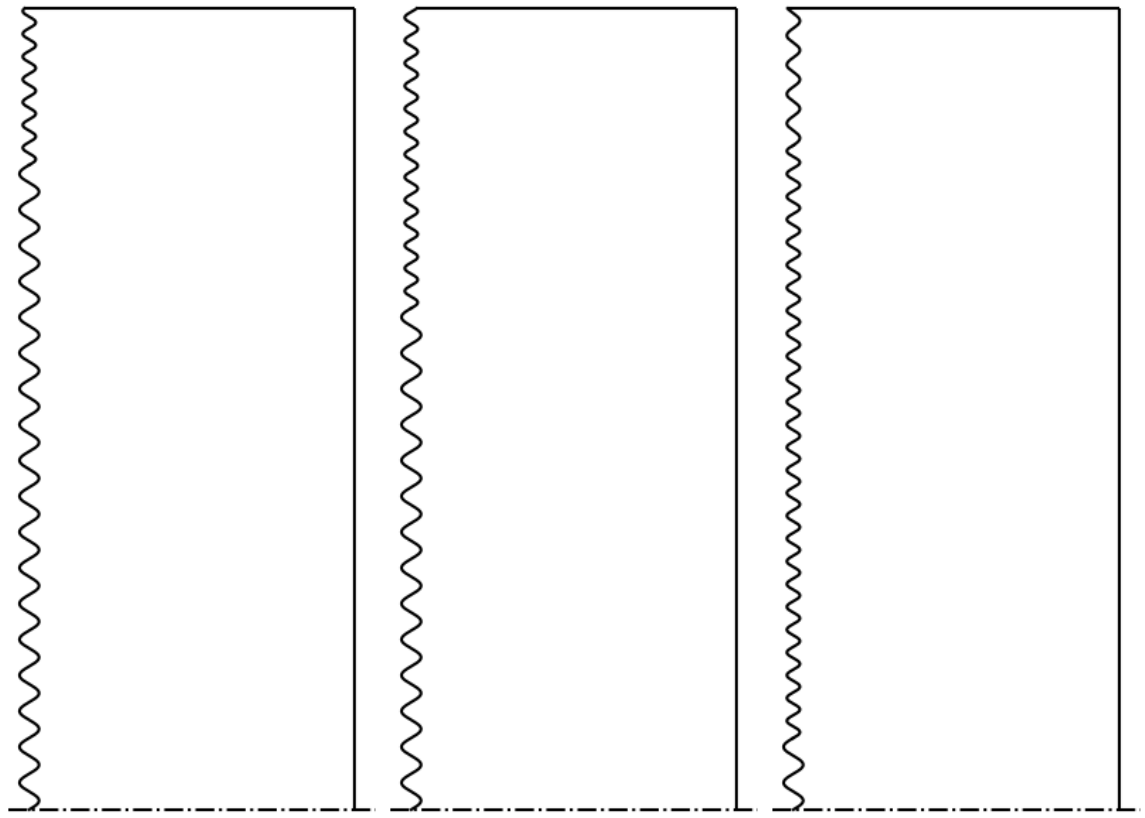

(a) Maximum $\bar{P}$ (b) Point A (c) Equal $\bar{P}$

Figure 4.6: Select half-blade designs from optimizing wind probability-weighted average fatigue life indicator and power output at the SWiFT Test Site for the 1:7 Scale Sandia 17-m with TSR as a variable. Note that the blades are curved, so this figure shows the frontal projection of the blades and tubercle locations.

5.9 % greater $\overline{FLI}$. Since the $A02\lambda07$ segments perform well at low TSR, the design TSR can drop, while also providing a lower range of forces compared to the $A03\lambda11$. So, at the expense of less than 2 W, the Point A design reduces the design TSR, providing an 11.6 % increase in $\overline{FLI}$ compared to the maximum $\bar{P}$ design.

Continuing to the left on the Pareto, more $A03\lambda11$ segments are replaced by $A02\lambda07$ while decreasing TSR. At the point with a similar maximum $\bar{P}$ of the uniform baseline blade, Equal $\bar{P}$, only the $A03\lambda11$ segment at the equator remains. The rest of the blade is $A02\lambda07$, with $A02\lambda09$ at the tips. Designs in this region, along with any further left on the Pareto at lower TSR, have varying shapes at the blade tips. This is likely from extremely low local TSR at the tips, resulting in mostly flat plate aerodynamic characteristics. So, based on the evaluated fitness of the optimization, there is minimal impact on the tubercle shape in this region. Regardless, the Equal $\bar{P}$ design provides a 56.8 % increase in $\overline{FLI}$ as a result of a 15.8 % lower TSR and a lower range of normal forces each rotation while still providing the same power output as the baseline.

4.3.2 Maximization of $\bar{P}_S$ and $\bar{P}_K$

To get an idea of the design robustness, the second optimization was performed on the 1:7 Scale Sandia 17-m to maximize the wind speed probability-weighted average power output using probability density functions from the SWiFT Test Site and Kingston, ON, $\bar{P}_S$ and $\bar{P}_K$, respectively. The resulting Pareto Front, shown in Figure 4.5 shows a similar trend that resulted from the H-type VAWT. As $\bar{P}_S$ increases, $\bar{P}_K$ increases linearly as well. Once again, $\bar{P}_S$ is greater than $\bar{P}_K$ since the SWiFT Test Site has a higher probable wind speed. It is also apparent that the Small-Scale Sandia produces more power than the Small H-type. This is a result of the greater swept area of the Small-Scale Sandia.

Unlike the Small H-type, this optimization does not result in a single optimal solution. The Maximum $\bar{P}_S$ design, described in Table 4.8, is an $A03\lambda11$ blade with a single $A02\lambda07$ segment on each tip operating at a TSR of 5.80, exactly like the Maximum $\bar{P}$ design in Figure 4.6. The maximum $\bar{P}_K$ design, on the other hand, is an $A03\lambda11$ blade with two $A02\lambda07$ segments on each tip operating at a slightly lower TSR of 5.76. This is the same blade leading edge as Point A in Figure 4.6. Despite the slightly lower TSR and blade leading edge, the Maximum $\bar{P}_K$ only provides 0.2 % more improvement in terms of $\bar{P}_K$, while there is a negligible difference in $\bar{P}_S$. This could be due to slight variations in the TSR resulting in maximum $\bar{P}$ with wind speed. Regardless, both designs provide an improvement over the baseline, with as much as a 13.0 % and 11.7 % increase in $\bar{P}_S$ and $\bar{P}_K$, respectively and the solution appears to be relatively robust with varying wind environments, requiring a minor change in TSR for a near negligible improvement in $\bar{P}$. If there was a significant difference in maximum $\bar{P}$ TSR with wind speed, a TSR schedule could be explored, where the design TSR varies with wind speed.

Table 4.8: Performance characteristics of the various designs from optimizing wind probability-weighted average power output at the SWiFT Test Site and Kingston, ON, for the 1:7 Scale Sandia 17-m with TSR as a variable.

Design	TSR	RPM at 15 m/s	$\bar{P}_S$ (W)	$\bar{P}_K$ (W)
Baseline	5.58	669.0	263.02	104.82
Maximum $\bar{P}_S$	5.80 (+3.9 %)	695.4	297.15 (+13.0 %)	116.92 (+11.5 %)
Maximum $\bar{P}_K$	5.76 (+3.2 %)	690.6	297.14 (+13.0 %)	117.09 (+11.7 %)

Values in parentheses denote percent difference compared to the Baseline.

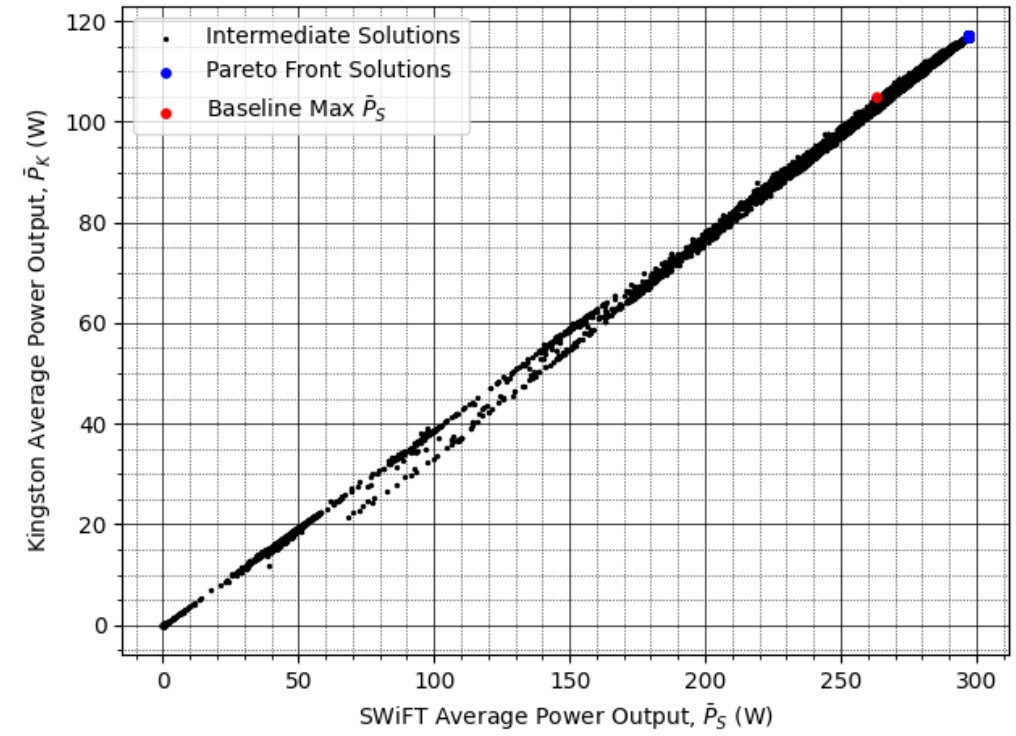

(a) All Solutions

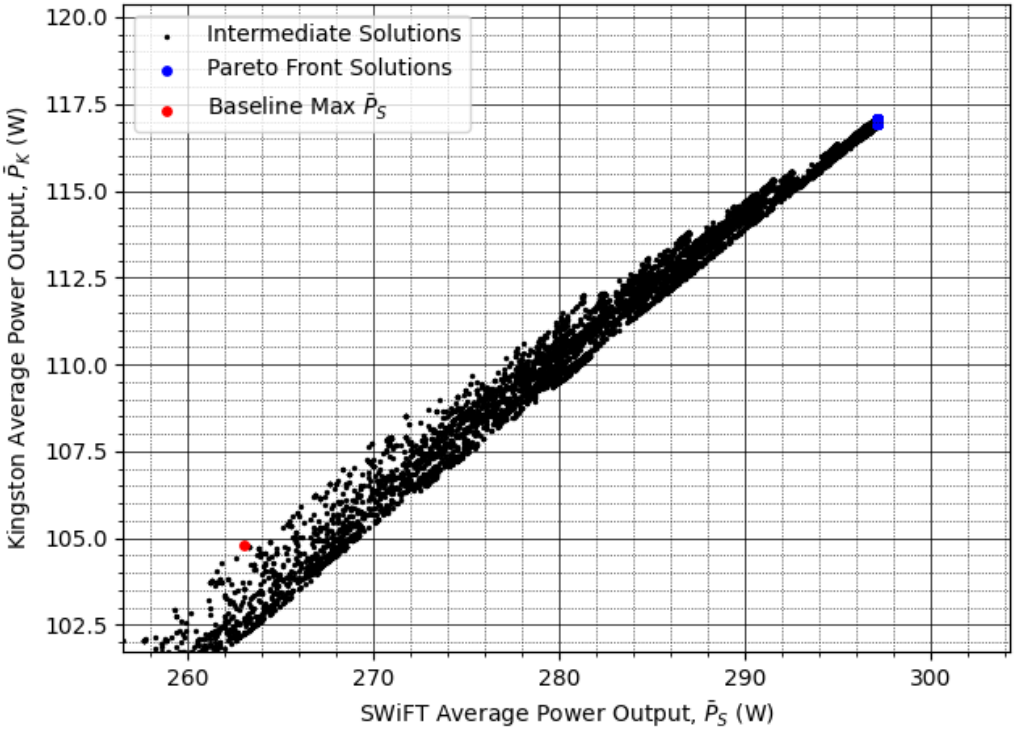

(b) Magnified View of the 256–304 W $\bar{P}_S$ Region

Figure 4.7: All solutions explored by NSGA-II optimizing wind probability-weighted average power output at the SWiFT Test Site and Kingston, ON, for the 1:7 Scale Sandia 17-m with TSR as a variable.

4.4 Summary

Overall, these optimizations have highlighted where an optimal VAWT design would exist when maximizing both wind probability-weighted power output and fatigue life. With both geometries, it was shown that the best solutions exist either at or below the TSR of maximum $\bar{P}$, depending on how much of a trade-off with fatigue life is desired. Since decreasing TSR below the TSR of maximum $\bar{P}$ results in a range of AoA in the post-stall regime, the front is dominated by different tubercle shapes, depending on which shapes give a higher $\bar{P}$ or $\overline{FLI}$. This can be explained by the stream-wise counter-rotating vortices produced by the tubercles, delaying flow separation and maintaining aerodynamic efficiency at higher AoAs, producing more torque than the baseline blade while simultaneously reducing the range of forces experienced by the blades due to their gradual stall onset. It was also shown that the preferred tubercle shape differs between turbine geometries. However, the optimizer focused on small amplitude tubercles, namely the $A02\lambda07$, $A02\lambda09$, and $A03\lambda11$. With smaller amplitudes, the produced stream-wise counter-rotating vortices are smaller and less detrimental to the aerodynamic efficiency (subsequently, the power output of the design) than large amplitude tubercles. Had span-wise flow on the blades been accounted for, the larger tubercle amplitudes may have been beneficial at the tips through flow compartmentalization and reduction of the blade tip vortex.

Analyzing the Pareto Fronts also gave potential designs that minimize the trade-offs between $\bar{P}$ and $\overline{FLI}$. For the Small-Scale H-type, the Maximum $\bar{P}$ design provides a 19.4 % improvement in $\bar{P}$ and 13.6 % higher $\overline{FLI}$ compared to the baseline blade. The design with the greatest $\overline{FLI}$ without sacrificing $\bar{P}$ below that of the baseline yielded a 34.1 % increase in $\overline{FLI}$. Alternatively, there is a corner in the Pareto (Point A) that provides a 15.9 % and 28.4 % greater $\bar{P}$ and $\overline{FLI}$ than the baseline, respectively. Further optimizations should combine $\bar{P}$ and $\overline{FLI}$ or actual fatigue life to maximize the power production over the life of the turbine to come to a single solution between these two objectives. It was also shown that these designs with tubercles are robust in varying wind speed environments. So, it is not necessary to create a new VAWT design for a different location when operating at a constant TSR. However, if designing for a constant RPM, as shown in Appendix E, the design RPM will change with varying wind speed environments to keep the TSR as close to the ideal for the majority of wind speeds. Since the constant RPM designs are not operating at ideal TSR for all wind speeds, at low wind speeds, they are rotating too fast, resulting in an unnecessary increase in $\overline{FLI}$. While for high wind speeds, they are rotating too slowly, resulting in inefficient AoAs that are detrimental to $\bar{P}$. As a result, the constant TSR designs have an order of magnitude larger $\overline{FLI}$ and greater $\bar{P}$. For these reasons, it would be best to incorporate wind speed feedback to operate the VAWTs at a design TSR. With these results coming from the first analysis and optimization of various tubercle shapes using the DMSTM, these results will be compared against preliminary experimental results.

5 Experimental Characterization of Tubercles on VAWT Blades

The previous chapters aimed to determine the performance improvements granted by applying tubercles to the leading edge of vertical axis wind turbine (VAWT) blades through a numerical analysis. It was found that tubercles can increase the wind speed probability-weighted power output while decreasing the rotational rate and the range of forces experienced in each rotation. Through a multi-objective optimization, it was determined that to best maximize the expected power output and fatigue life, the turbine should be rotating slower, or at a lower tip speed ratio (TSR), than required for maximum average wind-probability weighted power output. This region is characterized by angles of attack (AoA) in the post-stall regime, where tubercles have been shown to excel. This chapter presents an initial effort to validate the computational findings experimentally.

5.1 Development of RMC VAWT Rig

Experimental VAWT research generally studies either the power and torque of the turbine, the forces experienced by the blades, or wake characteristics. These can either be conducted outside or in a wind or water tunnel. To collect power data, the turbine should be connected to a generator, motor, or brake [87, 95, 105, 106]. To get instantaneous torque data throughout rotation, a torque sensor can be connected between the turbine and the load [105, 106]. For blade loading, some studies have used strain gauges at either end of the blade to determine the normal and tangential forces on the blade each rotation [107]. Wind tunnel testing allows for control of the wind speed, leading to the quick acquisition of complete power curves. Outdoor testing, on the other hand, is dependent on sufficient wind variation to get a full power curve. With the consistent speed from a wind tunnel, the start-up characteristics of different turbines can be compared equally since there are no variations in wind speed, unlike that experienced outdoors. Turbines in wind tunnels, however, are limited by the size of the tunnel while also considering blockage effects. This often leads to turbines with small radii, requiring high RPM to get a full range of tip speed ratios for power curves [87, 95, 105, 106]. Considering the complexity required for blade loading data, it was decided that the RMC VAWT rig, shown in Figure 5.1, should focus on power and torque collection. In the context of this thesis, although blade loading data could show the decreased range of forces resulting from leading-edge tubercles, power and torque data can confirm the improvement in power output provided by tubercles at lower TSRs.

Figure 5.1: RMC VAWT setup during outdoor testing at the point of the RMC peninsula. The RMC VAWT Rig is on the left and the weather station is on the right.

5.1.1 Thesis Rig Design Objectives

Considering the different experimental methods for VAWTs, the main focus of the RMC VAWT rig was operational flexibility. It was designed to easily switch between wind tunnel and outdoor testing to have the option to get both startup characteristics and power curves. This also meant that the turbine should be easily removed/attached to the driven system and load to change the turbine geometry if needed. As a result, the rig could be used for different VAWT experiments in the future, including blade loading. For startup characteristics, the rig should be able to measure rotational speed, while also using a feedback control system to maintain a constant RPM or TSR for efficient collection of power curves. Finally, with the turbine operating outdoors where the wind is not controllable, it was necessary to have redundant control and braking of the turbine to ensure safe operation. In summary, the design objectives for the RMC VAWT rig were:

- Collect torque and rotational speed data,
- Ability for feedback to set a constant RPM or TSR,
- Portable design for different wind tunnels and outdoor locations,
- Versatile turbine mounting system,
- Safe operation and redundant braking system, and
- Wireless control and data acquisition.

5.1.2 Thesis Rig Design Constraints

The initial overarching design constraint was to minimize the cost of the RMC VAWT rig. However, as design decisions were made, further constraints were added. With the air bearing system described in Section 5.1.4, the maximum axial load limit of the thrust face bushings are 145 lbs. Thus, the rotating portion of the turbine cannot weigh more than 145 lbs. The thrust bushings also have a maximum radial load limit of 65 lbs each. Therefore, the forces in the bearing to counteract the moment caused by the aerodynamic forces acting on the turbine must not exceed this limit. To minimize cost and turbine weight, it was then decided to 3D print the turbine blades. The largest 3D printer available at RMC was a *Stratasys* Fortus 380mc that has a $356 \times 305 \times 305$ mm build volume. So, the blades must fit within the build volume. The design constraints for the RMC VAWT Rig are summarized as:

- Minimum overall cost,
- Should fit through a standard doorway,
- Turbine must weigh less than 145 lbs,
- Moment due to aerodynamic forces must result in less than 65 lbs on each thrust bushing, and
- Turbine blades must be able to be printed on a $356 \times 305 \times 305$ mm build volume.

5.1.3 Thesis Rig Design Summary

The final RMC VAWT Rig can be seen in Figure 5.1. In the shown configuration, it has a 3-blade turbine, with the blades 3D printed. However, the turbine can be quickly replaced with a different configuration, if desired, by removing only three bolts. The turbine is attached to an air bearing that eliminates radial and axial forces. Attached to the other side of the air bearing is a *Burster* 8656-5020 rotary precision torque sensor for torque and RPM measurement, and a *Magtrol* HB-450 magnetic hysteresis brake to provide a load on the turbine. The data collection and control were done remotely through a *Raspberry Pi* 5 coupled with an *Arduino* Uno. Wind data is collected either by an *Omega* PX163 pressure transducer and pitot tube when used in the wind tunnel, or by an *Airmar WeatherStation*© PB-150 when used outside. While RPM or TSR feedback is possible with the hardware, it requires further tuning before it can be used effectively for experimentation. All the instrumentation is mounted on a robust aluminum extrusion cart, allowing for ease of transport. The cart also has hydraulic legs on each corner, allowing the rig to be raised off its wheels to the height required for the wind tunnel. Overall, the RMC VAWT Rig was able to meet all of its objectives while remaining within its constraints, except for a functioning RPM/TSR feedback, which requires further work before it can function properly. Each of these systems will be discussed in detail in the following sections.

5.1.4 Air Bearing and Braking System

The RMC VAWT uses an air bearing coupled to a hysteresis brake to provide resistance to the rotation of the turbine while minimizing the radial and axial loading from the turbine, leaving mostly rotational loads for the hysteresis brake. The idea of using an air bearing for wind turbine testing was provided by Professor Aaron Altman from the University of Dayton through private communication, where he also provided engineering drawings for their air bearing design [108]. This design was used in his student's Master's thesis [105,106].

The air bearing consists of a custom stainless steel bearing housing, two *NewWay* 1.25 in internal diameter thrust face bushings, and a custom 1.25 in diameter shaft, all shown in Figure 5.2. The thrust bushings, with opposite orientations to restrict axial and radial movement, have porous carbon faces that create a thin layer of air in the less than a thousandth of an inch gap between the bushings and the shaft. Each bushing requires 60 psi of air and has a radial and axial load limit of 65 and 145 lbs, respectively. Each bushing requires at most an air flow rate of 0.35 CFM.

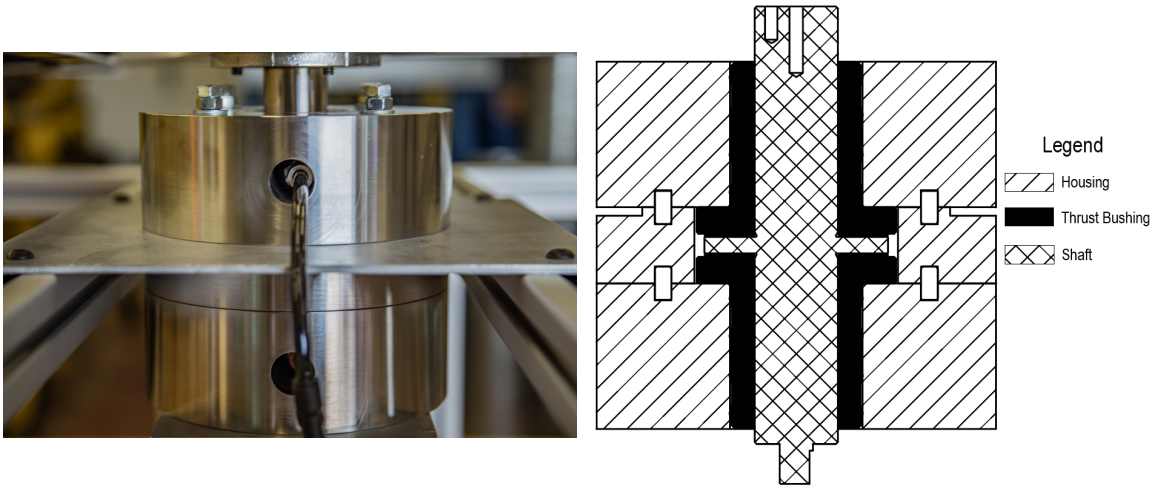

(a) Air Bearing (b) Cross-Section

Figure 5.2: The air bearing used on the RMC VAWT rig and its cross-section.

Figure 5.3: *MAXIMUM* one gallon air compressor used on the RMC VAWT rig.

Air is supplied to the bearing from a *MAXIMUM* 1 gallon air compressor, shown in Figure 5.3. It can provide 0.7 CFM at 90 psi, which is sufficient to supply both thrust bushings. The compressor has a manual twist knob regulator to set the required pressure or completely cut off the air supply to the bearing. Before going to the air bearing, the air passes through a series of filters for preparation, shown in Figure 5.4. From left to right in the figure (airflow direction), there is a *NORGREN* F73G series 25 μm filter, followed by a *NORGREN* F73C series 0.01 μm filter to prevent particulates from contaminating the thrust bushings. Finally, the air passes through a *Speedaire* 5 cfm dryer desiccant to remove any water vapour or oils before going to the air bearing.

Figure 5.4: Air preparation filters and desiccant used for the air bearing on the RMC VAWT rig.

Coupled to the lower end of the air bearing is a *Magtrol* HB-450 magnetic hysteresis brake, as shown in Figure 5.5. It produces torque through a magnetic air gap, depending on the current provided. It has a hysteresis in the resulting torque whether the current is increasing or decreasing, with an example torque-current curve shown in Figure 5.6. A downside of hysteresis brakes is the potential for cogging torque, which is a result of formed salient poles passing over the stator teeth, causing a cogging effect when attempting to rotate the brake, even if no current is applied. This is avoided by completely removing the current before the brake stops. However, if the salient poles form, they can be removed by increasing the current to at or above the level it was before rotation stopped, then manually turning the brake while decreasing the current to zero. This phenomenon had an influence on the control VAWT rig, as well as testing procedures. The current was supplied to the brake using a *Magtrol* 5210-2 Power Supply, shown in Figure 5.7. It varies the current linearly between 0 and 500 mA through either the 10-turn potentiometer on the front or the 0-5 VDC input on the back while on the medium scale setting. This provides current for the full scale of the hysteresis brake with a rated current of 442 mA.

Figure 5.5: *Magtrol* HB-450 magnetic hysteresis brake on the RMC VAWT Rig.

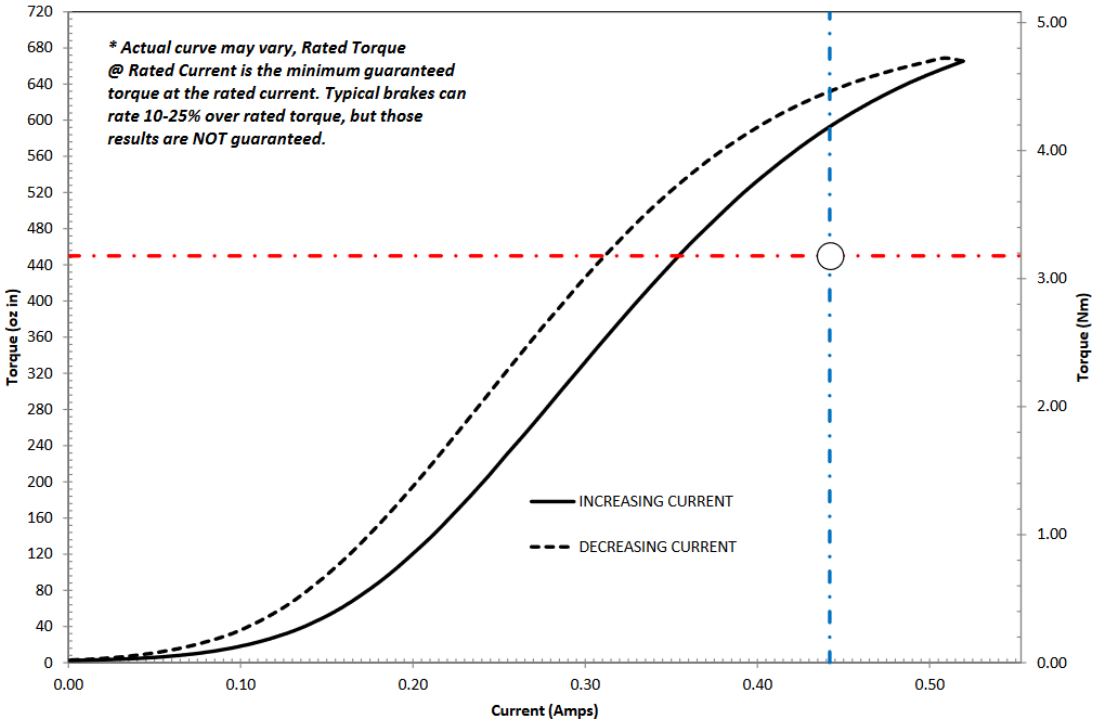

Figure 5.6: Torque hysteresis curve of the *Magtrol* HB-450 hysteresis brake.

Figure 5.7: *Magtrol* 5210-2 power supply for the hysteresis brake.

With this air bearing, the shaft will come to a complete stop without any supply of air. So, in the event of a brake failure, the air supply can be shut off, and the turbine would stop. If there is a power outage and the brake is inoperative, the compressor will stop running, ceasing turbine rotation after the compressor's accumulator empties.

5.1.5 Main Turbine

The main turbine geometry has the same dimensions as the Small H-type used in Chapters 3 and 4, described in Table 5.1. It is attached to the top of the air bearing shaft with three bolts, making it simple to remove the turbine for transportation or replace it with a different geometry. The turbine consists of an upper and lower support arm disc, each constructed from a single piece of 1/8 in thick aluminum sheet cut on a water jet. They are held together at the centre by a 0.75 m long hollow aluminum shaft. There are two holes on the ends of each support arm for fastening the blades to the turbine. Between the upper turbine support arm disc and the top of the centre shaft is an additional support arm disc made of 1/4 in plywood, also cut on a water jet, to provide additional stiffness and dampening to the blades.

The turbine blades were made using fused deposition modelling (FDM) of acrylonitrile styrene acrylate (ASA) with a *Stratasys* Fortus 380mc 3D printer that has a $356 \times 305 \times 305$ mm build volume. With this limitation, the 0.75 m long blades were printed upright in three 0.25 m segments without supports. The internal design of the blades, shown in Figure 5.8, aimed to minimize weight and print time without compromising the structural and aerodynamic integrity of the blade, while also remaining consistent between tubercle shapes. The outer skin and all interior supports are created using two passes of the extruder. This ensures a single continuous deposition of material on the outside surface of the blade, covering the seams created as the extruder starts/stops each segment on the interior. The seam created by the surface pass was placed at the trailing edge of the blade. The interior also has two holes at $0.25c$ and $0.625c$ for 3/8 in aluminum tubing, with 1/4 in - 20 threads on either end to bolt each blade to the support arms at a zero-degree installation angle.

The internal supports also have circular cutouts to further reduce the weight of the blades. The blades were modelled in *CATIA* at full length, then sliced into three segments to ensure the tubercle leading edge aligns. The model was parameterized to change the tubercle amplitude and wavelength without requiring a redesign of the internal structure. With the blades being printed upright (the span-wise direction normal to the build plate), the overhang of the tubercle peaks tended to degrade the surface finish in that region, specifically for large amplitude to wavelength ratio shapes. However, for the shapes examined in this chapter, this degradation was not present.

Table 5.1: Geometric characteristics of the RMC VAWT

Characteristic	Value
Height (m)	0.75
Radius (m)	0.5
Chord (m)	0.1524
Number of Blades	3
Swept Area, S (m^2)	1.5
Solidity, σ	0.146
Blade Shape	NACA 0018

Figure 5.8: Cross-section of the 3D printed turbine blades used on the RMC VAWT.

5.1.6 Data Acquisition and Control

The RMC VAWT has a variety of data acquisition systems depending on whether it is operating in a wind tunnel or outdoors. Regardless of the configuration, the RMC VAWT uses a *Burster* 8656-5020 rotary precision torque sensor coupled between the air bearing and the hysteresis brake. *LoveJoy* AL075 jaw-type couplers with nitrile butadiene rubber spiders were used to minimize the effects of potential shaft misalignment. This assembly is shown in Figure 5.9. The torque sensor provides torque and rotational rate readings up to ±20 Nm and 10 000 RPM, respectively. Although the sensor comes with the proprietary software, *DigiVision*, a USB serial interface was created in *Python* to coordinate the different systems in one software. The torque sensor uses a Query-Response system, so the created code sends queries for the required data and then decodes the response. The rig also has a *Monarch Instruments* ROS-W optical LED sensor, connected to a *Monarch Instruments* ATC-1B panel tachometer for visual RPM monitoring during manual operation.

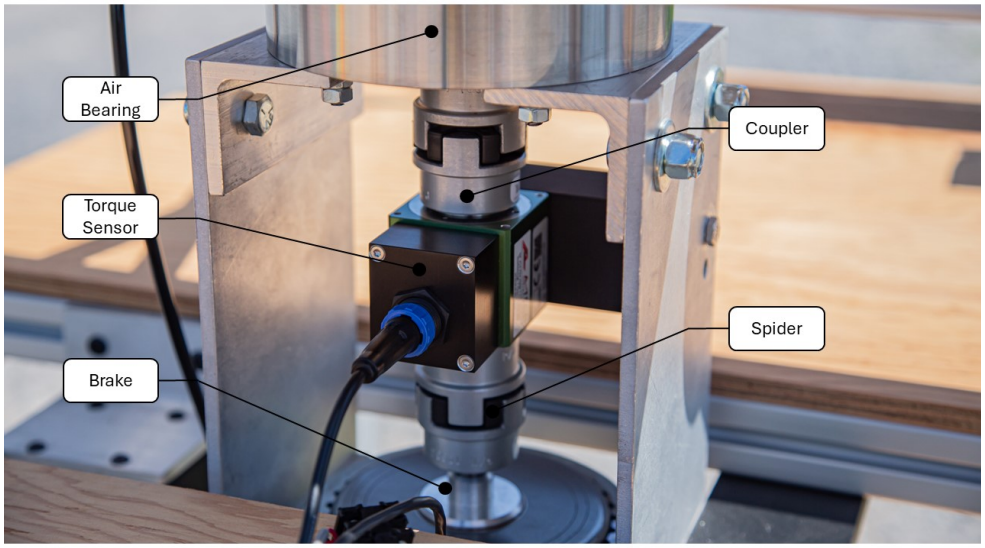

Figure 5.9: *Burster* 8656-5020 rotary precision torque sensor mounted in the RMC VAWT rig.

During outdoor operation, the rig has an *Airmar WeatherStation*© PB-150 mounted on a tripod located upstream and off to the side of the turbine, with the weather station levelled and in line with the rotor equator. Unlike the torque sensor, it only requires a single query and then will repeatedly send the response through serial using the National Marine Electronics Association (NMEA) 0183 standard. Depending on the query, it will send a different packet of data. For this testing, wind speed and direction are recorded. An RS-232 to USB converter is used to connect the weather station to a computer, where a *Python* script is used to decode and store the data. During wind tunnel testing, the weather station is replaced by a pitot tube connected to an *Omega* PX163 pressure transducer, providing a voltage differential depending on the pressure difference. During both wind tunnel and outdoor experiments, an *Oakton*© WD-03316-80 barometer with a digital thermometer was used for ambient temperature and pressure measurements.

The RMC VAWT is primarily controlled remotely through a *Raspberry Pi* 5 that has a quad-core 2.4 GHz processor. A *VNC* server was used to connect to the *Raspberry Pi* with a computer workstation through an onboard router. Since the *Raspberry Pi* only has digital pins, an *Arduino* Uno was used for all digital and analog inputs and outputs, while the *Raspberry Pi* handles all serial communications, including sending and receiving data to the *Arduino* Uno. The control and data collection systems on the RMC VAWT rig is shown in Figure 5.10.

The *Raspberry Pi* uses *Python*'s threading module to run the various data acquisition and control scripts concurrently, instead of in series. The main script orchestrates the experiments by running through a desired list of test points (RPM, TSR, brake current, etc.), starting the recording of data after a set settling time, and stopping the recording of data in each of the data acquisition threads after a desired amount of time. There are a total of four threads used. Three of them are for data acquisition. They are constantly reading and decoding the serial ports from the weather station, torque sensor, and *Arduino*

Uno, but only record data to a comma-separated value (CSV) file when directed to by the main script. The final thread controls the *Arduino* Uno, sending it the desired brake current depending on the required test condition. The *Arduino* uses pulse width modulation (PWM) to simulate an analog input to the brake power supply, with a value of 0 to 255 corresponding to 0 to 5 VDC input on the back of the power supply. This corresponds to 0 to 500 mA being sent to the hysteresis brake. So, the *Arduino* can adjust the brake current with a resolution of about 1.96 mA. The *Arduino* also receives a 0-5 V analog input from the *Monarch Instruments* ATC-1B panel tachometer corresponding to a 0 to 1023 value in the *Arduino*. The panel tachometer was programmed to output 5 V at 1023 RPM, giving 1 RPM resolution through the *Arduino*. During wind tunnel testing, the *Arduino* also receives 0 to 5 V input from the *Omega PX163* pressure transducer, resulting in another 0 to 1023 value that is used to calculate the pressure difference, Δp, between the static and total pressure ports. These values are sent through serial to the *Raspberry Pi*, allowing for a feedback loop changing brake current to result in a desired RPM or TSR.

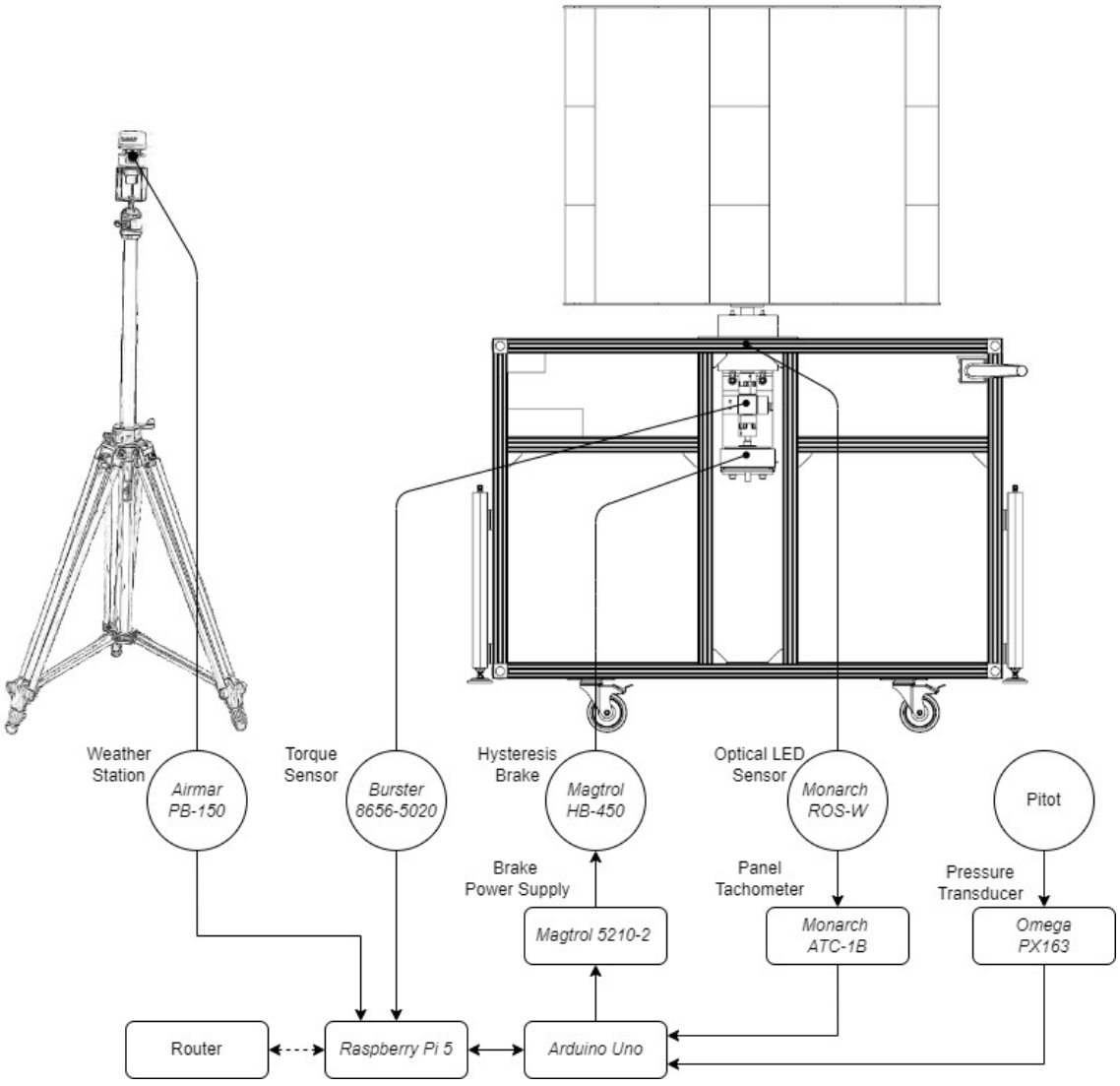

Figure 5.10: Schematic diagram of the RMC VAWT rig. Note that the Pitot tube and *Omega PX163* replace the *Airmar* PB-150 during wind tunnel operation.

5.1.7 VAWT Rig Cart

All the previously described systems were mounted on the VAWT rig cart, as shown in Figure 5.11, for enhanced portability. Most of the cart is constructed of 1.5 in square hollow t-slotted aluminum rails, supported in the corners by 1.5 in aluminum gussets. The shelves are made of 1/2 in plywood, giving space for all the systems, including the weather station and its tripod, during transport. The *Raspberry Pi* and *Arduino* Uno are located behind the brake power supply and are fastened directly to the plywood shelving. The cart has 4 in diameter polyurethane rubber caster wheels in each of the four corners of the cart, each with a weight capacity of 265 lbs. The corners also have hydraulic legs operated using a hand crank hydraulic pump for a total weight capacity of 1 000 lbs. This combination eases transitions between different height wind tunnels and outdoor testing. Each foot on the hydraulic legs can be adjusted manually to level the entire turbine.

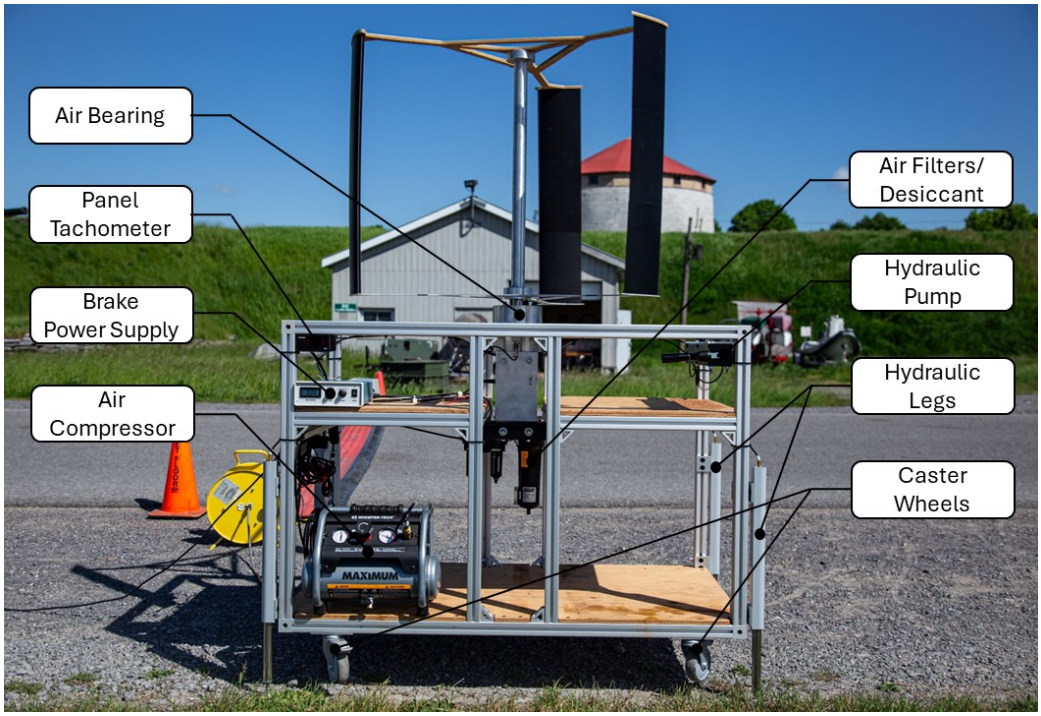

Figure 5.11: RMC VAWT Rig cart during outdoor testing at the point of the RMC peninsula. Note that the *Raspberry Pi* 5 and *Arduino* Uno are located behind the brake power supply.

5.2 Methodology

This section presents the experimental objectives, data measurements, their uncertainty, and the procedure for testing. The results using the double-multiple streamtube model (DMSTM) found that leading-edge tubercles provide improved power output over the straight leading-edge baseline, especially at TSRs below the TSR corresponding to the maximum baseline power output, as a result of stream-wise counter-rotating vortices delaying flow separation and maintaining a higher aerodynamic efficiency post-stall than the baseline. The analysis also found that leading-edge tubercles expand the envelope of positive

power generation at lower TSR and wind speeds, suggesting improved startup capability, also supported by Du *et al.* [84].

5.2.1 Experimental Objectives

With the RMC VAWT Rig constructed, the objectives for the experimental campaign were:

- Evaluate the performance of the straight leading-edge baseline blade and various tubercle shapes of different amplitude and wavelengths,
- Compare the experimental results to the DMSTM predictions,
- Examine power output and power coefficient at a variety of wind speeds and TSRs, and
- Compare the startup characteristics of different tubercle shapes compared to the baseline.

5.2.2 Data Measurements

The experimental campaign aimed to characterize the various tubercle shapes by comparing power output, P, and power coefficient, C_P, for a range of TSR, $\hat{\lambda}$, each defined using equations 5.1, 5.2, and 5.3, respectively. Startup characteristics were compared using the rotational rate, Ω, in RPM.

$$P = T_\mathrm{b}\omega \tag{5.1}$$

$$C_P = \frac{P}{0.5\rho S V_\infty^3} \tag{5.2}$$

$$\hat{\lambda} = \frac{\omega R}{V_\infty} \tag{5.3}$$

The rotational velocity, ω, was calculated by converting the RPM measured by the *Burster* 8656-5020 torque sensor to radians per second. The wind speed, V, was measured directly using the *Airmar* PB-150 during outdoor testing. During wind tunnel testing, the *Omega* PX163 pressure transducer was used to calculate V using Bernoulli's equation from its measured pressure differential, Δp. Ambient temperature and pressure were measured using an *Oakton*© WD-03316-8 at the beginning of each test to calculate the air density, ρ, using the ideal gas law. The turbine frontal area, S, is constant for the turbine geometry studied, determined by $S = 4RH$, where R is the turbine radius and H is the turbine half height. Finally, the torque from the turbine blades, T_b, was calculated by subtracting the residual torque, T_res resulting from friction in the air bearing, torque sensor, and hysteresis brake to the measured torque, T, from the *Burster* 8656-5020. T_res was determined using a spool-down method, which will be discussed in the following section. A second method of determining the torque produced by the blades was used in addition to the torque sensor measurements and will be explained in Section 5.2.4.

A sample histogram of torque, RPM, and velocity data collected during wind tunnel data is presented in Figure 5.12. Both V and RPM were shown to approximate normal distributions. So, the average value was assumed to be the representative value for the data set. Torque, on the other hand, has two distinct normal distributions, with the lower distribution being nearly half the magnitude. These values, when plotted with time, show

two distinct horizontal lines throughout the entire time sampled. This shows that, while the turbine is in a steady state, torque changes throughout rotation. However, this could indicate that the measurements are phase-locked, since there should be intermediate torque values between the two peaks. A power spectral density (PSD) plot of the torque data set was created and is shown in Figure 5.13. There are two distinct peaks at approximately 4.9 and 9.8 Hz, corresponding to the first and second harmonics of the turbine rotational rate. Due to the low sampling frequency of T of approximately 20 Hz and the relatively high RPM, the actual blade passing frequency of approximately 14.75 Hz was not captured since the Nyquist Frequency of this sensor is approximately 10 Hz. Since the minimum and maximum torques produced by the turbine occur once per blade pass, as the turbine would be in these orientations three times per rotation, not all maximum or minimum torques were captured. However, since the aim of this experimental campaign was to get the steady-state performance of the turbine, and not throughout the rotation, this torque data was averaged in each data set and assumed to represent the steady-state value of torque.

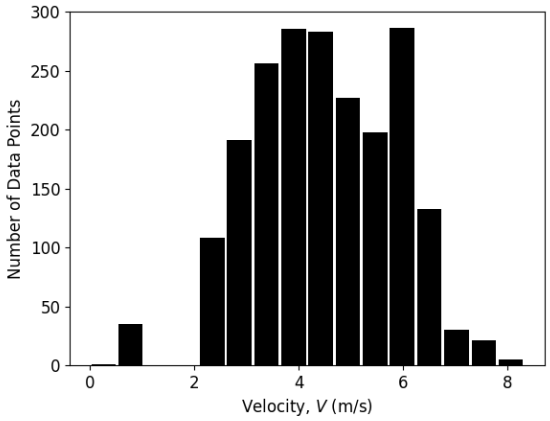

(a) Velocity from *Omega* PX163

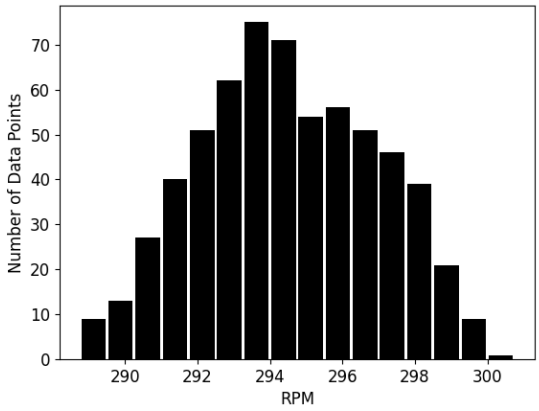

(b) RPM from *Burster* 8656-5020

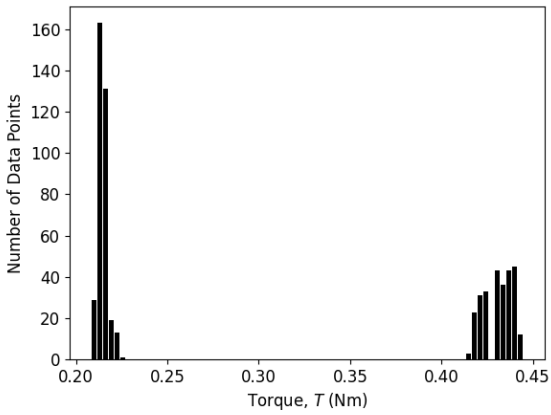

(c) Torque from *Burster* 8656-5020

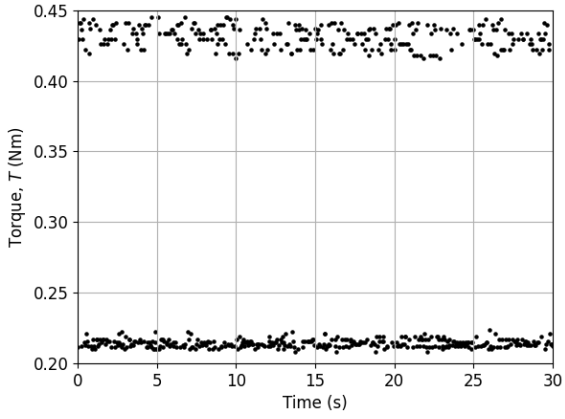

(d) Torque with Time

Figure 5.12: Sample histograms of data measurements during wind tunnel testing of the baseline blade with the wind tunnel motor at 40 Hz.

During outdoor testing, the value for each data point could not be averaged like the results from the wind tunnel testing due to the variation of the wind velocity during each test condition. A PSD of all wind speed data collected during testing, shown in Figure 5.14, does not indicate any consistent variation in the wind, such as time between and duration

of gusts, other than most of the variations occurring at low frequencies below 0.75 Hz. This aligns with the results of individual data sets obtained on different days and is consistent with the random nature of the wind. As a result, the outdoor data was binned into 10-second segments, where the results in each were averaged. This allowed the different sampling rate data to be aligned, while also averaging the effect of wind variations and the dynamic reactions of the turbine in response.

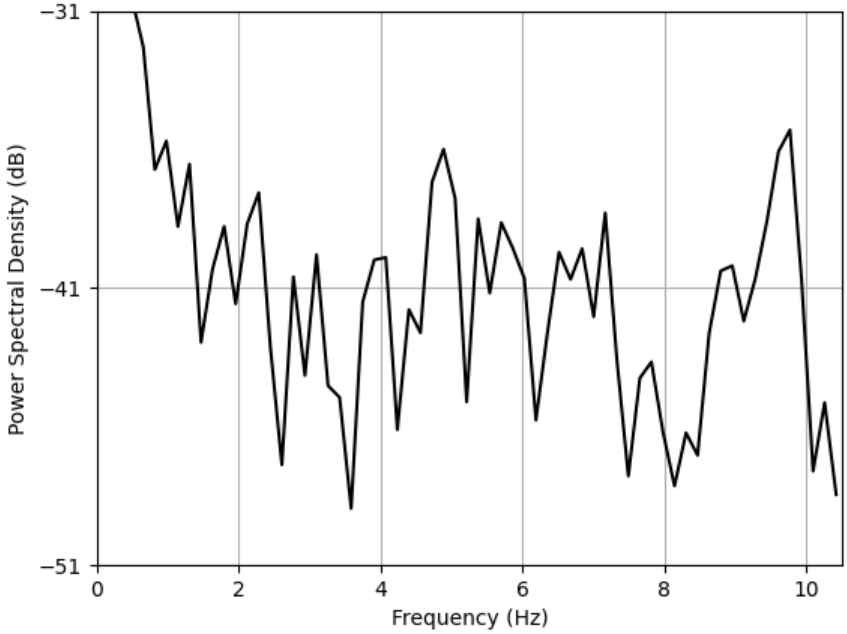

Figure 5.13: Power spectral density of torque measurements during wind tunnel testing of the baseline blade with the wind tunnel motor at 40 Hz.

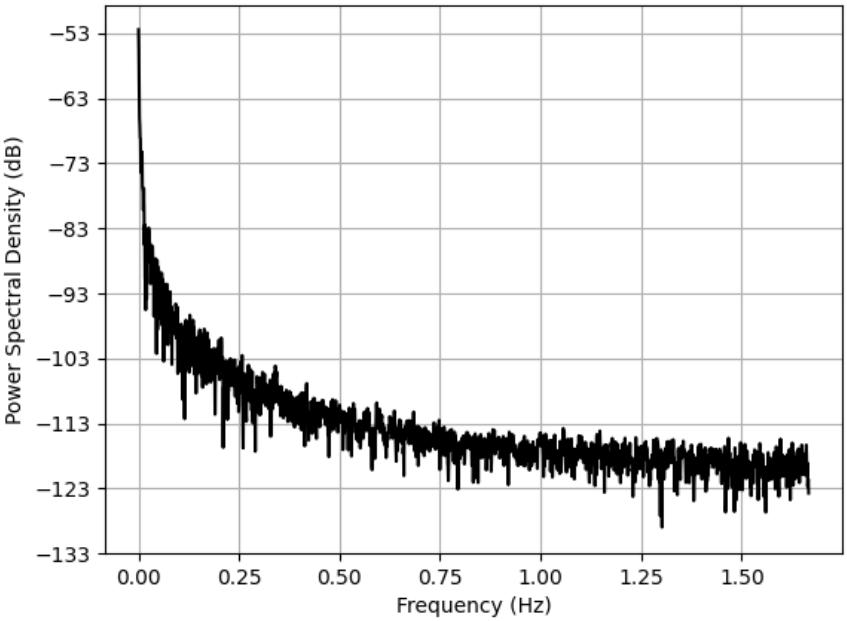

Figure 5.14: Power spectral density of all wind speed measurements during outdoor testing.

5.2.3 Residual Torque Measurement

The residual torque, T_{res}, of the RMC VAWT Rig was determined using the spool-down method described by Edwards *et al.* [109]. The entire turbine and blades were removed from the VAWT Rig, leaving only the air bearing, torque sensor, hysteresis brake and couplers. This system was then spun up to 550 RPM using a hand power drill, well beyond the operating range of the experimental turbine. Once up to speed, the drill was removed, and the system was free to decelerate to a complete stop. The rotational speed was recorded using the *Burster* 8656-5020 torque sensor, allowing for the calculation of instantaneous angular acceleration, ξ, and subsequently the instantaneous torque resulting from friction by multiplying by the mass moment of inertia of the system, I_{rig}.

$$T_{\text{res},i} = I_{\text{rig}} \left(\frac{d\omega}{dt} \right) = I_{\text{rig}} \xi_i \tag{5.4}$$

$$\xi_i = \frac{\omega_{i+1} - \omega_i}{t_{i+1} - t_i} \tag{5.5}$$

The instantaneous angular acceleration was calculated using a forward finite difference method so that ξ at t_i is determined by the change of ω over t_i to t_{i+1}. This was calculated for all readings between 400 and zero RPM for six runs. The mass moment of inertia of the system without the turbine and blades was calculated by summing the moments of inertia of the individual components, summarized in Table 5.2. The couplers, hysteresis brake, and torque sensor moments of inertia were found on either the product website or manual, while the air bearing shaft was determined using *Solidworks'* mass property tool.

Table 5.2: Summary of the mass moment of inertia of the individual components of the RMC VAWT Rig without the turbine and blades.

Component	Quantity	Mass Moment of Inertia, I (kg m^2)
Burster 8656-5020	1	8.49×10^{-6}
LoveJoy Couplers	2	7.08×10^{-5}
Magtrol HB-450	1	7.40×10^{-4}
Air Bearing Shaft	1	2.45×10^{-4}
	Total (I_{rig})	1.06×10^{-3}

All spool-down tests, shown in Figure 5.15, consistently show deceleration from 400 to 0 RPM within 3.6 to 3.8 s, with all tests having good agreement throughout the spool-down. As RPM decreases, the rate of change of RPM decreases, suggesting lower frictional torque at lower RPM. This is confirmed by 5.15 (b), which shows a relatively linear increase (negatively) in residual torque as RPM increases. This plot shows the calculated T_{res} from all data points from the six spool-down runs without data processing. The equally spaced horizontal lines of data are a result of the torque sensor resolution of 0.25 RPM. From the results, a line of best fit was determined, giving T_{res} for varying RPM. The resulting T_{res} was subtracted from the experimental results depending on the RPM to give the torque produced by the turbine, removing the effect of friction in the measurement system.

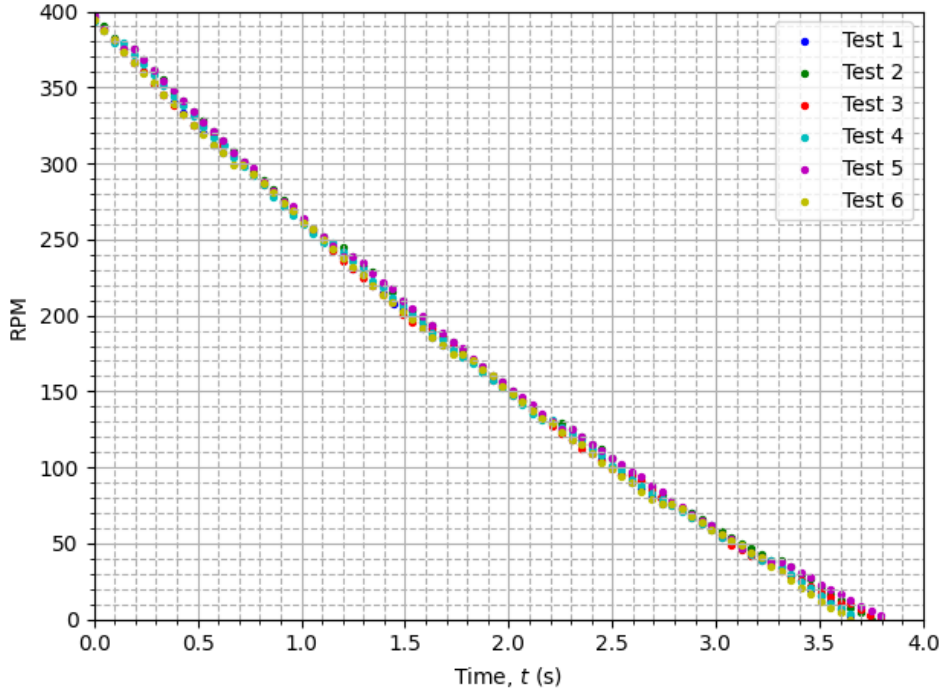

(a) RPM

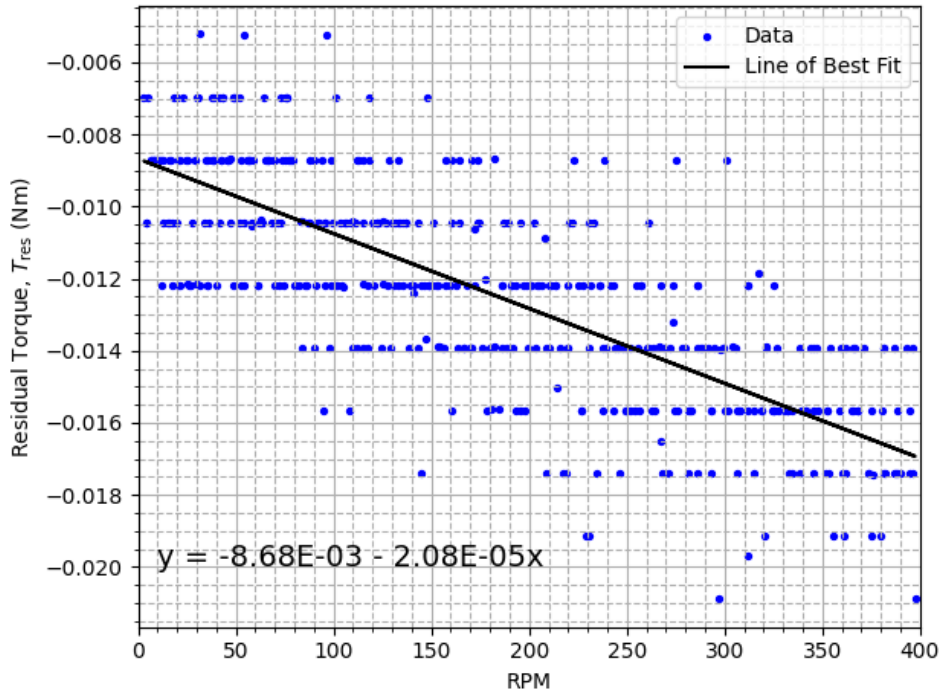

(b) Residual Torque

Figure 5.15: RPM and residual torque of the driven system on the RMC VAWT Rig with the turbine and blades removed during spool-down testing. Note that the uncertainty for RPM is ± 0.25 RPM, and for T_{res} is $\pm 1.05 \times 10^{-3}$ Nm.

5.2.4 Spool-Up Torque Measurement

Similar to the spool-down method used to calculate the residual torque, T_{res}, in the driven system of the RMC VAWT Rig, a spool-up method was used to determine the power curves using acceleration during start-up. Edwards *et al.* [109] suggest using a motor to spin a turbine above its maximum operating TSR, then letting it spool down with wind to determine the contribution of torque from the blades for the entire range of operational TSR, generating the power curves. If the turbine has a net positive torque, a brake can be used to increase the torque in the system and prevent the turbine from 'cutting in', ensuring deceleration. If the turbine is self-starting, however, the acceleration during startup can be used to calculate the torque throughout the range of operational TSR, as used by Du *et al.* [84]. The main difference between spool-up and steady-state torque measurements is that the spool-up is dynamic, and the wake is not fully developed like in the steady-state case. Edwards *et al.* [109] varied the torque applied from the brake during spool-down testing to change the rate of deceleration and found that it had a negligible impact on the results, suggesting that this method can be considered quasi-steady. So, in addition to the steady torque measurements using the torque sensor, the spool-up method was used to create another series of power curves by calculating the torque using the instantaneous acceleration throughout the start-up of the turbine. Now, by multiplying the rate of change of ω throughout start-up by the mass moment of inertia of the driven system, I_{rig}, in addition to the mass moment of inertia of the turbine itself, I_{turb}, the overall torque acting on the system can be determined. After subtracting T_{res} from the friction in the driven system, the torque produced by the blades, T_{b} can be determined for the operational range of TSR.

$$T_i = (I_{\text{rig}} + I_{\text{turb}}) \left(\frac{d\omega}{dt} \right) = (I_{\text{rig}} + I_{\text{turb}})\, \xi_i \tag{5.6}$$

$$\xi_i = \frac{\omega_{i+1} - \omega_i}{t_{i+1} - t_i} \tag{5.7}$$

$$T_{\text{b}} = T_i - T_{\text{res}} \tag{5.8}$$

The mass moment of inertia of the turbine, I_{turb}, was determined by summing the contributions of the individual components. The turbine blades were approximated as point masses at R from the axis of rotation. With most of the mass coming from the aluminum tubing through the blades (located at R), along with the local structure radius variations (blade thickness, internal structure, etc.) in blades being negligible compared to the radius of the turbine, this is a suitable estimate. Since the blades were constructed using a consistent internal structure, all blades have the same mass, within less than 1%. So, the same mass moment of inertia was used. Finally, the mass moment of inertia of the upper and lower blade support arm discs, in addition to the central shaft and hubs, was determined using *Solidworks'* mass property tool. A summary of the components' mass moment of inertia is shown in Table 5.3.

Table 5.3: Summary of the mass moment of inertia of the individual components of the RMC VAWT Rig turbine.

Component	Quantity	Mass Moment of Inertia, I ($\mathrm{kg\,m^2}$)
Turbine Blades	3	1.33×10^{-1}
Aluminum Support Arm Disc	2	5.98×10^{-2}
Plywood Support Arm Disc	1	2.50×10^{-2}
Centre Shaft	1	4.02×10^{-4}
Centre Shaft Hubs	2	1.45×10^{-4}
	Total (I_{turb})	5.43×10^{-1}

5.2.5 Uncertainty Analysis

A summary of the uncertainty of the measurement devices used during the experimental campaign can be seen in Table 5.4. With the data measurements presented in Section 5.2.2 shown to follow normal distributions, the average value was assumed to be the representative value of the individual sets of data. Thus, the uncertainty was calculated using the Kline and McClintock uncertainty propagation method [110]. The derivations of equations for the uncertainty are shown in Appendix F.

Table 5.4: Uncertainty of the various measurement devices used during the experimental campaign on the RMC VAWT Rig.

Component	Parameter	Symbol	Uncertainty	Units
Burster 8656-5020	Relative Non-linearity	U_{lin}	0.04	Nm
	Relative Hysteresis	U_{hys}	0.03	Nm
	Tolerance of Sensitivity	U_{s}	0.05	Nm
	T Effect on Sensitivity	TK_{s}	0.003	Nm/K
	T Effect on Zero Point	TK_0	0.003	Nm/K
	Rotational Speed	Ω	0.25	RPM
Airmar PB-150	Wind Speed ($< 10\,\mathrm{kts}$)	V_∞	1.0 or 10 %	kts
	Wind Speed ($\geq 10\,\mathrm{kts}$)	V_∞	2.0 or 5 %	kts
Oakton© WD-03316-8	Temperature	T_∞	1.00	K
	Pressure	p_∞	1.00	mbar
Omega PX163	Pressure Differential	Δp	1 %	inH20

5.2.6 Test Procedure

To ensure consistent and safe operation of the RMC VAWT Rig, the following steps were performed before each test:

1. Ensure the cart is in the proper position and levelled at the required height,
2. Check all turbine bolts, couplers, and connections,
3. Turn on the air compressor and ensure the regulator is off to stop the turbine from rotating,

4. Set up the weather station upstream and off to the side of the turbine at the height of the turbine equator,
5. Connect to the RMC VAWT Rig using the *RealVNC* viewer and run the *Python* script, and
6. Set the air pressure regulator to 60 psi, spin the turbine by hand to check for cogging in the hysteresis brake, and turn off the regulator.

With the RMC VAWT Rig setup, start-up data, torque measurements, or both can be collected with minimal input from the operator as most steps are performed through the *Python* script. The steps are the same when performing wind tunnel and outdoor testing, with the exception that the wind tunnel wind speed is allowed to settle before starting the procedure. For a startup, the steps followed were:

1. Initiate startup run through *Python* script,
2. Hysteresis brake current is set to zero,
3. Data collection starts,
4. Set air pressure regulator to 60 psi allowing the turbine to spin,
5. Once the turbine is fully started, stop the Startup script, cease data collection, and
6. Turn off the air pressure regulator to stop the turbine, repeat as necessary.

Torque measurement runs are initiated after the turbine is started, either after a startup run or after starting the turbine by hand. Although the VAWT Rig can use a feedback loop to operate at a constant RPM or TSR, further refinement of the feedback system is necessary since it was too delayed to react to the reduction in torque at TSR below peak power, resulting in the turbine stalling and coming to a stop. Consequently, the results shown are from increasing torque through increments of the hysteresis brake current without any feedback system. When describing brake current increments, the term 'brake value' will be used, where one brake value is 1 of 255, corresponding to 0 to 500 mA being supplied to the brake. In other words, one brake value is about 1.96 mA. In the future, instead of increasing the brake value, the torque measurement runs could cycle through a list of TSR or RPM using the feedback system to fill out the P or C_P curves. However, the following steps were followed while increasing torque through brake value:

1. Ensure brake control pin from the *Arduino* is plugged into the brake power supply,
2. Set air pressure regulator to 60 psi and start the turbine,
3. Once the turbine is fully started, initiate the torque measurement run through *Python* script,
4. Increase brake value by two (one during wind tunnel testing)
5. Wait 30 seconds for the turbine to settle
6. Data collection for 10 minutes (30 seconds during wind tunnel testing)
7. Repeat steps 4-6 until turbine stops (< 50 RPM), and
8. Set brake value to zero, repeating runs as required.

5.2.7 Wind Tunnel

Given the size of the initial rotor geometry used on the RMC VAWT Rig, no adequately sized closed-circuit wind tunnels were available at RMC. So, to minimize area blockage effects, the RMC Open Jet Wind Tunnel was used, which is shown in Figure 5.16. It is a blow-down tunnel powered by a variable frequency (0-60 Hz) motor. The outlet size was 37.75×37.75 in, which required an expansion section following the original 16×16 in test

section. Although there was a settling chamber before the original test section, another settling chamber and mesh grid were used after the expansion section to aid flow straightening following the expansion. To characterize the flow, a survey was performed at five rotor radii (1.5 m) from the tunnel exit, where the turbine was placed during testing. The survey consisted of velocity measurements using the *Omega* PX163 pressure transducer at normalized rotor half heights, h/H, $\in \{0, -0.5, -1.0\}$ and normalized rotor radii, r/R, $\in \{0, 0.5, 1.0, 1.25\}$. These positions correspond to the bottom left corner of the tunnel when looking upstream. This corner was chosen to be representative of the entire tunnel to be conservative, since there was a low-velocity zone in the corner that was not present in the other corners. These positions were measured at wind tunnel motor frequencies of 20, 40, and 60 Hz, corresponding to an area-weighted average wind speed (across the wind turbine frontal area) of 2.17, 4.54, and 7.61 m/s, respectively. The resulting contours are shown in Figure 5.17.

(a) Wind tunnel and RMC VAWT Rig (b) Wind tunnel sections

Figure 5.16: RMC Open Jet Wind Tunnel.

The flow surveys show that the jet is not uniform and the difference in velocity due to the 'dead zone' in the lower right corner compared to the area-weighted average and maximum increases with wind tunnel speed. Although the other corners did not qualitatively experience the same near-zero velocity, it is still a detriment to turbine performance since it is a lower V when the AoA is low and efficient, compared to the high V at high and inefficient AoA near the centre of the jet. Furthermore, since V decreases towards the edge of the jet, the local TSR is also changing. Consequently, the results should not be compared to other wind tunnel experiments, and are not representative of outdoor operation, where, although varying in magnitude, the flow is relatively uniform. This region of low V flow is likely due to flow separation as the flow expands following the original 16×16 in test section. Further work should replace the contraction to expansion sections with a proper contraction immediately following the blow-down fan setting chamber, so an expansion section is not required, and results can be compared to other research. Nonetheless, the wind tunnel provided consistency to compare the baseline to tubercle blades and a safe and controllable environment to fine-tune the RMC VAWT Rig software before testing outside. The survey

area-weighted average V was compared to the pitot tube mounted on the tunnel exit, which shows good agreement at high wind tunnel motor frequencies. This is summarized in Table 5.5. With this agreement, the velocity used to calculate TSR and C_P used the pitot tube measurement.

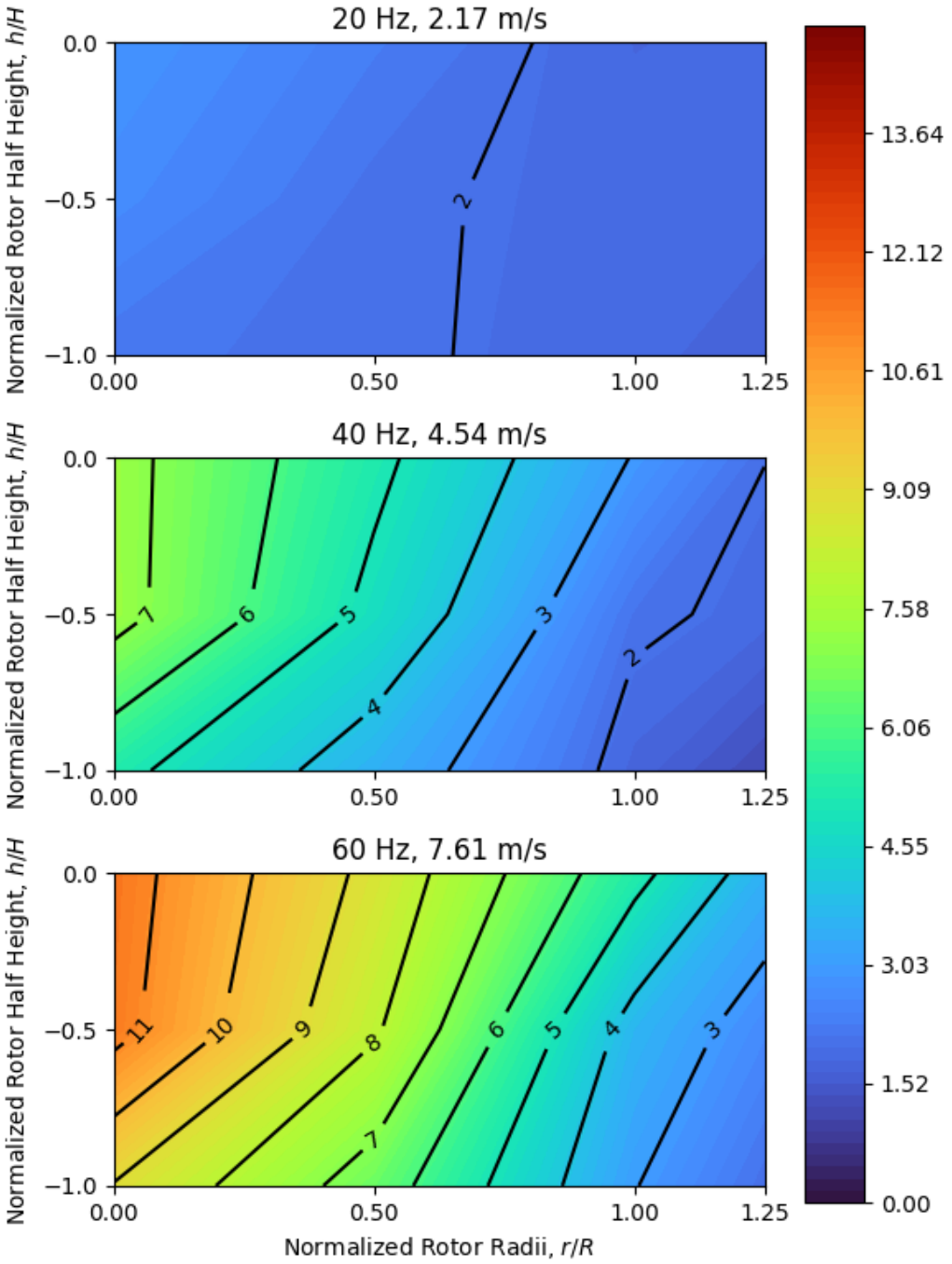

Figure 5.17: Survey of the flow velocity, in meters per second, at five turbine radii (2.5 m) from the exit of the RMC Open Jet Wind Tunnel. The survey shows the bottom right corner of the flow when looking upstream, with the centre of the tunnel exit at (0,0).

Table 5.5: Wind tunnel survey results compared to wind tunnel pitot measurements.

Motor Frequency, f (Hz)	Survey Area-Weighted Average V (m/s)	Pitot V (m/s)
20	2.17	1.77 (−18.4 %)
40	4.54	4.58 (+0.9 %)
60	7.61	7.52 (−1.2 %)

Values in parentheses denote percent difference compared to the Survey Area-Weighted Average V.

5.2.8 Outdoor Location

The RMC VAWT rig was located at the tip of the RMC campus peninsula during outdoor testing, commonly called Point Frederick or 'The Point'. The peninsula is on Lake Ontario, with the point being the most southern part of the peninsula. Point Frederick is also home to Fort Frederick, a part of the Kingston Fortifications and Point Frederick Buildings National Historical Sites of Canada. The fort features soil ramparts, some distance from the Lake Ontario shore, that can be seen in the background of Figure 5.11, obstructing wind when coming from certain directions. In cases where the wind is obstructed, no data was collected. As a result, a limited location for the RMC VAWT Rig was available, as shown in Figure 5.18. The rig was placed on the opposite side of Point Frederick Drive from the RMC Mechanical and Aerospace Engineering Department's old jet engine test cell. This location reduced the unusable wind directions resulting from the ramparts to between westerly and northeasterly, shown in Figure 5.18 as the dashed red lines. With Kingston's prevailing winds being southwesterly, this location provided the most conditions for data collection. The old jet engine test cell provided electricity for the rig, along with a place to remotely operate the rig. The rig was placed as close to the shore as possible to keep the turbine away from the road. However, there is minimal traffic on Point Frederick Drive, so this had minimal impact on the results.

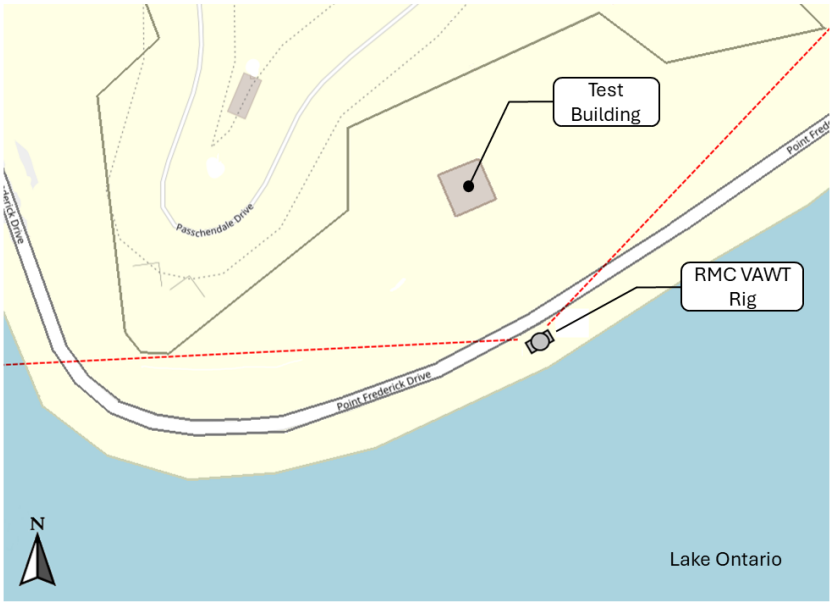

Figure 5.18: Map detailing location of RMC VAWT Rig during outdoor testing on Point Frederick in Kingston, ON. Map data from OpenStreetMap [111]. The red dashed lines denote the limit of usable wind directions, where the fort ramparts obscure the wind.

5.3 Initial Results of the RMC VAWT Rig

This section presents the results from the experimental campaign, including wind tunnel and outdoor testing, yielding startup and torque measurements. The startup subsections present comparisons in the startup characteristics, along with power curves derived using the spool-up method. The power curve subsections present the power curves derived through incrementally increasing the loading on the hysteresis brake and directly measuring the torque. The power curves generated using wind tunnel data were used to validate the DMSTM against the baseline. Power curves generated outside were used to compare the performance characteristics of various leading-edge tubercle shapes to the baseline straight leading edge.

5.3.1 Wind Tunnel Startup

Using the startup data collected during the wind tunnel testing, the startup characteristics of the baseline turbine were compared to the $A03\lambda11$ turbine. Based on the acceleration of the turbine throughout startup, the power coefficient curves were also determined by the spool-up method and compared to the DMSTM result. This was repeated for a range of wind tunnel motor frequencies, f, resulting in a range of wind tunnel velocities. Through the wind tunnel jet survey, the tunnel pitot velocity reading was shown to match closely to the area-weighted average velocity resulting from the survey for most of the range of frequencies, especially at higher frequencies. There was a significant deviation at 20 Hz, but the lowest frequency tested was 27.5 Hz. Despite this, the discrepancy was consistent, so the results between the two blades could be compared. However, it should not be compared directly to other research. Furthermore, only one tubercle shape was tested in the wind tunnel due to the wind tunnel's velocity distortion and its effect on the results.

Table 5.6 details the startup characteristics of each blade for all wind tunnel speeds examined. TSR and power coefficient plots for 32.5 and 45.0 Hz are shown in Figures 5.19 and 5.20, respectively. The plots for the remaining wind tunnel frequencies are shown in Appendix G. Overall, the baseline blade showed significantly better startup times, higher maximum TSRs, and larger maximum C_P than the $A03\lambda11$. The difference in start time tended to increase with increasing wind tunnel velocity, corresponding to a lower relative C_P compared to the baseline with increasing wind tunnel velocity. Eventually, at a wind tunnel frequency of 45 and 47.5 Hz, the $A03\lambda11$ was unable to start, while the baseline did. It is important to note that the magnitude of C_P at low wind tunnel frequencies, namely 27.5 and 30.0 Hz, is above the Betz limit of 0.593, and even above the slightly higher estimates for vertical axis wind turbines, ranging between 0.61 to 0.66 [112]. This higher C_P could be attributed to a higher area-weighted average velocity at these low frequencies since the coefficients were calculated using the tunnel pitot, which was shown to under-predict the velocity at low frequencies. This is supported by the lower and more reasonable values of C_P as wind tunnel frequency increases. Another cause could be the non-uniform flow from the tunnel, providing higher energy flow where it is beneficial and low energy flow where it would normally be detrimental to performance. The last, but most probable cause of the error, is that the area-weighted average velocity was surveyed from the portion of the tunnel with a dead zone, so the remainder of the tunnel would have even higher velocities. Since C_P is normalized with V^3, a higher V would result in more reasonable C_P values.

Table 5.6: Summary of wind tunnel startup results of the $A03\lambda11$ blades compared to the baseline.

f(Hz)/ V (m/s)	Shape	Maximum TSR	Start Time (s)	Maximum C_P	TSR of Maximum C_P
27.5/ 2.9	Baseline	4.00	108	0.68	3.11
	$A03\lambda11$	3.85 (−3.8 %)	163 (+50.9 %)	0.32 (−52.9 %)	3.05 (−1.9 %)
30.0/ 3.2	Baseline	4.04	89	0.65	2.55
	$A03\lambda11$	3.78 (−6.4 %)	148 (+66.3 %)	0.34 (−47.7 %)	2.93 (+14.9 %)
32.5/ 3.6	Baseline	3.85	82	0.55	2.39
	$A03\lambda11$	3.78 (−1.8 %)	125 (+52.4 %)	0.29 (−47.3 %)	2.94 (+23.0 %)
37.5/ 4.4	Baseline	3.68	57	0.51	2.53
	$A03\lambda11$	3.62 (−1.6 %)	96 (+68.4 %)	0.26 (−49.0 %)	3.04 (+20.2 %)
42.5/ 5.0	Baseline	3.74	52	0.53	2.77
	$A03\lambda11$	3.45 (−7.8 %)	100 (+92.3 %)	0.30 (−43.4 %)	2.73 (−1.4 %)
45.0/ 5.4	Baseline	3.54	65	0.49	2.45
	$A03\lambda11$	1.45 (−59.0 %)	-	0.05 (−89.9 %)	1.25 (−49.0 %)
47.5/ 5.7	Baseline	3.50	141	0.50	2.50
	$A03\lambda11$	1.37 (−60.9 %)	-	0.04 (−92.0 %)	1.17 (−53.2 %)

Values in parentheses denote percent difference compared to the baseline. A dash for start time indicates the turbine did not start.

From Figure 5.19 (a), the baseline blade reaches peak TSR within 82 seconds while it takes the $A03\lambda11$ 125 seconds. While their curves are similar below a TSR of 0.5, the baseline quickly increases rotational rate, having both a higher peak acceleration, determined by the slope of the curves, along with a higher curvature or jerk, changing the acceleration quicker than the $A03\lambda11$. They both have similar peak TSR, with the baseline and $A03\lambda11$ reaching 3.85 and 3.78, respectively. The higher acceleration and jerk present themselves in the power coefficient curves shown in Figure 5.19 (b), where the baseline has a steeper increase to a higher peak C_P of 0.55 at a TSR of 2.39, compared to the peak C_P of the $A03\lambda11$ of 0.29 at a TSR of 3.04. Both blades experience a slight dip in C_P around a TSR of 2.25. This figure also presents the DMSTM estimate of the baseline blade at the same free stream velocity. Despite the significantly smaller magnitude curve, the DMSTM predicts a similar shape and matches the higher TSR results, accurately predicting the TSR that yields insufficient torque to further accelerate the turbine. The error is likely due to the lower tunnel frequencies having a higher area-weighted average velocity compared to the tunnel pitot measurement, in addition to the velocity in the surveyed corner being lower than the remainder of the tunnel, giving a higher magnitude C_P than the DMSTM. Furthermore, if a higher velocity was used in the DMSTM, the data would scale up and to the left due to Re effects. The lack of data at low TSRs could be attributed to the non-uniform wind tunnel flow, as well as the DMSTM being unable to correctly model the flow when the turbine is drag-driven and not fully started, along with the known convergence problems at lower TSRs.

Figure 5.20 presents the startup and power coefficient curves resulting from both the baseline and $A03\lambda11$ blades for a wind tunnel motor frequency of 45.0 Hz, resulting in a tunnel velocity of 5.4 m/s measured by the wind tunnel pitot tube. At this tunnel velocity, along with 5.7 m/s (47.5 Hz), the $A03\lambda11$ was unable to start. In this case, both turbines have

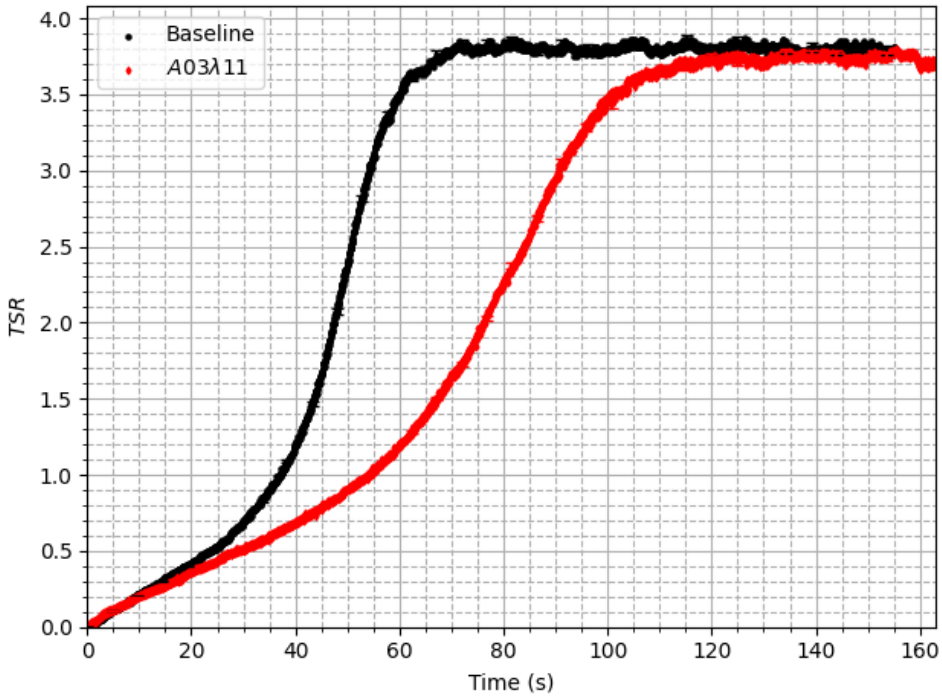

(a) Startup

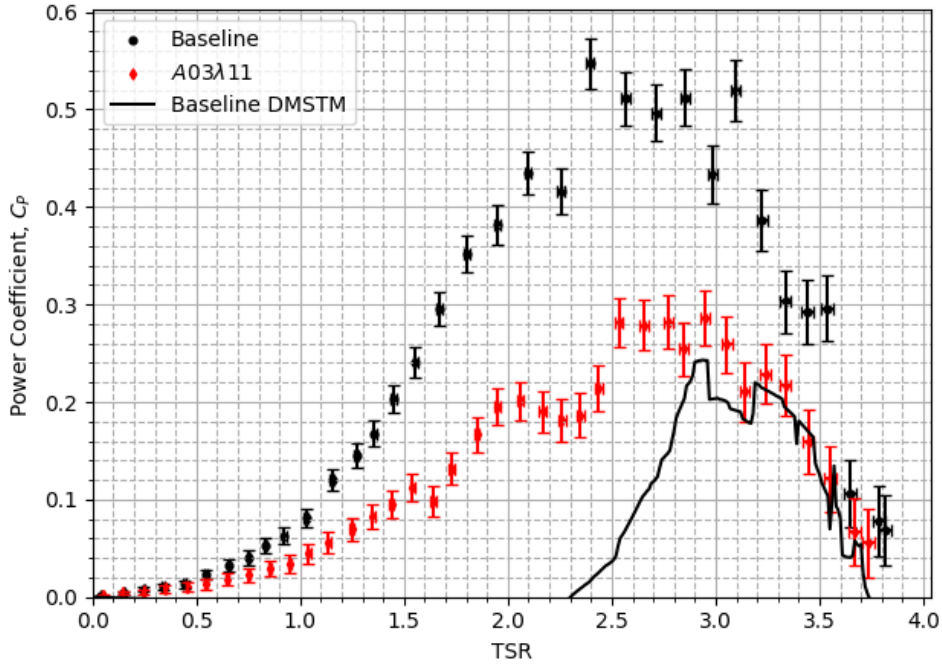

(b) Power Coefficient

Figure 5.19: Startup and spool-up power coefficient curves of the $A03\lambda11$ blades compared to the baseline in the wind tunnel at a motor frequency of 32.5 Hz.

a similar spool-up to a TSR of 0.5, at which point the baseline turbine has an increase in acceleration up to a TSR of about 1.5. Although both turbines reach a TSR of 1.5, the $A03\lambda11$ remains at this TSR, while the baseline rapidly starts after approximately 20 s, up to a maximum TSR of 3.5. An interesting characteristic of these startup curves is the sudden change of acceleration to zero at a TSR of about 1.5, unlike other studies where the curves will gradually plateau, then either accelerate again or remain unstarted [84]. This may be a result of the non-uniform tunnel flow present at higher tunnel velocities. Regardless, the power coefficient curves are also shown, which show a more reasonable maximum C_P for the baseline turbine, closer to the DMSTM estimates. The sudden change in acceleration to zero also presents itself in the baseline curve, resulting in a drop in C_P towards zero at a TSR of 1.5. The baseline blade then rapidly increases towards its peak C_P of 0.49 at a TSR of 2.45, while the $A03\lambda11$ turbine has no data above a TSR of 1.5 since it was unable to start. The smaller slope that the $A03\lambda11$ had during startup also presents a reduced C_P compared to the baseline.

With the $A03\lambda11$ unable to start, this indicates that it is unable to produce enough torque to overcome the residual torque in the driven system. Since the residual torque was found to be linearly proportional to RPM, which for a given TSR varies linearly with velocity, while lift and drag vary with the square of velocity, this degradation in startup performance must be from a reduction in turbine torque coefficient that was not present in the lower velocity startups, not from increased residual torque. The most probable cause is the increased distortion of the tunnel jet as the motor frequency increases. This could change the AoA throughout rotation such that it adversely affects the turbine torque, potentially in a region that has more effect on the tubercle blades than the baseline. Without adequate time to make a proper tunnel contraction to prevent flow separation and non-uniformity resulting from the expansion section of the tunnel, no further shapes were tested in the wind tunnel. Instead, outdoor characteristics were also examined to show results in relatively uniform flow despite varying magnitudes.

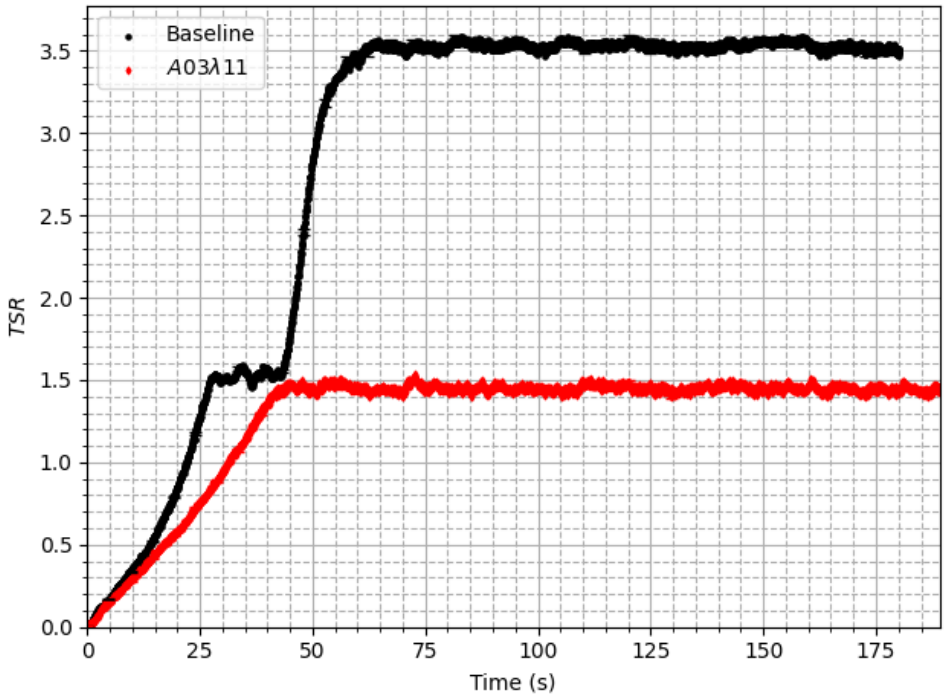

(a) Startup

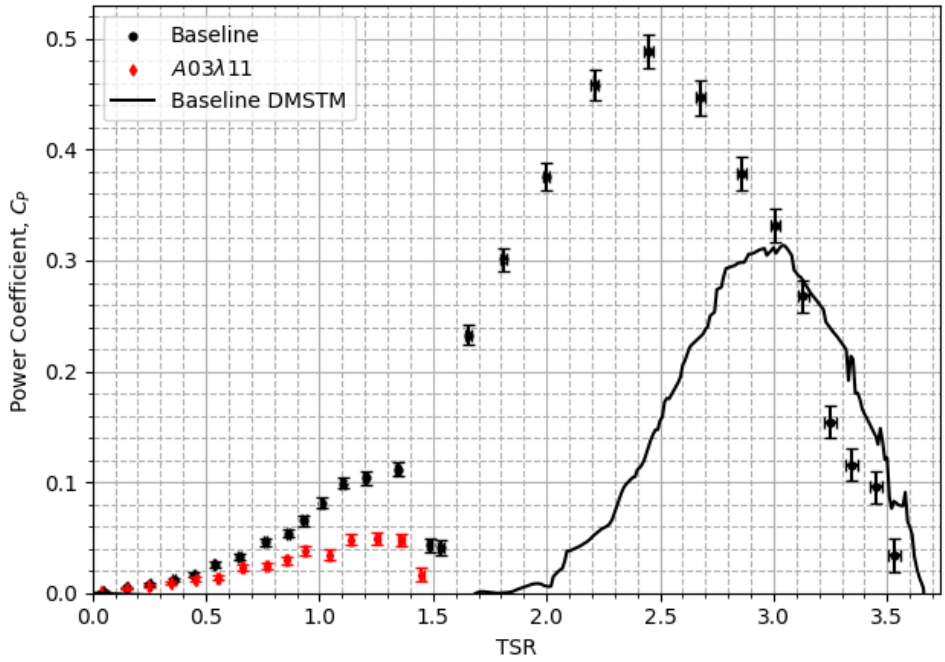

(b) Power Coefficient

Figure 5.20: Startup and spool-up power coefficient curves of the $A03\lambda11$ blades compared to the baseline in the wind tunnel at a motor frequency of 45.0 Hz.

5.3.2 Outdoor Startup

This section presents select startup characteristics and spool-up power coefficient curves with the RMC VAWT Rig outside to provide a more uniform flow than the wind tunnel. However, this came at the expense of uncontrollable and variable wind speeds, requiring different post-processing along with reduced repeatability of startup characteristics. The startup curves were created by averaging every second of data. This allowed weather station data to be compared with torque sensor data due to their differing sampling rates. The main drawback of the generated curves is that the response of the turbine rotational speed to a change in wind speed is not captured in the same averaged data, resulting in sudden drops and spikes in TSR, especially when the turbine has reached its peak TSR. Due to time constraints, only the $A02\lambda09$ turbine was compared to the baseline. The remaining startup curves not presented in this section can be found in Appendix G.

The startup curves, along with the corresponding wind speed for both the baseline and $A02\lambda09$ turbines with an overall average wind speed of 6.4 and 7.2 m/s, respectively, are shown in Figure 5.21. These sample startup curves were chosen for their similar average wind speeds, along with a relatively consistent wind speed throughout the duration of startup compared to the other tests performed, even considering the variations in wind speed of up to 2 m/s. Despite the higher average wind speed for the $A02\lambda09$ turbine, the baseline significantly outperforms during startup. The baseline reaches its maximum TSR of about 1.85 around 50 seconds before the $A02\lambda09$ reaches its maximum TSR of 1.60. Although the startup curves are similar up to a TSR of 0.5, after this point, the baseline has a greater slope, as a result of higher torque throughout the spool-up. After reaching the maximum TSR, the variations of TSR are a result of decreases in wind speed. However, with the turbine retaining RPM due to its momentum, the TSR increases.

Another sample of startup curves is presented in Figure 5.22, with the baseline and $A02\lambda09$ having an average wind speed throughout startup of 4.9 and 5.0 m/s, respectively. At this lower wind speed compared to that shown in Figure 5.21, the $A02\lambda09$ turbine was unable to start. The baseline and $A02\lambda09$ turbines match startup similarly until a TSR of 0.25, where the $A02\lambda09$ then plateaus to a maximum TSR of about 0.4. Whereas, the baseline reaches an average maximum TSR of approximately 2.0. It was found that for average wind speeds at or below 5.8 m/s, the $A02\lambda09$ was unable to start. The $A02\lambda09$ turbine required at least an average wind speed of 7.0 m/s to start (no startups were evaluated between 5.8 and 7.0 m/s). Unlike the wind tunnel startups, where the rate of change of TSR is suddenly zero when the turbine is unable to start, the outdoor startup TSR gradually plateaus as expected, and to a much lower TSR. Furthermore, with increasing wind speed, the aerodynamic forces increase more than the additional friction resulting from increased RPM for the same TSR, allowing the $A02\lambda09$ to start once the wind speed is great enough. However, this was not the case for the wind tunnel startups presented in Section 5.3.1, where the $A03\lambda11$ turbine was able to start at low wind speeds but not at higher wind speeds. Although the wind tunnel test used a different tubercle shape, this indicates that the distorted flow of the wind tunnel is a factor during startup and should be corrected for future tests.

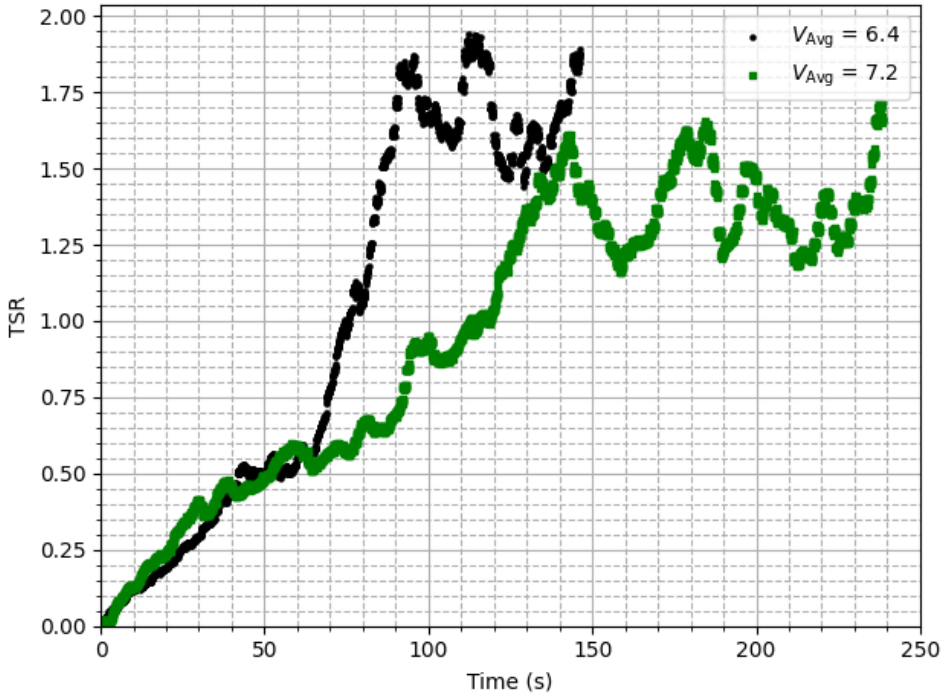

(a) TSR

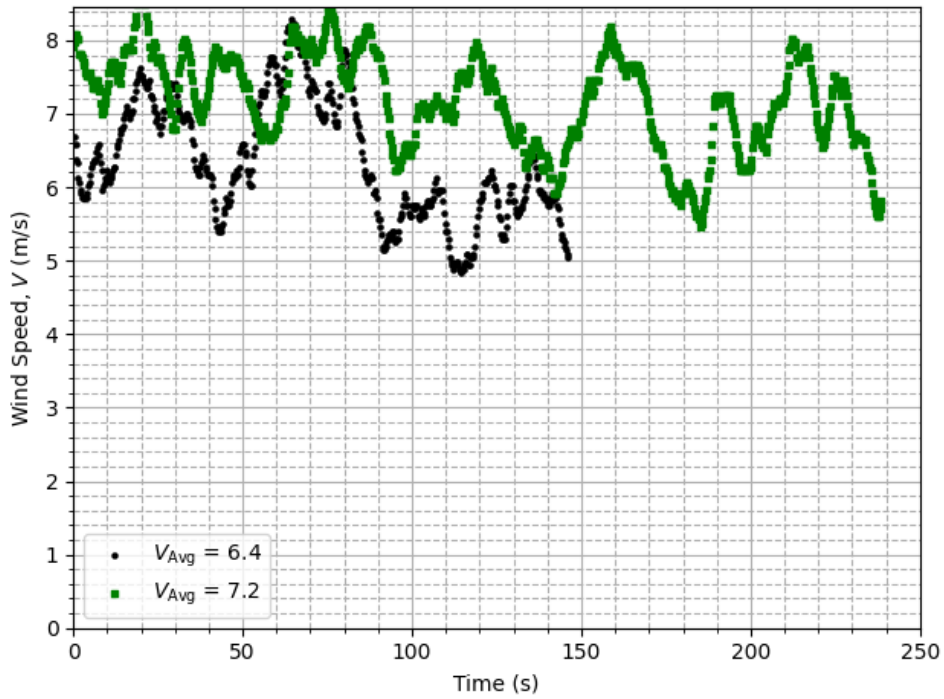

(b) Wind Speed

Figure 5.21: Outdoor startup TSR and wind speed of the $A02\lambda09$ blades compared to the baseline at an average wind speed of 7.2 and 6.4 m/s, respectively.

The inability of the $A02\lambda09$ turbine to start at lower wind speeds also shows that it was producing less torque than the baseline blade since it was unable to overcome the friction in the driven system. This outcome was the opposite of research from Du *et al.* [84], where the tubercle turbine was able to self-start, whereas the baseline turbine of the same aspect ratio (AR) could not. In that research, a three-bladed ($AR = 6$) turbine was used to compare an $A02\lambda7.5$ tubercle shape to the baseline NACA 0021 profile. For all solidities tested (1.0, 0.81, 0.67), the tubercle turbine consistently outperformed the baseline. However, at a solidity of 0.67, no turbine was able to start, but the tubercle turbine still outperformed. In this thesis, the blades have an AR of 4.92 while the turbine has a solidity of 0.914. By increasing AR through increased blade span, like in the case of Du *et al.* [84], not only does the turbine produce more torque through increased swept area, but the blades are additionally more aerodynamic efficient by having more lifting surface between the two blade tip vortices. With the turbine examined in this thesis having a lower aspect ratio with similar solidity, the upwind blade tip vortices could be adversely interacting with a larger portion of the downwind counter-rotating stream-wise vortices (CRSWV) produced by the tubercle blades, compared to the work by Du *et al.* [84]. Another cause could be the interaction between the upwind blade wake and CRSWVs with the downwind blades, inhibiting the creation of CRSWVs and subsequently reducing lift on the blade in the downwind. Thus, the tubercle turbine would suffer from its inherent poor low AoA performance compared to the baseline, without its primary performance gain at high AoA. This interaction would not have been captured by the DMSTM, explaining the discrepancy between the estimated performance improvements with the DMSTM and the experimental results. These interactions could vary with AR and turbine solidity or number of blades, which could change with the airfoil shape as well. Therefore, further research should examine various ARs and solidities through changing blade length and number of blades, respectively.

Through the spool-up method, the power and power coefficient curves shown in Figure 5.23 were created. All startups were binned into 0.1 wide TSR bins and averaged, giving the overall average power and power coefficients of all the startups. The baseline power coefficient curve diverges from the $A02\lambda09$ at a TSR of 0.25, where the baseline has a greater slope up to its maximum power coefficient of 0.037 at a TSR of 1.25. The $A02\lambda09$ turbine, on the other hand, reaches its peak power coefficient of 0.011 at a TSR of 0.95. The resulting power coefficients are much lower than those determined in the wind tunnel. This is likely a result of the relatively uniform flow outside compared to the distorted flow velocity of the wind tunnel used. The variation in power coefficient would also be affected by the varying wind speed during outdoor testing, giving different TSRs and power coefficients as the flow slows down, while the turbine's response to the change in wind is delayed.

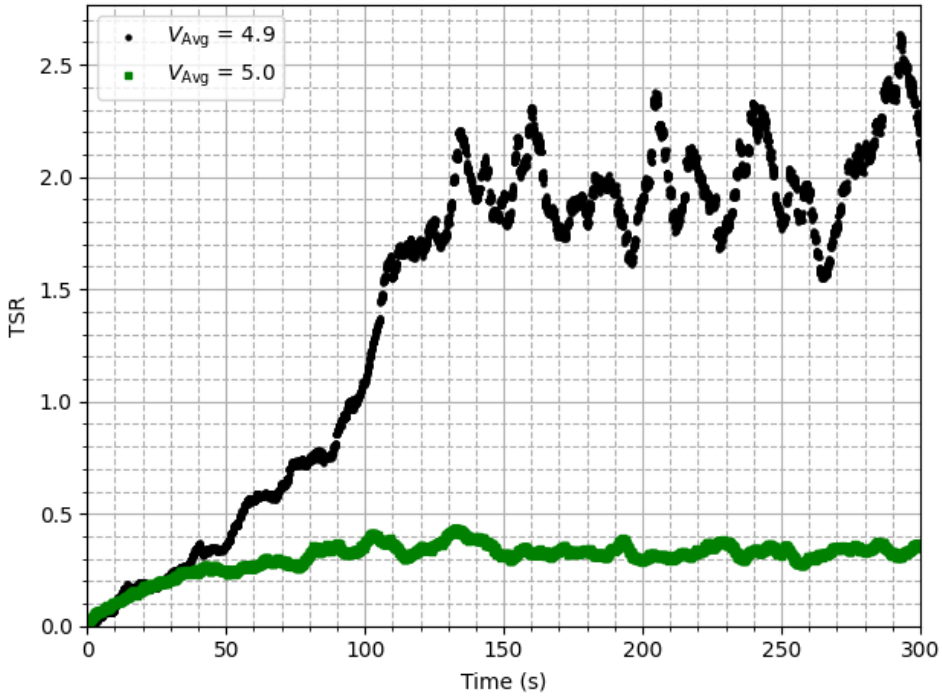

(a) TSR

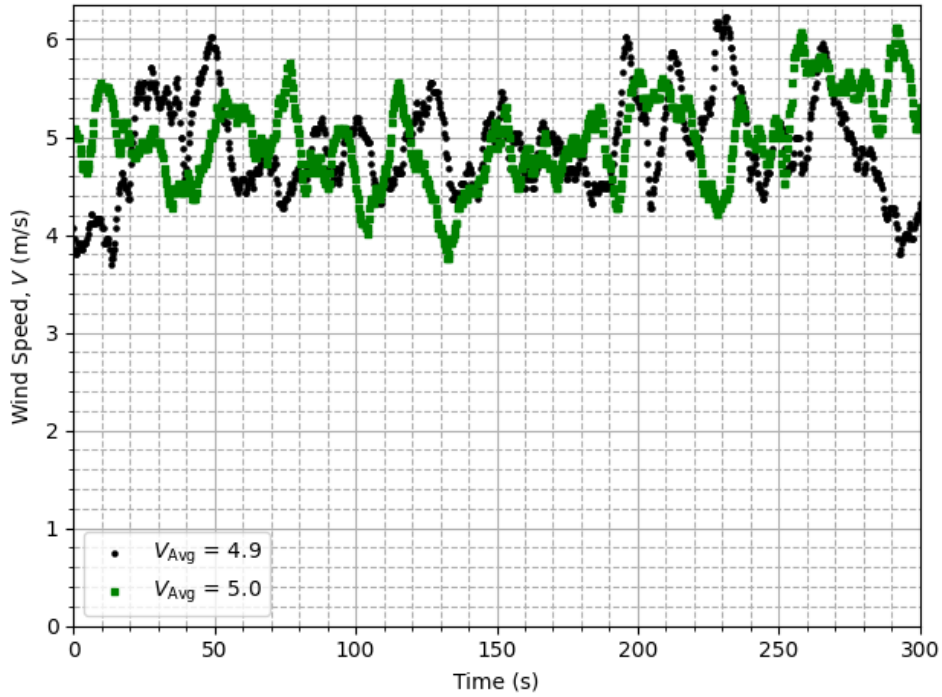

(b) Wind Speed

Figure 5.22: Outdoor startup TSR and wind speed of the $A02\lambda09$ blades compared to the baseline at an average wind speed of 5.0 and 4.9 m/s, respectively.

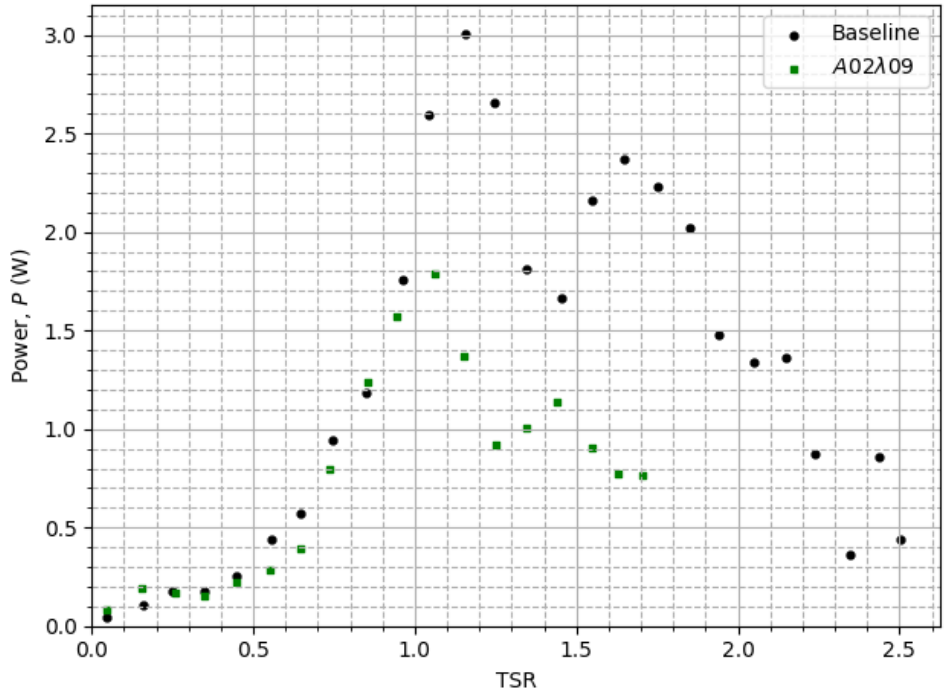

(a) Power

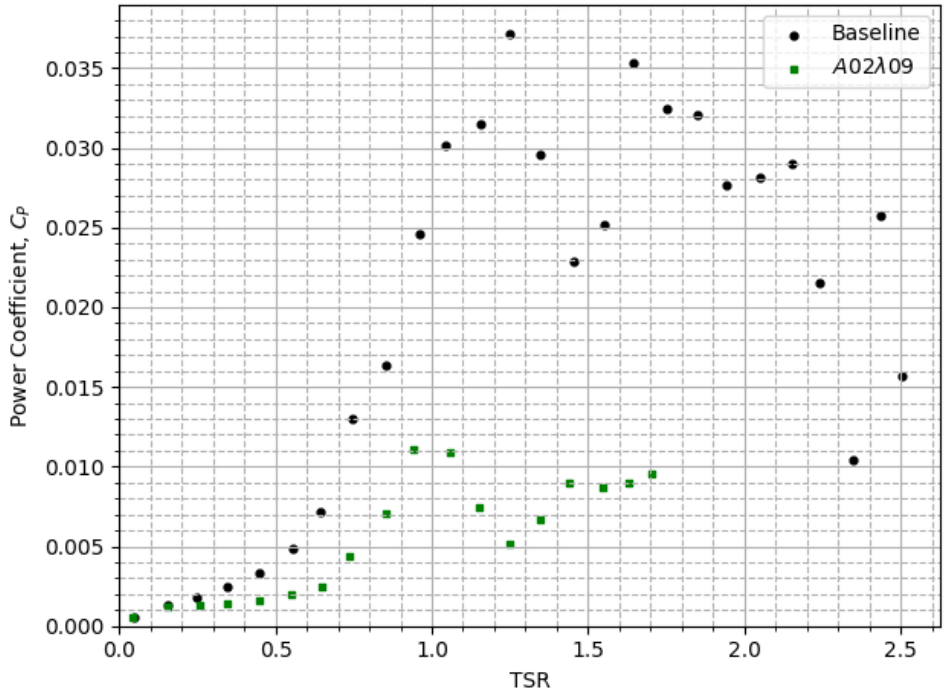

(b) Power Coefficient

Figure 5.23: Outdoor power and power coefficient curves $A02\lambda09$ blades compared to the baseline using the spool-up technique.

5.3.3 Outdoor Power Curves

Once the turbine was started outside, the torque was gradually increased by incrementing the brake value by two (out of 255 for full scale) every 10 minutes until the turbine came to a stop. This was repeated on different days to get a variety of wind speeds. Every ten seconds of data were then averaged to provide the power and power coefficient with TSR graphs shown in Figure 5.24. It is clear that the baseline turbine significantly outperforms the $A02\lambda09$. The baseline reaches a higher TSR of around 2.5, compared to the $A02\lambda09$ with a maximum TSR of 1.5. Throughout the entire range, including low TSR where tubercles were expected to show improvement, the baseline produces both higher power and power coefficients, aligning with the results from the spool-up testing outdoors and in the wind tunnel. The spread of data in these figures is a result of both Reynolds number effects and the delayed response of the turbine to wind speed variations, instantaneously changing the TSR. There is also a distinct lack of data around a TSR of 1.5. This is a result of the turbine passing peak torque, causing a rapid reduction in RPM. Interestingly, the $A02\lambda09$ turbine does not have any data beyond a TSR of 1.5. This suggested that either the $A02\lambda09$ was unable to start, or that its entire power curve occurs throughout a narrower range of TSR. With the outside startup results showing the unstarted $A02\lambda09$ reaching a maximum TSR of 0.4, the latter must be the case.

Figure 5.25 shows the variation of both TSR and RPM with wind speed. Both blades were evaluated in a similar range of wind speeds, up to 10 m/s. With increasing wind speed, the baseline was able to achieve a higher rate of increasing RPM since it was able to reach higher TSRs. Interestingly, maximum TSR is not constant with wind speed. Instead, it decreases with wind speed. This is caused by greater frictional forces resulting from the higher RPM required to maintain a constant TSR. Instead, both the baseline and $A02\lambda09$ turbine are limited by a maximum RPM of around 320 and 180, respectively. This further affirms that the $A02\lambda09$ is producing less torque than the baseline at the maximum TSR of the $A02\lambda09$, making it unable to overcome the residual torque in the system. Below a TSR of 1.5, the baseline has data parallel to the front of maximum TSR for the $A02\lambda09$ with wind speed. This corresponds to the data around a constant RPM of 135, which also contains $A02\lambda09$ data. This was the data collected after maximum torque was reached.

Overall, this chapter discussed the development and construction of the RMC VAWT Rig and presented preliminary experimental results. Based on the limited initial results obtained for the Small-Scale H-type VAWT in this thesis, the straight leading edge turbine outperforms the $A02\lambda09$ and $A03\lambda11$ turbines in terms of power output, power coefficient, and self-starting time and capability. However, a more comprehensive study should be conducted to confirm these findings. Both wind tunnel and outdoor startup tests found that the tubercle turbines were unable to generate sufficient torque to overcome the increased residual torque of the driven system, resulting in either a lower maximum TSR or the inability to self-start. This could be a result of the upwind blade-tip vortices and/or upwind wake and CRSWVs interacting with the downwind blades. These interactions would prevent the formation of CRSWVs in the downwind region, negating the positive effects of leading-edge tubercles while still experiencing increased drag. Although this is contrary to other experimental research that found that leading-edge tubercles enhance self-starting capability [84], this suggests that there is a combination of turbine geometry parameters, such as solidity, AR, and number of blades, that would minimize the upwind blade wake in-

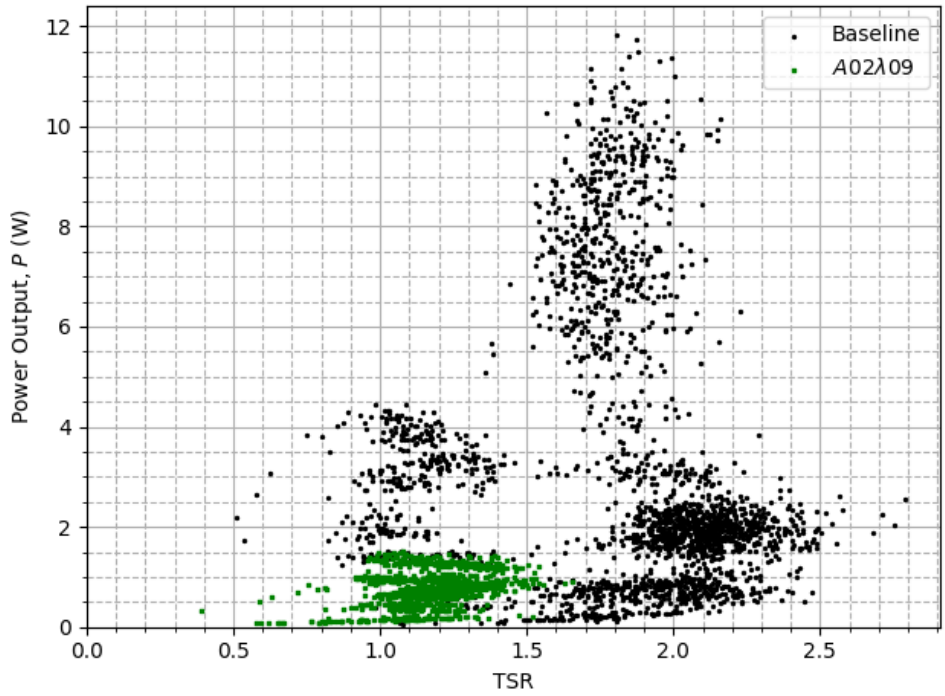

(a) Power

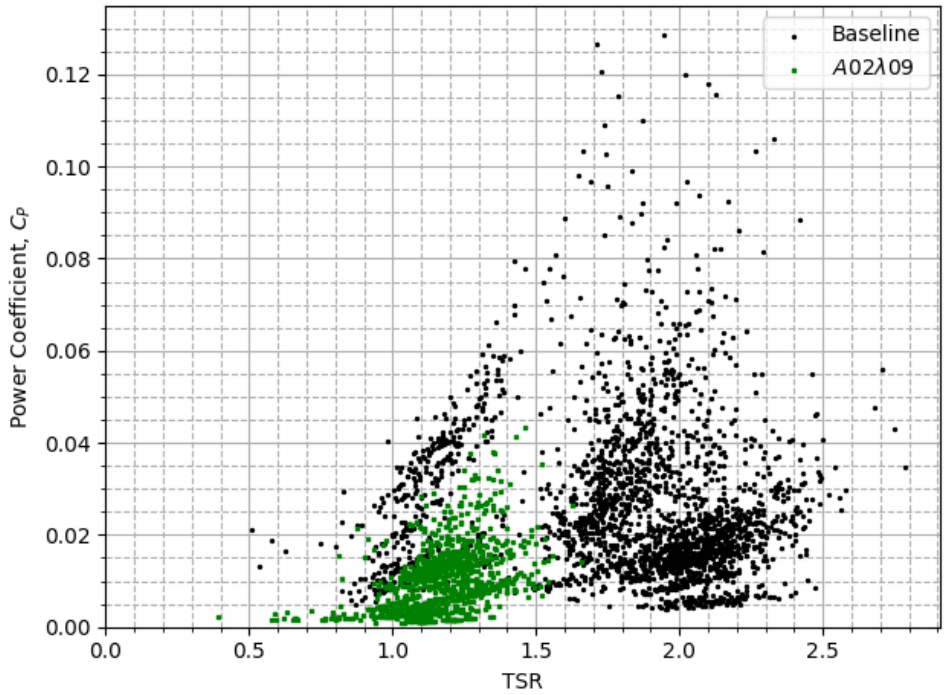

(b) Power Coefficient

Figure 5.24: Outdoor power and power coefficient curves $A02\lambda09$ blades compared to the baseline using torque sensor measurements. Each data point is a result from a ten second average.

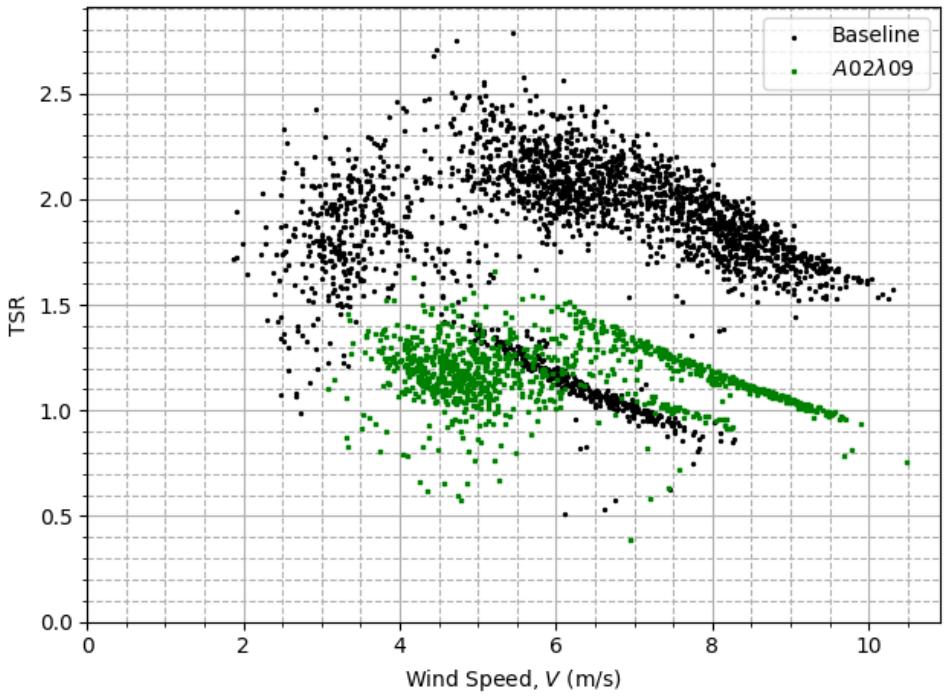

(a) TSR

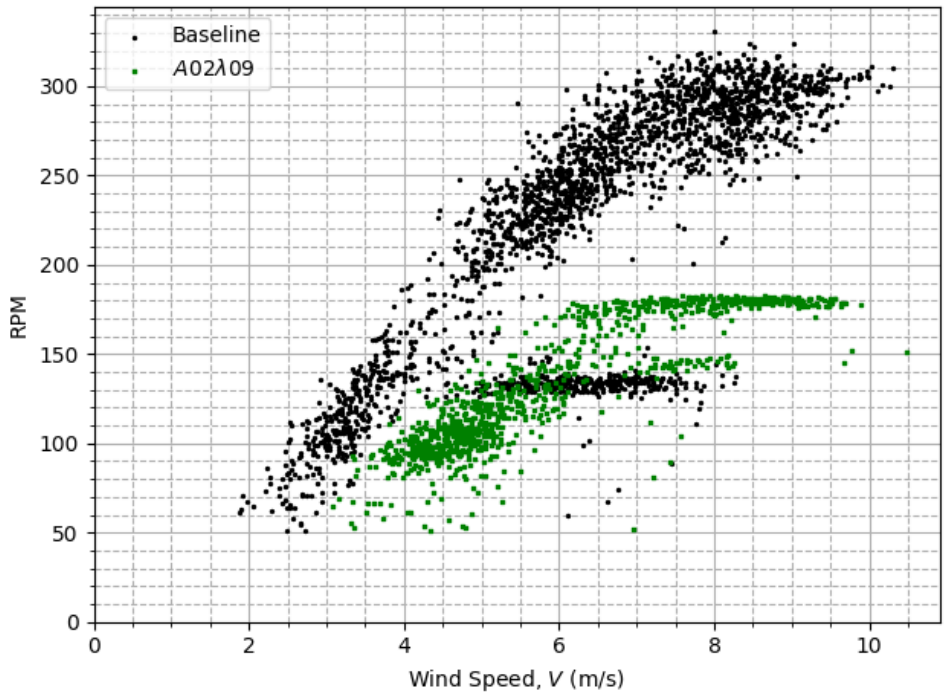

(b) RPM

Figure 5.25: Rotational rate and TSR of the $A02\lambda09$ blades compared to the baseline using during torque measurements. Each data point is a result from a ten second average.

teraction with the downwind blades. Therefore, further research should examine the effect of varying these parameters on self-starting capability and power output, while also evaluating more tubercle shapes. Varying AR can be done by varying the blade span and/or blade chord. However, varying only the blade span would keep the solidity and Reynolds number effects consistent. Additionally, increasing the span will result in a greater overall torque throughout the spool-up, resulting in greater acceleration and higher maximum TSR. Thus, the changes in performance should be compared relative to the baseline straight leading edge of the same geometric configuration. If increasing AR through greater span results in tubercle turbines outperforming the baseline, then the degraded performance observed in this study is likely a result of upwind blade tip vortex interactions with the downwind, preventing the formation of CRSWVs near the blade tips. Alternatively, if changing solidity through either varying turbine radius or number of blades has a positive effect on the tubercle turbine performance, this would suggest a different mechanism. In this case, the observed performance degradation would be due to the upwind blade wake and CRSWVs inhibiting the downwind blade from producing CRSWVs. Further startup characteristics should be evaluated in a wind tunnel to ensure a consistent wind speed. However, should the RMC Open Jet Wind Tunnel be used, a proper contraction should be made to minimize the distortion of flow velocity. Further outdoor testing should incorporate TSR feedback to get more data beyond the maximum torque TSR, eliminating the lack of data around a TSR of 1.5 and enabling a more complete assessment of turbine performance.

6 Conclusion and Recommendations

6.1 Conclusion

The initial computational analysis of leading-edge tubercles on VAWT blades applied the double-multiple stream tube model (DMSTM), adding to the current body of research by using an experimental database with various tubercle shapes. Power and power coefficient contours were generated for a range of tip speed ratios (TSR) and wind speeds for each tubercle shape, allowing the difference in these performance characteristics between a baseline straight leading edge blade to be calculated. It was found that tubercles can provide a wider operating range of TSR compared to the baseline, specifically enhancing the lower TSR limit by producing counter-rotating stream-wise vortices that delay stall, reducing the adverse torque in the post-stall region of rotation. Although this did not significantly enhance maximum power output, tubercle blades would have improved self-starting capability since they can produce more power at lower TSRs experienced during startup. Tubercles were found to increase wind probability-weighted average power output, $\bar{P}$, by as much as 22.7 % with the $A02\lambda07$, with some tubercle shapes reducing the TSR of maximum $\bar{P}$. It was also found that increasing tubercle amplitude decreased $\bar{P}$ and generally narrowed the operating range of TSR due to the larger vortices producing more drag and consequently increasing adverse torque. Some tubercle shapes, including the $A02\lambda07$ that had the highest $\bar{P}$, also decreased the maximum forces experienced by the blades each rotation due to the gradual stalling of the blade, reducing peak $C_{l_{\max}}$. While this is normally a disadvantage for other applications, this would correspond to reduced cyclic stresses during operation. Coupled with the reduced operating TSR offered by tubercles, this would correspond to improved fatigue life, requiring less maintenance and improving the overall cost per unit of energy captured by the turbine.

Some tubercle amplitude and wavelength combinations were shown to either improve wind probability-weighted average power output, reduce the peak forces experienced throughout rotation, or enhance low TSR performance, each contributing to either the fatigue life of the turbine or the energy produced from the wind. Thus, there exists a span-wise combination of tubercle shapes along the blade leading edge that balances both the fatigue life and average power output, potentially optimizing the energy produced throughout the turbine's life and consequently its cost per unit of energy. To date, there have been no optimizations of leading edge tubercles applied to VAWT blades that do not rely on a design of experiments due to the computational cost of CFD. Further, no studies have performed multi-objective optimizations on this topic. So, to explore this design space, a multi-objective design optimization was carried out using an H-type and Φ-rotor VAWT geometry. Using Non-Dominated Sorting Genetic Algorithm II (NSGA-II) coupled with the DMSTM, $\bar{P}$ and fatigue life indicator, $\overline{FLI}$, were maximized by varying the tubercle shape along the span

and the rotational rate or TSR. To assess design robustness in different wind environments, a separate optimization was performed where the wind probability-weighted average power outputs using the SWiFT Test Site and Kingston, Ontario wind probability distributions were maximized. It was found that for both geometries tested, the best solutions existed either at or below the TSR of maximum $\bar{P}$, depending on how much of a trade-off of $\bar{P}$ for $\overline{FLI}$ was desired. With decreasing TSR below that of maximum $\bar{P}$, the range of angles of attack (AoA) extends into the post-stall regime. Thus, the resulting Pareto Fronts were dominated by different tubercle shapes, depending on which shapes gave a higher $\bar{P}$ or $\overline{FLI}$. This was a result of the stream-wise counter-rotating vortices produced by the tubercles, delaying flow separation, and maintaining aerodynamic efficiency at post-stall angles while simultaneously reducing the peak normal forces experienced due to the gradual stall onset. The optimizer tended to prefer smaller amplitude tubercle shapes that produce smaller stream-wise counter-rotating vortices, causing less of a detriment to pre-stall aerodynamic efficiency compared to larger amplitude tubercle shapes. The resultant Pareto Fronts also gave potential designs that minimize the trade-offs between $\bar{P}$ and $\overline{FLI}$. For the Small-Scale H-type, the Maximum $\bar{P}$ design provided a 19.4 % improvement in $\bar{P}$ and 13.6 % higher $\overline{FLI}$ compared to the baseline blade. The design with the greatest $\overline{FLI}$ without sacrificing $\bar{P}$ below that of the baseline gave a 34.1 % increase in $\overline{FLI}$. Alternatively, Point A provided a balance between both variables, with 15.9 % and 28.4 % greater $\bar{P}$ and $\overline{FLI}$ than the baseline, respectively. The maximum $\bar{P}$ design was shown to be robust in another wind environment, with the tubercle shapes outperforming the baseline in terms of $\bar{P}$ and $\overline{FLI}$ in both analyzed wind environments.

To validate the findings of the DMSTM and the multi-objective optimization, the RMC VAWT rig was designed and constructed. With it being able to operate outside or in a wind tunnel, preliminary startup and steady-state torque measurements were collected in both environments. This contributed to the limited number of experimental studies applying leading-edge tubercles to VAWT blades and presented the first study that investigated more than one tubercle shape. Using the Small-Scale H-type VAWT geometry presented in this thesis, the straight leading edge turbine was found to outperform the $A02\lambda09$ and $A03\lambda11$ turbines in terms of power output, power coefficient, and self-starting time and capability. The limited wind tunnel and outdoor startup tests found that the tubercle turbines were unable to produce enough torque to overcome the increased residual torque of the driven system, resulting in either lower maximum TSRs or the inability to self-start. This is hypothesized to be a result of the upwind blade-tip vortices and/or upwind wake and stream-wise counter-rotating vortices (CRSWV) interacting with the downwind blades, preventing the formation of CRSWVs in this region, negating the positive effects of leading-edge tubercles, while still suffering from the increased drag. These interactions would not have been captured in the DMSTM. Since this is contrary to other experimental research that found that leading-edge tubercles enhance self-starting capability, a more comprehensive experimental campaign is required. Further work should focus on the effect of turbine geometry parameters, such as solidity, AR, and number of blades, that would minimize the upwind blade wake/vortices interaction with the downwind blades.

6.2 Recommendations for Future Work

To further improve the DMSTM, the aerodynamic database should be extended to include high Re data. Although the DMSTM was not allowed to extrapolate with Re, improvements were shown to occur in regions that did not require extrapolation. Thus, the benefit of tubercles was not negated. However, having higher Re data would allow for larger-scale simulations, with the potential for turbine geometry (turbine height and radius, blade chord length, etc.) to be considered in the optimization. If a new database is created, it should be done either through experimental load cell data in a wind tunnel or CFD so that it does not rely on pressure tap data and require the correction used in the present database.

Additional optimizations should include a structural analysis to approximate the life of the turbine. This would allow the multi-objective optimization to be combined into a single objective, such as lifetime power produced or cost per unit of energy. This would give the optimal design, as opposed to the series of designs along the Pareto Front, which could show the full potential of leading-edge tubercles on VAWT blades. With a higher Re database and a structural analysis, different turbine geometries could be compared as well. Another design objective that could be considered is startup capability. Based on the range of usable TSR yielded by the DMSTM for each wind speed, assuming the turbine has a constant mass moment of inertia between designs, the time to start could be estimated using a similar method to the Spool-Up torque method but in reverse. Since the acceleration and subsequently the time to reach maximum TSR are dependent on the torque throughout the range of operable TSR, the startup performance for each wind speed could be estimated, and then the wind speed-probability weighted average startup performance could be determined.

Finally, with the preliminary experimental measurements contradicting the analytical results, as well as previous experimental work by other authors, it is evident that either more testing is required, or other interactions were not captured by the DMSTM, such as upwind blade wake/vortices interaction with the downwind blades. To explore this possibility, further experimental research should vary geometric parameters such as solidity, AR, and number of blades. Changing the solidity and number of blades would affect the upwind blade-wake interaction with the downwind blade. Changing AR through increasing span would minimize the area affected by the upwind blade tip vortex. Additionally, further research, whether in a wind tunnel or outside, should include TSR feedback control. This would allow data to be collected at TSRs below the maximum power TSR, where tubercles and the ideal designs for maximizing $\bar{P}$ and $\overline{FLI}$ would have the greatest performance.

Bibliography

[1] Hannah Ritchie, Max Roser, and Pablo Rosado. Energy. *Our World in Data*, 2022. https://ourworldindata.org/energy.

[2] J.F. Manwell, J.G. McGowan, and A.L. Rogers. *Wind Energy Explained: Theory, Design, and Application*. John Wiley and Sons, Ltd, 2nd edition, 2009.

[3] I. Paraschivoiu. *Wind Turbine Design - With Emphasis on Darrieus Concept*. Presses Internationales Polytechnique, 2002.

[4] A.J. Buchner, J. Soria, D. Honnery, and A.J. Smits. Dynamic stall in vertical axis wind turbines: Scaling and topological considerations. *Journal of Fluid Mechanics*, 814:746–766, 2018.

[5] C.S. Ferreira, G. Van Kuik, G. Van Busel, and F. Scrano. Visualization by PIV of dynamic stall on a vertical axis wind turbine. *Experiments in Fluids*, 46:97–108, 2008.

[6] F.E. Fish and J.M. Battle. Hydrodynamic design of the humpback whale flipper. *Journal of Morphology*, 225(1):51–60, November 1995.

[7] D.S. Miklosovic, M.M. Murray, L.E. Howle, and F.E. Fish. Leading-edge tubercles delay stall on humpback whale flippers. *Physics of Fluids*, 16(5):L39–L42, May 2004.

[8] H. Johari, C. Henoch, D. Custodio, and A. Levshin. Effects of leading-edge protuberances on airfoil performance. *AIAA Journal*, 45:2634–2642, 2007.

[9] S. Sudhakar, N. Karthikeyan, and L. Venkatakrishnan. Influence of leading edge tubercles on aerodynamic characteristics of a high aspect-ratio uav. *Aerospace Science and Technology*, 69:281–289, October 2017.

[10] P. Watts and F.E. Fish. The influence of passive, leading edge tubercles on wing performance. In *Proceedings of the Twelfth International Symposium on Unmanned Untethered Submersible Technology (UUST01), Autonomous Undersea Systems Inst.*, Lee, NH, August 2001.

[11] K.L. Hansen, R.M. Kelso, and B.B. Dally. Performance variations of leading-edge tubercles for distinct airfoil profiles. *AIAA Journal*, 49:185–194, 2011.

[12] M.D. Bolzon, R.M. Kelso, and M. Arjomandi. Tubercles and their applications. *Journal of Aerospace Engineering*, 29:1–10, 2015.

[13] Luke H. Peristy, Ruben E. Perez, Asad Asghar, and William D. Allan. Reynolds number effect of leading edge tubercles on airfoil aerodynamics. In *34th AIAA Applied Aerodynamics Conference*, number 2016-3260, Washington, DC, 2016.

[14] John T. Hrynuk and Douglas G. Bohl. The effects of leading-edge tubercles on dynamic stall. *Journal of Fluid Mechanics*, 893:A5, 2020.

[15] Maurice N. Nayman and Ruben E. Perez. Improving dynamic stall effects using leading edge tubercles. In *AIAA AVIATION 2022 Forum*, number 2022-3529, Chicago, IL, 2022.

[16] Thomas Ackermann and Lennart Söder. An overview of wind energy-status 2002. *Renewable and Sustainable Energy Reviews*, 6(1):67–127, 2002.

[17] James Blyth. On the application of windmills to the production of electric currents. *Transactions of the Royal Scottish Society of Art*, 1, 1892.

[18] Paul Gipe and Erik Möllerström. An overview of the history of wind turbine development: Part i—the early wind turbines until the 1960s. *Wind Engineering*, 46(6):1973–2004, 2022.

[19] Trevor J. Price. James Blyth — Britain's first modern wind power pioneer. *Wind Engineering*, 29(3):191–200, 2005.

[20] Erik Möllerström, Paul Gipe, Jos Beurskens, and Fredric Ottermo. A historical review of vertical axis wind turbines rated 100 kW and above. *Renewable and Sustainable Energy Reviews*, 105:1–13, 2019.

[21] Georges Jean Marie Darrieus. Turbine having its rotating shaft transverse to the flow of the current. *US Patent no. 1835018*, December 1931.

[22] Sandra Eriksson, Hans Bernhoff, and Mats Leijon. Evaluation of different turbine concepts for wind power. *Renewable and Sustainable Energy Reviews*, 12(5):1419–1434, 2008.

[23] Willy Tjiu, Tjukup Marnoto, Sohif Mat, Mohd Hafidz Ruslan, and Kamaruzzaman Sopian. Darrieus vertical axis wind turbine for power generation i: Assessment of Darrieus VAWT configurations. *Renewable Energy*, 75:50–67, 2015.

[24] Muhammad Mahmood Aslam Bhutta, Nasir Hayat, Ahmed Uzair Farooq, Zain Ali, Sh. Rehan Jamil, and Zahid Hussain. Vertical axis wind turbine – a review of various configurations and design techniques. *Renewable and Sustainable Energy Reviews*, 16(4):1926–1939, 2012.

[25] Thomas G. Carne. Eole turbine photos. Technical report, Sandia National Lab. Albuquerque, NM, 2007.

[26] Senad Apelfröjd, Sandra Eriksson, and Hans Bernhoff. A review of research on large scale modern vertical axis wind turbines at Uppsala university. *Energies*, 9(7), 2016.

[27] Quiet revolution vertical axis wind turbines. https://www.quietrevolution.com/.

[28] Robert Whittlesey, Sebastian Liska, and John Dabiri. Fish schooling as a basis for vertical axis wind turbine farm design. *Bioinspiration & biomimetics*, 5:035005, 09 2010.

[29] John O Dabiri. Potential order-of-magnitude enhancement of wind farm power density via counter-rotating vertical-axis wind turbine arrays. *Journal of Renewable and Sustainable Energy*, 3(4), 2011.

[30] Zhenzhou Zhao, Dingding Wang, Tongguang Wang, Wenzhong Shen, Huiwen Liu, and Ming Chen. A review: Approaches for aerodynamic performance improvement of lift-type vertical axis wind turbine. *Sustainable Energy Technologies and Assessments*, 49:101789, 2022.

[31] M.H. Mohamed. Performance investigation of H-rotor Darrieus turbine with new airfoil shapes. *Energy*, 47(1):522–530, 2012. Asia-Pacific Forum on Renewable Energy 2011.

[32] Ying Wang, Sheng Shen, Gaohui Li, Diangui Huang, and Zhongquan Zheng. Investigation on aerodynamic performance of vertical axis wind turbine with different series airfoil shapes. *Renewable Energy*, 126:801–818, 2018.

[33] A.R. Sengupta, A. Biswas, and R. Gupta. Studies of some high solidity symmetrical and unsymmetrical blade H-Darrieus rotors with respect to starting characteristics, dynamic performances and flow physics in low wind streams. *Renewable Energy*, 93:536–547, 2016.

[34] M. Elkhoury, T. Kiwata, and E. Aoun. Experimental and numerical investigation of a three-dimensional vertical-axis wind turbine with variable-pitch. *Journal of Wind Engineering and Industrial Aerodynamics*, 139:111–123, 2015.

[35] Shengmao Li and Yan Li. Numerical study on the performance effect of solidity on the straight-bladed vertical axis wind turbine. In *2010 Asia-Pacific Power and Energy Engineering Conference*, pages 1–4, 2010.

[36] Qing'an Li, Takao Maeda, Yasunari Kamada, Junsuke Murata, Kento Shimizu, Tatsuhiko Ogasawara, Alisa Nakai, and Takuji Kasuya. Effect of solidity on aerodynamic forces around straight-bladed vertical axis wind turbine by wind tunnel experiments (depending on number of blades). *Renewable Energy*, 96:928–939, 2016.

[37] Abdolrahim Rezaeiha, Hamid Montazeri, and Bert Blocken. Towards optimal aerodynamic design of vertical axis wind turbines: Impact of solidity and number of blades. *Energy*, 165:1129–1148, 2018.

[38] Yann Staelens, F. Saeed, and I. Paraschivoiu. A Straight-Bladed Variable-Pitch VAWT Concept for Improved Power Generation. ASME 2003 Wind Energy Symposium:146–154, 01 2003.

[39] W. F. J. Olsman and T. Colonius. Numerical simulation of flow over an airfoil with a cavity. *AIAA Journal*, 49(1):143–149, 2011.

[40] Elyas Sobhani, Mohammad Ghaffari, and Mohammad Javad Maghrebi. Numerical investigation of dimple effects on darrieus vertical axis wind turbine. *Energy*, 133:231–241, 2017.

[41] Mazharul Islam, David S.-K. Ting, and Amir Fartaj. Aerodynamic models for darrieus-type straight-bladed vertical axis wind turbines. *Renewable and Sustainable Energy Reviews*, 12(4):1087–1109, 2008.

[42] Andrew Barnes, Daniel Marshall-Cross, and Ben Richard Hughes. Towards a standard approach for future vertical axis wind turbine aerodynamics research and development. *Renewable and Sustainable Energy Reviews*, 148:111221, 2021.

[43] Brian Hand and Andrew Cashman. Aerodynamic modeling methods for a large-scale vertical axis wind turbine: A comparative study. *Renewable Energy*, 129:12–31, 2018.

[44] Xin Jin, Gaoyuan Zhao, KeJun Gao, and Wenbin Ju. Darrieus vertical axis wind turbine: Basic research methods. *Renewable and Sustainable Energy Reviews*, 42:212–225, 2015.

[45] R.J. Templin. Aerodynamic performance theory for the NRC vertical-axis wind turbine. Technical report LTR-LA-160, 1974.

[46] James H. Strickland. Darrieus turbine: a performance prediction model using multiple streamtubes. 1975.

[47] I. Paraschivoiu. Double-multiple streamtube model for darrieus wind turbines. In *Wind Turbine Dynamics*. NASA Lewis Research Center, 1981.

[48] Harold C. Larsen. Summary of a vortex theory for the cyclogiro. In *Proceedings of the second US national conferences on wind engineering research*, 1975.

[49] Ir H. Hirsch and A.C. Mandal. A cascade theory for the aerodynamic performance of darrieus wind turbines. *Wind Engineering*, pages 164–175, 1987.

[50] Masoud Ghasemian, Z. Najafian Ashrafi, and Ahmad Sedaghat. A review on computational fluid dynamic simulation techniques for darrieus vertical axis wind turbines. *Energy Conversion and Management*, 149:87–100, 2017.

[51] Jian Chen, Hongxing Yang, Mo Yang, Hongtao Xu, and Zuohuan Hu. A comprehensive review of the theoretical approaches for the airfoil design of lift-type vertical axis wind turbine. *Renewable and Sustainable Energy Reviews*, 51:1709–1720, 2015.

[52] Pedro Francisco Silva Trentin, Pedro Henrique Barsanaor de Barros Martinez, Gabriel Bertacco dos Santos, Elóy Esteves Gasparin, and Leandro Oliveira Salviano. Screening analysis and unconstrained optimization of a small-scale vertical axis wind turbine. *Energy*, 240:122782, 2022.

[53] Fahad Rafi Butt and Tariq Talha. Optimization of the geometry and the span-wise positioning of the leading-edge tubercles on a helical vertical-axis marine turbine blade. In *Proceedings of the World Congress on Engineering*, July 2019.

[54] Syed Saddam ul Hassan, M. Tariq Javaid, Umar Rauf, Sheharyar Nasir, Aamer Shahzad, and Shuaib Salamat. Systematic investigation of power enhancement of vertical axis wind turbines using bio-inspired leading edge tubercles. *Energy*, 270:126978, 2023.

[55] Zhenyu Wang, Yuchen Wang, and Mei Zhuang. Improvement of the aerodynamic performance of vertical axis wind turbines with leading-edge serrations and helical blades using CFD and Taguchi method. *Energy Conversion and Management*, 177:107–121, 2018.

[56] Frank E. Fish. Performance constraints on the maneuverability of flexible and rigid biological systems. In *International symposium on unmanned untethered submersible technology*, pages 394–406. Citeseer, 1999.

[57] Dennis M. Bushnell and Kenneth J. Moore. Drag reduction in nature. *Annual Review of Fluid Mechanics*, 23:65–79, 1991.

[58] A. Druzhinin, E. Orlova, A. Volkov, A. Parygin, A. Naumov, A. Ryzhenkov, A. Vikhlyantsev, J. Šoukal, M. Sedlar, Martin Komárek, F. Pochylý, Pavel Rudolf, and Simona Fialová. Enhancing the efficiency of small-scale and microhydroturbines using nature-imitation technologies for the development of autonomous energy sources. *Thermal Engineering*, 66(12):944–952, June 2019.

[59] Alexi Levert-Beaulieu, Ruben E. Perez, and Peter W. Jansen. Euler-based aerodynamic shape optimization of leading edge tubercles in transonic flow. In *AIAA Scitech 2019 Forum*, number 2019-0852, San Diego, CA, 2019.

[60] William D. Allan, Asad Asghar, and Ruben E. Perez. Application of deployable tubercles as high-lift leading-edge devices. In *AIAA Scitech 2019 Forum*, number 2019-0852, San Diego, CA, 2019.

[61] Stewart J. Reid, Ruben E. Perez, and Asad Asghar. Characterization of tubercle effects on finite span wings. In *AIAA Aviation 2019 Forum*, number 2019-3294, Dallas, TX, 2019.

[62] Satpreet Singh Sidhu, Ruben E. Perez, William D. Allan, and Asad Asghar. Novel parameters for the performance evaluations of leading edge tubercles on airfoils. In *AIAA AVIATION 2020 FORUM*, number 2020-2691, 2020.

[63] F.E. Fish and G.V. Lauder. Passive and active flow control by swimming fishes and mammals. *Annual Review of Fluid Mechanics*, 38(1):193–224, 2006.

[64] Eric G. Paterson, Robert V. Wilson, and Fred Stern. General-purpose parallel unsteady RANS ship hydrodynamics code: CFDSHIP-IOWA. Technical report, Iowa Inst of Hydraulic Research, Iowa City, IA, 2003.

[65] Derrick Custodio. *The effect of humpback whale-like leading edge protuberances on hydrofoil performance*. PhD thesis, Worcester Polytechnic Institute, 2007.

[66] Hugo Carreira Pedro and Marcelo Kobayashi. *Numerical Study of Stall Delay on Humpback Whale Flippers*. 2008.

[67] Michael. D. Bolzon, Richard M. Kelso, and Maziar Arjomandi. Tubercles and their applications. *Journal of Aerospace Engineering*, 29(1):04015013, 2016.

[68] John C. Lin. Review of research on low-profile vortex generators to control boundary-layer separation. *Progress in Aerospace Sciences*, 38(4):389–420, 2002.

[69] Ernst A. van Nierop, Silas Alben, and Michael P. Brenner. How bumps on whale flippers delay stall: An aerodynamic model. *Phys. Rev. Lett.*, 100:054502, Feb 2008.

[70] Kristy Lee Hansen. *Effect of Leading Edge Tubercles on Airfoil Performance*. PhD thesis, The University of Adelaide, July 2012.

[71] B. Stein and M.M. Murray. Stall mechanism analysis of humpback whale flipper models. *Proceedings of Unmanned Untethered Submersible Technology (UUST), UUST05*, 5, 2005.

[72] Zhaoyu Wei, T.H. New, and Y.D. Cui. An experimental study on flow separation control of hydrofoils with leading-edge tubercles at low reynolds number. *Ocean Engineering*, 108:336–349, 2015.

[73] Timothy Wang. Aircraft wing stall control device and method, October 27 1987. US Patent 4,702,441.

[74] Chang Cai, Teng Zhou, Shuhong Liu, Zhigang Zuo, Yinan Zhang, and Qing'an Li. Modeling of the compartmentalization effect induced by leading-edge tubercles. *Physics of Fluids*, 34(8), August 2022. 087104.

[75] Asad Asghar, Ruben E. Perez, and William Allan. Application of leading edge tubercles to enhance propeller performance. In *2018 Applied Aerodynamics Conference*, number 2018-3647, Atlanta, GA, 2018.

[76] Asad Asghar, Ruben E. Perez, and William D. Allan. Further parametric investigation of leading edge tubercles on the propeller performance. In *AIAA Scitech 2019 Forum*, number 2019-0850, San Diego, CA, 2019.

[77] Felix Junho Sim. Investigation of blown tubercles with application to tilt-wing aircraft. Masters of applied science, Royal Military College of Canada, May 2023.

[78] Ryley R. Colpitts and Ruben E. Perez. Application of leading-edge tubercles on rotor blades. *AIAA Journal*, 61(1):255–270, 2023.

[79] Ryley R. Colpitts, Dillon Hesketh, and Ruben E. Perez. Experimental characterization of leading edge tubercles on rotor blades. In *AIAA Scitech 2022 Forum*, number 2022-1966, San Diego, CA, 2022.

[80] Ryley R. Colpitts, Maurice Nayman, and Ruben E. Perez. Optimization of leading edge tubercles applied to helicopter rotor blades. In *AIAA Scitech 2021 Forum*, number 2021-0733, 2021.

[81] Stacey Chan. A fundamental study of mini-turbine blades for urban applications. MA Thesis, Cornell University, January 2014.

[82] Longhuan Du. *Numerical and experimental investigations of Darrieus wind turbine start-up and operation*. PhD Thesis, Durham University, 2016.

[83] R.E. Sheldahl and P.C. Klimas. Aerodynamic characteristics of seven symmetrical airfoil sections through 180-degree angle of attack for use in aerodynamic analysis of vertical axis wind turbines. SAND 80-2114, 1981.

[84] Longhuan Du, Robert G. Dominy, and Grant Ingram. Experimental investigation of the performance of H-Darrieus wind turbines with tubercle leading edge blades. In *Turbo Expo: Power for Land, Sea, and Air*, volume 84249, page V012T42A001. American Society of Mechanical Engineers, 2020.

[85] Chi-Jeng Bai, Yang-You Lin, San-Yih Lin, and Wei-Cheng Wang. Computational fluid dynamics analysis of the vertical axis wind turbine blade with tubercle leading edge. *Journal of Renewable and Sustainable Energy*, 7(3), June 2015. 033124.

[86] Surya Sridhar, Jeena Joseph, and Jayakrishnan Radhakrishnan. Implementation of tubercles on vertical axis wind turbines (vawts): An aerodynamic perspective. *Sustainable Energy Technologies and Assessments*, 52:102109, 2022.

[87] Afonso N.C. Gonçalves, José M.C. Pereira, and João M.M. Sousa. Passive control of dynamic stall in a h-darrieus vertical axis wind turbine using blade leading-edge protuberances. *Applied Energy*, 324:119700, 2022.

[88] Yan Yan, Eldad Avital, John Williams, and Jiahuan Cui. Aerodynamic performance improvements of a vertical axis wind turbine by leading-edge protuberance. *Journal of Wind Engineering and Industrial Aerodynamics*, 211:104535, 2021.

[89] Punit Prakash, Praveen Laws, Nishant Mishra, and Santanu Mitra. *Computational Analysis of Symmetric and Cambered Blade Darrieus Vertical Axis Wind Turbine With Bio-Mimicked Blade Design*, pages 225–240. IGI Global, 2022.

[90] Muhammad Ahmad and Muhammad Hassam Zafar. Enhancing vertical axis wind turbine efficiency through leading edge tubercles: A multifaceted analysis. *Ocean Engineering*, 288:116026, 2023.

[91] Yanfeng Zhang, Zhiping Guo, Xinyu Zhu, Yuan Li, Xiaowen Song, Chang Cai, Yasunari Kamada, Takao Maeda, and Qing'an Li. Investigation of aerodynamic forces and flow field of an h-type vertical axis wind turbine based on bionic airfoil. *Energy*, 242:122999, 2022.

[92] Zhenyu Wang and Mei Zhuang. Leading-edge serrations for performance improvement on a vertical-axis wind turbine at low tip-speed-ratios. *Applied Energy*, 208:1184–1197, 2017.

[93] Ian Carlo M. Lositaño and Louis Angelo M. Danao. The performance of a vertical axis wind turbine with camber and tubercle leading edge as blade passive motion controls. In *Proceedings of the World Congress on Engineering*, volume 2, 2018.

[94] Punit Prakash, Leela Krishna Pendyala, Rajiv Chandra Teladevalapalli, and Santanu Mitra. A real-time experimental investigation of thin cambered tubercle blades for performance improvement of darrieus vertical axis wind turbine. In *2023 7th International Conference on Green Energy and Applications (ICGEA)*, pages 257–261, 2023.

[95] Nishant Mishra, Punit Prakash, Anand Sagar Gupta, Jishnav Dawar, Alok Kumar, and Santanu Mitra. Numerical and experimental investigations on a bio-inspired design of darrieus vertical axis wind turbine blades with leading edge tubercles. In *Applications of Nature-Inspired Computing in Renewable Energy Systems*, pages 211–224. IGI Global, 2022.

[96] Yaoran Chen, Jie Su, Zhaolong Han, Yongsheng Zhao, Dai Zhou, He Yang, Yan Bao, and Hang Lei. A shape optimization of ϕ-shape darrieus wind turbine under a given range of inlet wind speed. *Renewable Energy*, 159:286–299, 2020.

[97] D.E. Berg. Improved double-multiple streamtube model for the Darrieus-type vertical-axis wind turbine. In *American Solar Energy Society Meeting*, Minneapolis, MN, June 1983.

[98] R.E. Gormont. A mathematical model of unsteady aerodynamics and radial flow for application to helicopter rotors. Technical Report 72-67, USAAMRDL, May 1973.

[99] Bernard Massé. *Description de deux programmes d'ordinateur pour le calcul des performances et des charges aérodynamiques pour les éoliennes à axe vertical*. Institut de recherche de l'Hydro-Québec, 1981.

[100] A. Willmer. Aerodynamic investigation into the feasibility of a 25 m vertical axis windmill. *Aero Rep*, 124, 1979.

[101] C.L. Kelley and B.L. Ennis. Swift site atmospheric characterization. Technical report, 2016.

[102] R.O. Nellums and M.H. Worstell. Test results of the DOE/Sandia 17 meter VAWT. 1979.

[103] Federal Aviation Administration. *Metallic Materials Properties Development and Standardization (MMPDS).* MMPDS-02. Battelle Memorial Institute, Columbus, OH, 2005.

[104] Kalyanmoy Deb, Amrit Pratap, Sameer Agarwal, and T. Meyarivan. A fast and elitist multiobjective genetic algorithm: NSGA-II. *IEEE transactions on evolutionary computation*, 6(2):182–197, 2002.

[105] Ian Jonathan Ross. Wind tunnel blockage corrections: an application to vertical-axis wind turbines. Master's thesis, University of Dayton, 2010.

[106] Ian Ross and Aaron Altman. Wind tunnel blockage corrections: Review and application to savonius vertical-axis wind turbines. *Journal of Wind Engineering and Industrial Aerodynamics*, 99(5):523–538, 2011.

[107] J.H. Strickland, B.T. Webster, and T. Nguyen. Vortex model of the darrieus turbine: an analytical and experimental study. *NASA STI/Recon Technical Report N*, 80:25887, 1980.

[108] Aaron Altman. Private Communication, July 2017.

[109] Jonathan M. Edwards, Louis Angelo Danao, and Robert J. Howell. Novel Experimental Power Curve Determination and Computational Methods for the Performance Analysis of Vertical Axis Wind Turbines. *Journal of Solar Energy Engineering*, 134(3):031008, August 2012.

[110] S.J. Kline and F.A. McClintock. Describing uncertainties in single-sample experiments. *Mechanical Engineering*, 75(1):3–8, 1953.

[111] OpenStreetMap contributors. Planet dump retrieved from https://planet.osm.org . `https://www.openstreetmap.org`, 2017.

[112] F. Thönnißen, M. Marnett, Benedikt Roidl, and Wolfgang Schröder. A numerical analysis to evaluate Betz's Law for vertical axis wind turbines. *Journal of Physics: Conference Series*, 753, 2016.

[113] D. Poirel, Y. Harris, and A. Benaissa. Aeroelastic dynamics of a NACA 0012 airfoil in the transitional Reynolds number regime. In *Proceedings of PVP 2006/ICPVT-11*, 2006.

[114] https://climate.weather.gc.ca/historical_data/search_historic_data_e.html.

[115] Wayne B. Nelson. *Applied life data analysis*. John Wiley & Sons, 2005.

[116] Frank Kursawe. A variant of evolution strategies for vector optimization. In Hans-Paul Schwefel and Reinhard Männer, editors, *Parallel Problem Solving from Nature*, pages 193–197, Berlin, Heidelberg, 1991. Springer.

[117] Kalyan Deb. *Multiobjective Optimization Using Evolutionary Algorithms*. Wiley, New York, 01 2001.

[118] Carlos Coello. Sample pareto fronts. `https://delta.cs.cinvestav.mx/~ccoello/EMOO/testfuncs/`. Accessed: 2025-06-02.

[119] Georg Wegener and Jürgen Andrae. Measurement uncertainty of torque measurements with rotating torque transducers in power test stands. *Measurement*, 40(7):803–810, 2007.

Appendices

A Experimental Tubercle Aerodynamic Database

This appendix provides the complete set of aerodynamic data collected for the tubercle aerodynamic database, both uncorrected and corrected using the method described in Section 3.1.6, shown in plotted and tabulated form.

A.1 Methodology

The 2D aerodynamic characteristics of various tubercle shape wings were experimentally determined using data collected in the closed-circuit wind tunnel at the Royal Military College of Canada (RMC) by Peristy *et al.* [13] and Sidhu *et al.* [62]. The wind tunnel is capable of producing freestream air speeds up to 60 m/s and has a 0.76 m x 1.08 m test section. An illustration of the RMC Large Subsonic Wind Tunnel is presented below in Figure A.1.

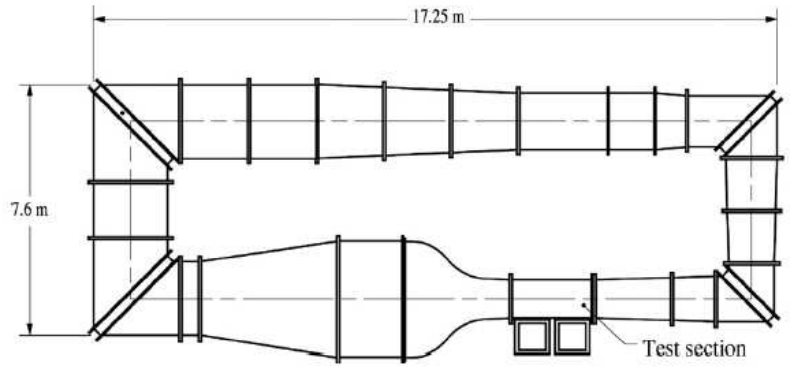

Figure A.1: RMC Large Subsonic Wind Tunnel [113].

The experimental wing, as shown in Figure A.2, has a chord length of 6 inches and a span of 18 inches with end plates. Using a *Scanivalve* ZOC22b/32Px to measure the pressure along the upper and lower surfaces of the wings, the quasi-2D aerodynamic characteristics were determined for the tubercle peaks and valleys. For Reynolds Numbers of 75 000, 150 000, and 300 000, local lift and drag coefficients were determined for angles up to 30°, where they were then shown to follow flat plate characteristics. Averaging the aerodynamic characteristics of the tubercle peak and valleys yielded the overall quasi-2D lift and drag

coefficients used in the aerodynamic database.

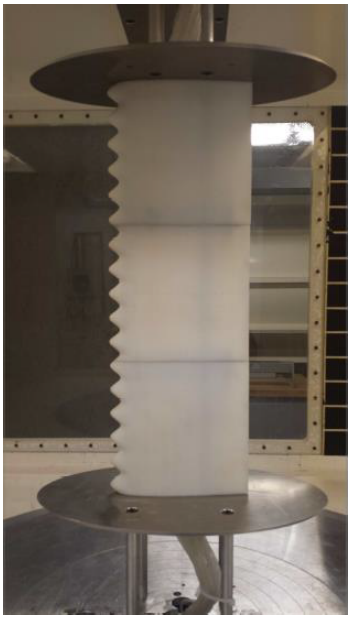

Figure A.2: Experimental Setup in Wind Tunnel.

A.2 Uncorrected Data

Table A.1: NACA 0018 Uncorrected Experimental Aerodynamic Data.

(a) $Re = 75\,000$

AoA	C_l	C_d
0.0	0.0301	-0.0259
2.0	0.2555	-0.0227
6.0	0.6384	0.0153
10.0	0.8136	0.0717
11.0	0.8343	0.0852
11.8	0.8518	0.1017
13.0	0.3446	0.1162
15.0	0.3713	0.1456
17.0	0.4773	0.2044
20.0	0.5591	0.2699
23.0	0.4543	0.2621
26.0	0.4706	0.2977
30.0	0.4936	0.3575
35.0	0.5658	0.4673
40.0	0.5976	0.5771
45.0	0.6062	0.6743
50.0	0.5889	0.7621
55.0	0.5514	0.8437
60.0	0.5052	0.9221
65.0	0.4388	0.9880
70.0	0.3637	1.0444
75.0	0.2887	1.0883
80.0	0.2107	1.1166
85.0	0.1328	1.1291
90.0	0.0520	1.1291

(b) $Re = 150\,000$

AoA	C_l	C_d
0.0	0.0445	-0.0386
2.0	0.2110	-0.0294
6.0	0.5320	0.0026
10.0	0.8400	0.0745
14.0	0.9067	0.1318
16.0	0.9366	0.1709
16.5	0.9390	0.1788
16.8	0.4631	0.1900
18.0	0.5384	0.1906
20.0	0.5419	0.2615
23.0	0.4450	0.2548
26.0	0.4623	0.2966
30.0	0.4901	0.3569
35.0	0.5658	0.4673
40.0	0.5976	0.5771
45.0	0.6062	0.6743
50.0	0.5889	0.7621
55.0	0.5514	0.8437
60.0	0.5052	0.9221
65.0	0.4388	0.9880
70.0	0.3637	1.0444
75.0	0.2887	1.0883
80.0	0.2107	1.1166
85.0	0.1328	1.1291
90.0	0.0520	1.1291

(c) $Re = 300\,000$

AoA	C_l	C_d
0.0	0.0445	-0.0386
2.0	0.2110	-0.0294
6.0	0.5320	0.0026
10.0	0.8400	0.0745
14.0	0.9067	0.1318
16.0	0.9366	0.1709
16.5	0.9390	0.1788
16.8	0.4631	0.1900
18.0	0.5384	0.1906
20.0	0.5419	0.2615
23.0	0.4450	0.2548
26.0	0.4623	0.2966
30.0	0.4901	0.3569
35.0	0.5658	0.4673
40.0	0.5976	0.5771
45.0	0.6062	0.6743
50.0	0.5889	0.7621
55.0	0.5514	0.8437
60.0	0.5052	0.9221
65.0	0.4388	0.9880
70.0	0.3637	1.0444
75.0	0.2887	1.0883
80.0	0.2107	1.1166
85.0	0.1328	1.1291
90.0	0.0520	1.1291

Table A.2: NACA 0018 $A02\lambda07$ Uncorrected Experimental Aerodynamic Data.

(a) $Re = 75\,000$

AoA	C_l	C_d
0.0	-0.0305	-0.0277
2.0	0.1060	-0.0252
6.0	0.3752	-0.0080
8.0	0.5458	0.0102
10.0	0.6022	0.0304
11.0	0.6485	0.0492
12.0	0.6615	0.0610
13.0	0.6691	0.0716
14.0	0.6741	0.0834
15.0	0.6438	0.0968
16.0	0.5196	0.1601
17.0	0.5012	0.1688
18.0	0.5520	0.2114
20.0	0.4669	0.2420
23.0	0.4864	0.2576
26.0	0.4631	0.2811
30.0	0.4659	0.3374
35.0	0.5658	0.4673
40.0	0.5976	0.5771
45.0	0.6062	0.6743
50.0	0.5889	0.7621
55.0	0.5514	0.8437
60.0	0.5052	0.9221
65.0	0.4388	0.9880
70.0	0.3637	1.0444
75.0	0.2887	1.0883
80.0	0.2107	1.1166
85.0	0.1328	1.1291
90.0	0.0520	1.1291

(b) $Re = 150\,000$

AoA	C_l	C_d
0.0	-0.0448	-0.0332
2.0	0.0730	-0.0301
4.0	0.2170	-0.0204
6.0	0.4205	0.0003
8.0	0.6249	0.0319
10.0	0.7161	0.0577
11.0	0.7364	0.0698
12.0	0.7477	0.0817
13.0	0.7493	0.0938
14.0	0.7404	0.1064
15.0	0.7480	0.1251
16.0	0.7151	0.1736
18.0	0.6806	0.2275
20.0	0.6754	0.2610
23.0	0.5268	0.2737
26.0	0.5122	0.3093
30.0	0.5128	0.3624
35.0	0.5658	0.4673
40.0	0.5976	0.5771
45.0	0.6062	0.6743
50.0	0.5889	0.7621
55.0	0.5514	0.8437
60.0	0.5052	0.9221
65.0	0.4388	0.9880
70.0	0.3637	1.0444
75.0	0.2887	1.0883
80.0	0.2107	1.1166
85.0	0.1328	1.1291
90.0	0.0520	1.1291

(c) $Re = 300\,000$

AoA	C_l	C_d
0.0	-0.0551	-0.0343
2.0	0.0829	-0.0321
4.0	0.2135	-0.0223
6.0	0.3557	-0.0058
8.0	0.5353	0.0172
10.0	0.7231	0.0559
11.0	0.8036	0.0755
12.0	0.8354	0.0884
13.0	0.8441	0.1033
14.0	0.8549	0.1192
15.0	0.8674	0.1366
16.0	0.8728	0.1552
17.0	0.7682	0.2069
18.0	0.6649	0.2338
20.0	0.7059	0.2774
23.2	0.6583	0.3142
26.0	0.5483	0.3224
30.0	0.5476	0.3805
35.0	0.5658	0.4673
40.0	0.5976	0.5771
45.0	0.6062	0.6743
50.0	0.5889	0.7621
55.0	0.5514	0.8437
60.0	0.5052	0.9221
65.0	0.4388	0.9880
70.0	0.3637	1.0444
75.0	0.2887	1.0883
80.0	0.2107	1.1166
85.0	0.1328	1.1291
90.0	0.0520	1.1291

Table A.3: NACA 0018 $A02\lambda09$ Uncorrected Experimental Aerodynamic Data.

(a) $Re = 75\,000$

AoA	C_l	C_d
0.0	0.0181	-0.0342
2.0	0.1200	-0.0309
6.0	0.5215	0.0045
8.0	0.6093	0.0282
10.0	0.6668	0.0495
11.0	0.6729	0.0607
12.0	0.6830	0.0713
13.0	0.6124	0.1186
14.0	0.5798	0.1383
15.0	0.5720	0.1507
16.0	0.5585	0.1605
17.0	0.5529	0.1714
18.0	0.5640	0.1863
19.0	0.5576	0.1980
20.0	0.6306	0.2424
23.0	0.4934	0.2408
26.0	0.4406	0.2675
30.0	0.4579	0.3193
35.0	0.5658	0.4673
40.0	0.5976	0.5771
45.0	0.6062	0.6743
50.0	0.5889	0.7621
55.0	0.5514	0.8437
60.0	0.5052	0.9221
65.0	0.4388	0.9880
70.0	0.3637	1.0444
75.0	0.2887	1.0883
80.0	0.2107	1.1166
85.0	0.1328	1.1291
90.0	0.0520	1.1291

(b) $Re = 150\,000$

AoA	C_l	C_d
0.0	0.0137	-0.0397
2.0	0.1304	-0.0358
6.0	0.4349	-0.0044
8.0	0.6279	0.0277
10.0	0.7083	0.0537
11.0	0.7390	0.0653
12.0	0.7710	0.0779
13.0	0.7979	0.0920
14.0	0.8153	0.1069
15.0	0.6226	0.1570
16.0	0.6224	0.1702
17.0	0.6221	0.1847
18.0	0.6190	0.2057
19.0	0.6221	0.2149
20.0	0.6189	0.2297
23.0	0.5075	0.2575
26.0	0.4996	0.2933
30.0	0.4864	0.3378
35.0	0.5658	0.4673
40.0	0.5976	0.5771
45.0	0.6062	0.6743
50.0	0.5889	0.7621
55.0	0.5514	0.8437
60.0	0.5052	0.9221
65.0	0.4388	0.9880
70.0	0.3637	1.0444
75.0	0.2887	1.0883
80.0	0.2107	1.1166
85.0	0.1328	1.1291
90.0	0.0520	1.1291

(c) $Re = 300\,000$

AoA	C_l	C_d
0.0	0.0091	-0.0410
2.0	0.1310	-0.0372
6.0	0.3884	-0.0093
8.0	0.5404	0.0188
10.0	0.7281	0.0540
11.0	0.7811	0.0743
12.0	0.8126	0.0899
13.0	0.8468	0.1065
14.0	0.8791	0.1240
15.0	0.8970	0.1403
16.0	0.9034	0.1601
17.0	0.6986	0.2104
18.0	0.6980	0.2245
19.0	0.6743	0.2366
20.0	0.6829	0.2519
23.0	0.6624	0.2987
26.0	0.5664	0.3138
30.0	0.5232	0.3614
35.0	0.5658	0.4673
40.0	0.5976	0.5771
45.0	0.6062	0.6743
50.0	0.5889	0.7621
55.0	0.5514	0.8437
60.0	0.5052	0.9221
65.0	0.4388	0.9880
70.0	0.3637	1.0444
75.0	0.2887	1.0883
80.0	0.2107	1.1166
85.0	0.1328	1.1291
90.0	0.0520	1.1291

Table A.4: NACA 0018 $A03\lambda11$ Uncorrected Experimental Aerodynamic Data.

(a) $Re = 75\,000$

AoA	C_l	C_d
0.0	0.0145	-0.0343
2.0	0.1201	-0.0277
6.0	0.6813	0.0178
8.0	0.7538	0.0423
10.0	0.8036	0.0686
11.0	0.8275	0.0851
12.0	0.8443	0.0993
13.0	0.8610	0.1180
14.0	0.8376	0.1488
15.0	0.7676	0.2005
16.0	0.7647	0.2162
17.0	0.7470	0.2323
18.0	0.7433	0.2513
20.0	0.7569	0.2913
23.0	0.5667	0.2876
26.0	0.5715	0.3469
30.0	0.5678	0.4031
35.0	0.5658	0.4673
40.0	0.5976	0.5771
45.0	0.6062	0.6743
50.0	0.5889	0.7621
55.0	0.5514	0.8437
60.0	0.5052	0.9221
65.0	0.4388	0.9880
70.0	0.3637	1.0444
75.0	0.2887	1.0883
80.0	0.2107	1.1166
85.0	0.1328	1.1291
90.0	0.0520	1.1291

(b) $Re = 150\,000$

AoA	C_l	C_d
0.0	-0.0013	-0.0384
2.0	0.1451	-0.0340
6.0	0.5545	0.0059
8.0	0.8029	0.0427
10.0	0.8967	0.0707
11.0	0.9228	0.0861
11.5	0.9346	0.0940
12.0	0.9513	0.1048
13.0	0.9625	0.1256
14.0	0.9561	0.1430
15.0	0.9396	0.1773
16.0	0.8542	0.2350
17.0	0.8623	0.2567
18.0	0.8508	0.2741
20.0	0.8388	0.3136
23.0	0.7878	0.3676
26.0	0.6263	0.3718
30.0	0.5893	0.4188
35.0	0.5658	0.4673
40.0	0.5976	0.5771
45.0	0.6062	0.6743
50.0	0.5889	0.7621
55.0	0.5514	0.8437
60.0	0.5052	0.9221
65.0	0.4388	0.9880
70.0	0.3637	1.0444
75.0	0.2887	1.0883
80.0	0.2107	1.1166
85.0	0.1328	1.1291
90.0	0.0520	1.1291

(c) $Re = 300\,000$

AoA	C_l	C_d
0.0	-0.0098	-0.0398
2.0	0.1503	-0.0357
6.0	0.4842	-0.0017
8.0	0.6915	0.0284
10.0	0.8962	0.0775
11.0	0.9616	0.0988
11.5	0.9805	0.1076
12.0	0.9968	0.1179
13.0	1.0126	0.1363
14.0	1.0448	0.1568
15.0	1.0935	0.1841
16.0	0.8641	0.2399
17.0	0.9328	0.2697
18.0	0.9329	0.2886
20.0	0.9062	0.3323
23.0	0.8410	0.3847
26.0	0.6491	0.3796
30.0	0.6321	0.3121
35.0	0.5658	0.4673
40.0	0.5976	0.5771
45.0	0.6062	0.6743
50.0	0.5889	0.7621
55.0	0.5514	0.8437
60.0	0.5052	0.9221
65.0	0.4388	0.9880
70.0	0.3637	1.0444
75.0	0.2887	1.0883
80.0	0.2107	1.1166
85.0	0.1328	1.1291
90.0	0.0520	1.1291

Table A.5: NACA 0018 $A04\lambda18$ Uncorrected Experimental Aerodynamic Data.

(a) $Re = 75\,000$

AoA	C_l	C_d
0.0	0.0014	-0.0238
2.0	0.0949	-0.0202
6.0	0.5342	0.0129
8.0	0.6018	0.0340
10.0	0.6476	0.0581
11.0	0.6421	0.0766
11.5	0.6044	0.0925
12.0	0.5739	0.0866
13.0	0.6203	0.1237
14.0	0.6302	0.1422
15.0	0.5588	0.1421
16.0	0.6044	0.1679
17.0	0.6143	0.1880
18.0	0.6304	0.2069
20.0	0.6194	0.2380
23.0	0.5806	0.2758
26.0	0.4530	0.2800
30.0	0.4486	0.3208
35.0	0.5658	0.4673
40.0	0.5976	0.5771
45.0	0.6062	0.6743
50.0	0.5889	0.7621
55.0	0.5514	0.8437
60.0	0.5052	0.9221
65.0	0.4388	0.9880
70.0	0.3637	1.0444
75.0	0.2887	1.0883
80.0	0.2107	1.1166
85.0	0.1328	1.1291
90.0	0.0520	1.1291

(b) $Re = 150\,000$

AoA	C_l	C_d
0.0	0.0005	-0.0301
2.0	0.1339	-0.0266
6.0	0.4747	0.0033
8.0	0.6901	0.0359
10.0	0.7583	0.0664
11.0	0.7748	0.0802
11.5	0.7832	0.0876
12.0	0.7930	0.0957
12.5	0.8010	0.1036
13.0	0.7858	0.1206
14.0	0.6257	0.1636
15.0	0.6348	0.1798
16.0	0.6172	0.1894
17.0	0.6309	0.2084
18.0	0.6409	0.2301
20.0	0.6176	0.2522
23.0	0.5998	0.2940
26.0	0.5271	0.3164
30.0	0.4987	0.3529
35.0	0.5658	0.4673
40.0	0.5976	0.5771
45.0	0.6062	0.6743
50.0	0.5889	0.7621
55.0	0.5514	0.8437
60.0	0.5052	0.9221
65.0	0.4388	0.9880
70.0	0.3637	1.0444
75.0	0.2887	1.0883
80.0	0.2107	1.1166
85.0	0.1328	1.1291
90.0	0.0520	1.1291

(c) $Re = 300\,000$

AoA	C_l	C_d
0.0	0.0059	-0.0310
2.0	0.1164	-0.0285
6.0	0.4110	-0.0029
8.0	0.5740	0.0227
10.0	0.7511	0.0598
11.0	0.8068	0.0767
11.5	0.8211	0.0839
12.0	0.8385	0.0913
12.5	0.8548	0.0989
13.0	0.8840	0.1105
14.0	0.9001	0.1280
16.0	0.8221	0.1830
18.0	0.7642	0.2363
20.0	0.6678	0.2785
23.0	0.7216	0.3341
26.0	0.6270	0.3496
30.0	0.5394	0.3721
35.0	0.5658	0.4673
40.0	0.5976	0.5771
45.0	0.6062	0.6743
50.0	0.5889	0.7621
55.0	0.5514	0.8437
60.0	0.5052	0.9221
65.0	0.4388	0.9880
70.0	0.3637	1.0444
75.0	0.2887	1.0883
80.0	0.2107	1.1166
85.0	0.1328	1.1291
90.0	0.0520	1.1291

Table A.6: NACA 0018 $A05\lambda13$ Uncorrected Experimental Aerodynamic Data.

(a) $Re = 75\,000$

AoA	C_l	C_d
0.0	0.0013	-0.0194
2.0	0.1287	-0.0152
6.0	0.6747	0.0251
8.0	0.7406	0.0498
10.0	0.7897	0.0766
11.0	0.8181	0.0923
11.5	0.8286	0.1004
12.0	0.8417	0.1095
12.5	0.8453	0.1188
13.0	0.8508	0.1276
13.5	0.8122	0.1494
14.0	0.7248	0.1907
14.5	0.7201	0.1984
15.0	0.7128	0.2044
16.0	0.7196	0.2224
17.0	0.7134	0.2414
18.0	0.7088	0.2582
20.0	0.6841	0.2877
23.0	0.6095	0.3073
26.0	0.5496	0.3277
30.0	0.5696	0.3860
35.0	0.5658	0.4673
40.0	0.5976	0.5771
45.0	0.6062	0.6743
50.0	0.5889	0.7621
55.0	0.5514	0.8437
60.0	0.5052	0.9221
65.0	0.4388	0.9880
70.0	0.3637	1.0444
75.0	0.2887	1.0883
80.0	0.2107	1.1166
85.0	0.1328	1.1291
90.0	0.0520	1.1291

(b) $Re = 150\,000$

AoA	C_l	C_d
0.0	0.0065	-0.0223
2.0	0.1567	-0.0186
6.0	0.5488	0.0141
8.0	0.7904	0.0508
10.0	0.8523	0.0792
11.0	0.8715	0.0937
11.5	0.8772	0.1012
12.0	0.8810	0.1088
12.5	0.8845	0.1168
13.0	0.8892	0.1258
13.5	0.8959	0.1357
14.0	0.9013	0.1461
15.0	0.6649	0.2094
16.0	0.6599	0.2268
17.0	0.8166	0.2347
18.0	0.7620	0.2678
20.0	0.7616	0.2999
23.0	0.6780	0.3242
26.0	0.5828	0.3410
30.0	0.5779	0.3909
35.0	0.5658	0.4673
40.0	0.5976	0.5771
45.0	0.6062	0.6743
50.0	0.5889	0.7621
55.0	0.5514	0.8437
60.0	0.5052	0.9221
65.0	0.4388	0.9880
70.0	0.3637	1.0444
75.0	0.2887	1.0883
80.0	0.2107	1.1166
85.0	0.1328	1.1291
90.0	0.0520	1.1291

(c) $Re = 300\,000$

AoA	C_l	C_d
0.0	-0.0038	-0.0238
2.0	0.1647	-0.0202
6.0	0.4901	0.0077
8.0	0.6964	0.0355
10.0	0.9206	0.0720
10.5	0.9698	0.0820
11.0	0.9978	0.0927
11.5	1.0113	0.1027
12.0	1.0266	0.1128
12.5	1.0341	0.1213
13.0	1.0486	0.1319
13.5	1.0130	0.1519
14.0	1.0108	0.1592
15.0	0.7215	0.2122
16.0	0.8801	0.2358
17.0	0.8280	0.2482
18.0	0.8355	0.2745
20.0	0.7754	0.3069
23.0	0.7357	0.3489
26.0	0.6485	0.3615
30.0	0.6092	0.4074
35.0	0.5658	0.4673
40.0	0.5976	0.5771
45.0	0.6062	0.6743
50.0	0.5889	0.7621
55.0	0.5514	0.8437
60.0	0.5052	0.9221
65.0	0.4388	0.9880
70.0	0.3637	1.0444
75.0	0.2887	1.0883
80.0	0.2107	1.1166
85.0	0.1328	1.1291
90.0	0.0520	1.1291

Table A.7: NACA 0018 $A06\lambda21$ Uncorrected Experimental Aerodynamic Data.

(a) $Re = 75\,000$

AoA	C_l	C_d
0.0	-0.0072	-0.0008
2.0	0.1188	0.0025
6.0	0.5672	0.0302
8.0	0.6402	0.0459
10.0	0.6921	0.0674
11.0	0.6864	0.0849
11.5	0.6502	0.0966
12.0	0.6482	0.1057
13.0	0.6554	0.1207
14.0	0.6473	0.1375
15.0	0.6670	0.1573
16.0	0.6782	0.1789
17.0	0.6914	0.2009
18.0	0.6984	0.2215
19.0	0.6883	0.2476
20.0	0.6951	0.2599
22.0	0.6438	0.2918
23.0	0.6343	0.3057
25.0	0.5816	0.3109
26.0	0.5283	0.3177
30.0	0.5027	0.3420
35.0	0.5658	0.4673
40.0	0.5976	0.5771
45.0	0.6062	0.6743
50.0	0.5889	0.7621
55.0	0.5514	0.8437
60.0	0.5052	0.9221
65.0	0.4388	0.9880
70.0	0.3637	1.0444
75.0	0.2887	1.0883
80.0	0.2107	1.1166
85.0	0.1328	1.1291
90.0	0.0520	1.1291

(b) $Re = 150\,000$

AoA	C_l	C_d
0.0	0.0085	0.0136
2.0	0.1607	0.0198
6.0	0.5273	0.0445
8.0	0.7813	0.0735
10.0	0.8784	0.1005
11.0	0.8960	0.0996
11.5	0.9064	0.1077
12.0	0.8586	0.1338
13.0	0.6822	0.1868
14.0	0.7234	0.2053
15.0	0.7154	0.2179
16.0	0.7182	0.2329
17.0	0.7657	0.2573
18.0	0.7855	0.2794
20.0	0.7824	0.3217
23.0	0.7295	0.3603
26.0	0.6903	0.3921
30.0	0.5911	0.4118
35.0	0.5658	0.4673
40.0	0.5976	0.5771
45.0	0.6062	0.6743
50.0	0.5889	0.7621
55.0	0.5514	0.8437
60.0	0.5052	0.9221
65.0	0.4388	0.9880
70.0	0.3637	1.0444
75.0	0.2887	1.0883
80.0	0.2107	1.1166
85.0	0.1328	1.1291
90.0	0.0520	1.1291

(c) $Re = 300\,000$

AoA	C_l	C_d
0.0	0.0003	0.0034
2.0	0.1683	0.0067
6.0	0.4854	0.0286
8.0	0.6671	0.0485
9.0	0.7683	0.0621
10.0	0.8751	0.0794
10.5	0.9160	0.0873
11.0	0.9443	0.0948
11.5	0.9691	0.1027
12.0	0.9836	0.1134
12.5	1.0112	0.1250
13.0	1.0257	0.1465
14.0	0.8125	0.1905
15.0	0.8426	0.2148
16.0	0.8052	0.2258
18.0	0.8498	0.2838
20.0	0.8334	0.3279
23.0	0.8054	0.3734
26.0	0.7862	0.4224
30.0	0.6122	0.4216
35.0	0.5658	0.4673
40.0	0.5976	0.5771
45.0	0.6062	0.6743
50.0	0.5889	0.7621
55.0	0.5514	0.8437
60.0	0.5052	0.9221
65.0	0.4388	0.9880
70.0	0.3637	1.0444
75.0	0.2887	1.0883
80.0	0.2107	1.1166
85.0	0.1328	1.1291
90.0	0.0520	1.1291

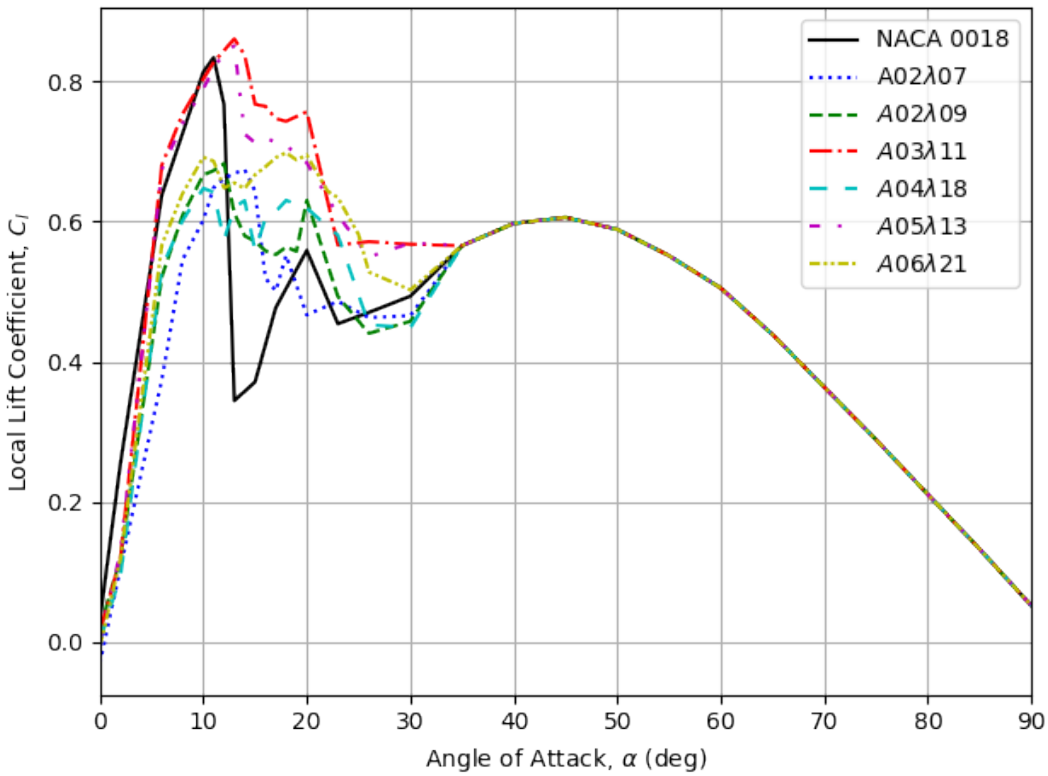

(a) C_l

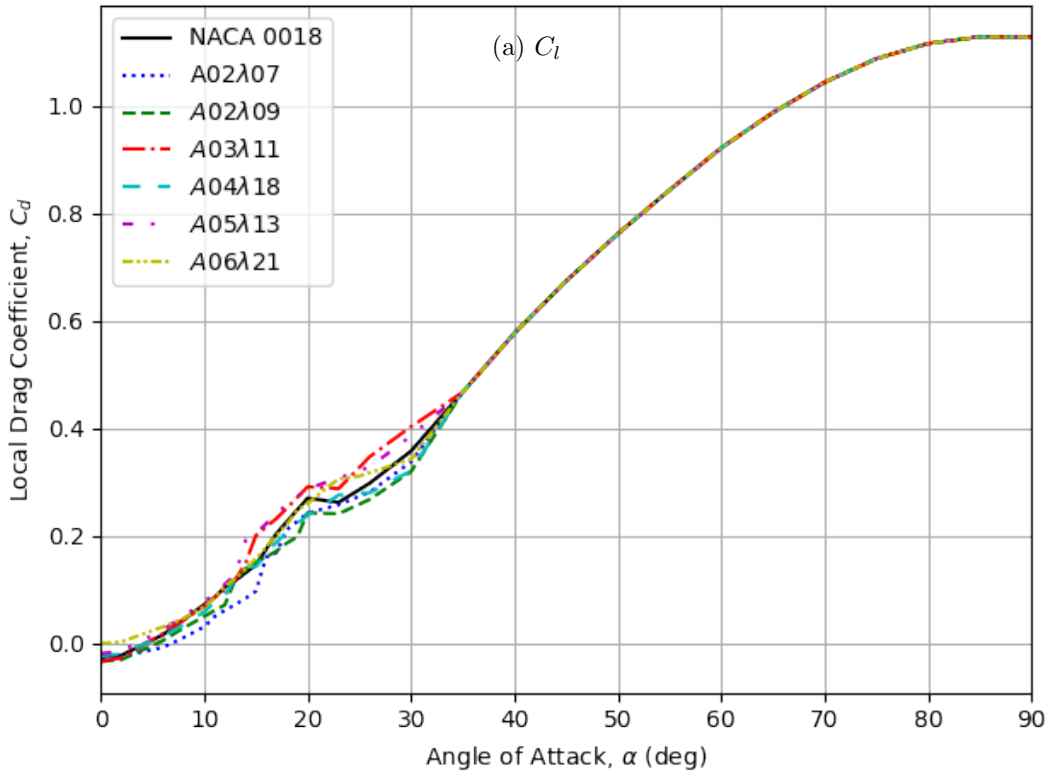

(b) C_d

Figure A.3: Uncorrected experimental lift and drag curves of the tubercle shapes at $Re = 75\,000$.

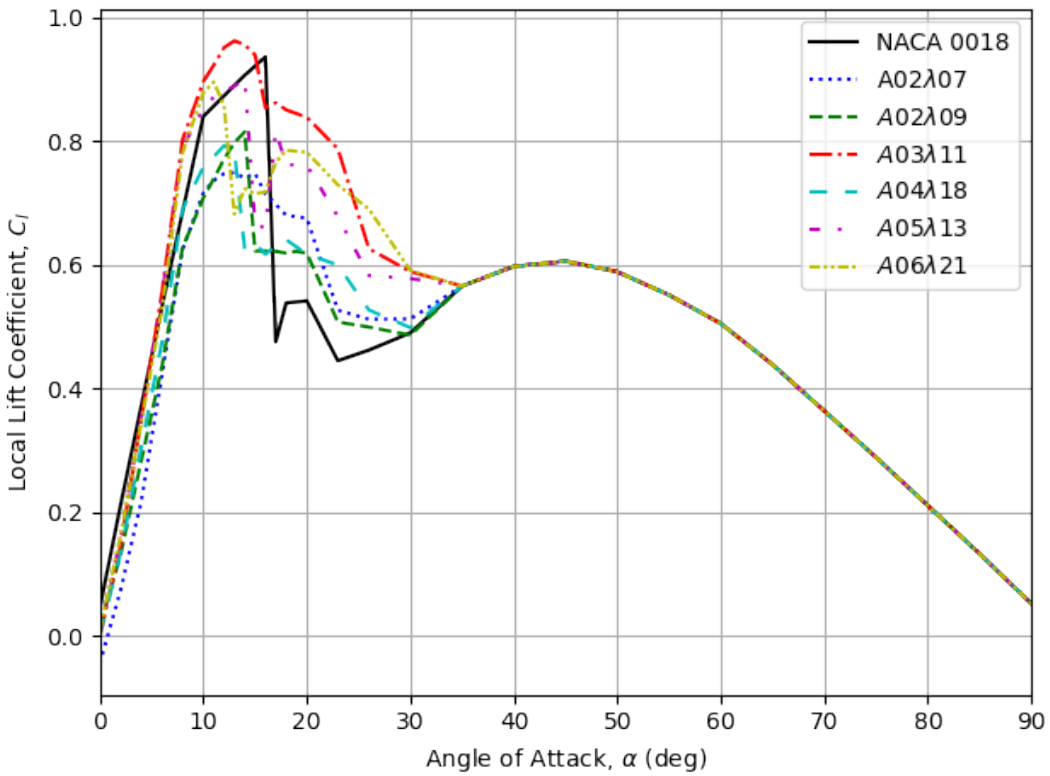

(a) C_l

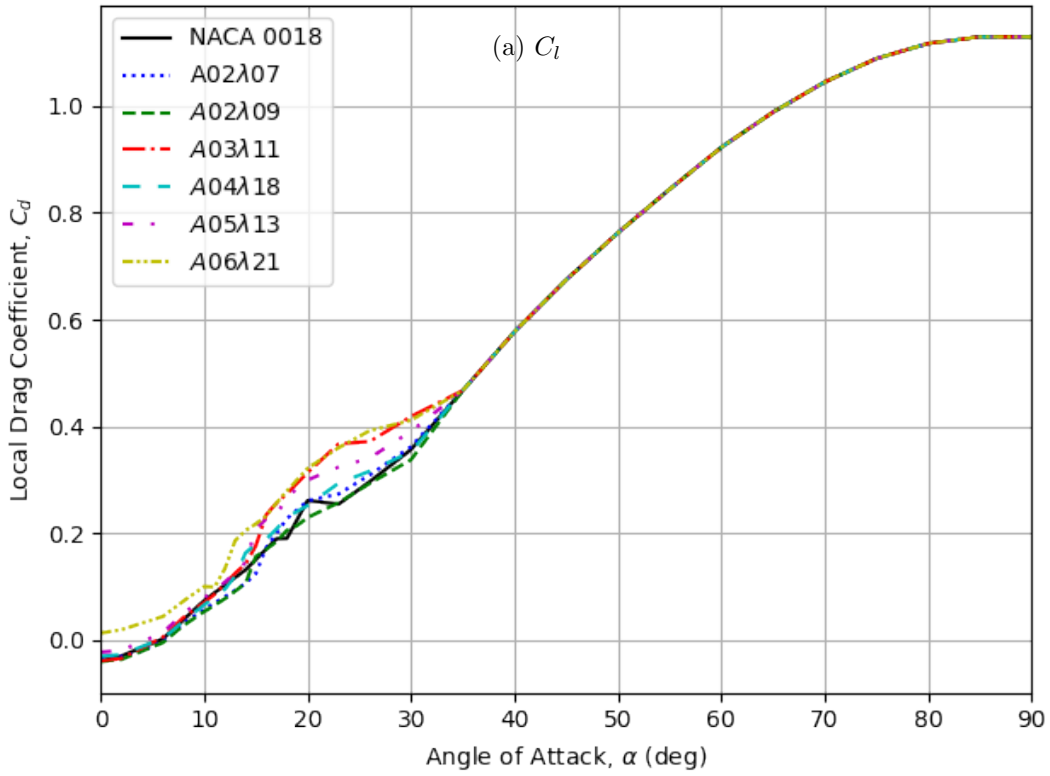

(b) C_d

Figure A.4: Uncorrected experimental lift and drag curves of the tubercle shapes at $Re = 150\,000$.

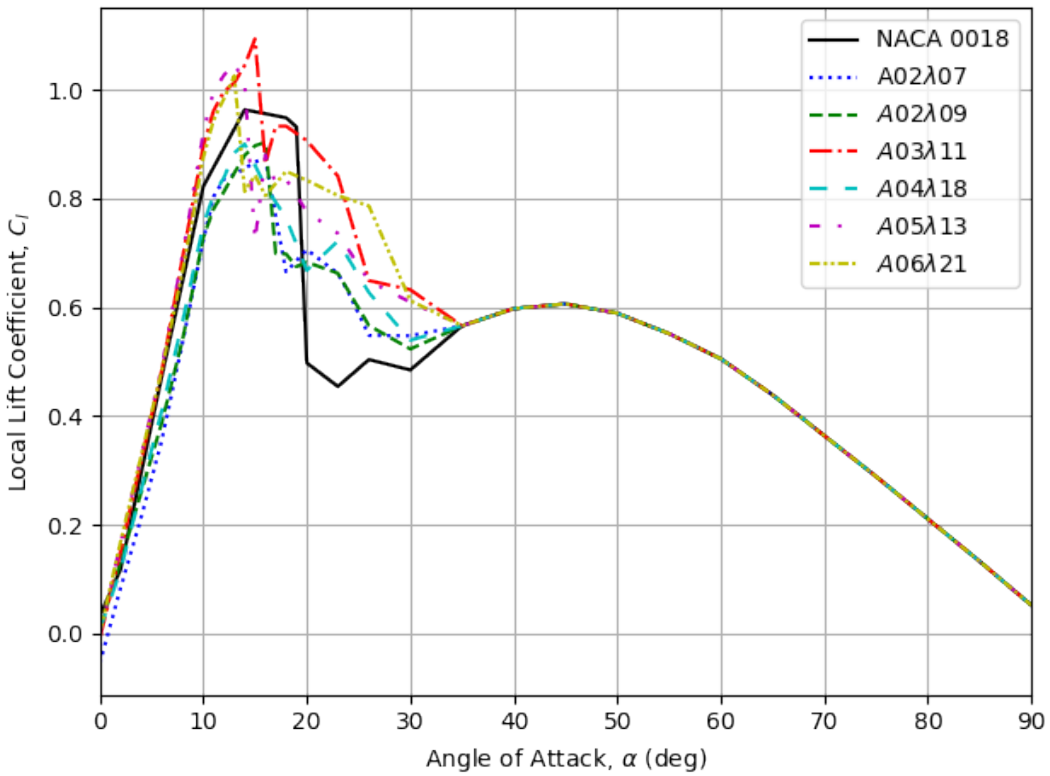

(a) C_l

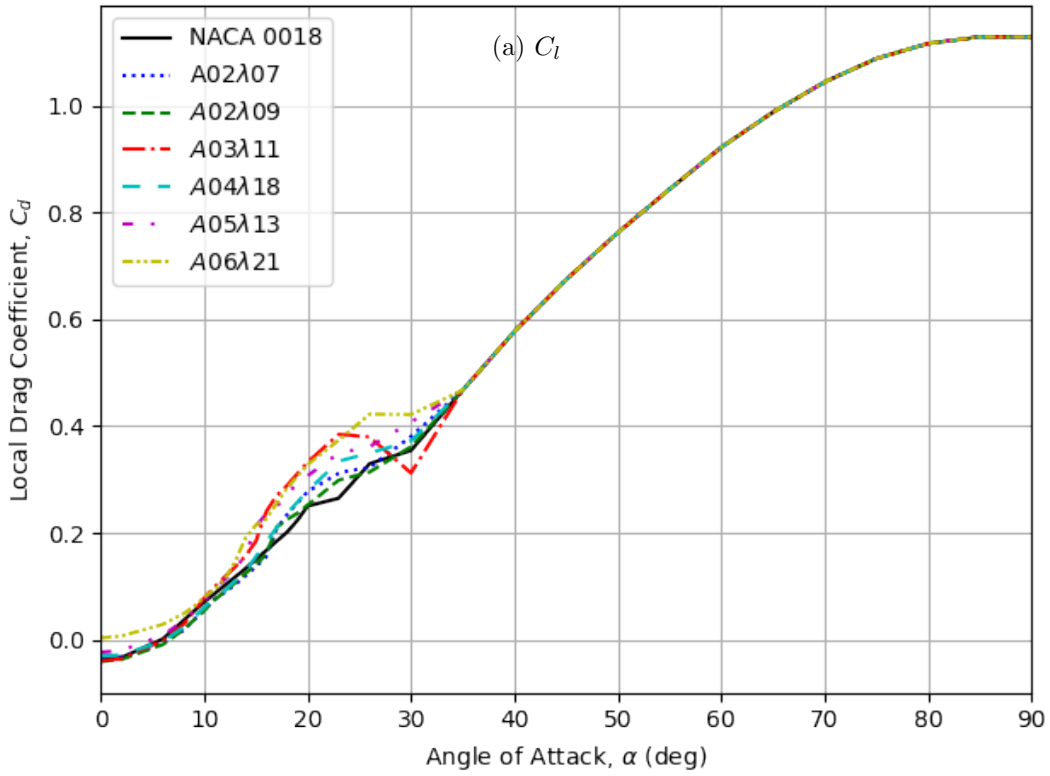

(b) C_d

Figure A.5: Uncorrected experimental lift and drag curves of the tubercle shapes at $Re = 300\,000$.

A.3 Corrected Data

Table A.8: NACA 0018 Corrected Experimental Aerodynamic Data.

(a) $Re = 75\,000$

AoA	C_l	C_d
0.0	0.0000	0.0162
1.0	0.0889	0.0163
2.0	0.1935	0.0167
3.0	0.2924	0.0172
4.0	0.3880	0.0181
5.0	0.4753	0.0192
6.0	0.5615	0.0206
7.0	0.6224	0.0223
8.0	0.7260	0.0435
9.0	0.7698	0.0576
10.0	0.8136	0.0717
11.0	0.8343	0.0852
12.0	0.7673	0.1041
13.0	0.3446	0.1162
14.0	0.3579	0.1309
15.0	0.3713	0.1456
16.0	0.4243	0.1750
17.0	0.4773	0.2044
18.0	0.5045	0.2262
19.0	0.5318	0.2480
20.0	0.5591	0.2699
21.0	0.5242	0.2673
22.0	0.4892	0.2647
23.0	0.4543	0.2621
24.0	0.4597	0.2739
25.0	0.4651	0.2858
26.0	0.4706	0.2977
27.0	0.4763	0.3126
30.0	0.4936	0.3575
35.0	0.5658	0.4673
40.0	0.5976	0.5771
45.0	0.6062	0.6743
50.0	0.5889	0.7621
55.0	0.5514	0.8437
60.0	0.5052	0.9221
65.0	0.4388	0.9880
70.0	0.3637	1.0444
75.0	0.2887	1.0883
80.0	0.2107	1.1166
85.0	0.1328	1.1291
90.0	0.0520	1.1291

(b) $Re = 150\,000$

AoA	C_l	C_d
0.0	0.0000	0.0110
1.0	0.1100	0.0129
2.0	0.2200	0.0131
3.0	0.3088	0.0137
4.0	0.4114	0.0144
5.0	0.5068	0.0153
6.0	0.5960	0.0166
7.0	0.6724	0.0181
8.0	0.7373	0.0198
9.0	0.7781	0.0217
10.0	0.7949	0.0238
11.0	0.8567	0.0888
12.0	0.8733	0.1031
13.0	0.8900	0.1175
14.0	0.9067	0.1318
15.0	0.9216	0.1514
16.0	0.9366	0.1709
17.0	0.4756	0.1901
18.0	0.5384	0.1906
19.0	0.5402	0.2260
20.0	0.5419	0.2615
21.0	0.5096	0.2592
22.0	0.4773	0.2570
23.0	0.4450	0.2548
24.0	0.4508	0.2688
25.0	0.4565	0.2827
26.0	0.4623	0.2966
27.0	0.4692	0.3116
30.0	0.4901	0.3569
35.0	0.5658	0.4673
40.0	0.5976	0.5771
45.0	0.6062	0.6743
50.0	0.5889	0.7621
55.0	0.5514	0.8437
60.0	0.5052	0.9221
65.0	0.4388	0.9880
70.0	0.3637	1.0444
75.0	0.2887	1.0883
80.0	0.2107	1.1166
85.0	0.1328	1.1291
90.0	0.0520	1.1291

(c) $Re = 300\,000$

AoA	C_l	C_d
0.0	0.0000	0.0101
1.0	0.1100	0.0102
2.0	0.2200	0.0104
3.0	0.3300	0.0107
4.0	0.4400	0.0112
5.0	0.5240	0.0121
6.0	0.6228	0.0132
7.0	0.7100	0.0145
8.0	0.7879	0.0159
9.0	0.8526	0.0176
10.0	0.8983	0.0194
11.0	0.9131	0.0215
12.0	0.9279	0.0235
13.0	0.9279	0.1174
14.0	0.9632	0.1331
15.0	0.9595	0.1501
16.0	0.9558	0.1671
17.0	0.9521	0.1841
18.0	0.9484	0.2011
19.0	0.9315	0.2230
20.0	0.4976	0.2502
21.0	0.4831	0.2551
22.0	0.4687	0.2599
23.0	0.4543	0.2648
24.0	0.4708	0.2864
25.0	0.4873	0.3080
26.0	0.5037	0.3296
27.0	0.4990	0.3358
30.0	0.4846	0.3543
35.0	0.5658	0.4673
40.0	0.5976	0.5771
45.0	0.6062	0.6743
50.0	0.5889	0.7621
55.0	0.5514	0.8437
60.0	0.5052	0.9221
65.0	0.4388	0.9880
70.0	0.3637	1.0444
75.0	0.2887	1.0883
80.0	0.2107	1.1166
85.0	0.1328	1.1291
90.0	0.0520	1.1291

Table A.9: NACA 0018 $A02\lambda07$ Corrected Experimental Aerodynamic Data.

(a) $Re = 75\,000$

AoA	C_l	C_d
0.0	-0.0606	0.0162
1.0	-0.0162	0.0162
2.0	0.0440	0.0162
3.0	0.1145	0.0162
4.0	0.1816	0.0162
5.0	0.2405	0.0162
6.0	0.2983	0.0162
7.0	0.4007	0.0162
8.0	0.5458	0.0102
9.0	0.5740	0.0203
10.0	0.6022	0.0304
11.0	0.6485	0.0492
12.0	0.6615	0.0610
13.0	0.6691	0.0716
14.0	0.6741	0.0834
15.0	0.6438	0.0968
16.0	0.5196	0.1601
17.0	0.5012	0.1688
18.0	0.5520	0.2114
19.0	0.5095	0.2267
20.0	0.4669	0.2420
21.0	0.4734	0.2472
22.0	0.4799	0.2524
23.0	0.4864	0.2576
24.0	0.4786	0.2654
25.0	0.4709	0.2733
26.0	0.4631	0.2811
27.0	0.4638	0.2952
30.0	0.4659	0.3374
35.0	0.5658	0.4673
40.0	0.5976	0.5771
45.0	0.6062	0.6743
50.0	0.5889	0.7621
55.0	0.5514	0.8437
60.0	0.5052	0.9221
65.0	0.4388	0.9880
70.0	0.3637	1.0444
75.0	0.2887	1.0883
80.0	0.2107	1.1166
85.0	0.1328	1.1291
90.0	0.0520	1.1291

(b) $Re = 150\,000$

AoA	C_l	C_d
0.0	-0.0893	0.0163
1.0	-0.0036	0.0152
2.0	0.0820	0.0124
3.0	0.1626	0.0110
4.0	0.2569	0.0110
5.0	0.3738	0.0110
6.0	0.4845	0.0142
7.0	0.5861	0.0136
8.0	0.6762	0.0132
9.0	0.6856	0.0110
10.0	0.6710	0.0110
11.0	0.7364	0.0698
12.0	0.7477	0.0817
13.0	0.7493	0.0938
14.0	0.7404	0.1064
15.0	0.7480	0.1251
16.0	0.7151	0.1736
17.0	0.6978	0.2006
18.0	0.6806	0.2275
19.0	0.6780	0.2442
20.0	0.6754	0.2610
21.0	0.6258	0.2652
22.0	0.5763	0.2695
23.0	0.5268	0.2737
24.0	0.5219	0.2855
25.0	0.5170	0.2974
26.0	0.5122	0.3093
27.0	0.5123	0.3226
30.0	0.5128	0.3624
35.0	0.5658	0.4673
40.0	0.5976	0.5771
45.0	0.6062	0.6743
50.0	0.5889	0.7621
55.0	0.5514	0.8437
60.0	0.5052	0.9221
65.0	0.4388	0.9880
70.0	0.3637	1.0444
75.0	0.2887	1.0883
80.0	0.2107	1.1166
85.0	0.1328	1.1291
90.0	0.0520	1.1291

(c) $Re = 300\,000$

AoA	C_l	C_d
0.0	-0.0872	0.0118
1.0	0.0491	0.0119
2.0	0.1853	0.0120
3.0	0.2717	0.0101
4.0	0.3580	0.0101
5.0	0.4242	0.0101
6.0	0.5051	0.0101
7.0	0.5950	0.0101
8.0	0.6755	0.0101
9.0	0.7469	0.0101
10.0	0.7994	0.0101
11.0	0.8594	0.0110
12.0	0.8706	0.0101
13.0	0.8441	0.1033
14.0	0.8549	0.1192
15.0	0.8674	0.1366
16.0	0.8728	0.1552
17.0	0.7682	0.2069
18.0	0.6649	0.2338
19.0	0.6854	0.2556
20.0	0.7059	0.2774
21.0	0.6912	0.2887
22.0	0.6766	0.3000
23.0	0.6620	0.3114
24.0	0.6283	0.3164
25.0	0.5883	0.3194
26.0	0.5483	0.3224
27.0	0.5481	0.3369
30.0	0.5476	0.3805
35.0	0.5658	0.4673
40.0	0.5976	0.5771
45.0	0.6062	0.6743
50.0	0.5889	0.7621
55.0	0.5514	0.8437
60.0	0.5052	0.9221
65.0	0.4388	0.9880
70.0	0.3637	1.0444
75.0	0.2887	1.0883
80.0	0.2107	1.1166
85.0	0.1328	1.1291
90.0	0.0520	1.1291

Table A.10: NACA 0018 $A02\lambda09$ Corrected Experimental Aerodynamic Data.

(a) $Re = 75\,000$

AoA	C_l	C_d
0.0	-0.0120	0.0162
1.0	0.0152	0.0162
2.0	0.0580	0.0162
3.0	0.1616	0.0162
4.0	0.2618	0.0162
5.0	0.3538	0.0162
6.0	0.4446	0.0162
7.0	0.5056	0.0162
8.0	0.6093	0.0282
9.0	0.6381	0.0389
10.0	0.6668	0.0495
11.0	0.6729	0.0607
12.0	0.6830	0.0713
13.0	0.6124	0.1186
14.0	0.5798	0.1383
15.0	0.5720	0.1507
16.0	0.5585	0.1605
17.0	0.5529	0.1714
18.0	0.5640	0.1863
19.0	0.5576	0.1980
20.0	0.6306	0.2424
21.0	0.5848	0.2419
22.0	0.5391	0.2413
23.0	0.4934	0.2408
24.0	0.4758	0.2497
25.0	0.4582	0.2586
26.0	0.4406	0.2675
27.0	0.4449	0.2805
30.0	0.4579	0.3193
35.0	0.5658	0.4673
40.0	0.5976	0.5771
45.0	0.6062	0.6743
50.0	0.5889	0.7621
55.0	0.5514	0.8437
60.0	0.5052	0.9221
65.0	0.4388	0.9880
70.0	0.3637	1.0444
75.0	0.2887	1.0883
80.0	0.2107	1.1166
85.0	0.1328	1.1291
90.0	0.0520	1.1291

(b) $Re = 150\,000$

AoA	C_l	C_d
0.0	-0.0308	0.0110
1.0	0.0543	0.0110
2.0	0.1394	0.0110
3.0	0.2240	0.0110
4.0	0.3225	0.0110
5.0	0.4138	0.0110
6.0	0.4989	0.0110
7.0	0.5948	0.0110
8.0	0.6792	0.0110
9.0	0.6832	0.0110
10.0	0.6633	0.0110
11.0	0.7390	0.0653
12.0	0.7710	0.0779
13.0	0.7979	0.0920
14.0	0.8153	0.1069
15.0	0.6226	0.1570
16.0	0.6224	0.1702
17.0	0.6221	0.1847
18.0	0.6190	0.2057
19.0	0.6221	0.2149
20.0	0.6189	0.2297
21.0	0.5818	0.2390
22.0	0.5446	0.2482
23.0	0.5075	0.2575
24.0	0.5049	0.2695
25.0	0.5022	0.2814
26.0	0.4996	0.2933
27.0	0.4963	0.3045
30.0	0.4864	0.3378
35.0	0.5658	0.4673
40.0	0.5976	0.5771
45.0	0.6062	0.6743
50.0	0.5889	0.7621
55.0	0.5514	0.8437
60.0	0.5052	0.9221
65.0	0.4388	0.9880
70.0	0.3637	1.0444
75.0	0.2887	1.0883
80.0	0.2107	1.1166
85.0	0.1328	1.1291
90.0	0.0520	1.1291

(c) $Re = 300\,000$

AoA	C_l	C_d
0.0	-0.0230	0.0101
1.0	0.1052	0.0101
2.0	0.2334	0.0101
3.0	0.3188	0.0101
4.0	0.4042	0.0101
5.0	0.4636	0.0101
6.0	0.5378	0.0101
7.0	0.6139	0.0101
8.0	0.6806	0.0101
9.0	0.7519	0.0101
10.0	0.8043	0.0101
11.0	0.8368	0.0101
12.0	0.8479	0.0116
13.0	0.8468	0.1065
14.0	0.8791	0.1240
15.0	0.8970	0.1403
16.0	0.9034	0.1601
17.0	0.6986	0.2104
18.0	0.6980	0.2245
19.0	0.6743	0.2366
20.0	0.6829	0.2519
21.0	0.6760	0.2675
22.0	0.6692	0.2831
23.0	0.6624	0.2987
24.0	0.6304	0.3037
25.0	0.5984	0.3088
26.0	0.5664	0.3138
27.0	0.5556	0.3257
30.0	0.5232	0.3614
35.0	0.5658	0.4673
40.0	0.5976	0.5771
45.0	0.6062	0.6743
50.0	0.5889	0.7621
55.0	0.5514	0.8437
60.0	0.5052	0.9221
65.0	0.4388	0.9880
70.0	0.3637	1.0444
75.0	0.2887	1.0883
80.0	0.2107	1.1166
85.0	0.1328	1.1291
90.0	0.0520	1.1291

Table A.11: NACA 0018 $A03\lambda11$ Corrected Experimental Aerodynamic Data.

(a) $Re = 75\,000$

AoA	C_l	C_d
0.0	-0.0156	0.0162
1.0	0.0134	0.0162
2.0	0.0581	0.0162
3.0	0.2015	0.0162
4.0	0.3417	0.0168
5.0	0.4736	0.0198
6.0	0.6043	0.0231
7.0	0.6577	0.0229
8.0	0.7538	0.0423
9.0	0.7787	0.0554
10.0	0.8036	0.0686
11.0	0.8275	0.0851
12.0	0.8443	0.0993
13.0	0.8610	0.1180
14.0	0.8376	0.1488
15.0	0.7676	0.2005
16.0	0.7647	0.2162
17.0	0.7470	0.2323
18.0	0.7433	0.2513
19.0	0.7501	0.2713
20.0	0.7569	0.2913
21.0	0.6935	0.2901
22.0	0.6301	0.2889
23.0	0.5667	0.2876
24.0	0.5683	0.3074
25.0	0.5699	0.3271
26.0	0.5715	0.3469
27.0	0.5706	0.3609
30.0	0.5678	0.4031
35.0	0.5658	0.4673
40.0	0.5976	0.5771
45.0	0.6062	0.6743
50.0	0.5889	0.7621
55.0	0.5514	0.8437
60.0	0.5052	0.9221
65.0	0.4388	0.9880
70.0	0.3637	1.0444
75.0	0.2887	1.0883
80.0	0.2107	1.1166
85.0	0.1328	1.1291
90.0	0.0520	1.1291

(b) $Re = 150\,000$

AoA	C_l	C_d
0.0	-0.0458	0.0111
1.0	0.0541	0.0110
2.0	0.1540	0.0110
3.0	0.2650	0.0111
4.0	0.3897	0.0137
5.0	0.5072	0.0166
6.0	0.6185	0.0198
7.0	0.7421	0.0218
8.0	0.8542	0.0240
9.0	0.8649	0.0219
10.0	0.8517	0.0200
11.0	0.9228	0.0861
12.0	0.9513	0.1048
13.0	0.9625	0.1256
14.0	0.9561	0.1430
15.0	0.9396	0.1773
16.0	0.8542	0.2350
17.0	0.8623	0.2567
18.0	0.8508	0.2741
19.0	0.8448	0.2939
20.0	0.8388	0.3136
21.0	0.8218	0.3317
22.0	0.8048	0.3496
23.0	0.7878	0.3676
24.0	0.7339	0.3690
25.0	0.6801	0.3704
26.0	0.6263	0.3718
27.0	0.6170	0.3836
30.0	0.5893	0.4188
35.0	0.5658	0.4673
40.0	0.5976	0.5771
45.0	0.6062	0.6743
50.0	0.5889	0.7621
55.0	0.5514	0.8437
60.0	0.5052	0.9221
65.0	0.4388	0.9880
70.0	0.3637	1.0444
75.0	0.2887	1.0883
80.0	0.2107	1.1166
85.0	0.1328	1.1291
90.0	0.0520	1.1291

(c) $Re = 300\,000$

AoA	C_l	C_d
0.0	-0.0419	0.0101
1.0	0.1054	0.0101
2.0	0.2526	0.0101
3.0	0.3572	0.0101
4.0	0.4617	0.0101
5.0	0.5403	0.0101
6.0	0.6337	0.0103
7.0	0.7373	0.0101
8.0	0.8317	0.0101
9.0	0.9116	0.0175
10.0	0.9724	0.0266
11.0	1.0173	0.0343
12.0	1.0320	0.0396
13.0	1.0126	0.1363
14.0	1.0448	0.1568
15.0	1.0935	0.1841
16.0	0.8641	0.2399
17.0	0.9328	0.2697
18.0	0.9329	0.2886
19.0	0.9195	0.3104
20.0	0.9062	0.3323
21.0	0.8845	0.3497
22.0	0.8627	0.3672
23.0	0.8410	0.3847
24.0	0.7770	0.3830
25.0	0.7130	0.3813
26.0	0.6491	0.3796
27.0	0.6448	0.3627
30.0	0.6321	0.3121
35.0	0.5658	0.4673
40.0	0.5976	0.5771
45.0	0.6062	0.6743
50.0	0.5889	0.7621
55.0	0.5514	0.8437
60.0	0.5052	0.9221
65.0	0.4388	0.9880
70.0	0.3637	1.0444
75.0	0.2887	1.0883
80.0	0.2107	1.1166
85.0	0.1328	1.1291
90.0	0.0520	1.1291

Table A.12: NACA 0018 $A04\lambda18$ Corrected Experimental Aerodynamic Data.

(a) $Re = 75\,000$

AoA	C_l	C_d
0.0	-0.0288	0.0183
1.0	-0.0058	0.0186
2.0	0.0329	0.0192
3.0	0.1459	0.0185
4.0	0.2556	0.0181
5.0	0.3570	0.0180
6.0	0.4572	0.0182
7.0	0.5081	0.0163
8.0	0.6018	0.0340
9.0	0.6247	0.0460
10.0	0.6476	0.0581
11.0	0.6421	0.0766
12.0	0.5739	0.0866
13.0	0.6203	0.1237
14.0	0.6302	0.1422
15.0	0.5588	0.1421
16.0	0.6044	0.1679
17.0	0.6143	0.1880
18.0	0.6304	0.2069
19.0	0.6249	0.2224
20.0	0.6194	0.2380
21.0	0.6064	0.2506
22.0	0.5935	0.2632
23.0	0.5806	0.2758
24.0	0.5381	0.2772
25.0	0.4956	0.2786
26.0	0.4530	0.2800
27.0	0.4519	0.2902
30.0	0.4486	0.3208
35.0	0.5658	0.4673
40.0	0.5976	0.5771
45.0	0.6062	0.6743
50.0	0.5889	0.7621
55.0	0.5514	0.8437
60.0	0.5052	0.9221
65.0	0.4388	0.9880
70.0	0.3637	1.0444
75.0	0.2887	1.0883
80.0	0.2107	1.1166
85.0	0.1328	1.1291
90.0	0.0520	1.1291

(b) $Re = 150\,000$

AoA	C_l	C_d
0.0	-0.0440	0.0194
1.0	0.0494	0.0185
2.0	0.1429	0.0159
3.0	0.2366	0.0160
4.0	0.3442	0.0161
5.0	0.4445	0.0165
6.0	0.5387	0.0172
7.0	0.6458	0.0171
8.0	0.7414	0.0171
9.0	0.7393	0.0163
10.0	0.7132	0.0158
11.0	0.7748	0.0802
12.0	0.7930	0.0957
13.0	0.7858	0.1206
14.0	0.6257	0.1636
15.0	0.6348	0.1798
16.0	0.6172	0.1894
17.0	0.6309	0.2084
18.0	0.6409	0.2301
19.0	0.6292	0.2412
20.0	0.6176	0.2522
21.0	0.6117	0.2661
22.0	0.6057	0.2800
23.0	0.5998	0.2940
24.0	0.5756	0.3014
25.0	0.5513	0.3089
26.0	0.5271	0.3164
27.0	0.5200	0.3255
30.0	0.4987	0.3529
35.0	0.5658	0.4673
40.0	0.5976	0.5771
45.0	0.6062	0.6743
50.0	0.5889	0.7621
55.0	0.5514	0.8437
60.0	0.5052	0.9221
65.0	0.4388	0.9880
70.0	0.3637	1.0444
75.0	0.2887	1.0883
80.0	0.2107	1.1166
85.0	0.1328	1.1291
90.0	0.0520	1.1291

(c) $Re = 300\,000$

AoA	C_l	C_d
0.0	-0.0262	0.0152
1.0	0.0962	0.0153
2.0	0.2187	0.0156
3.0	0.3134	0.0136
4.0	0.4081	0.0118
5.0	0.4769	0.0104
6.0	0.5604	0.0101
7.0	0.6419	0.0101
8.0	0.7142	0.0101
9.0	0.7803	0.0101
10.0	0.8273	0.0101
11.0	0.8626	0.0122
12.0	0.8737	0.0131
13.0	0.8840	0.1105
14.0	0.9001	0.1280
15.0	0.8611	0.1555
16.0	0.8221	0.1830
17.0	0.7931	0.2097
18.0	0.7642	0.2363
19.0	0.7160	0.2574
20.0	0.6678	0.2785
21.0	0.6857	0.2970
22.0	0.7037	0.3156
23.0	0.7216	0.3341
24.0	0.6901	0.3393
25.0	0.6585	0.3444
26.0	0.6270	0.3496
27.0	0.6051	0.3552
30.0	0.5394	0.3721
35.0	0.5658	0.4673
40.0	0.5976	0.5771
45.0	0.6062	0.6743
50.0	0.5889	0.7621
55.0	0.5514	0.8437
60.0	0.5052	0.9221
65.0	0.4388	0.9880
70.0	0.3637	1.0444
75.0	0.2887	1.0883
80.0	0.2107	1.1166
85.0	0.1328	1.1291
90.0	0.0520	1.1291

Table A.13: NACA 0018 $A05\lambda13$ Corrected Experimental Aerodynamic Data.

(a) $Re = 75\,000$

AoA	C_l	C_d
0.0	-0.0288	0.0227
1.0	0.0111	0.0233
2.0	0.0668	0.0243
3.0	0.2064	0.0253
4.0	0.3428	0.0267
5.0	0.4708	0.0284
6.0	0.5978	0.0303
7.0	0.6478	0.0303
8.0	0.7406	0.0498
9.0	0.7651	0.0632
10.0	0.7897	0.0766
11.0	0.8181	0.0923
12.0	0.8417	0.1095
13.0	0.8508	0.1276
14.0	0.7248	0.1907
15.0	0.7128	0.2044
16.0	0.7196	0.2224
17.0	0.7134	0.2414
18.0	0.7088	0.2582
19.0	0.6965	0.2730
20.0	0.6841	0.2877
21.0	0.6592	0.2942
22.0	0.6344	0.3007
23.0	0.6095	0.3073
24.0	0.5895	0.3141
25.0	0.5696	0.3209
26.0	0.5496	0.3277
27.0	0.5546	0.3423
30.0	0.5696	0.3860
35.0	0.5658	0.4673
40.0	0.5976	0.5771
45.0	0.6062	0.6743
50.0	0.5889	0.7621
55.0	0.5514	0.8437
60.0	0.5052	0.9221
65.0	0.4388	0.9880
70.0	0.3637	1.0444
75.0	0.2887	1.0883
80.0	0.2107	1.1166
85.0	0.1328	1.1291
90.0	0.0520	1.1291

(b) $Re = 150\,000$

AoA	C_l	C_d
0.0	-0.0380	0.0273
1.0	0.0638	0.0264
2.0	0.1656	0.0239
3.0	0.2722	0.0246
4.0	0.3926	0.0255
5.0	0.5058	0.0266
6.0	0.6128	0.0280
7.0	0.7330	0.0299
8.0	0.8417	0.0320
9.0	0.8364	0.0302
10.0	0.8072	0.0286
11.0	0.8715	0.0937
12.0	0.8810	0.1088
13.0	0.8892	0.1258
14.0	0.9013	0.1461
15.0	0.6649	0.2094
16.0	0.6599	0.2268
17.0	0.8166	0.2347
18.0	0.7620	0.2678
19.0	0.7618	0.2839
20.0	0.7616	0.2999
21.0	0.7337	0.3080
22.0	0.7059	0.3161
23.0	0.6780	0.3242
24.0	0.6463	0.3298
25.0	0.6145	0.3354
26.0	0.5828	0.3410
27.0	0.5816	0.3535
30.0	0.5779	0.3909
35.0	0.5658	0.4673
40.0	0.5976	0.5771
45.0	0.6062	0.6743
50.0	0.5889	0.7621
55.0	0.5514	0.8437
60.0	0.5052	0.9221
65.0	0.4388	0.9880
70.0	0.3637	1.0444
75.0	0.2887	1.0883
80.0	0.2107	1.1166
85.0	0.1328	1.1291
90.0	0.0520	1.1291

(c) $Re = 300\,000$

AoA	C_l	C_d
0.0	-0.0359	0.0224
1.0	0.1156	0.0231
2.0	0.2671	0.0239
3.0	0.3695	0.0224
4.0	0.4719	0.0212
5.0	0.5483	0.0204
6.0	0.6395	0.0197
7.0	0.7427	0.0176
8.0	0.8366	0.0156
9.0	0.9262	0.0183
10.0	0.9968	0.0211
11.0	1.0535	0.0282
12.0	1.0619	0.0345
13.0	1.0486	0.1319
14.0	1.0108	0.1592
15.0	0.7215	0.2122
16.0	0.8801	0.2358
17.0	0.8280	0.2482
18.0	0.8355	0.2745
19.0	0.8055	0.2907
20.0	0.7754	0.3069
21.0	0.7622	0.3209
22.0	0.7490	0.3349
23.0	0.7357	0.3489
24.0	0.7066	0.3531
25.0	0.6776	0.3573
26.0	0.6485	0.3615
27.0	0.6387	0.3729
30.0	0.6092	0.4074
35.0	0.5658	0.4673
40.0	0.5976	0.5771
45.0	0.6062	0.6743
50.0	0.5889	0.7621
55.0	0.5514	0.8437
60.0	0.5052	0.9221
65.0	0.4388	0.9880
70.0	0.3637	1.0444
75.0	0.2887	1.0883
80.0	0.2107	1.1166
85.0	0.1328	1.1291
90.0	0.0520	1.1291

Table A.14: NACA 0018 $A06\lambda21$ Corrected Experimental Aerodynamic Data.

(a) $Re = 75\,000$

AoA	C_l	C_d
0.0	-0.0373	0.0414
1.0	0.0019	0.0415
2.0	0.0569	0.0419
3.0	0.1721	0.0399
4.0	0.2840	0.0382
5.0	0.3877	0.0367
6.0	0.4902	0.0355
7.0	0.5439	0.0310
8.0	0.6402	0.0459
9.0	0.6662	0.0567
10.0	0.6921	0.0674
11.0	0.6864	0.0849
12.0	0.6482	0.1057
13.0	0.6554	0.1207
14.0	0.6473	0.1375
15.0	0.6670	0.1573
16.0	0.6782	0.1789
17.0	0.6914	0.2009
18.0	0.6984	0.2215
19.0	0.6883	0.2476
20.0	0.6951	0.2599
21.0	0.6695	0.2759
22.0	0.6438	0.2918
23.0	0.6343	0.3057
24.0	0.6080	0.3083
25.0	0.5816	0.3109
26.0	0.5283	0.3177
27.0	0.5219	0.3238
30.0	0.5027	0.3420
35.0	0.5658	0.4673
40.0	0.5976	0.5771
45.0	0.6062	0.6743
50.0	0.5889	0.7621
55.0	0.5514	0.8437
60.0	0.5052	0.9221
65.0	0.4388	0.9880
70.0	0.3637	1.0444
75.0	0.2887	1.0883
80.0	0.2107	1.1166
85.0	0.1328	1.1291
90.0	0.0520	1.1291

(b) $Re = 150\,000$

AoA	C_l	C_d
0.0	-0.0360	0.0632
1.0	0.0668	0.0636
2.0	0.1696	0.0624
3.0	0.2699	0.0611
4.0	0.3839	0.0599
5.0	0.4907	0.0590
6.0	0.5913	0.0584
7.0	0.7177	0.0565
8.0	0.8326	0.0547
9.0	0.8450	0.0522
10.0	0.8333	0.0499
11.0	0.8960	0.0996
12.0	0.8586	0.1338
13.0	0.6822	0.1868
14.0	0.7234	0.2053
15.0	0.7154	0.2179
16.0	0.7182	0.2329
17.0	0.7657	0.2573
18.0	0.7855	0.2794
19.0	0.7839	0.3005
20.0	0.7824	0.3217
21.0	0.7648	0.3346
22.0	0.7471	0.3475
23.0	0.7295	0.3603
24.0	0.7164	0.3709
25.0	0.7033	0.3815
26.0	0.6903	0.3921
27.0	0.6655	0.3971
30.0	0.5911	0.4118
35.0	0.5658	0.4673
40.0	0.5976	0.5771
45.0	0.6062	0.6743
50.0	0.5889	0.7621
55.0	0.5514	0.8437
60.0	0.5052	0.9221
65.0	0.4388	0.9880
70.0	0.3637	1.0444
75.0	0.2887	1.0883
80.0	0.2107	1.1166
85.0	0.1328	1.1291
90.0	0.0520	1.1291

(c) $Re = 300\,000$

AoA	C_l	C_d
0.0	-0.0317	0.0496
1.0	0.1194	0.0501
2.0	0.2706	0.0508
3.0	0.3710	0.0478
4.0	0.4713	0.0451
5.0	0.5457	0.0428
6.0	0.6348	0.0407
7.0	0.7257	0.0346
8.0	0.8073	0.0287
9.0	0.8860	0.0266
10.0	0.9513	0.0284
11.0	1.0001	0.0303
12.0	1.0189	0.0352
13.0	1.0257	0.1465
14.0	0.8125	0.1905
15.0	0.8426	0.2148
16.0	0.8052	0.2258
17.0	0.8275	0.2548
18.0	0.8498	0.2838
19.0	0.8416	0.3059
20.0	0.8334	0.3279
21.0	0.8240	0.3430
22.0	0.8147	0.3582
23.0	0.8054	0.3734
24.0	0.7990	0.3897
25.0	0.7926	0.4060
26.0	0.7862	0.4224
27.0	0.7427	0.4222
30.0	0.6122	0.4216
35.0	0.5658	0.4673
40.0	0.5976	0.5771
45.0	0.6062	0.6743
50.0	0.5889	0.7621
55.0	0.5514	0.8437
60.0	0.5052	0.9221
65.0	0.4388	0.9880
70.0	0.3637	1.0444
75.0	0.2887	1.0883
80.0	0.2107	1.1166
85.0	0.1328	1.1291
90.0	0.0520	1.1291

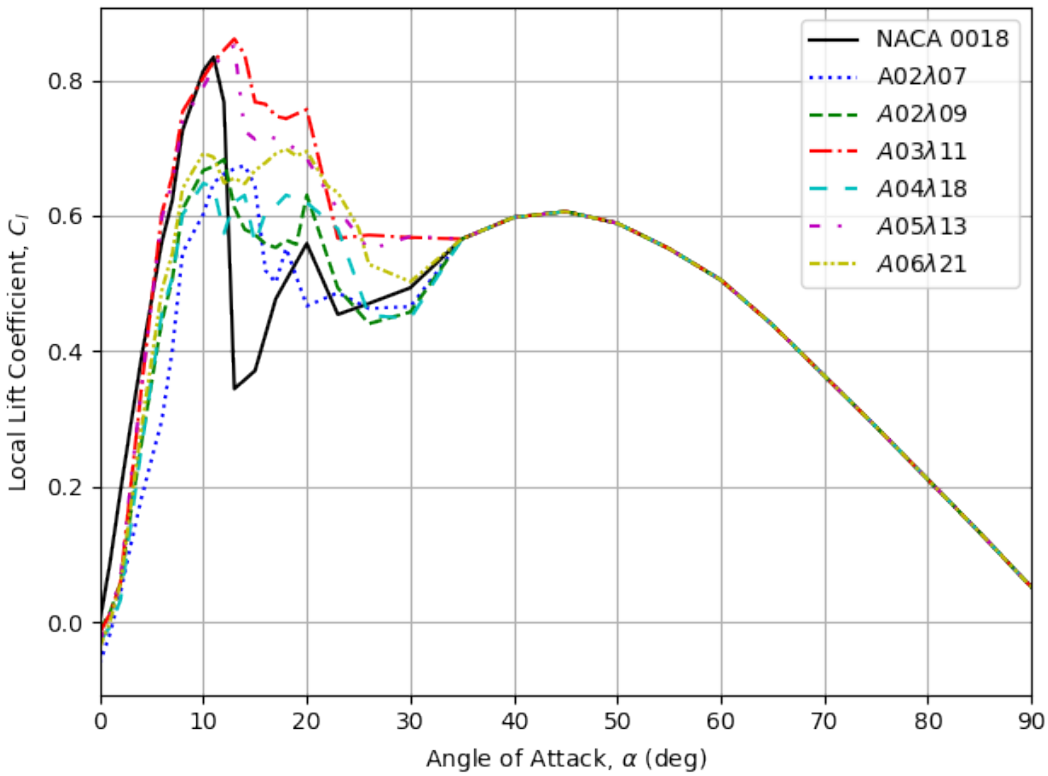

(a) C_l

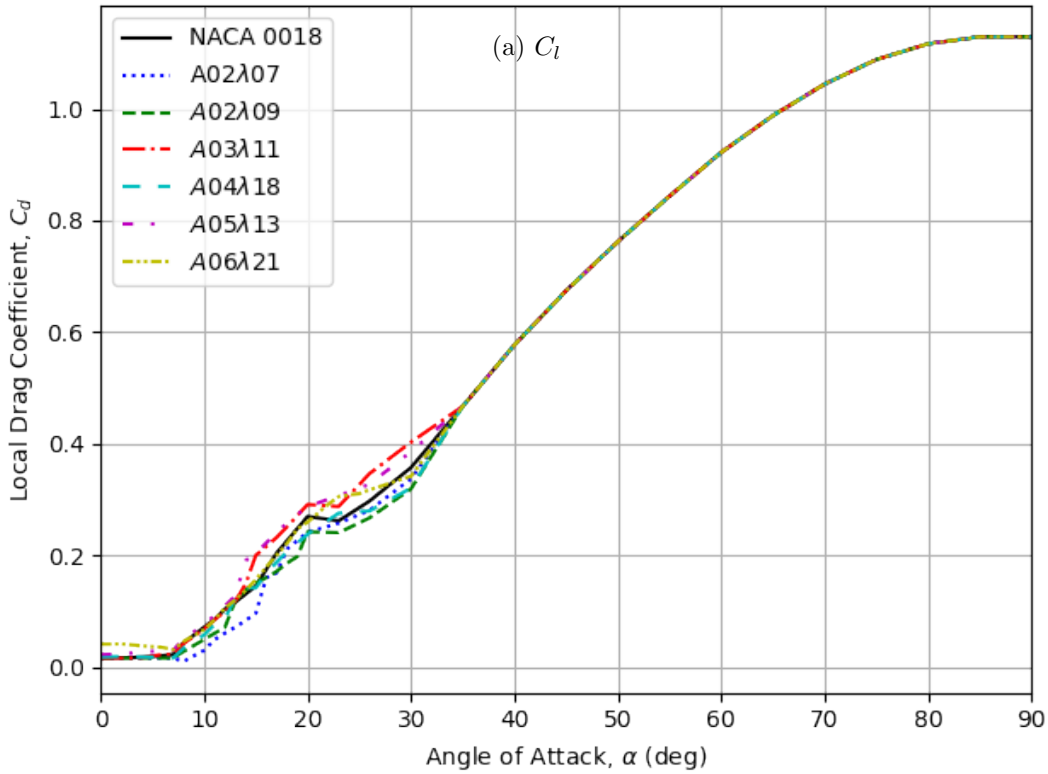

(b) C_d

Figure A.6: Corrected experimental lift and drag curves of the tubercle shapes at $Re = 75\,000$.

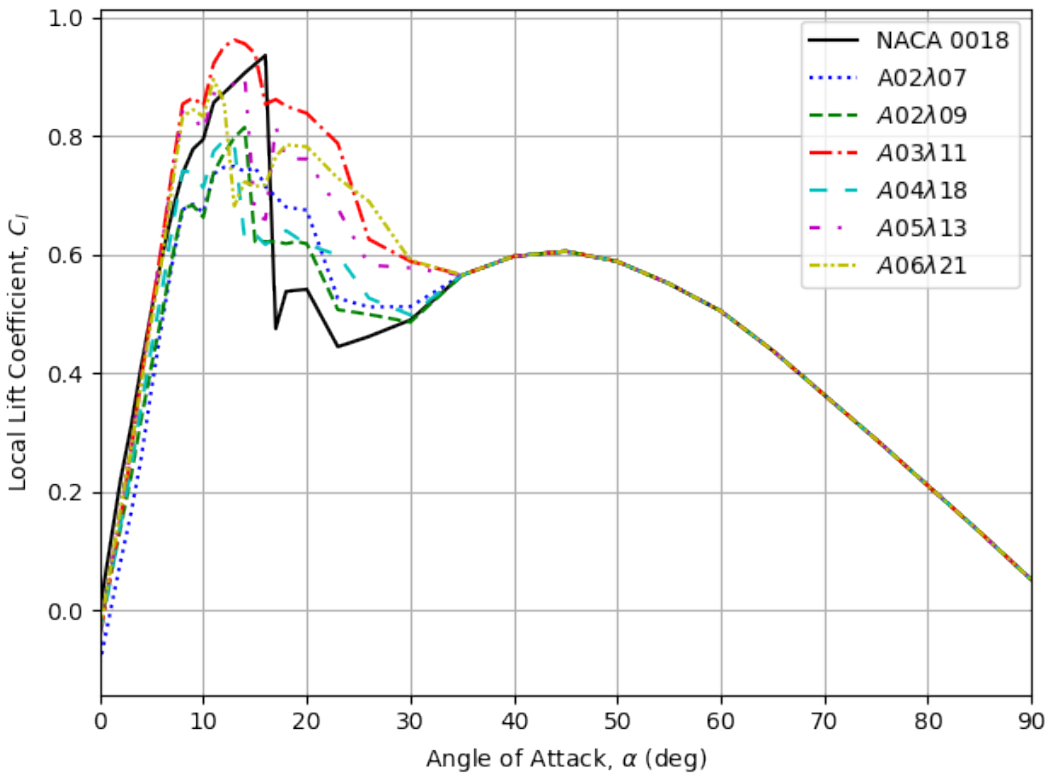

(a) C_l

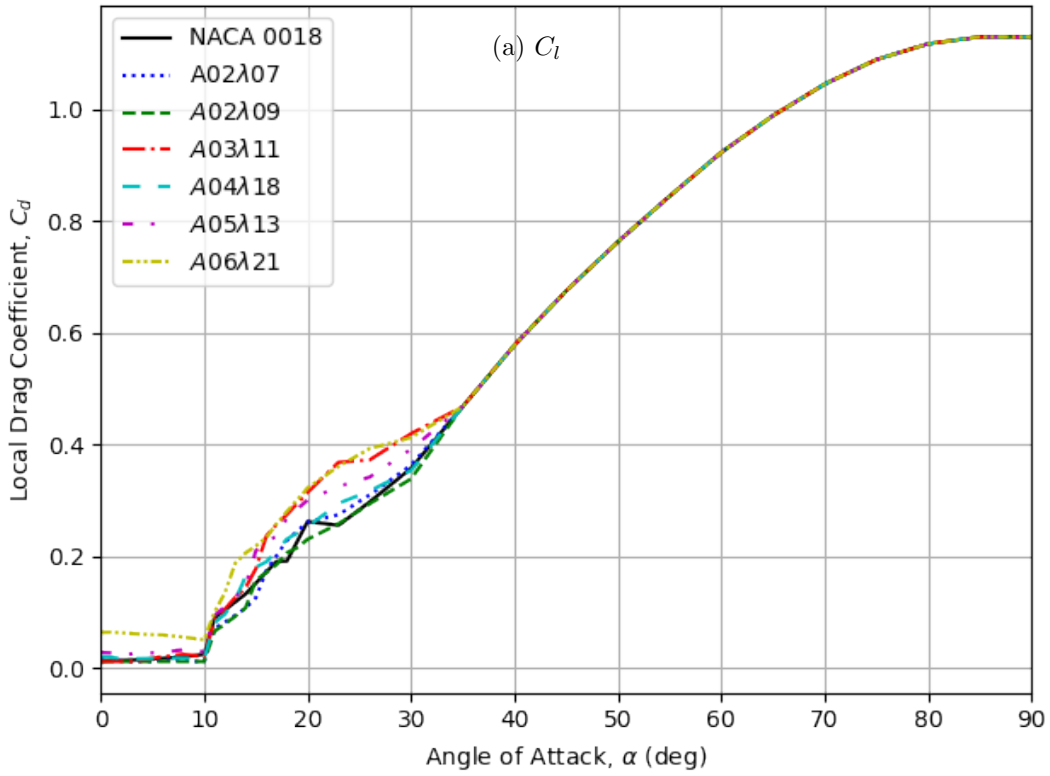

(b) C_d

Figure A.7: Corrected experimental lift and drag curves of the tubercle shapes at $Re = 150\,000$.

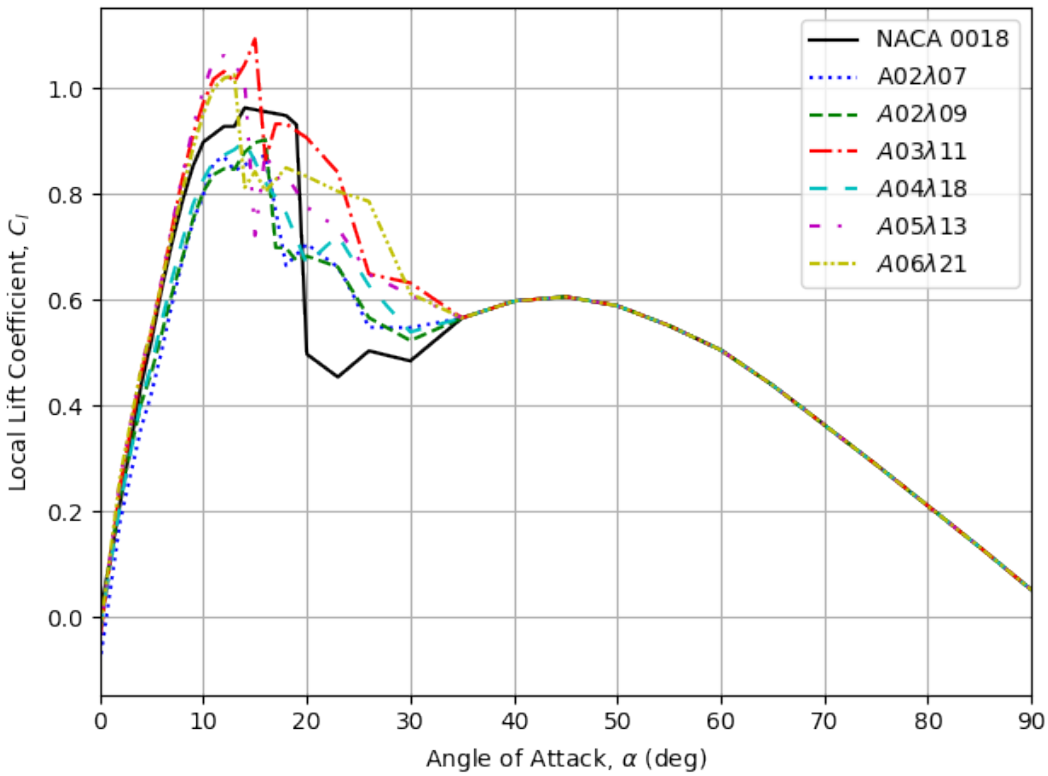

(a) C_l

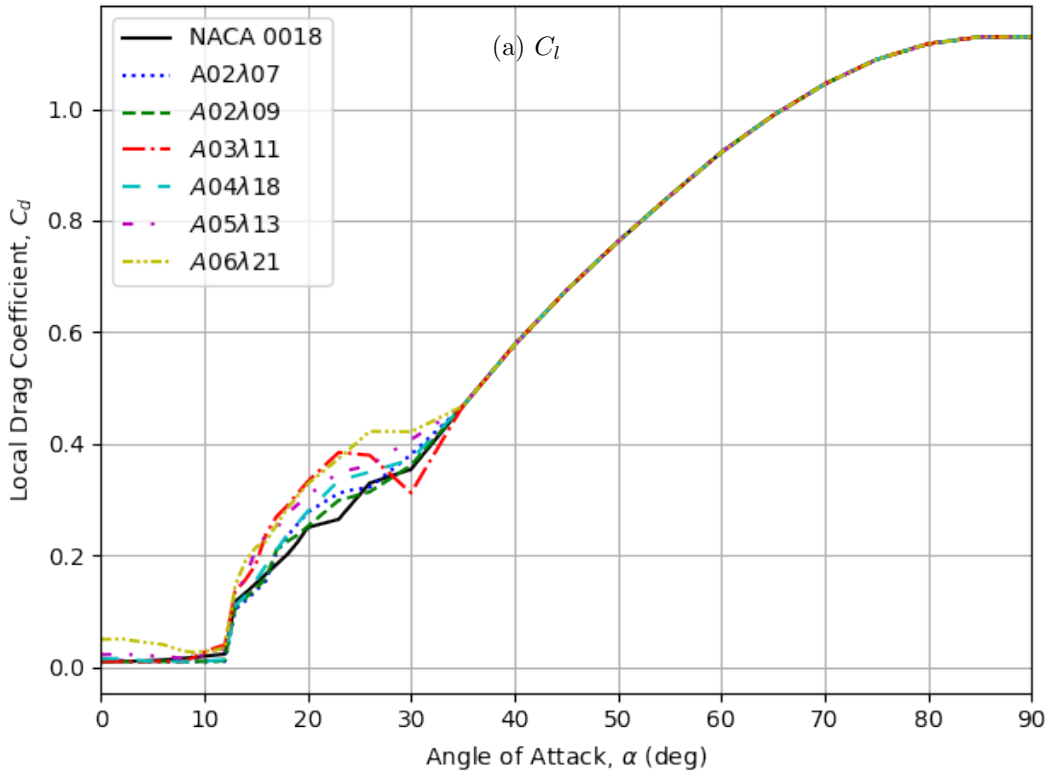

(b) C_d

Figure A.8: Corrected experimental lift and drag curves of the tubercle shapes at $Re = 300\,000$.

B Wind Probability Distribution of Kingston, Ontario

This appendix describes how the Weibull distribution was determined for Kingston, Ontario. The distribution is based on hourly weather data recorded at the Kingston Airport from October 2014 to April 2024, provided online by the Government of Canada [114]. The empirical cumulative distribution function for the wind speeds collected, $\hat{F}(V)$, was determined, and graphed on a Weibull Plot, shown in Figure B.1.

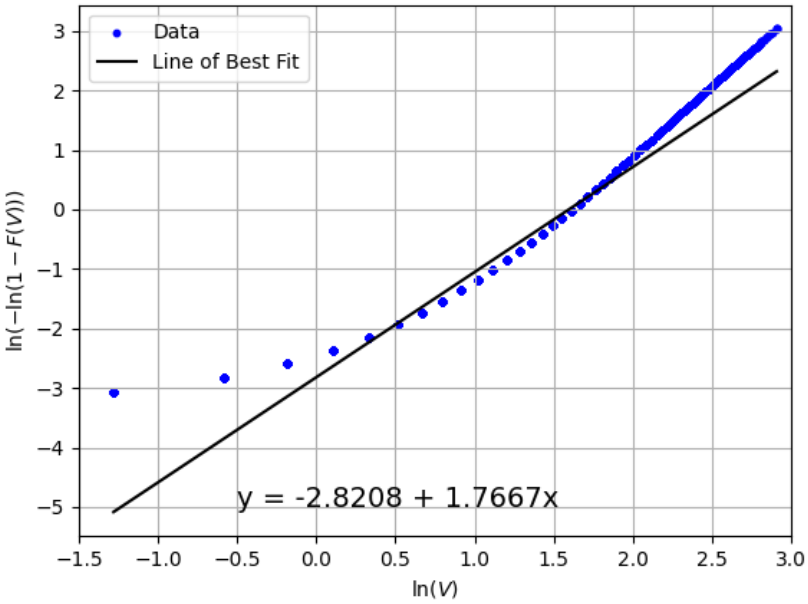

Figure B.1: Weibull plot of wind speeds recorded at the Kingston, ON, Airport from October 2014 to April 2024.

Since the Weibull plot axes came from a linearization of the cumulative distribution function, the Weibull shape and scale parameters, k and $\tilde{\lambda}$, respectively, can be determined by the line of best fit, following the equation below [115].

$$\ln(-\ln(1-\hat{F}(V))) = k\ln V - k\ln\tilde{\lambda} \tag{B.1}$$

Using m and b from the equation of the line of best fit gives a k and $\tilde{\lambda}$ of 1.767 and 4.936, respectively. Plotting the resultant Weibull distribution against the probability of different winds speeds by method of bins in Kingston, ON, gives Figure B.2. The resulting Weibull provides good agreement for most of the wind speeds. However, there is some under-prediction of the peak probability at a wind speed of approximately 3 m/s, and minor over-prediction at higher wind speeds.

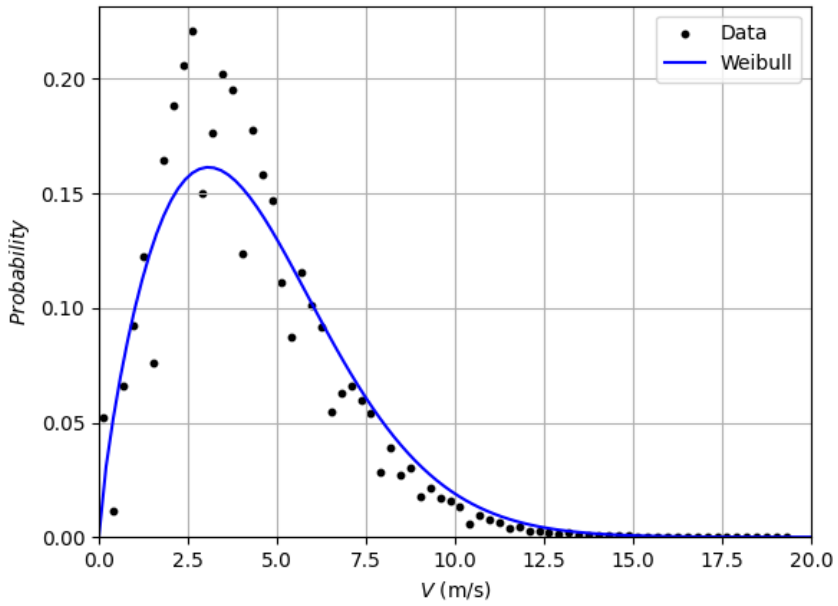

Figure B.2: Weibull distribution of wind speeds recorded at the Kingston, ON, Airport from October 2014 to April 2024, compared to the wind speed probability by method of bins.

C Additional DMSTM Results

This appendix presents additional results for the Small-Scale H-type VAWT presented in Section 3.2.1 and the 1:7 Scale Sandia 17-m presented in Section 4.3.

C.1 Small-Scale H-Type VAWT with Tubercles

This section presented the additional results for the Small-Scale H-type VAWT. Power contours for the various tubercles shapes as a function of wind speed and TSR are presented, followed by the difference in power contours compared to the baseline straight leading edge blade. The wind speed probability-weighted power output is then presented as a function of TSR, providing the ideal operating TSR to extract the most energy from the wind, on average, in comparison to the baseline blade.

C.1.1 Power Contours with TSR

Table C.1: Location and value of maximum wind speed probability-weighted average power with constant TSR for tubercle shapes compared to the baseline.

Shape	TSR of Maximum $\bar{P}$	Maximum $\bar{P}$
Baseline	2.79	68.9
$A02\lambda07$	2.90	80.75 (+17.1%)
$A02\lambda09$	2.90	82.16 (+19.2%)
$A03\lambda11$	2.62	67.84 (−1.6%)
$A04\lambda18$	2.90	74.96 (+8.7%)
$A05\lambda13$	2.57	50.23 (−27.1%)
$A06\lambda21$	2.57	27.42 (−60.2%)

Values in parentheses denote percent difference compared to the Baseline.

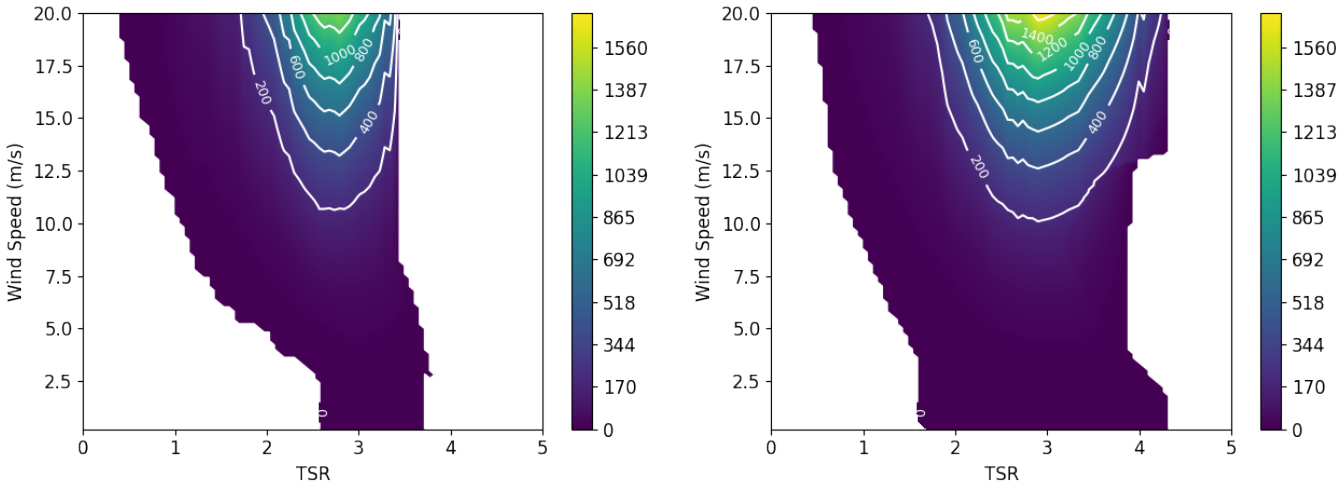

(a) Baseline

(b) $A02\lambda07$

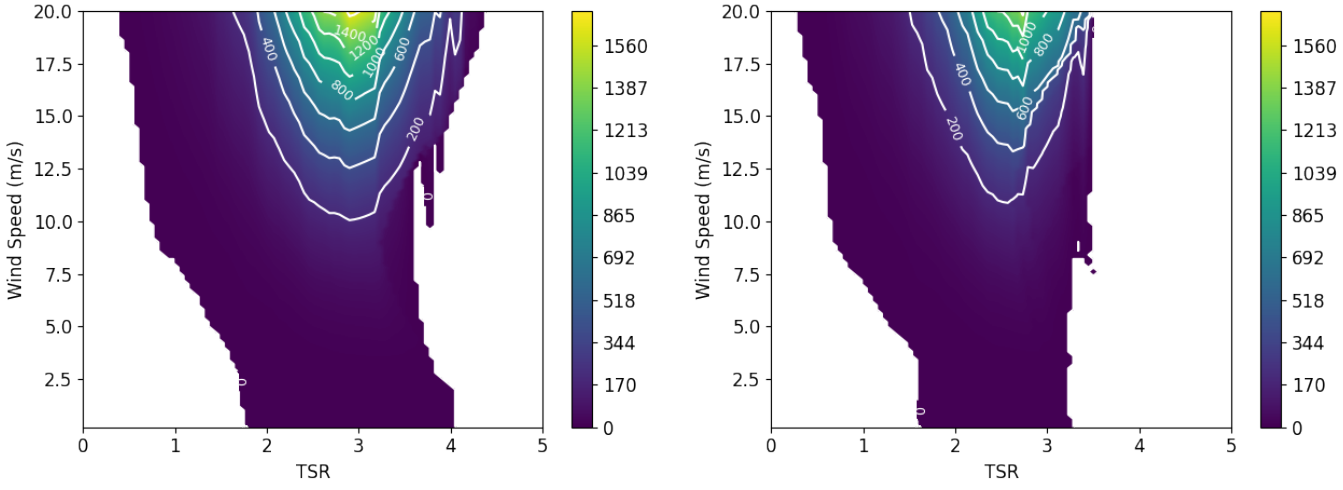

(c) $A02\lambda09$

(d) $A03\lambda11$

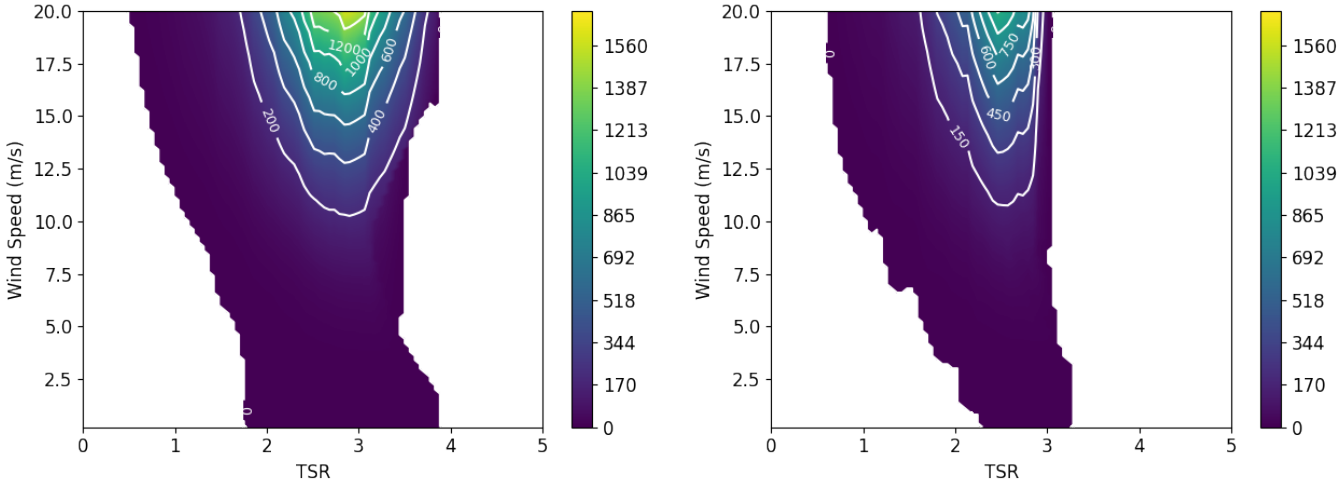

(e) $A04\lambda18$

(f) $A05\lambda13$

Figure C.1: Power contours, in watts, with TSR of various tubercle shapes applied to the Small-Scale H-type VAWT.

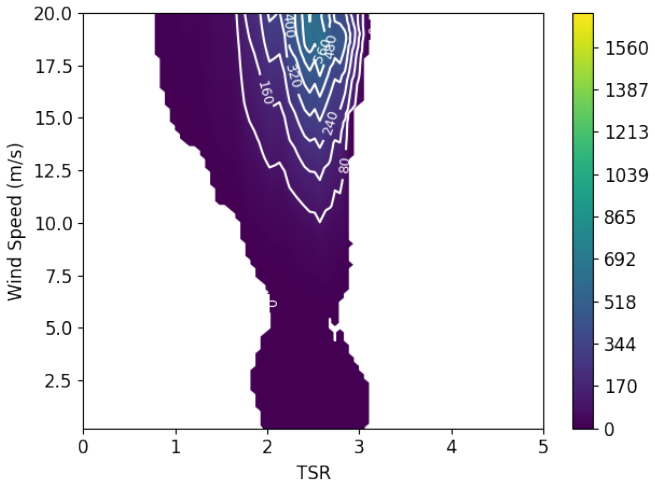

(g) $A06\lambda21$

Figure C.1: Power contours, in watts, with TSR of various tubercle shapes applied to the Small-Scale H-type VAWT.

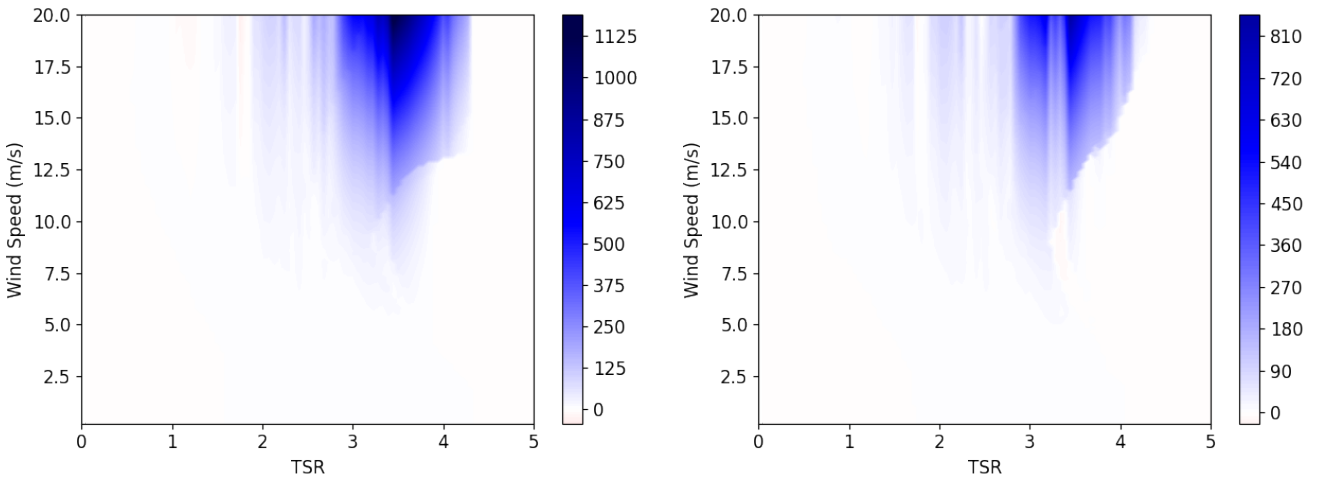

(a) $A02\lambda07$

(b) $A02\lambda09$

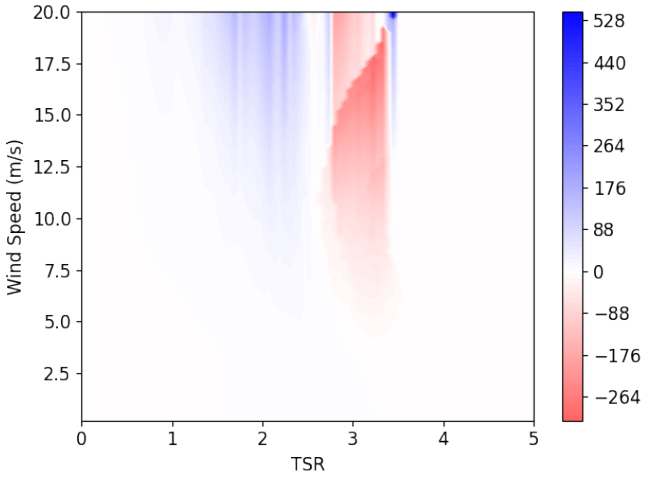

(c) $A03\lambda11$

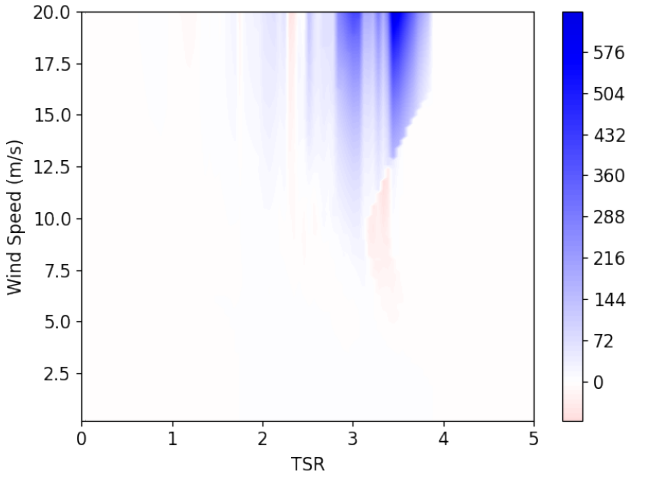

(d) $A04\lambda18$

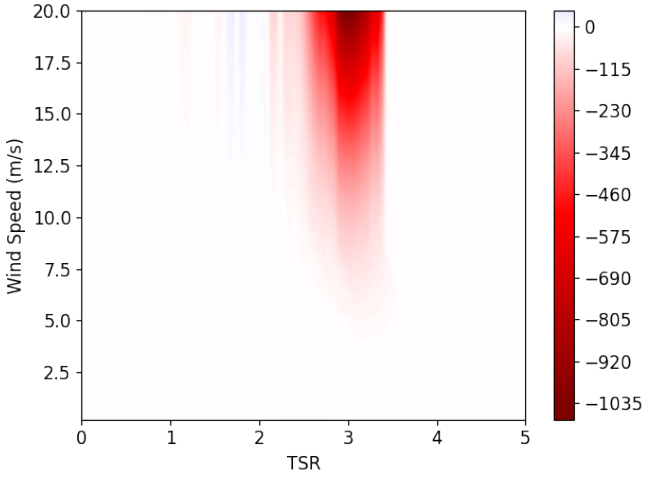

(e) $A05\lambda13$

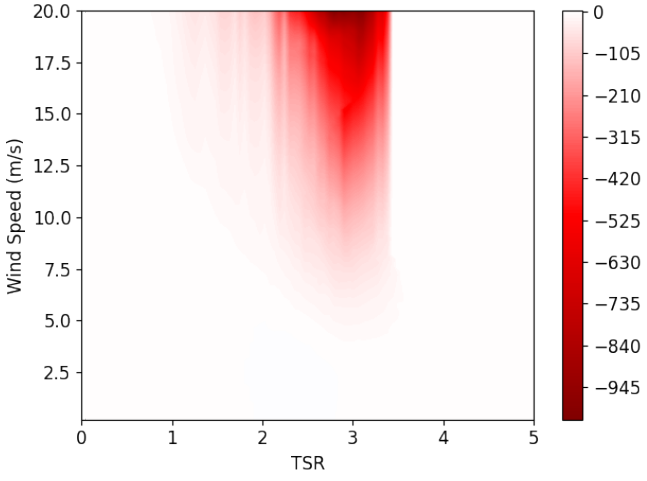

(f) $A06\lambda21$

Figure C.2: Change in power contours compared to the baseline, in watts, with TSR of various tubercle shapes applied to the Small-Scale H-type VAWT.

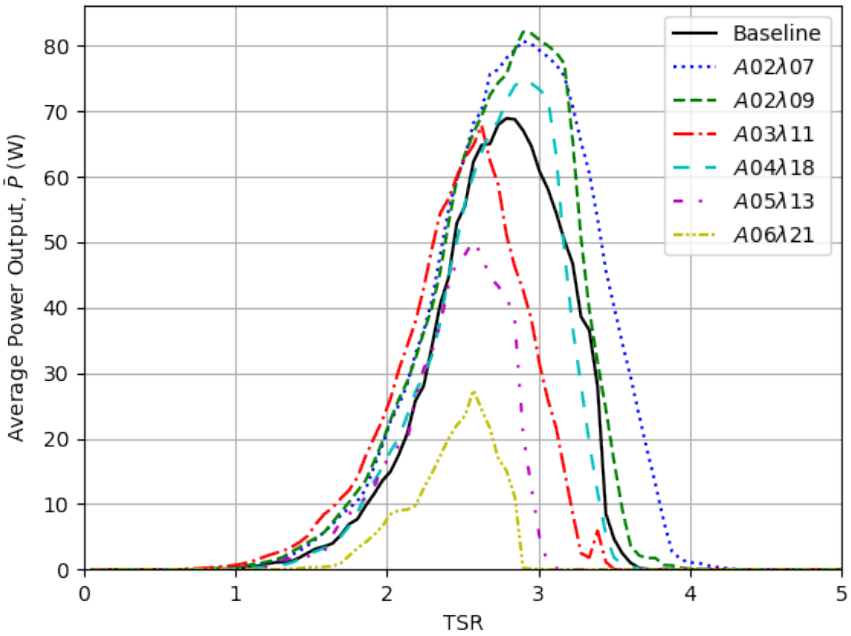

Figure C.3: Wind speed probability-weighted average power with constant TSR for the Small-Scale H-type VAWT with various tubercle shapes.

C.2 1:7 Scale Sandia 17-m with Tubercles

This section presents a comprehensive analysis of the performance of the 1:7 Scale Sandia 17-m with tubercles, similar to that presented in Chapter 3 for the Small-Scale H-type VAWT. This includes power contours as a function of wind speed and rotational rate, followed by power and power coefficient contours as a function of wind speed and TSR. The wind speed probability-weighted average power and power coefficients are also presented.

C.2.1 Power Contours

Table C.2: Location and value of maximum power output for tubercle shapes compared to the baseline when applied to the 1:7 Scale Sandia 17-m.

Shape	RPM of Maximum P	V of Maximum P (m/s)	Maximum P (W)
Baseline	800.0	20.0	5393.4
$A02\lambda07$	800.0	20.0	5254.7 (-2.6%)
$A02\lambda09$	800.0	20.0	5038.9 (-6.6%)
$A03\lambda11$	800.0	20.0	5778.4 ($+7.1\%$)
$A04\lambda18$	800.0	20.0	5049.7 (-6.4%)
$A05\lambda13$	750.0	20.0	5277.4 (-2.2%)
$A06\lambda21$	643.8	20.0	3651.9 (-32.3%)

Values in parentheses denote percent difference compared to the Baseline.

Table C.3: Location and value of maximum wind probability-weighted average power output with constant RPM for tubercle shapes compared to the baseline when applied to the 1:7 Scale Sandia 17-m.

Shape	RPM of Maximum $\bar{P}$	Maximum $\bar{P}$ (W)
Baseline	406.2	217.1
$A02\lambda07$	406.2	220.8 ($+1.7\%$)
$A02\lambda09$	406.2	230.9 ($+6.3\%$)
$A03\lambda11$	425.0	253.4 ($+16.7\%$)
$A04\lambda18$	400.0	204.8 (-5.7%)
$A05\lambda13$	375.0	164.8 (-24.1%)
$A06\lambda21$	343.8	63.9 (-70.6%)

Values in parentheses denote percent difference compared to the Baseline.

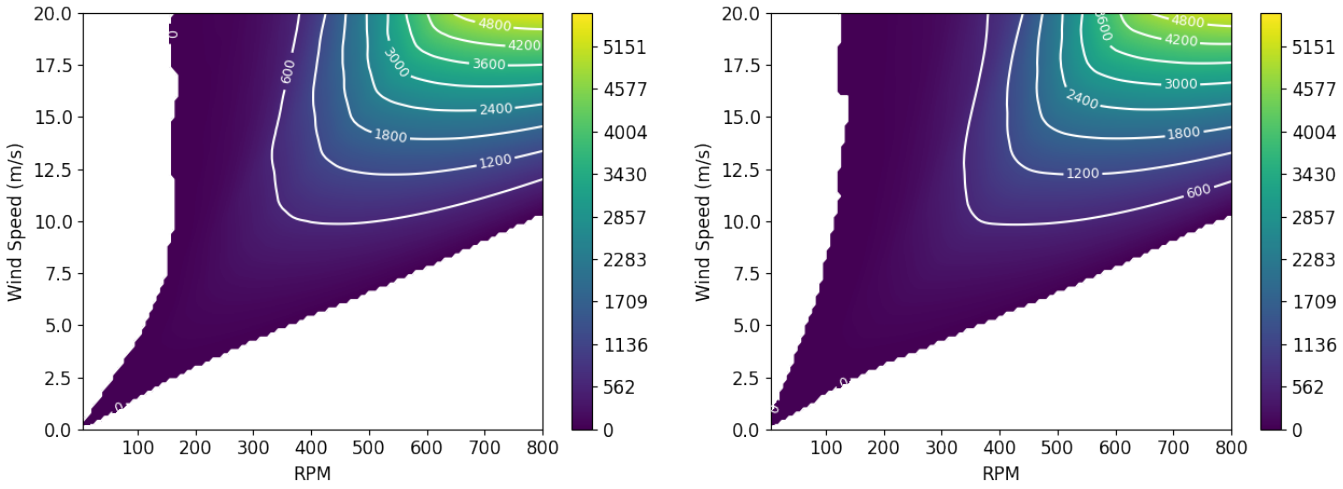

(a) Baseline

(b) $A02\lambda07$

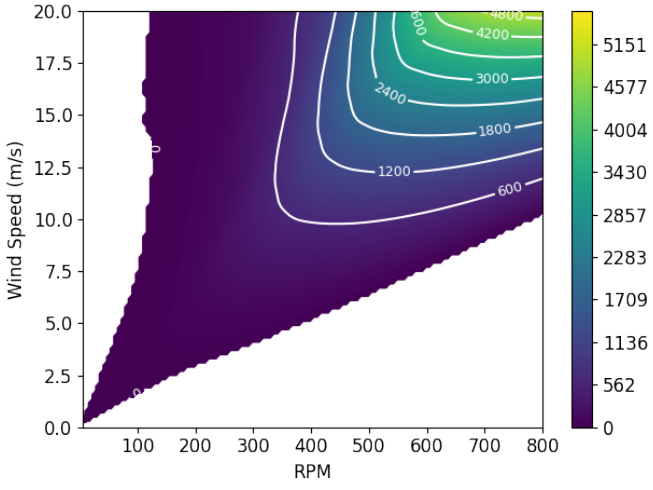

(c) $A02\lambda09$

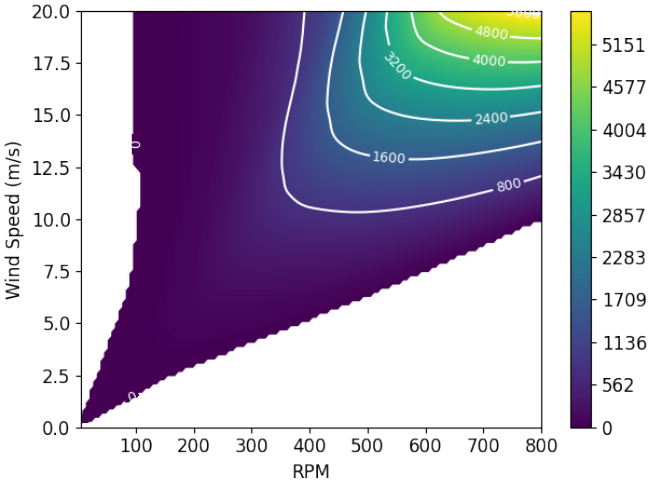

(d) $A03\lambda11$

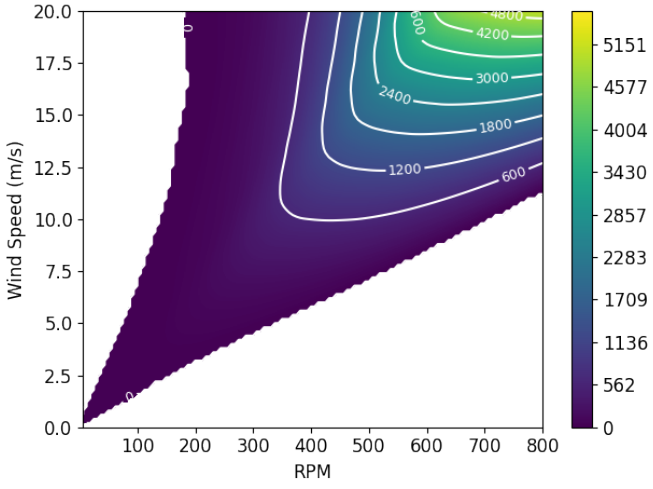

(e) $A04\lambda18$

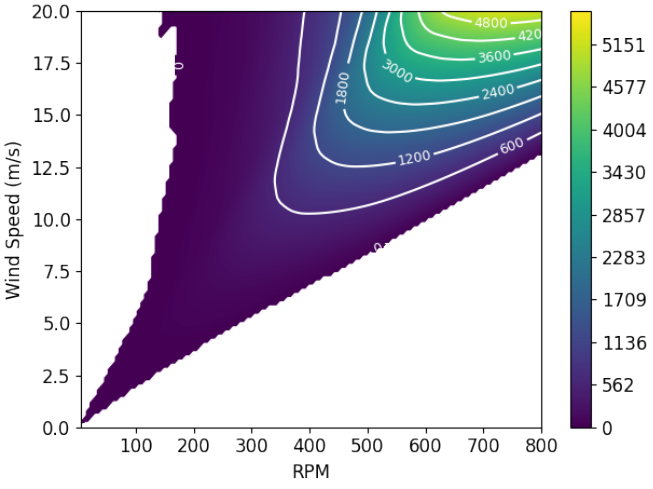

(f) $A05\lambda13$

Figure C.4: Power contours, in watts, of various tubercle shapes applied to the 1:7 Scale Sandia 17-m.

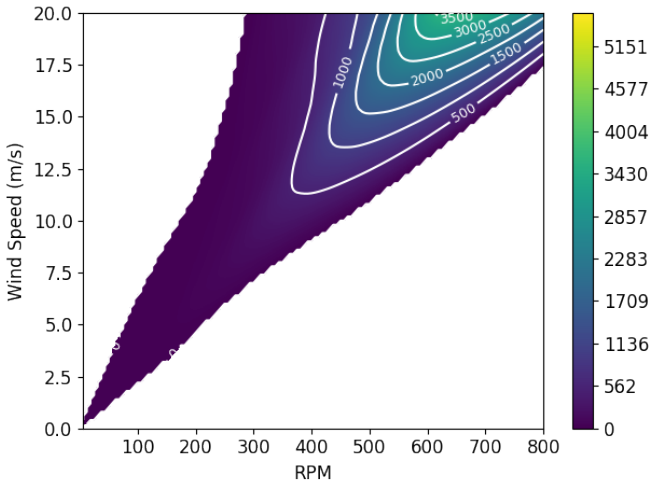

(g) $A06\lambda21$

Figure C.4: Power contours, in watts, of various tubercle shapes applied to the 1:7 Scale Sandia 17-m.

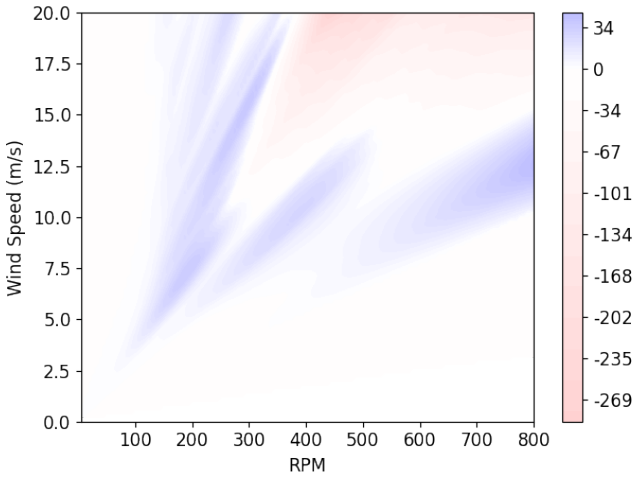

(a) $A02\lambda07$

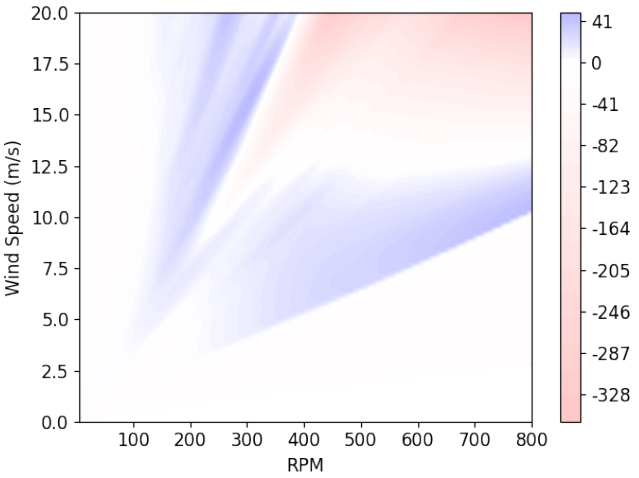

(b) $A02\lambda09$

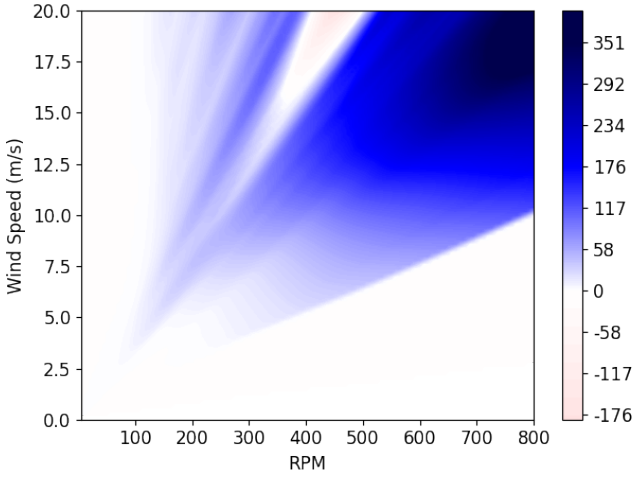

(c) $A03\lambda11$

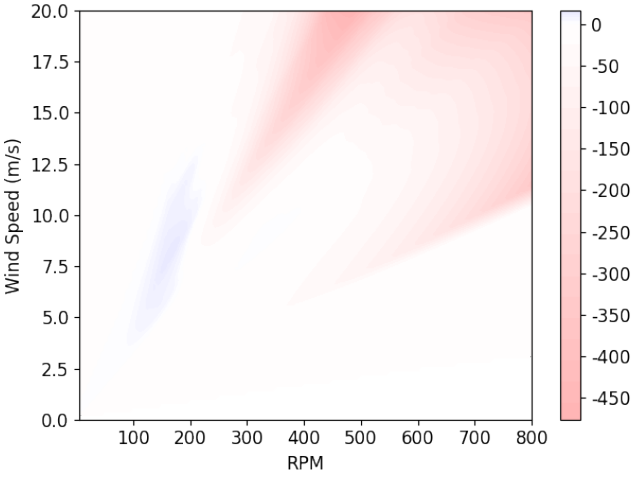

(d) $A04\lambda18$

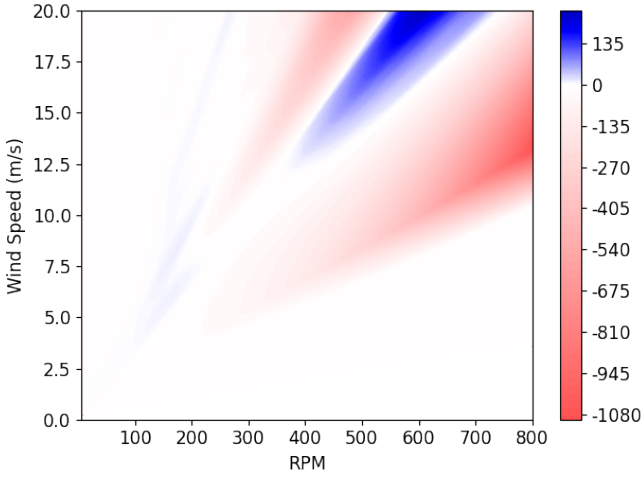

(e) $A05\lambda13$

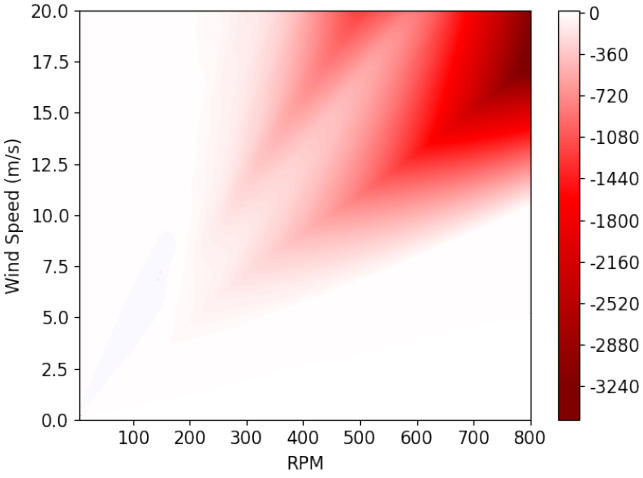

(f) $A06\lambda21$

Figure C.5: Change in power contours compared to the baseline, in watts, of various tubercle shapes applied to the 1:7 Scale Sandia 17-m.

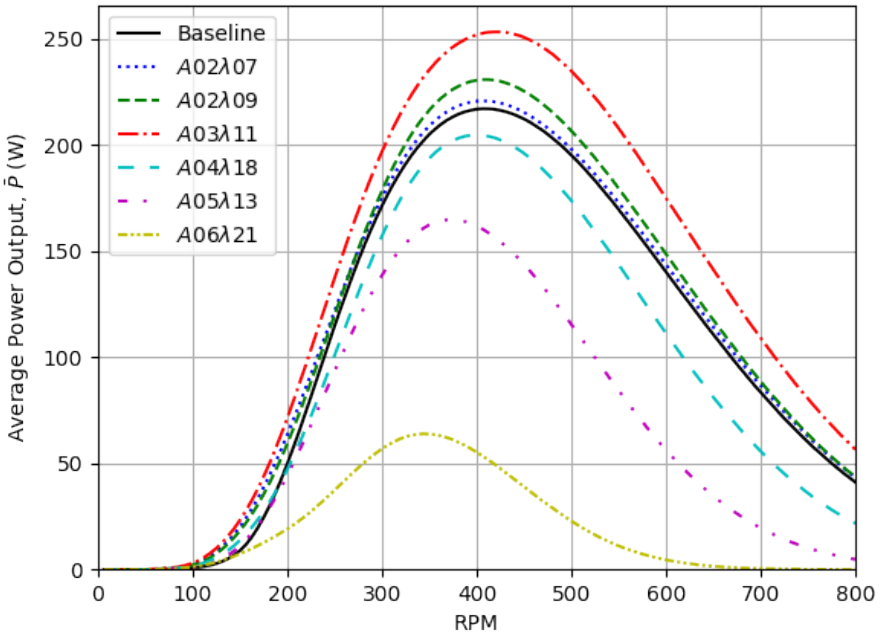

Figure C.6: Wind probability-weighted average power output for the 1:7 Scale Sandia 17-m with constant RPM for various tubercle shapes.

C.2.2 Power Coefficient Contours

Table C.4: Location and value of maximum power coefficient for tubercle shapes compared to the baseline when applied to the 1:7 Scale Sandia 17-m.

Shape	TSR of Maximum C_P	V of Maximum C_P (m/s)	Maximum C_P
Baseline	5.30	20.0	0.58
$A02\lambda07$	5.36	16.8	0.57 (−2.2%)
$A02\lambda09$	5.47	12.4	0.56 (−3.4%)
$A03\lambda11$	5.58	14.2	0.64 (+10.9%)
$A04\lambda18$	5.20	14.4	0.55 (−4.8%)
$A05\lambda13$	4.65	20.0	0.56 (−2.7%)
$A06\lambda21$	4.05	19.4	0.39 (−32.6%)

Values in parentheses denote percent difference compared to the Baseline.

Table C.5: Location and value of maximum wind probability-weighted average power coefficient with constant RPM for tubercle shapes compared to the baseline when applied to the 1:7 Scale Sandia 17-m.

Shape	TSR of Maximum $\bar{C}_P$	Maximum $\bar{C}_P$
Baseline	5.47	0.46
$A02\lambda07$	5.03	0.47 (+1.3%)
$A02\lambda09$	5.69	0.48 (+3.1%)
$A03\lambda11$	5.80	0.50 (+9.3%)
$A04\lambda18$	5.36	0.44 (−4.9%)
$A05\lambda13$	4.87	0.35 (−23.8%)
$A06\lambda21$	4.38	0.20 (−56.7%)

Values in parentheses denote percent difference compared to the Baseline.

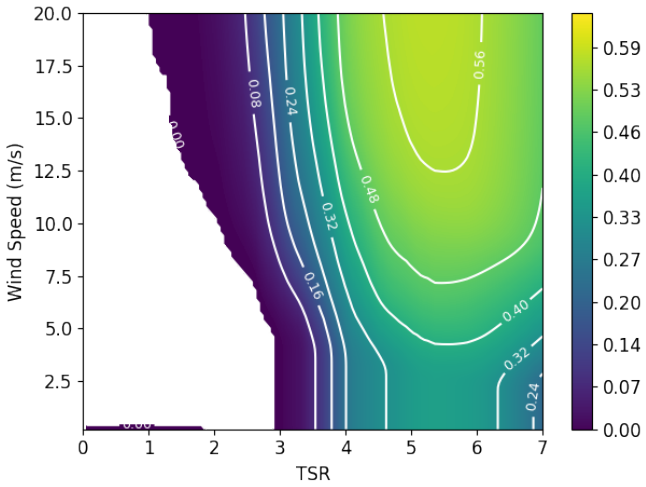

(a) Baseline

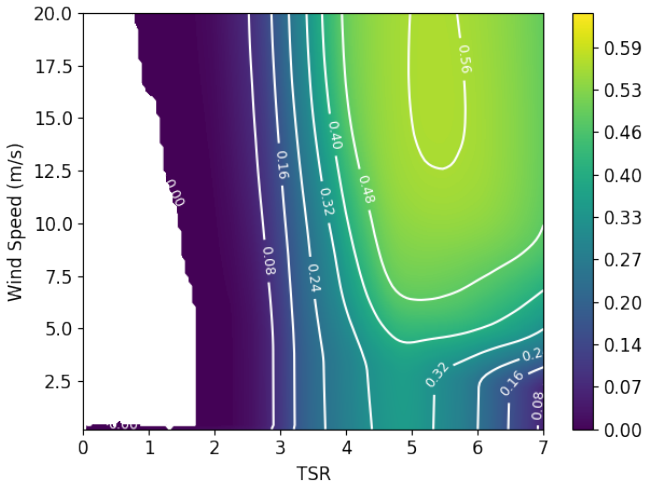

(b) $A02\lambda07$

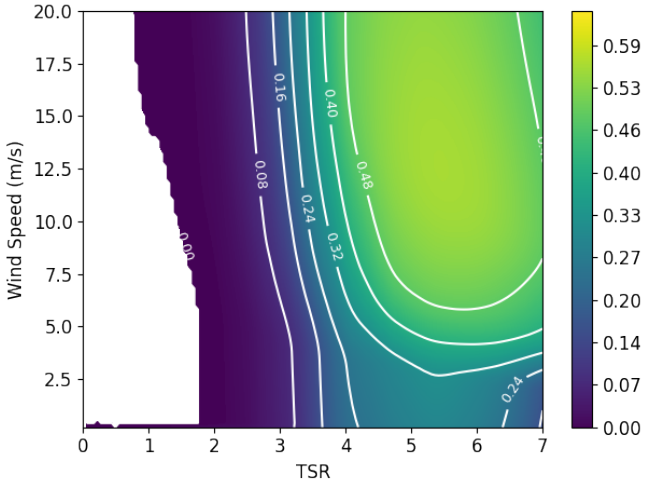

(c) $A02\lambda09$

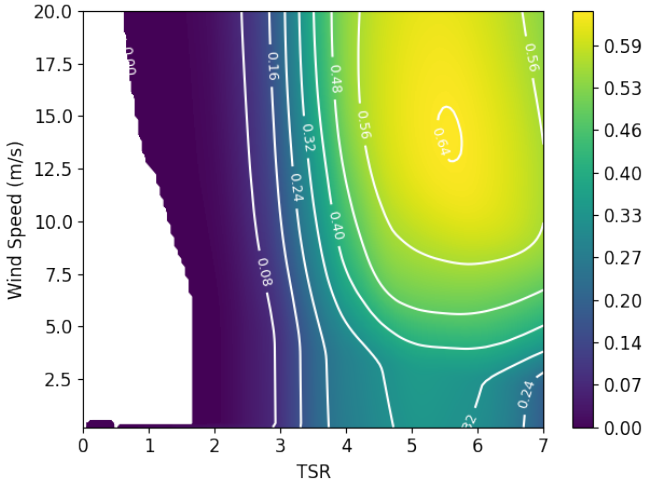

(d) $A03\lambda11$

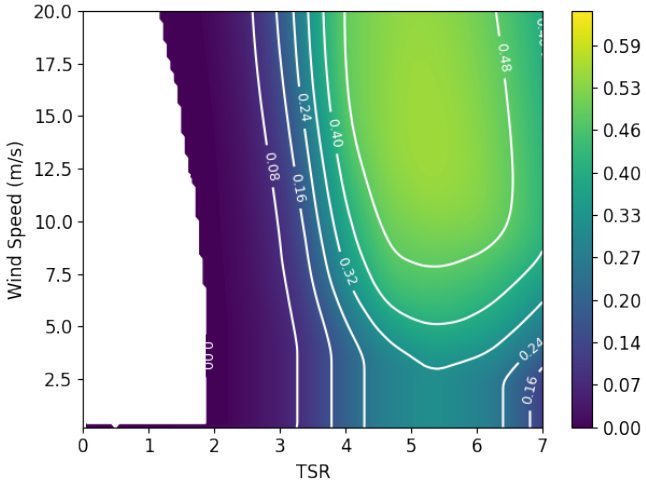

(e) $A04\lambda18$

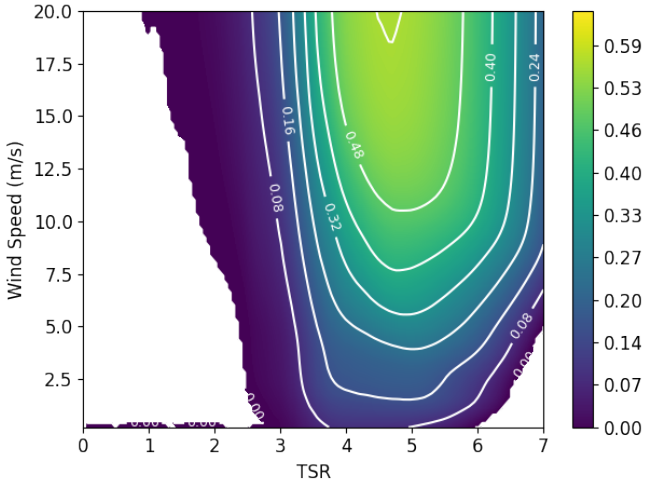

(f) $A05\lambda13$

Figure C.7: Power coefficient contours of various tubercle shapes applied to the 1:7 Scale Sandia 17-m.

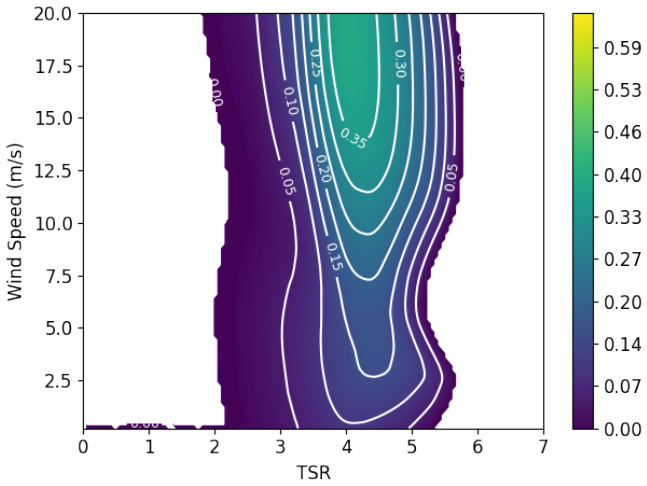

(g) $A06\lambda21$

Figure C.7: Power coefficient contours of various tubercle shapes applied to the 1:7 Scale Sandia 17-m.

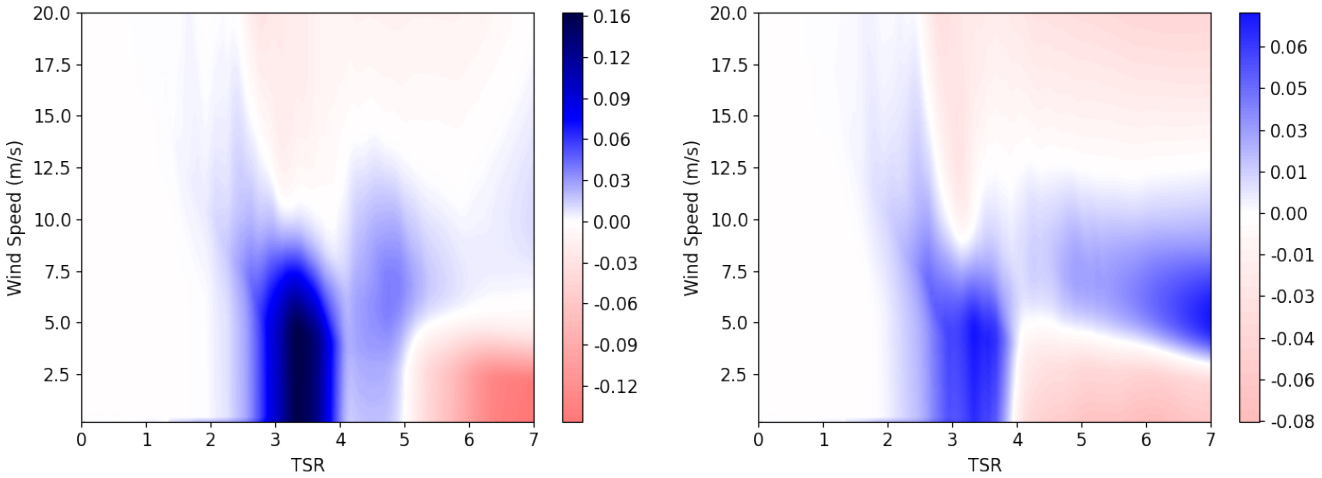

(a) $A02\lambda07$

(b) $A02\lambda09$

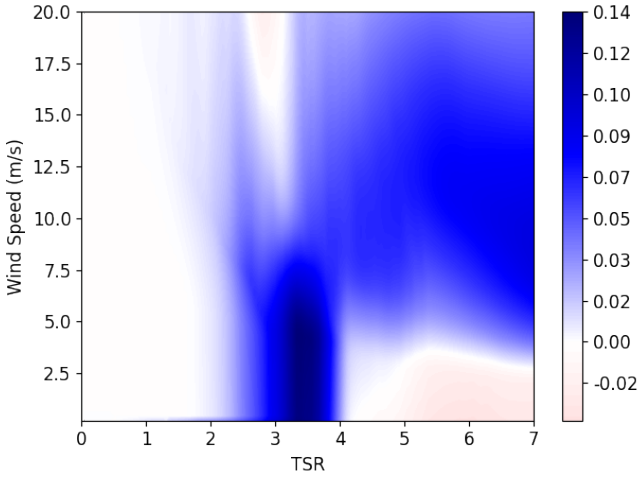

(c) $A03\lambda11$

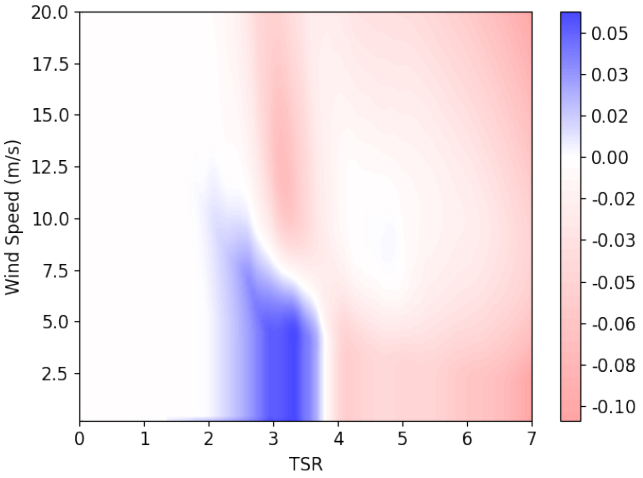

(d) $A04\lambda18$

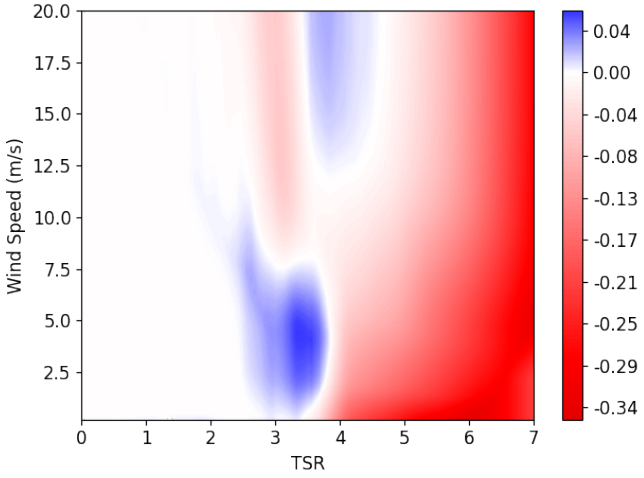

(e) $A05\lambda13$

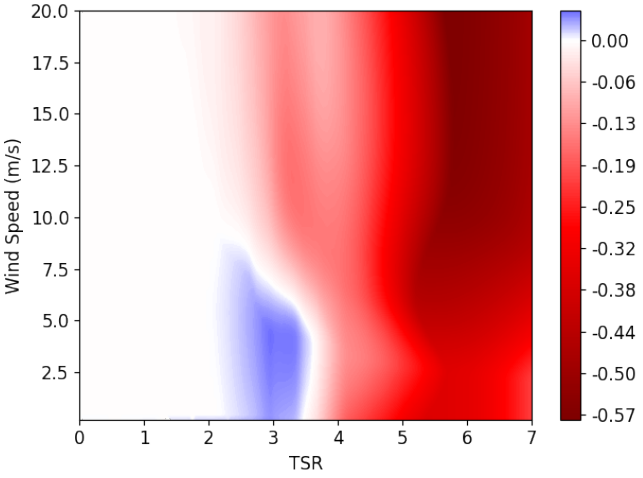

(f) $A06\lambda21$

Figure C.8: Change in power coefficient contours compared to the baseline of various tubercle shapes applied to the 1:7 Scale Sandia 17-m.

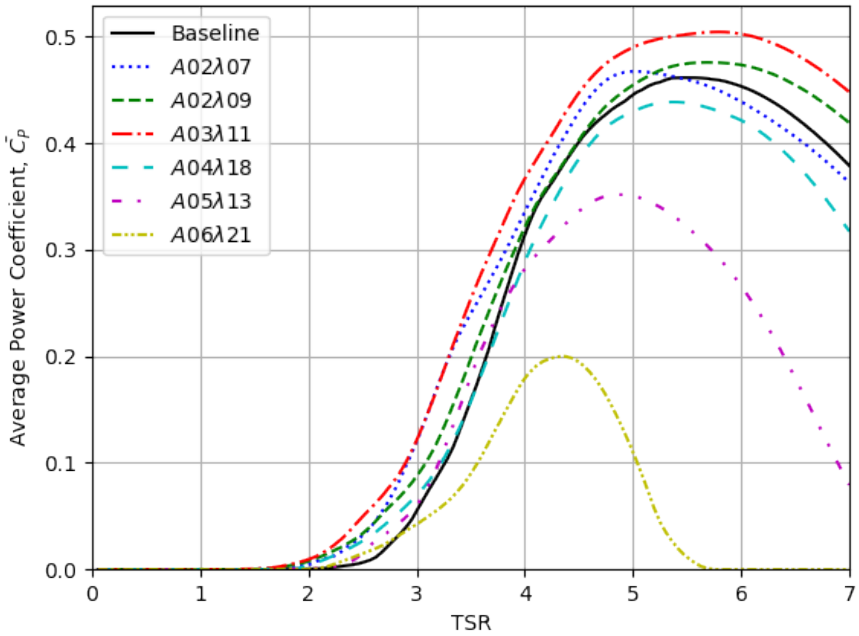

Figure C.9: Wind probability-weighted average power coefficient for the 1:7 Scale Sandia 17-m with constant RPM for various tubercle shapes.

C.2.3 Power Contours with TSR

Table C.6: Location and value of maximum wind probability-weighted average power output with constant TSR for tubercle shapes compared to the baseline when applied to the 1:7 Scale Sandia 17-m.

Shape	TSR of Maximum $\bar{P}$	Maximum $\bar{P}$
Baseline	5.58	245.70
$A02\lambda07$	5.25	249.31 (+1.5%)
$A02\lambda09$	5.63	253.93 (+3.3%)
$A03\lambda11$	5.80	277.56 (+13.0%)
$A04\lambda18$	5.36	238.55 (−2.9%)
$A05\lambda13$	4.81	209.17 (−14.9%)
$A06\lambda21$	4.32	118.46 (−51.8%)

Values in parentheses denote percent difference compared to the Baseline.

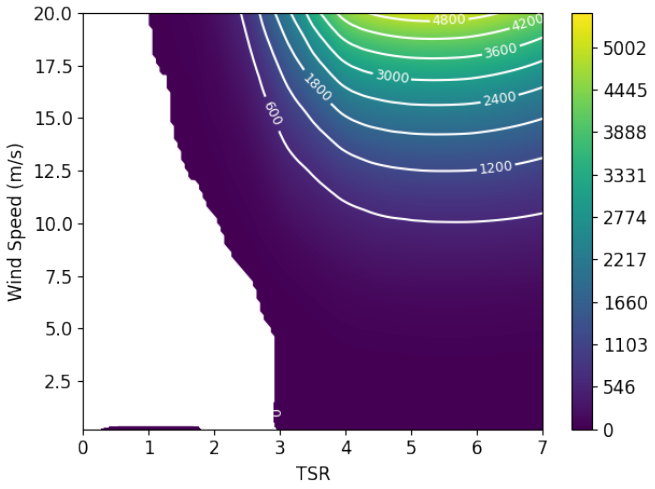

(a) Baseline

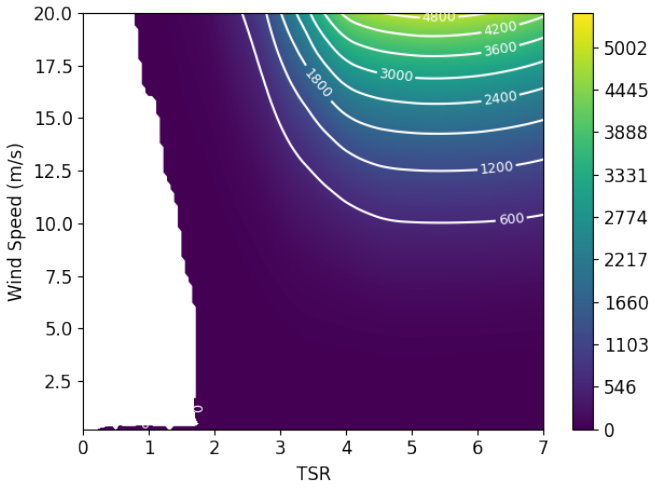

(b) $A02\lambda07$

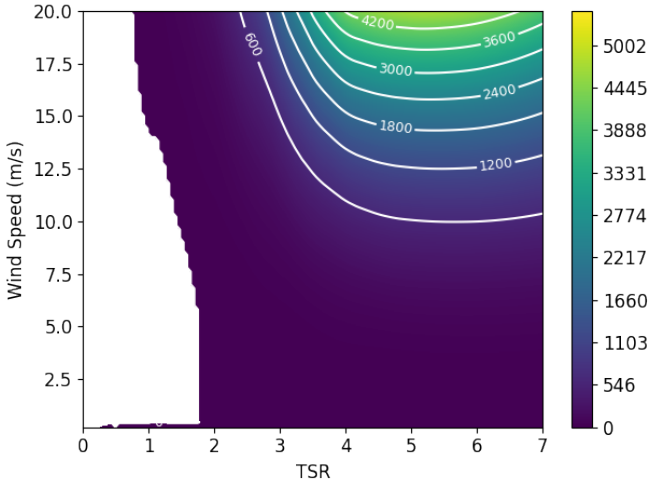

(c) $A02\lambda09$

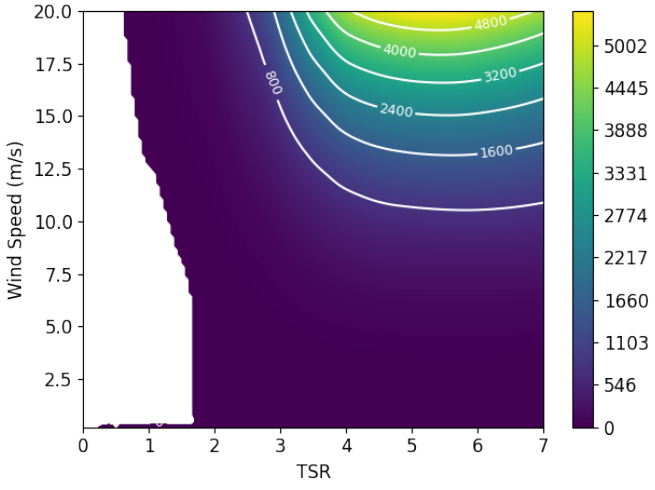

(d) $A03\lambda11$

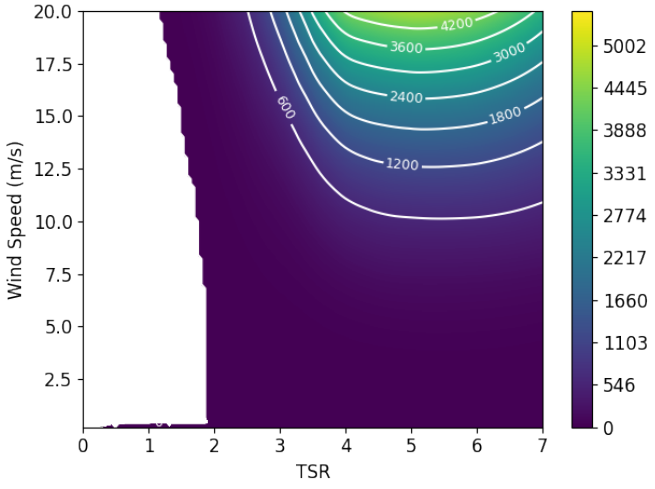

(e) $A04\lambda18$

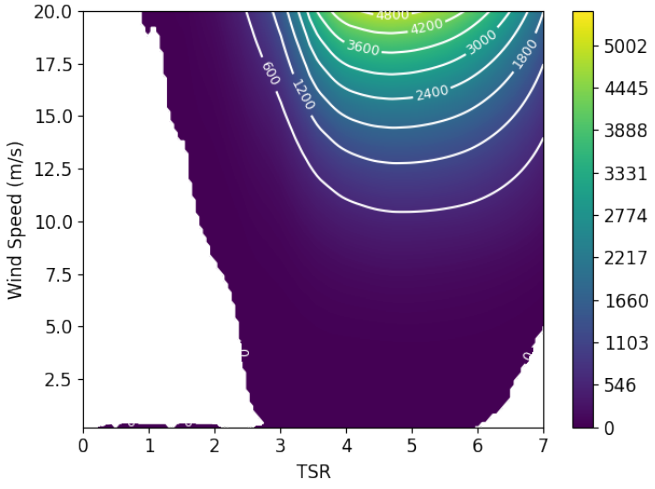

(f) $A05\lambda13$

Figure C.10: Power contours, in watts, of various tubercle shapes applied to the 1:7 Scale Sandia 17-m.

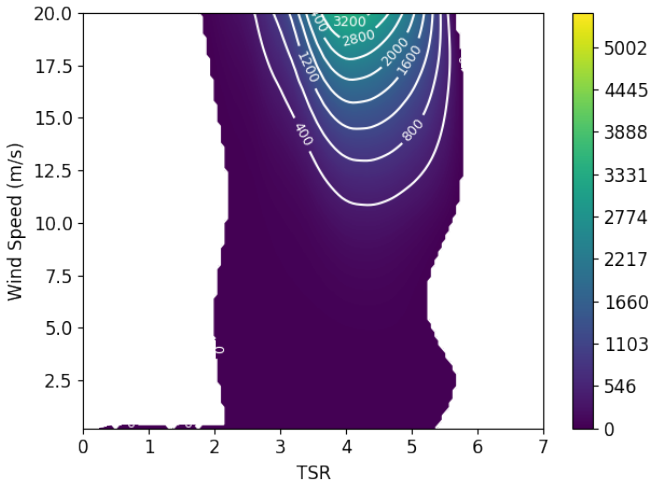

(g) $A06\lambda21$

Figure C.10: Power contours, in watts, of various tubercle shapes applied to the 1:7 Scale Sandia 17-m.

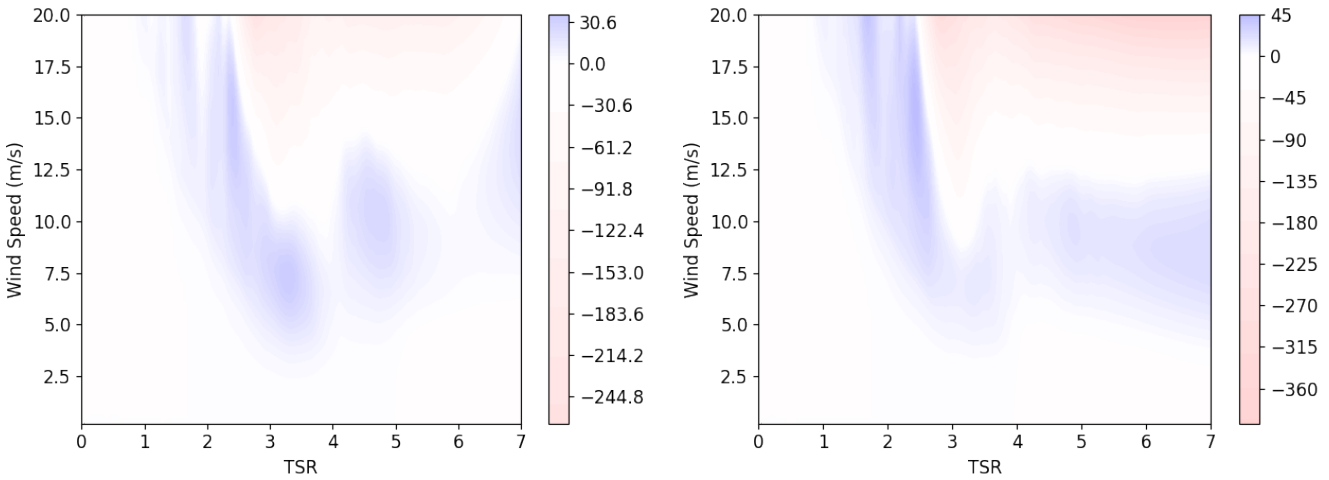

(a) $A02\lambda07$

(b) $A02\lambda09$

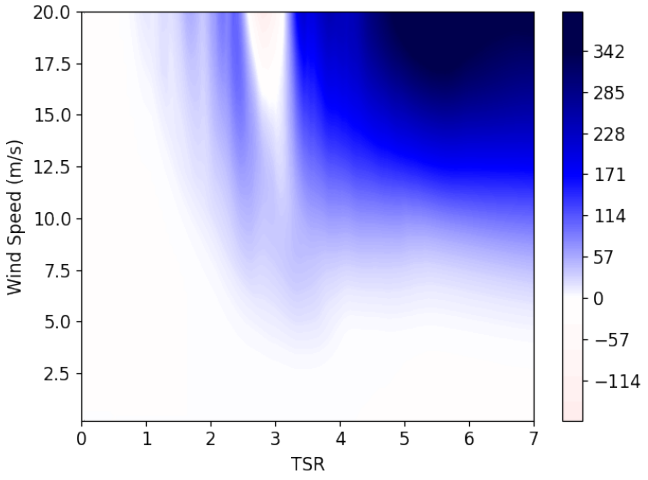

(c) $A03\lambda11$

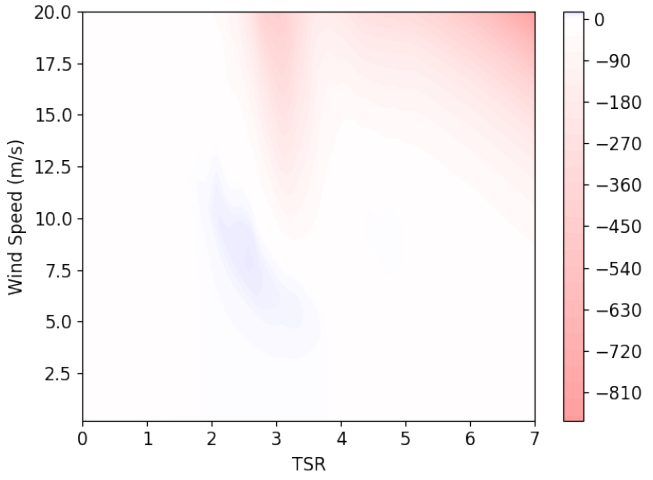

(d) $A04\lambda18$

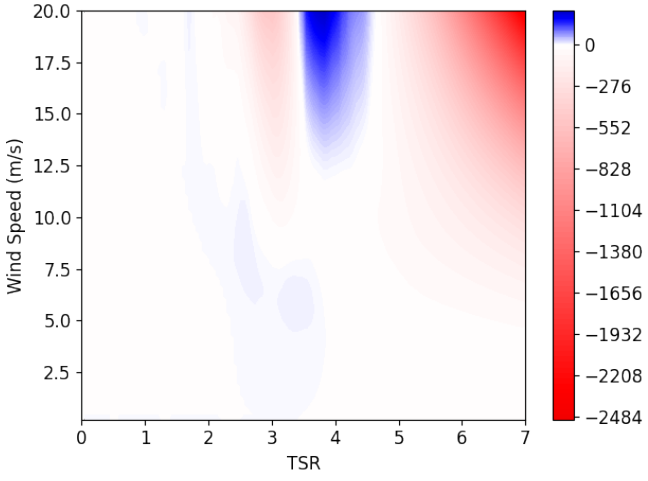

(e) $A05\lambda13$

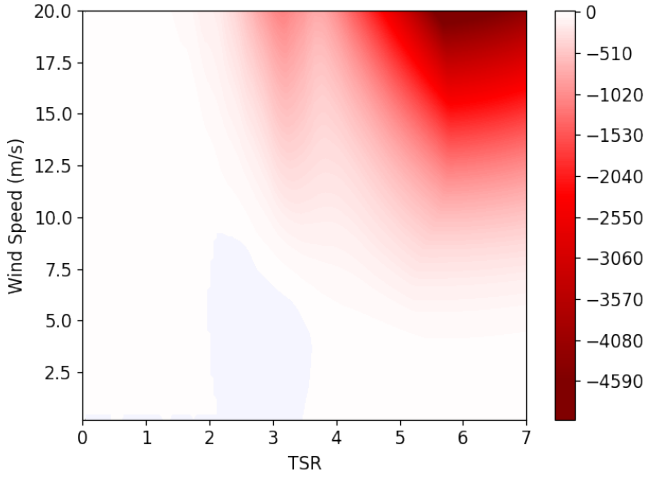

(f) $A06\lambda21$

Figure C.11: Change in power contours compared to the baseline, in watts, of various tubercle shapes applied to the 1:7 Scale Sandia 17-m.

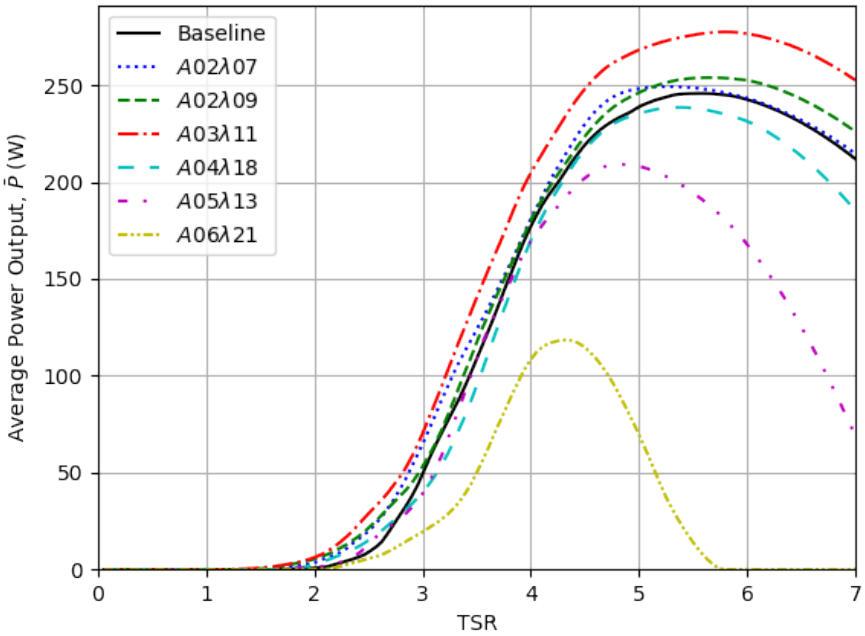

Figure C.12: Wind probability-weighted average power for the 1:7 Scale Sandia 17-m with constant TSR for various tubercle shapes.

D Non-Dominated Sorting Genetic Algorithm II

This appendix describes the optimization algorithm used in Chapter 4, along with a validation of the algorithm. Non-Dominated Sorting Genetic Algorithm II (NSGA-II) is a multi-objective evolutionary algorithm developed by Deb et Al. [104] to handle elitism and population diversity using a fast sorting method. Instead of using a weighted-sum method with various weights to generate the Pareto Frontier, NSGA-II advances the front towards the Pareto Frontier each generation. This is done through a change in mating pool selection by introducing non-domination fronts and crowding distance.

D.1 Fast Non-Dominated Sorting

Following evaluation, the parent and children populations are combined. Each member is compared to every other member to determine if either member dominates the other. A member is dominating if it is no worse than the other member for all objective functions and strictly better than that member for at least one objective. For each member, a list of members it dominates, and the number of members it is dominated by is stored. Any member that is not dominated is considered to be in the 1st Front.

Now, for every member in this front, the domination counter of the members they dominate is reduced by one. Members now with a domination count of zero are in the 2nd front. This process is repeated until there are no members without an assigned front.

D.2 Crowding Distance

For each front and objective function, the members are put in descending order of objective function value. Then, the crowding distance of each member, d_i, is calculated using the following equation, adding the contribution from each objective, where f is the objective function values of the members in that front [104]:

$$d_i = d_i + \frac{f_{i+1} - f_{i-1}}{f_{max} - f_{min}} \tag{D.1}$$

For the members on the extremes of the front, they are given a crowding distance of infinity. This ensures the extremes are maintained.

D.3 Binary Tournament Selection and Crossover

With the fronts and crowding distances calculated, the mating pool can be determined. To ensure the elites from the generation are preserved, members of the least dominated front (1st front, then 2nd, etc.) have priority. If the mating pool cannot be filled by all members of the next front, the front is ordered by crowding distance, giving priority to the members with the greatest crowding distance.

With the mating pool filled, the parents are chosen through a binary tournament selection. For each pair of children, 2 pairs of parents are randomly chosen from the pool. Each pair of parents then undergoes a tournament selection. The parent in the lowest front gets chosen. If both parents are in the same front, then the parent with the greatest crowding distance is chosen. If both parents also have the same crowding distance, then a parent is selected at random.

With both parents selected, the children chromosomes are determined through a cross over operation. With a random number less than the crossover probability, a crossover point is randomly chosen in the parent chromosomes, where the two parents swap the remainder of their chromosomes, creating the children. If crossover does not occur, the children chromosomes are identical to their parents.

Following crossover, each gene in each chromosome is given the chance to mutate. If a random number is less than the mutation probability, mutation occurs and that gene changes to a random number within the bounds of that gene. Now, the next generation is created, and the process is repeated until convergence or a set number of generations.

D.4 Validation

To validate the coded NSGA-II used in this thesis, the KUR problem was used. It is defined as follows [116, 117]:

$$\begin{aligned}
\text{Minimize:} \quad f_1(x) &= \sum_{i=1}^{n-1} \left(-10 \exp\left(-0.2\sqrt{x_i^2 + x_{i+1}^2} \right) \right) \\
f_2(x) &= \sum_{i=1}^{n} \left(|x_i|^{0.8} + 5 \sin x_i^3 \right) \\
\text{Where:} \quad n &= 3 \\
\text{Subject to:} \quad x &\in [-5, 5]
\end{aligned}$$

The KUR problem was solved using the created *Python* NSGA-II code, using the same parameters that were used in Chapter 4. These are shown in Table D.1. The resulting solution from the NSGA-II code is presented against the pareto front provided by Dr. Carlos Coello's website [118] in Figure D.1. NSGA-II provides good agreement to the entire front, including the single point at approximately (-20,0).

Table D.1: Summary of NSGA-II Parameters.

Parameter	Value
Population Size	100
Maximum Generations	250
Crossover Rate	0.80
Mutation Rate	0.15

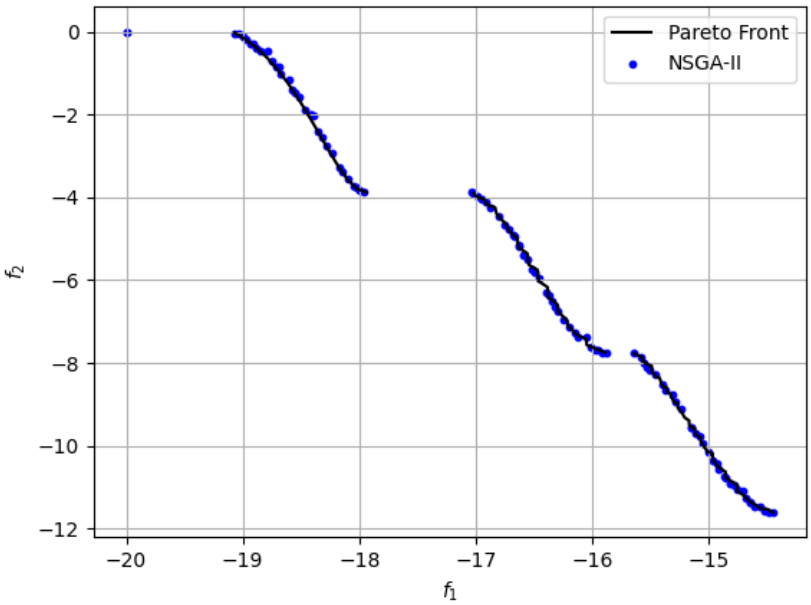

Figure D.1: Validation of the NSGA-II code solution of the KUR problem, compared to the Pareto front solution provided by Dr. Carlos Coello's website [118].

E Optimization Results with Variable RPM

This appendix presents the multi-objective optimization results using NSGA-II for the problem presented in Chapter 4 with RPM as a variable in the design of the Small Scale H-style VAWT described in Section 3.2.1 and the 1:7 Scale Sandia 17-m in Section 4.3. This supplements the results of Chapter 4, which present the designs with TSR as a variable, by showing how a design will change if there is no feedback with wind speed to determine the operating RPM required for the design TSR. Instead, the turbine will target a single RPM regardless of wind speed.

E.1 Small Scale H-Type VAWT

This section covers the results for the Small Scale H-style VAWT described in Section 3.2.1 when rotational rate is a variable instead of TSR.

E.1.1 Maximization of $\overline{FLI}$ and $\bar{P}$

Table E.1: Performance characteristics of the various designs from optimizing wind probability-weighted average fatigue life indicator and power output at the SWiFT Test Site for the Small Scale H-type VAWT with RPM as a variable.

Design	RPM	$\overline{FLI}(\times 10^{-5})$	$\bar{P}$ (W)
Baseline	481.2	5.88	37.55
Maximum $\bar{P}$	481.0 (0.0 %)	5.32 (−9.5 %)	47.47 (+26.4 %)
Point A	479.7 (−0.3 %)	6.14 (+4.4 %)	46.25 (+23.2 %)
Point B	441.4 (−8.3 %)	6.96 (+18.4 %)	43.11 (+14.8 %)
Equal $\bar{P}$	406.1 (−15.6 %)	7.86 (+33.7 %)	37.55 (0.0 %)

Values in parentheses denote percent difference compared to the Baseline.

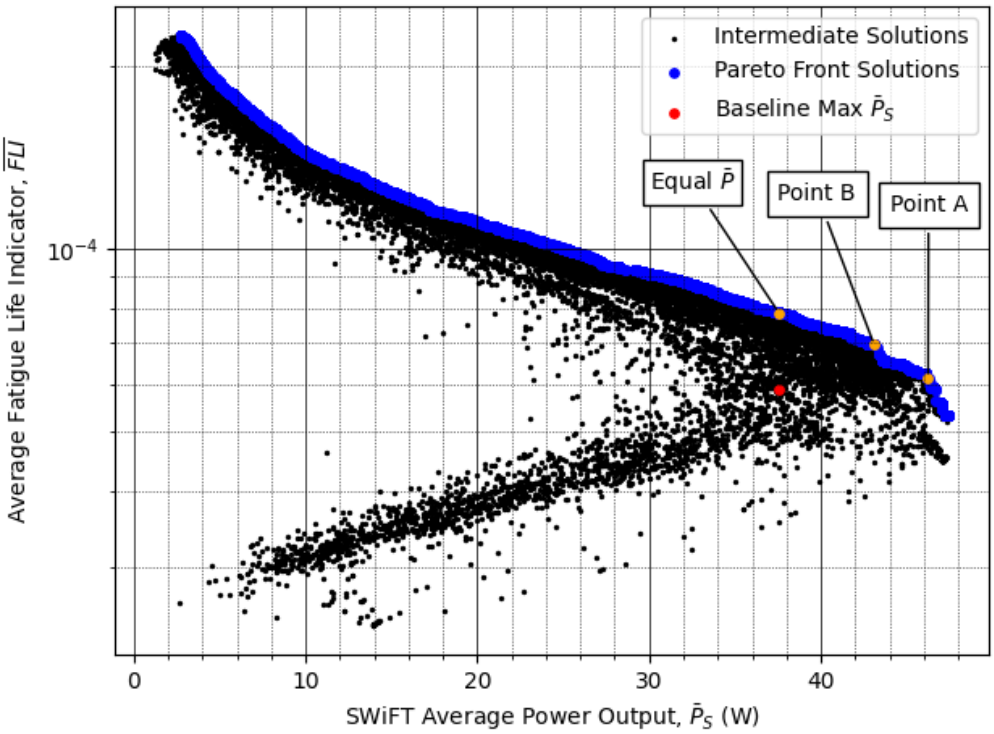

(a) All Solutions

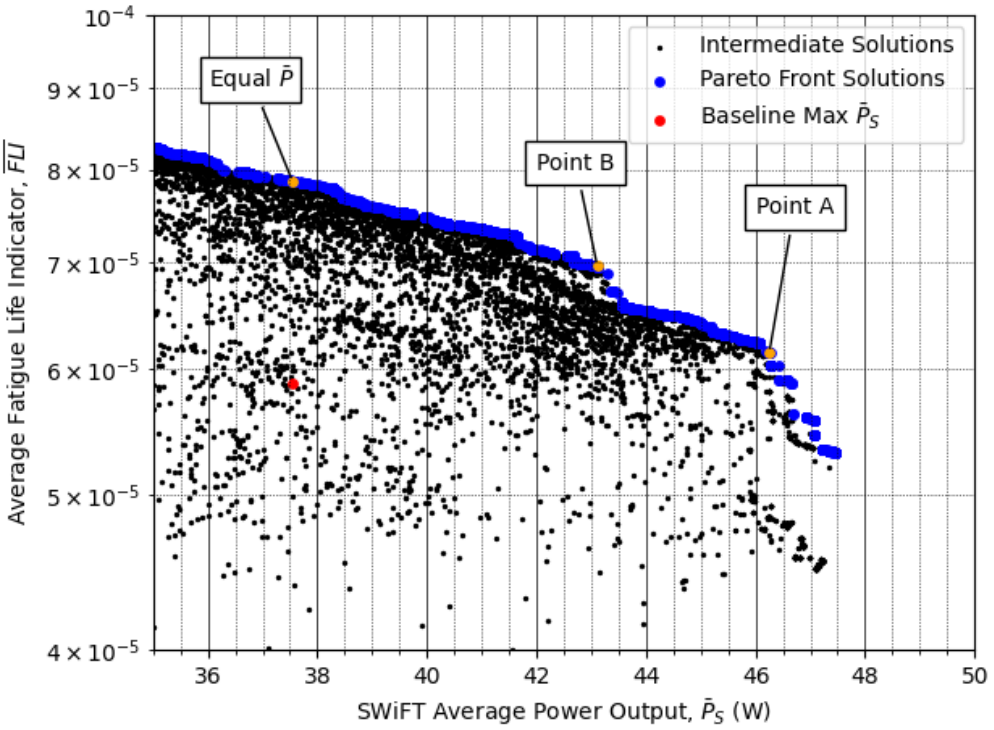

(b) Magnified View of the 35–50 W $\bar{P}_S$ Region

Figure E.1: All solutions explored by NSGA-II optimizing wind probability-weighted average fatigue life indicator and power output at the SWiFT Test Site for the Small Scale H-type VAWT with RPM as a variable.

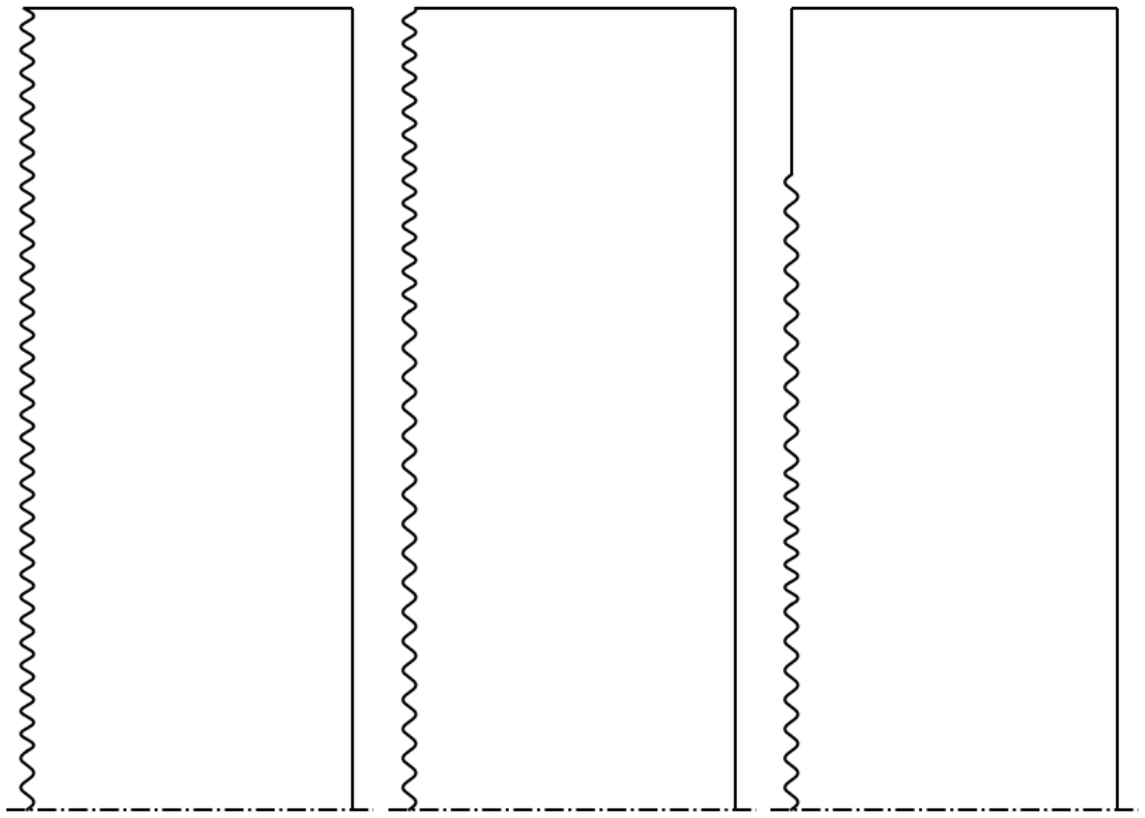

(a) Maximum $\bar{P}$ (b) Point A (c) Equal $\bar{P}$ of Baseline

Figure E.2: Select half-blade designs from optimizing wind probability-weighted average fatigue life indicator and power output at the SWiFT Test Site for the Small Scale H-type VAWT with RPM as a variable.

E.1.2 Maximization of $\bar{P}_S$ and $\bar{P}_K$

Table E.2: Performance characteristics of the various designs from optimizing wind probability-weighted average power output at the SWiFT Test Site and Kingston, ON, for the Small Scale H-type VAWT with RPM as a variable.

Design	RPM	$\bar{P}_S$	$\bar{P}_K$ (W)
Baseline	481.2	37.55	11.81
Maximum $\bar{P}_S$	487.6 (+1.3 %)	48.03 (+27.9 %)	15.55 (+31.7 %)
Maximum $\bar{P}_K$	440.3 (−8.5 %)	44.46 (+18.4 %)	16.01 (+35.6 %)

Values in parentheses denote percent difference compared to the Baseline.

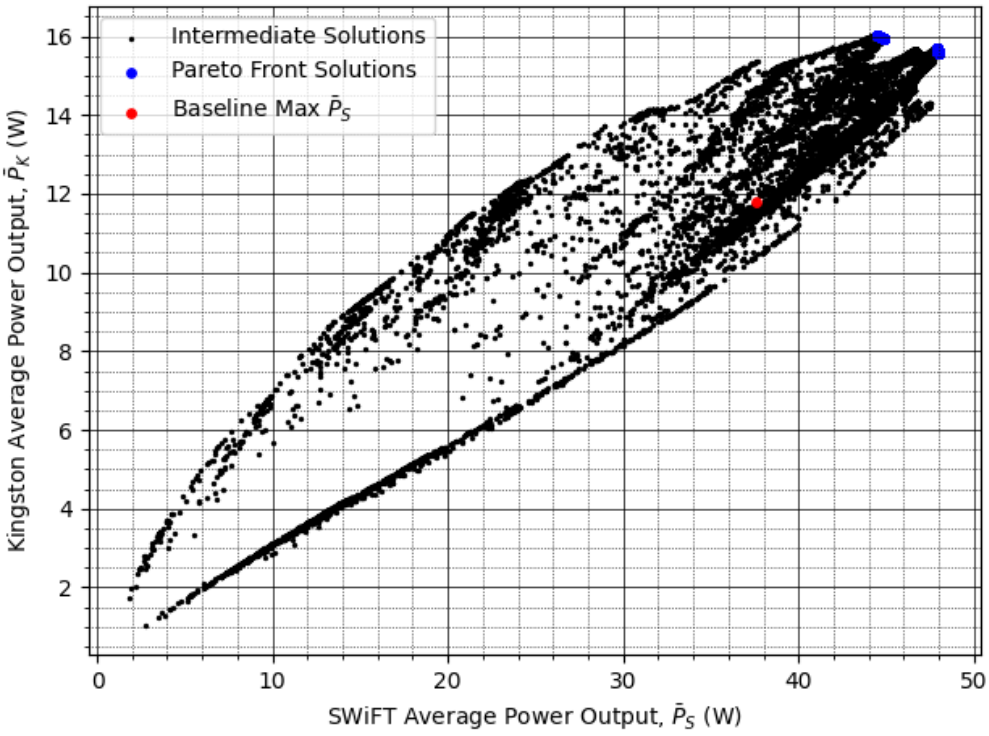

(a) All Solutions

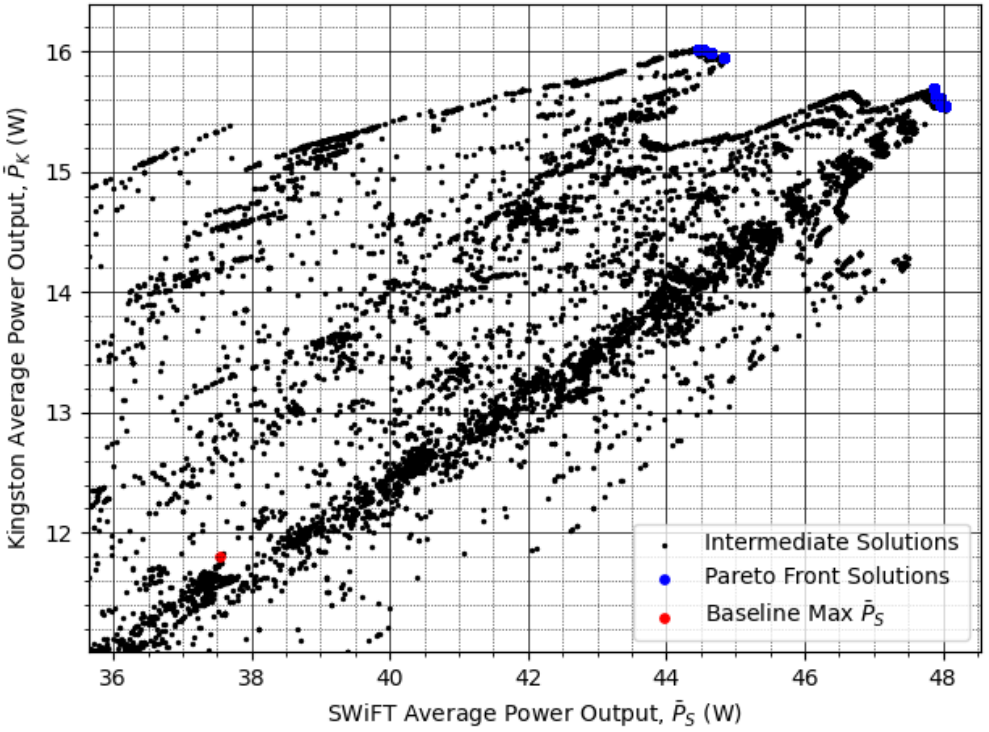

(b) Magnified View of the 65.5–48.5 W $\bar{P}_S$ Region

Figure E.3: All solutions explored by NSGA-II optimizing wind probability-weighted average power output at the SWiFT Test Site and Kingston, ON, for the Small Scale H-type VAWT with RPM as a variable.

E.2 1:7 Scale Sandia 17-m

This section covers the results for the 1:7 Scale Sandia 17-m VAWT described in Section 4.3 when rotational rate is a variable instead of TSR.

E.2.1 Maximization of $\overline{FLI}$ and $\bar{P}$

Table E.3: Performance characteristics of the various designs from optimizing probability-weighted average fatigue life indicator and power output at the SWiFT Test Site for the 1:7 Scale Sandia 17-m with RPM as a variable.

Design	RPM	$\overline{FLI}(\times 10^{-5})$	$\bar{P}$ (W)
Baseline	406.2	1.56	217.47
Maximum $\bar{P}$	425.0 (+4.6 %)	1.38 (−11.5 %)	253.85 (+16.7 %)
Equal $\bar{P}$	323.3 (−20.4 %)	2.26 (+44.9 %)	217.44 (0.0 %)

Values in parentheses denote percent difference compared to the Baseline.

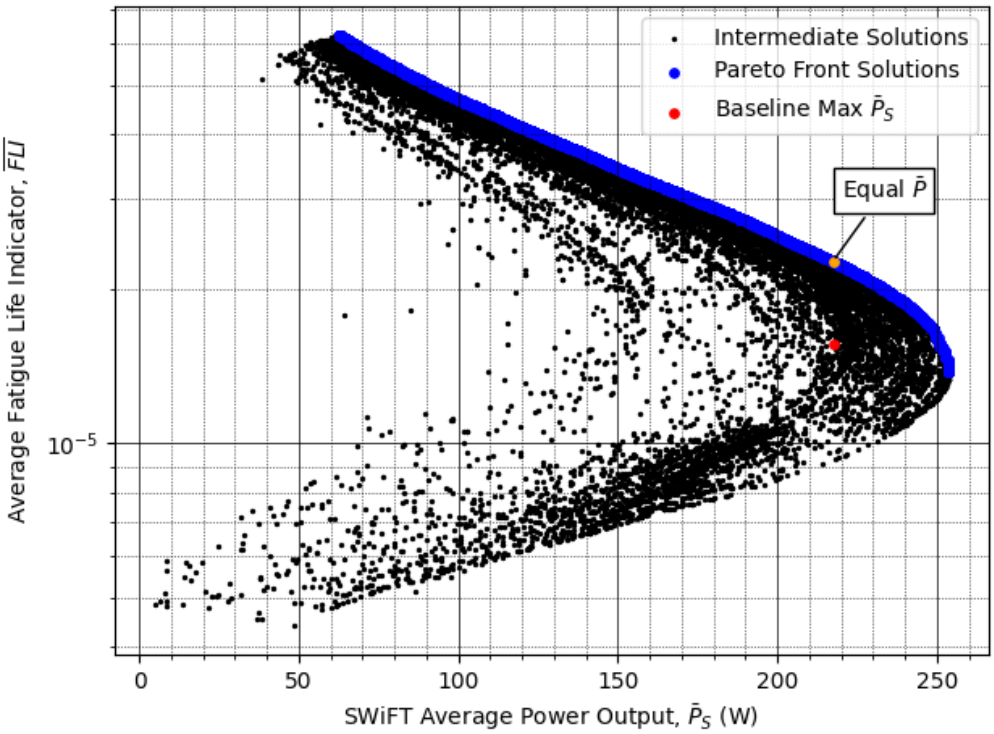

(a) All Solutions

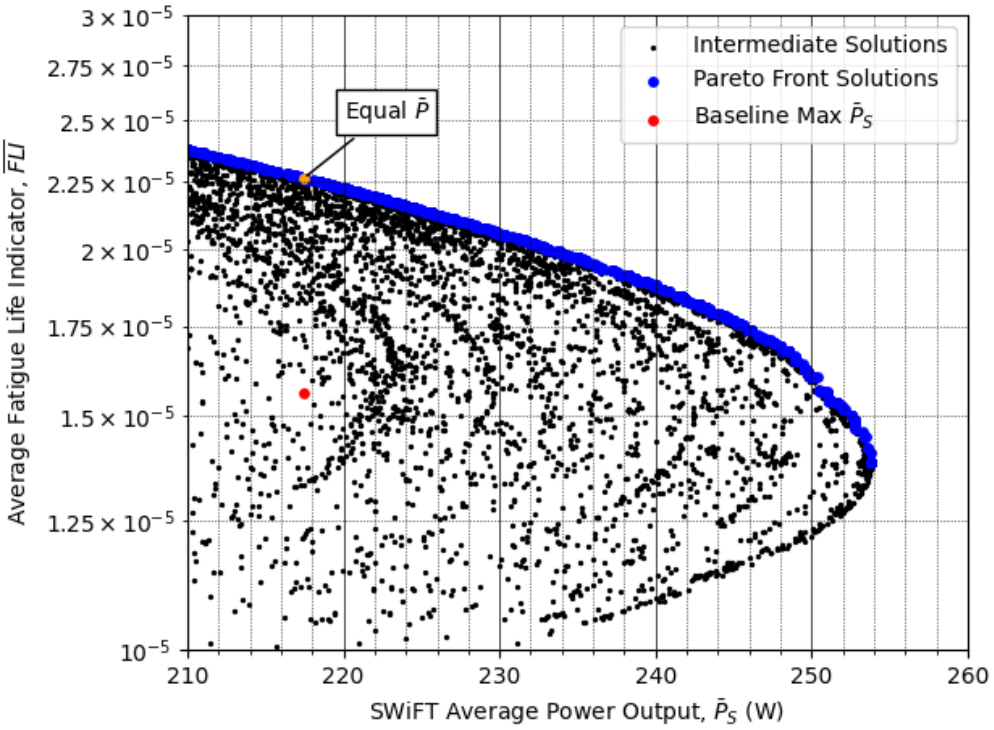

(b) Magnified View of the 210–260 W $\bar{P}_S$ Region

Figure E.4: All solutions explored by NSGA-II optimizing wind probability-weighted average fatigue life indicator and power output at the SWiFT Test Site for the 1:7 Scale Sandia 17-m with RPM as a variable.

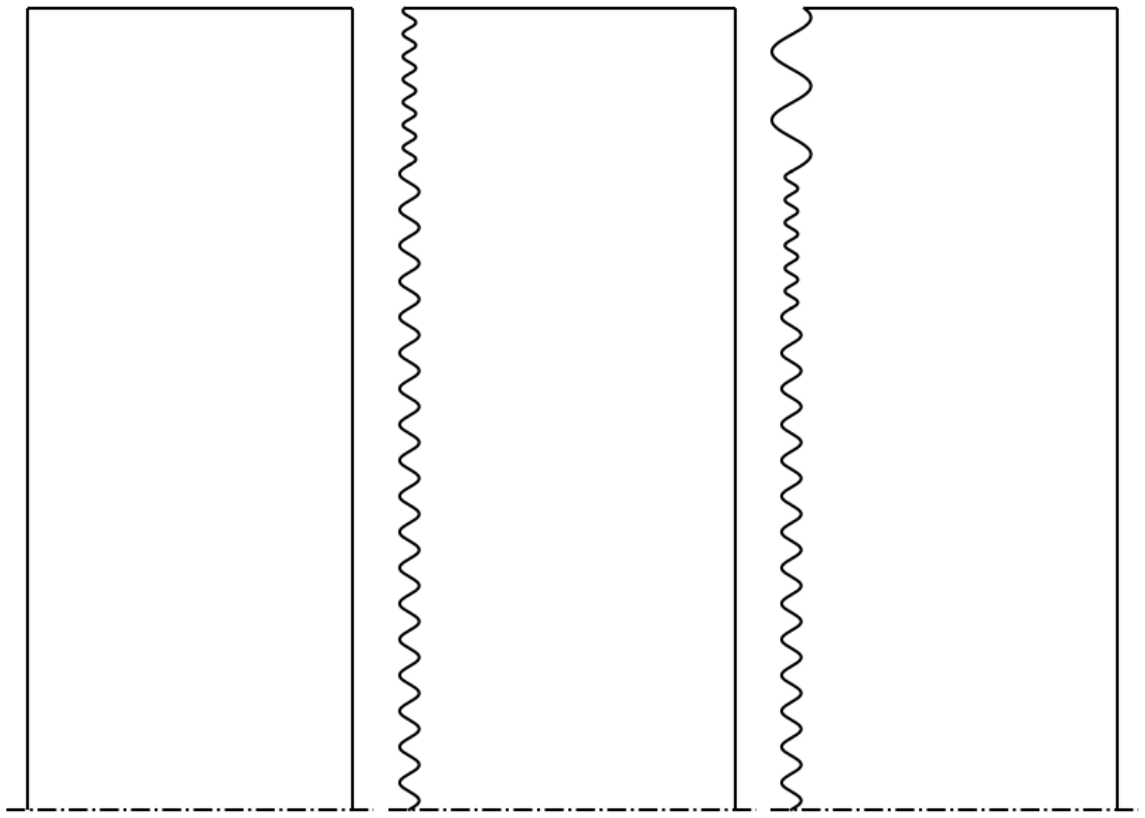

(a) Baseline (b) Maximum $\bar{P}$ & Point D (c) Equal $\bar{P}$ of Baseline

Figure E.5: Select half-blade designs from optimizing probability-weighted average fatigue life indicator and power output at the SWiFT Test Site for the 1:7 Scale Sandia 17-m with RPM as a variable. Note that the real blades are curved, so this figure shows the frontal projection of the blades and tubercle locations.

E.2.2 Maximization of $\bar{P}_S$ and $\bar{P}_K$

Table E.4: Performance characteristics of the various designs from optimizing probability-weighted average power output at the SWiFT Test Site and Kingston, ON, for the 1:7 Scale Sandia 17-m with RPM as a variable..

Design	RPM	$\bar{P}_S$	$\bar{P}_K$ (W)
Baseline	406.2	217.47	73.53
Maximum $\bar{P}_S$	423.2 (+4.2 %)	253.86 (+16.7 %)	86.21 (+17.2 %)
Maximum $\bar{P}_K$	369.5 (−9.0 %)	244.69 (+12.5 %)	88.51 (+20.4 %)

Values in parentheses denote percent difference compared to the Baseline.

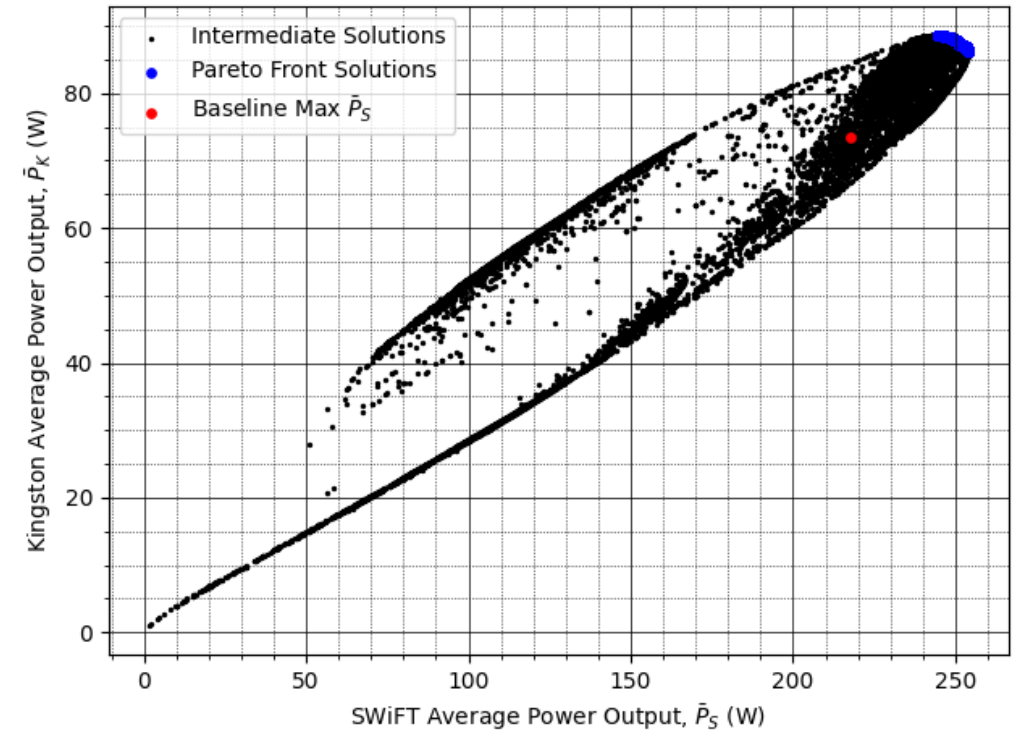

(a) All Solutions

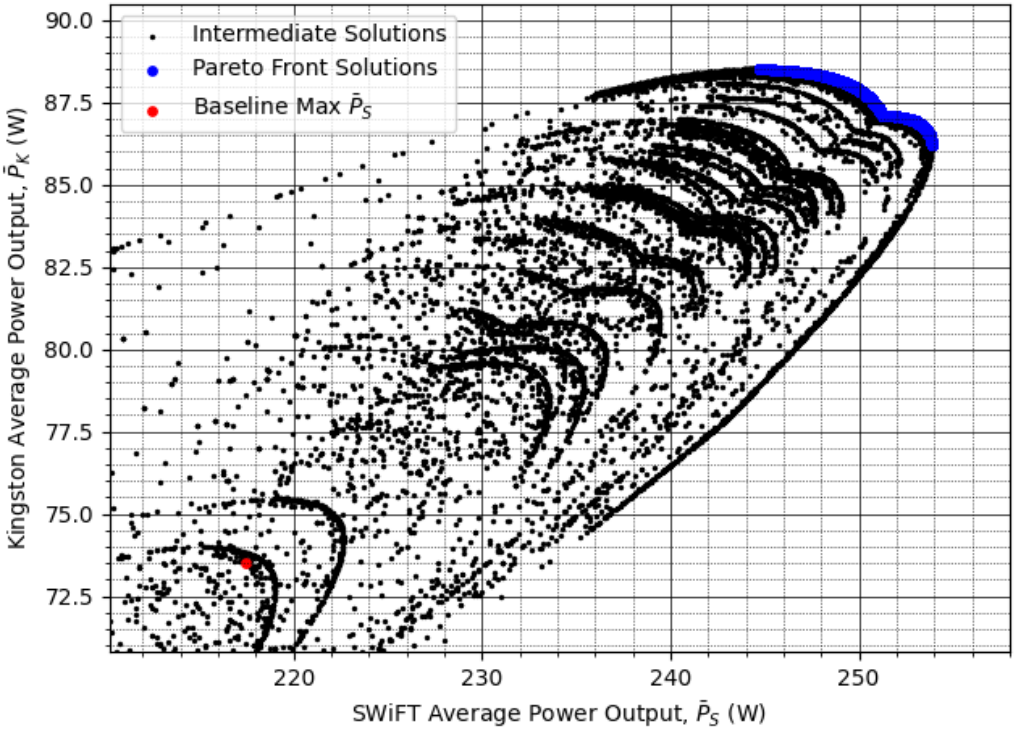

(b) Magnified View of the 210–258 W $\bar{P}_S$ Region

Figure E.6: All solutions explored by NSGA-II optimizing probability-weighted average power output at the SWiFT Test Site and Kingston, ON, for the 1:7 Scale Sandia 17-m with RPM as a variable.

F Experimental Uncertainty Calculations

This appendix details the derivation of uncertainty calculations used during the post-processing of all the experimental data, including both wind tunnel and outdoor testing. The uncertainty using both the torque sensor and spool up method are shown. The uncertainty was calculated using the Kline and McClintock uncertainty propagation method [110].

F.1 Air Density

The ambient density of air, ρ, was calculated using the ideal gas law, using the ambient temperature, T_∞, and pressure, p_∞, from the *Oakton*© WD-03316-8.

$$\rho = \frac{p_\infty}{R_{\text{air}} T_\infty} \tag{F.1}$$

where R_{air} is the specific gas constant of dry air ($287.05 \frac{J}{kg\,K}$). The uncertainty of ρ was then determined by:

$$\begin{aligned} \delta\rho &= \pm\sqrt{\left(\frac{\partial\rho}{\partial p_\infty}\delta p_\infty\right)^2 + \left(\frac{\partial\rho}{\partial T_\infty}\delta T_\infty\right)^2} \\ &= \pm\sqrt{\left(\frac{1}{R_{\text{air}} T_\infty}\delta p_\infty\right)^2 + \left(-\frac{p_\infty}{R_{\text{air}} T_\infty^2}\delta T_\infty\right)^2} \end{aligned} \tag{F.2}$$

F.2 Wind Tunnel Velocity

The wind tunnel velocity was measured using an *Omega* PX163 pressure transducer attached to a pitot tube at the wind tunnel exit. The pressure transducer provides the difference in pressure between the total and static pressure ports, which allows the velocity to be calculated using Bernoulli's equation, giving velocity as:

$$V = \sqrt{\frac{2\Delta p}{\rho}} \tag{F.3}$$

The uncertainty of velocity is then expressed as:

$$\begin{aligned}\delta V &= \pm\sqrt{\left(\frac{\partial V}{\partial \Delta p}\delta\Delta p\right)^2 + \left(\frac{\partial V}{\partial \rho}\delta\rho\right)^2} \\ &= \pm\sqrt{\left(\sqrt{\frac{1}{2\rho\Delta p}}\delta\Delta p\right)^2 + \left(-\sqrt{\frac{\Delta p}{2\rho^3}}\delta\rho\right)^2}\end{aligned} \tag{F.4}$$

F.3 Tip Speed Ratio

The tip speed ratio (TSR), $\hat{\lambda}$, was calculated by dividing the tip speed by wind speed, V. The tip speed is the product of rotational speed ω and turbine radius, R. ω was measured from the *Burster* 8656-5020 torque sensor, while V was either measured using the *Airmar* PB-150 weather station during outdoor testing, or calcSulated from the measure pressure differential from the *Omega* PX163 pressure transducer during wind tunnel testing. This gives TSR as:

$$\hat{\lambda} = \frac{\omega R}{V} \tag{F.5}$$

The uncertainty of $\hat{\lambda}$ is then determined by:

$$\begin{aligned}\delta\hat{\lambda} &= \pm\sqrt{\left(\frac{\partial\hat{\lambda}}{\partial\omega}\delta\omega\right)^2 + \left(\frac{\partial\hat{\lambda}}{\partial V}\delta V\right)^2} \\ &= \pm\sqrt{\left(\frac{R}{V}\delta\omega\right)^2 + \left(-\frac{\omega R}{V^2}\delta V\right)^2}\end{aligned} \tag{F.6}$$

F.4 Residual Torque

The residual torque, T_{res}, was determined by multiplying the instantaneous deceleration by the mass moment of inertia of the driven system, which includes the air bearing, couplers, torque sensor, and hysteresis brake, during spool down of the driven system. The deceleration was determined by the difference between two measurements of rotational speed from the *Burster* 8656-5020 torque sensor, $\Delta\omega$, where the uncertainty is twice the uncertainty of a single rotational speed measurement. The time between these measurements was determined from the *Raspberry Pi* internal clock, so there was assumed to be no uncertainty with this variable. The mass moment of inertia of the driven system, I_{rig}, was calculated by summing the contribution of the individual components, which were provided by either the manufacturer or *Solidworks'* mass properties tool. So, it was assumed that there was no uncertainty with I_{rig}.

$$T_{\text{res},i} = I_{\text{rig}}\frac{\omega_{i+1} - \omega_i}{t_{i+1} - t_i} = I_{\text{rig}}\left(\frac{\Delta\omega}{\Delta t}\right) \tag{F.7}$$

The resulting residual torque throughout six spool down runs was plotted, along with a line of best fit in Figure 5.15. The line of best fit is approximately in the centre of the spread of data, so the uncertainty of the equation of the line of best fit was assumed to be:

$$\begin{aligned}\delta T_{\text{res},i} &= \pm\sqrt{\left(\frac{\partial T_{\text{res},i}}{\partial \Delta\omega}\delta\Delta\omega\right)^2} \\ &= \pm I_{\text{rig}}\frac{1}{\Delta t}2\delta\omega\end{aligned} \tag{F.8}$$

F.5 Spool Up Torque

Similar to T_{res}, the torque produced throughout startup, T, was calculated by multiplying the total mass moment of inertia of both the driven system and the turbine itself, I_{rig} and I_{turb}, respectively, by the instantaneous acceleration throughout startup. This is given by:

$$T_i = (I_{\text{rig}} + I_{\text{turb}})\,\frac{\omega_{i+1} - \omega_i}{t_{i+1} - t_i} = (I_{\text{rig}} + I_{\text{turb}})\left(\frac{\Delta\omega}{\Delta t}\right) \tag{F.9}$$

The only difference between the spool up torque uncertainty and the residual torque uncertainty calculation is the presence of an uncertainty in I_{turb}, calculated by summing the contribution of all individual components of the turbine geometry/rotor's mass moment of inertia. All components except for the blade were determined using *Solidworks'* mass properties tool, so no uncertainty was assumed to be associated with these contributions. The blades, on the other hand, were measured on a scale with an uncertainty of $\pm\,1$ g and assumed to be point masses at R from the axis of rotation.

$$\begin{aligned}\delta T_i &= \pm\sqrt{\left(\frac{\partial T_i}{\partial \Delta\omega}\delta\Delta\omega\right)^2 + \left(\frac{\partial T_i}{\partial I_{\text{turb}}}\delta I_{\text{turb}}\right)^2} \\ &= \pm\sqrt{\left((I_{\text{rig}} + I_{\text{turb}})\,\frac{1}{\Delta t}2\delta\omega\right)^2 + \left(\frac{\Delta\omega}{\Delta t}\delta I_{\text{turb}}\right)^2}\end{aligned} \tag{F.10}$$

F.6 Torque Sensor

The *Burster* 8656-5020 torque sensor has a variety of sources of uncertainty, namely the relative non-linearity, U_{lin}, relative hysteresis, U_{hyst}, tolerance of sensitivity, U_{s}, effect of temperature on sensitivity, TK_{s}, and the effect of temperature on zero point, TK_0. Wegener and Andrae [119] suggest rooting the sum of squares of all contributions to determine the uncertainty of the torque sensor. During wind tunnel and outdoor testing, the temperature had little variation, so the effect of temperature was assumed to be negligible. The measured torque values were well below the full scale of the torque sensor, so the effect of hysteresis was assumed to be negligible as well. Thus, the uncertainty of the torque sensor measurements, δT, was assumed to be:

$$\delta T = \sqrt{U_{\text{lin}}^2 + U_{\text{s}}^2} \tag{F.11}$$

F.7 Blade Torque

The torque produced by the blades, T_b, was determined by subtracting the residual torque, T_res, from either the torque calculated during the spool up method, or the torque directly measured from the *Burster* 8656-5020 torque sensor, T, as described in the following equation:

$$T_\mathrm{b} = T - T_\mathrm{res} \tag{F.12}$$

The uncertainty is then given by:

$$\begin{aligned} \delta T_\mathrm{b} &= \pm\sqrt{\left(\frac{\partial T_\mathrm{b}}{\partial T}\delta T\right)^2 + \left(\frac{\partial T_\mathrm{b}}{\partial T_\mathrm{res}}\delta T_\mathrm{res}\right)^2} \\ &= \pm\sqrt{(\delta T)^2 + (\delta T_\mathrm{res})^2} \end{aligned} \tag{F.13}$$

F.8 Power

The power of the turbine, P was determined by multiplying the average blade torque throughout rotation, T_b, by the rotational speed of the turbine, ω. This gives power extracted as:

$$P = T_\mathrm{b}\omega \tag{F.14}$$

Thus, the uncertainty in power is given by:

$$\begin{aligned} \delta P &= \pm\sqrt{\left(\frac{\partial P}{\partial T_\mathrm{b}}\delta T_\mathrm{b}\right)^2 + \left(\frac{\partial P}{\partial \omega}\delta\omega\right)^2} \\ &= \pm\sqrt{(\omega\delta T_\mathrm{b})^2 + (T_\mathrm{b}\delta\omega)^2} \end{aligned} \tag{F.15}$$

F.9 Coefficient of Power

Lastly, the coefficient of power, C_P was calculated by the equation:

$$C_P = \frac{P}{0.5\rho S V^3} \tag{F.16}$$

where P was calculated as explained in Section F.8 using either the torque sensor torque or spool up method, while the air density, ρ, was determined as described Section F.1, and the wind speed, V, was either determined by an *Omega* PX163 pressure transducer attached to a pitot tube during wind tunnel testing, or the *Airmar* PB-150 weather station during outdoor testing, each with an associated uncertainty. This gives the overall uncertainty of C_P as:

$$\begin{aligned} \delta C_P &= \pm\sqrt{\left(\frac{\partial C_P}{\partial P}\delta P\right)^2 + \left(\frac{\partial C_P}{\partial \rho}\delta\rho\right)^2 + \left(\frac{\partial C_P}{\partial V}\delta V\right)^2} \\ &= \pm\sqrt{\left(\frac{2}{\rho S V^3}\delta P\right)^2 + \left(-\frac{P}{0.5\rho^2 S V^3}\delta\rho\right)^2 + \left(-\frac{6P}{\rho S V^4}\delta V\right)^2} \end{aligned} \tag{F.17}$$

G Additional Experimental Results

This appendix provides additional experimental results obtained using the RMC VAWT Rig, either in the RMC Open Jet Wind Tunnel, described in Section 5.2.7, or outside. The results show start-up performance and power output using two different methods, either the spool up torque method, detailed in Section 5.2.4, or using the RMC VAWT Rig's hysteresis brake.

G.1 Wind Tunnel Startup

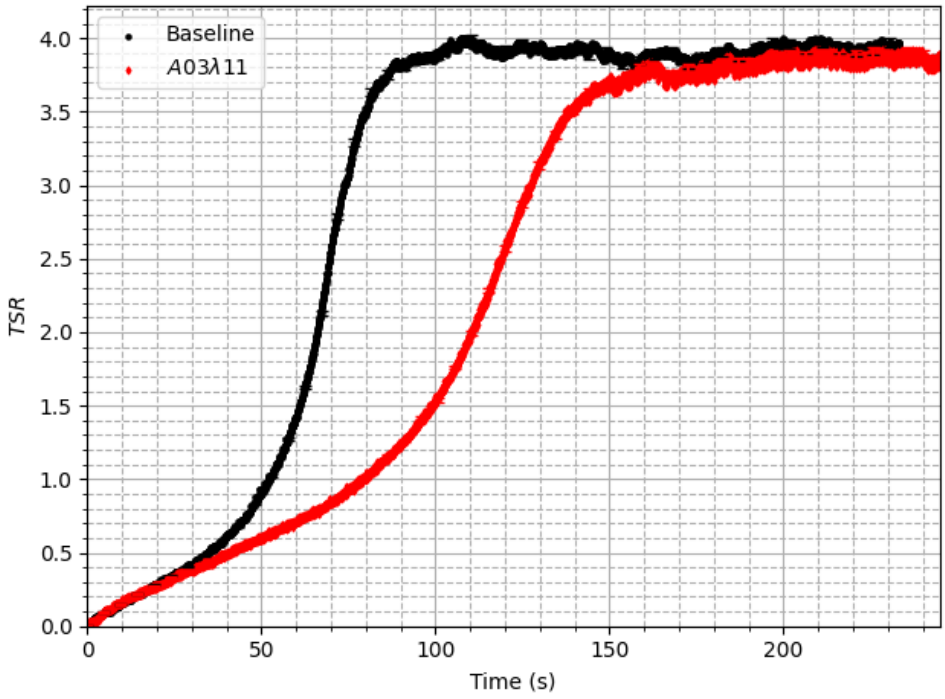

(a) Startup

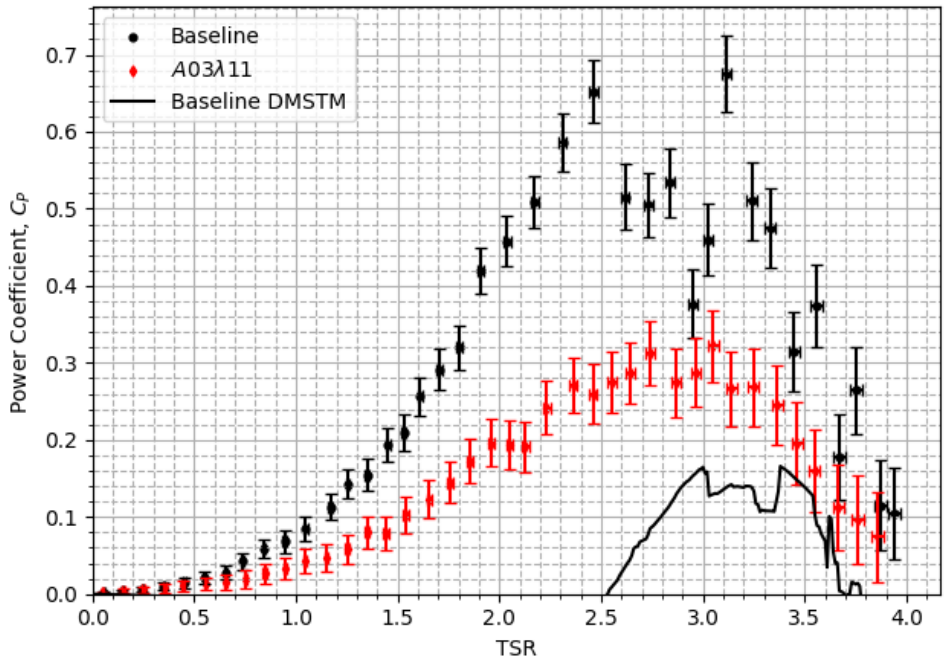

(b) Power Coefficient

Figure G.1: Startup and spool up power coefficient curves of the $A03\lambda11$ blades compared to the baseline in the wind tunnel at a motor frequency of 27.5 Hz.

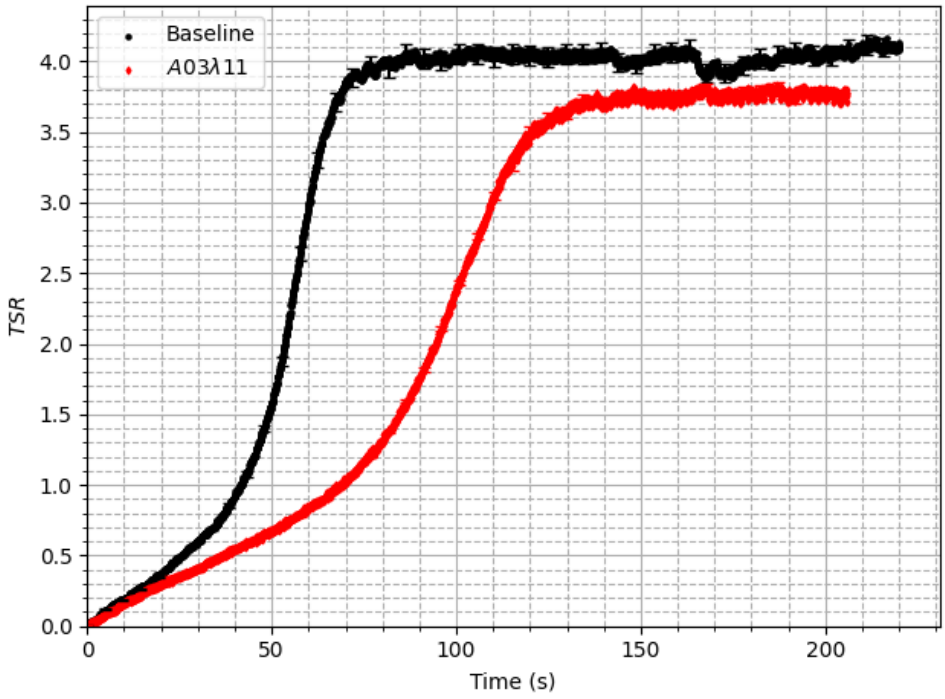

(a) Startup

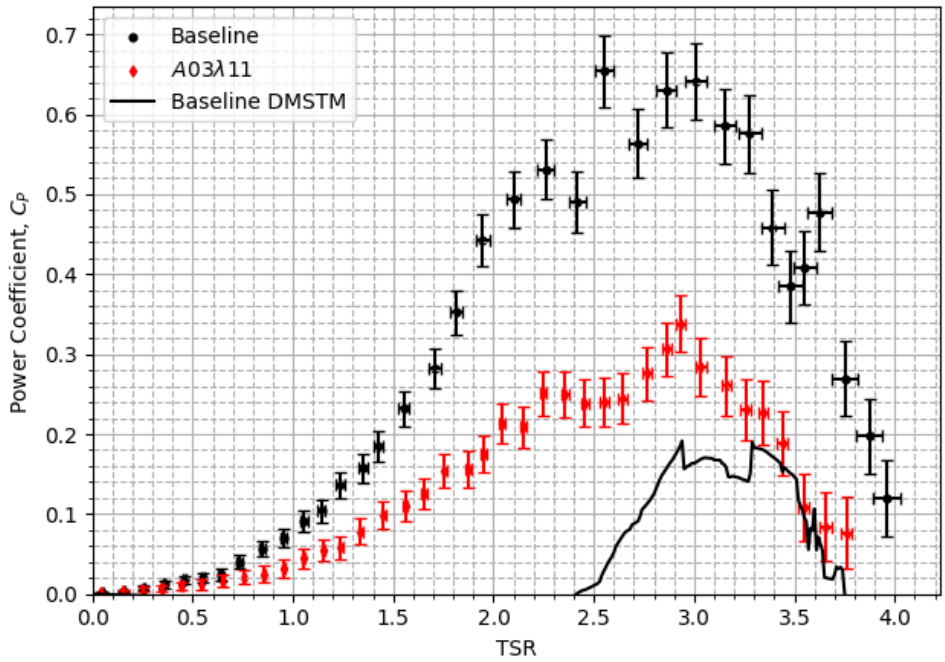

(b) Power Coefficient

Figure G.2: Startup and spool up power coefficient curves of the $A03\lambda11$ blades compared to the baseline in the wind tunnel at a motor frequency of 30.0 Hz.

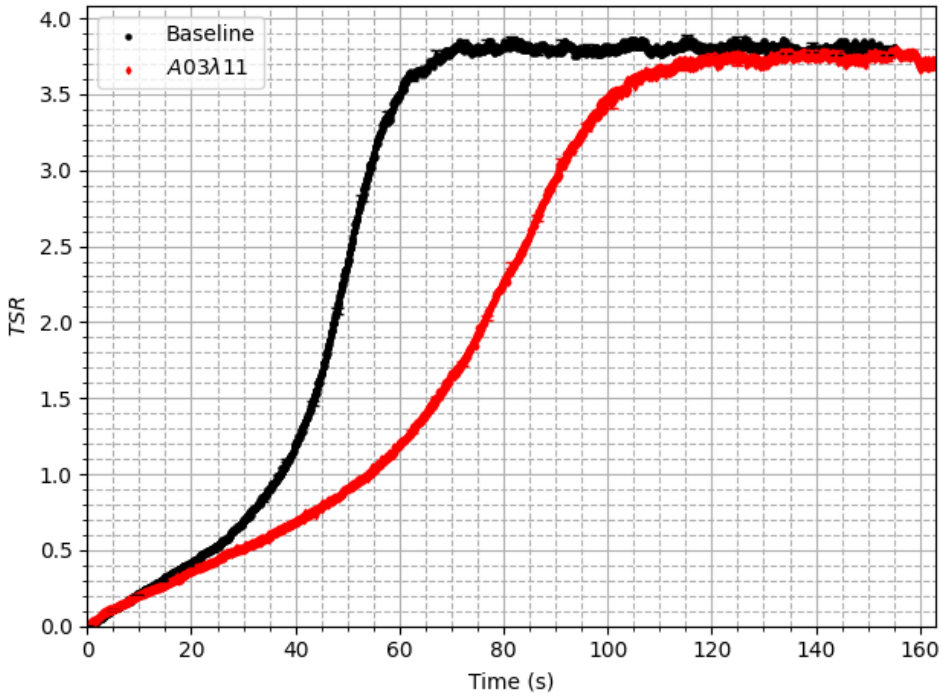

(a) Startup

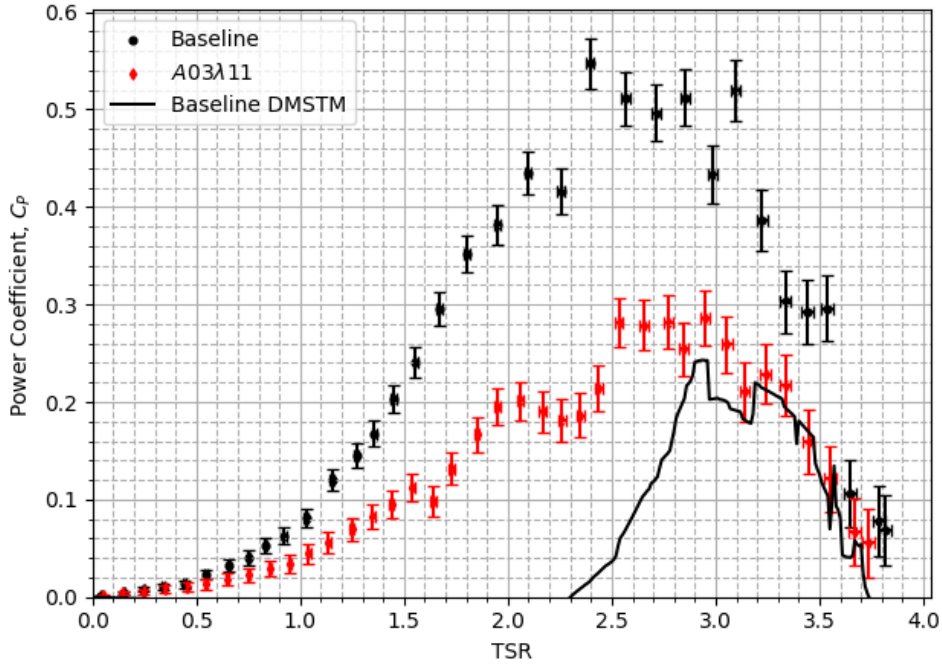

(b) Power Coefficient

Figure G.3: Startup and spool up power coefficient curves of the $A03\lambda11$ blades compared to the baseline in the wind tunnel at a motor frequency of 32.5 Hz.

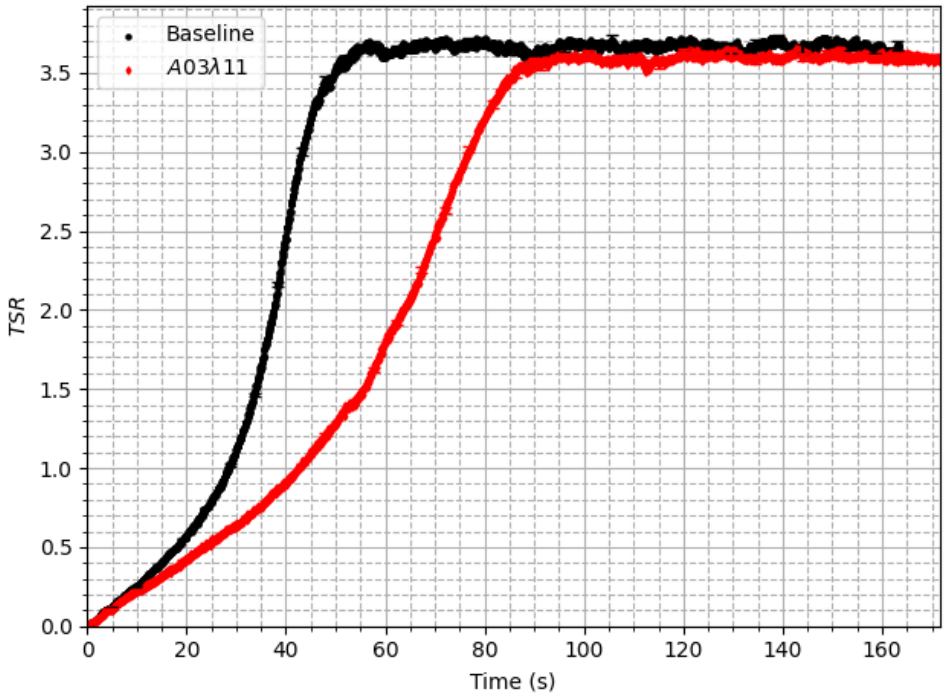

(a) Startup

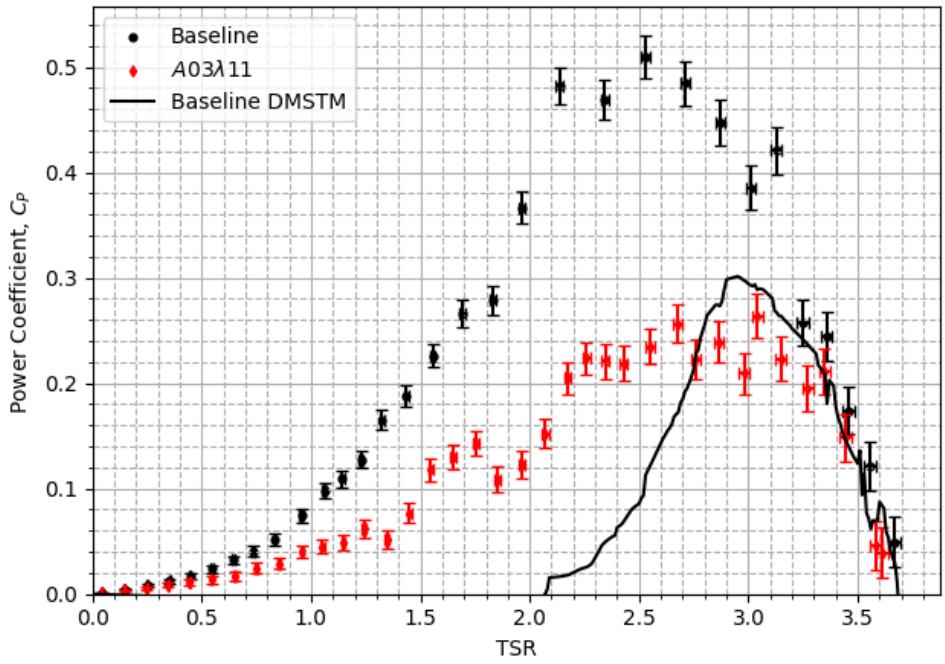

(b) Power Coefficient

Figure G.4: Startup and spool up power coefficient curves of the $A03\lambda11$ blades compared to the baseline in the wind tunnel at a motor frequency of 37.5 Hz.

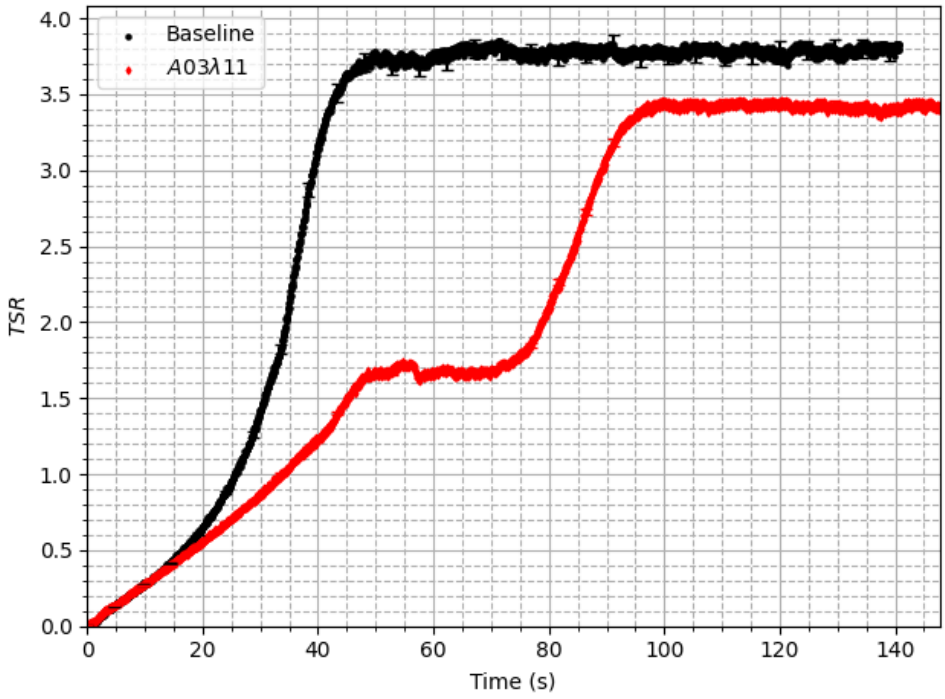

(a) Startup

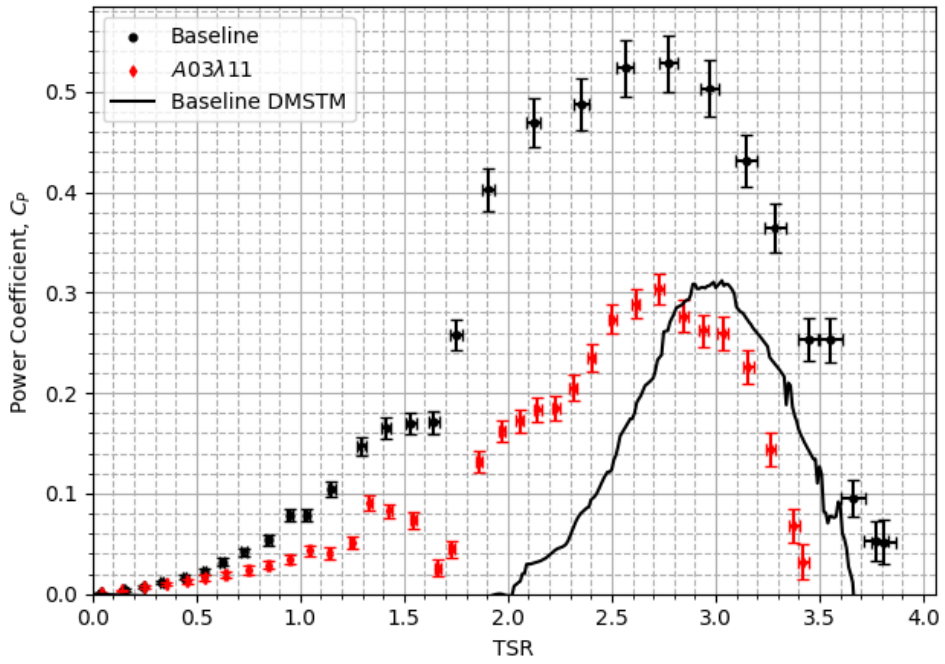

(b) Power Coefficient

Figure G.5: Startup and spool up power coefficient curves of the $A03\lambda11$ blades compared to the baseline in the wind tunnel at a motor frequency of 42.5 Hz.

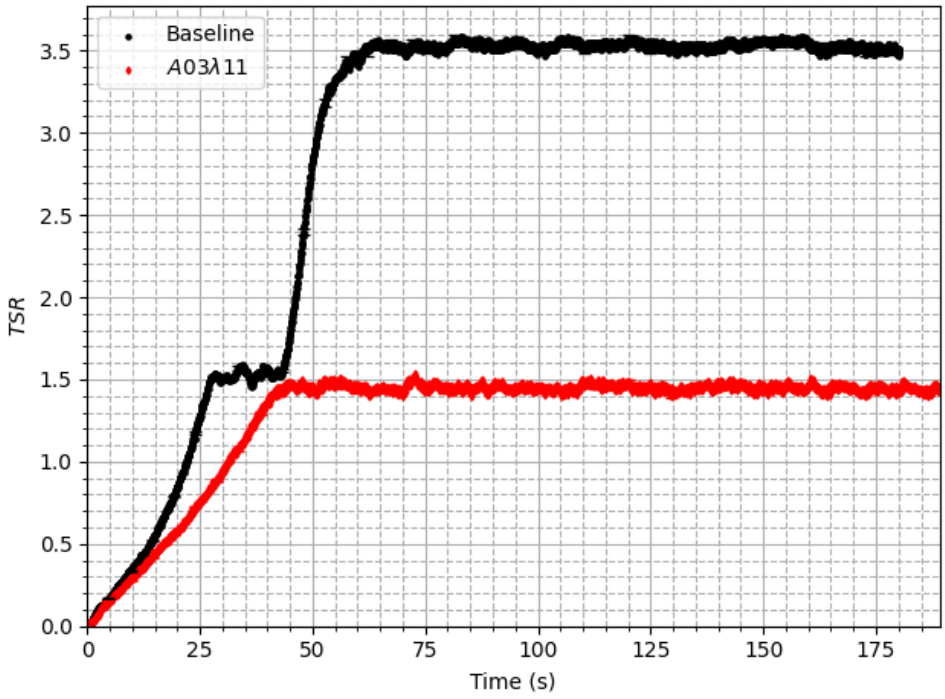

(a) Startup

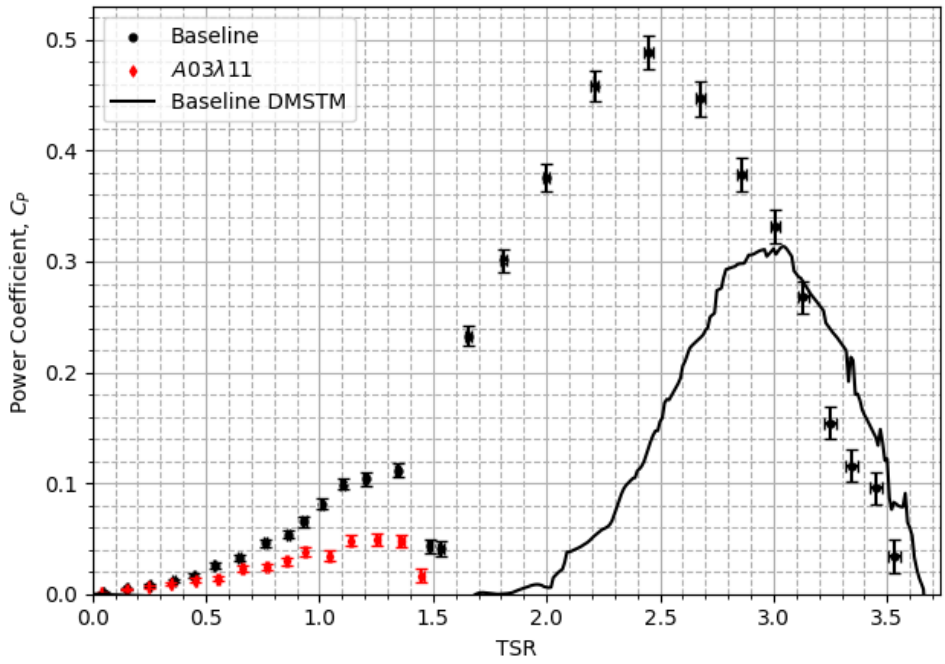

(b) Power Coefficient

Figure G.6: Startup and spool up power coefficient curves of the $A03\lambda11$ blades compared to the baseline in the wind tunnel at a motor frequency of 45.0 Hz.

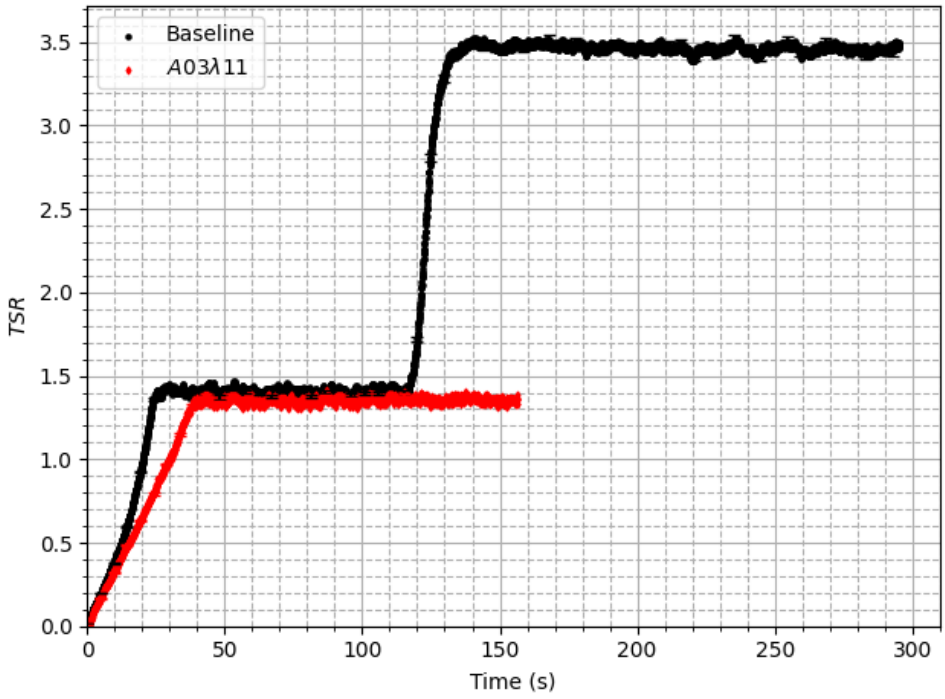

(a) Startup

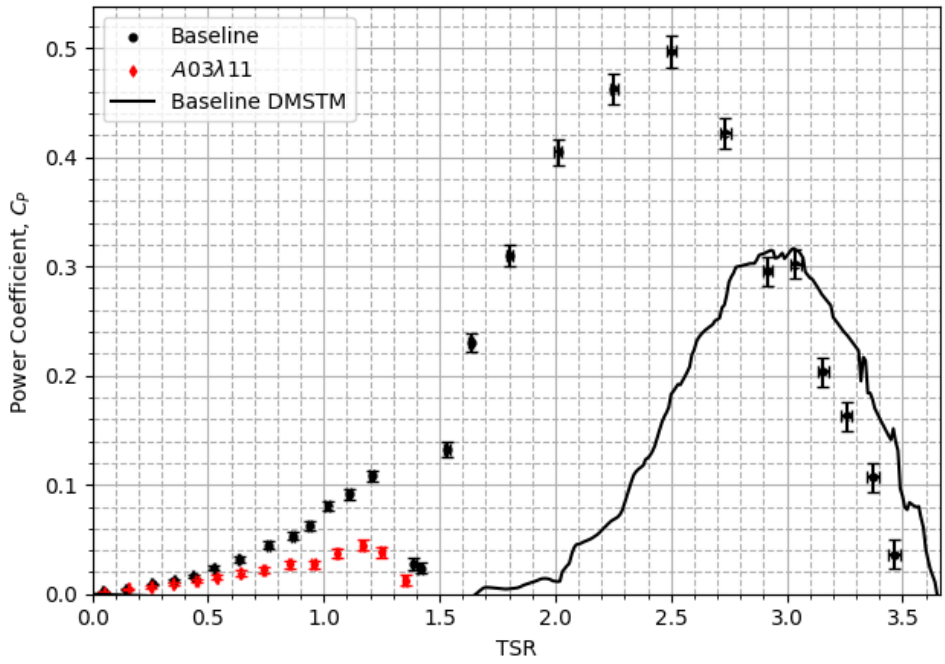

(b) Power Coefficient

Figure G.7: Startup and spool up power coefficient curves of the $A03\lambda11$ blades compared to the baseline in the wind tunnel at a motor frequency of 47.5 Hz.

G.2 Wind Tunnel Power Curves

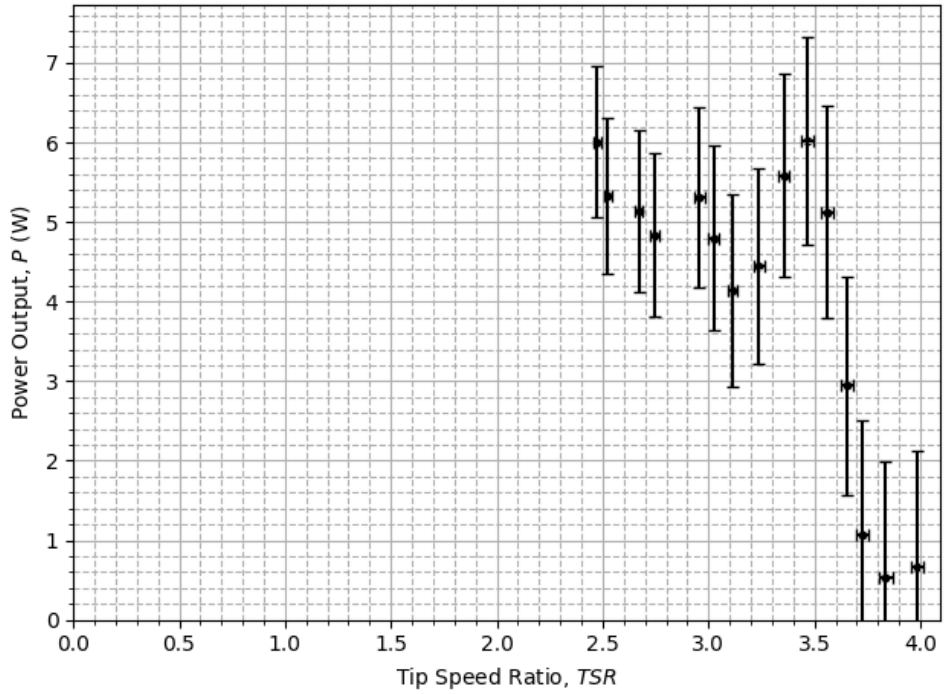

(a) Power

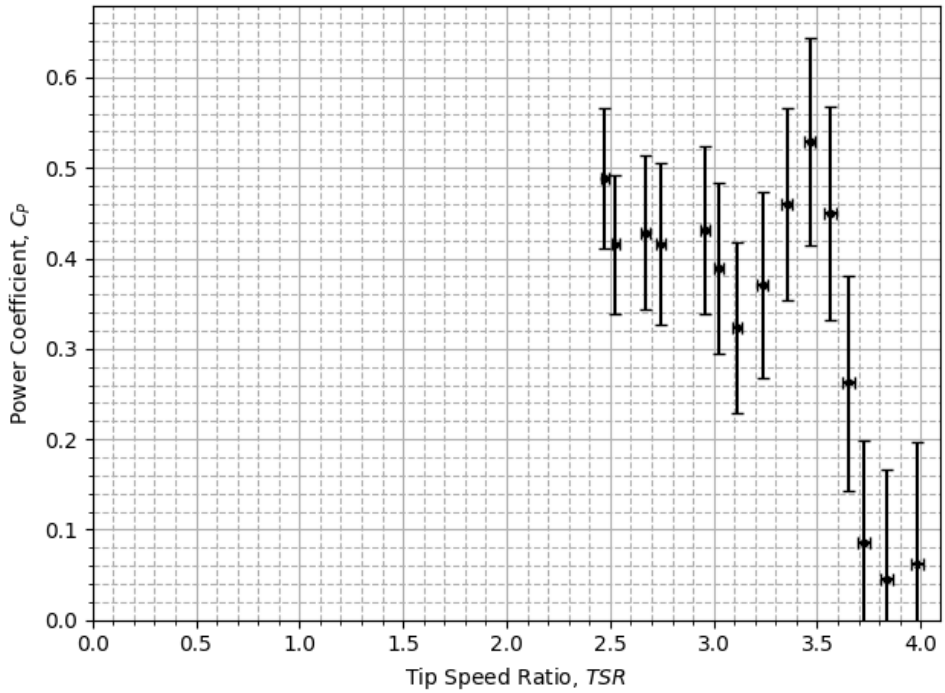

(b) Power Coefficient

Figure G.8: Power and power coefficient curves of the baseline blades in the wind tunnel at a motor frequency of 27.5 Hz using steady state torque measurements.

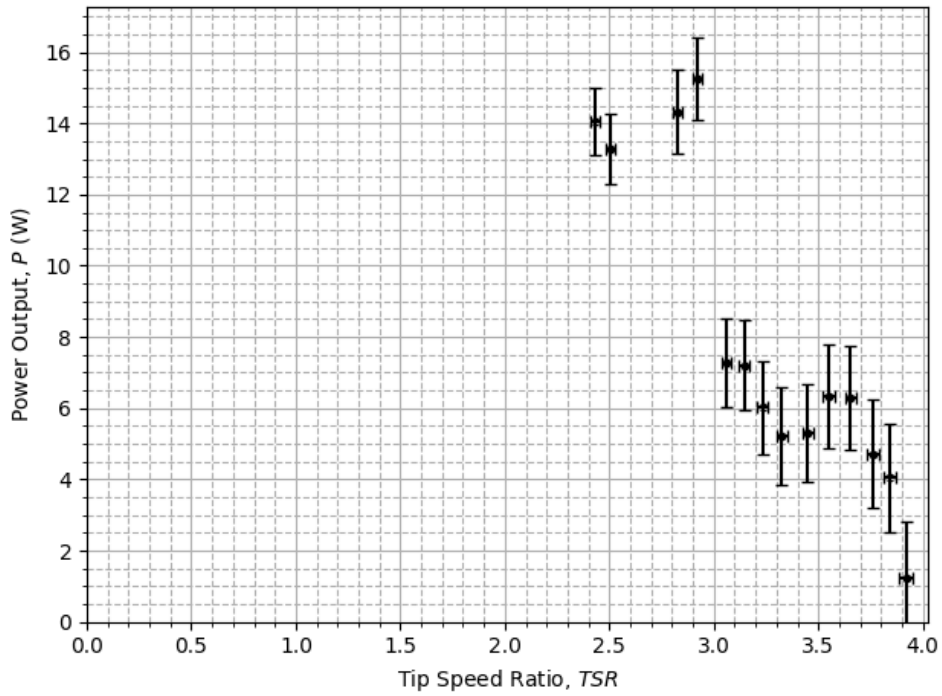

(a) Power

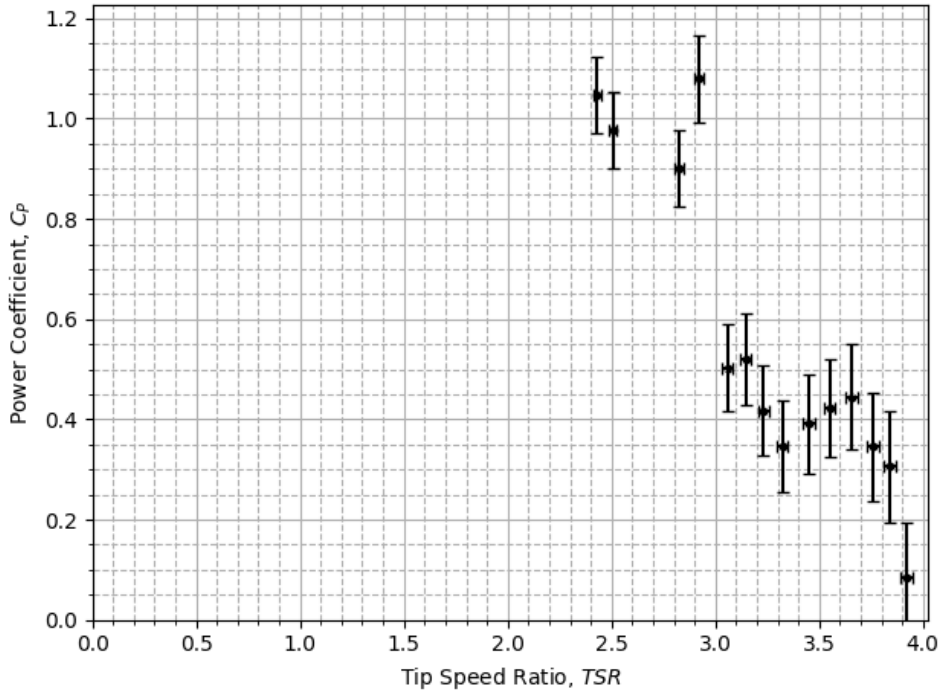

(b) Power Coefficient

Figure G.9: Power and power coefficient curves of the baseline blades in the wind tunnel at a motor frequency of 30.0 Hz using steady state torque measurements.

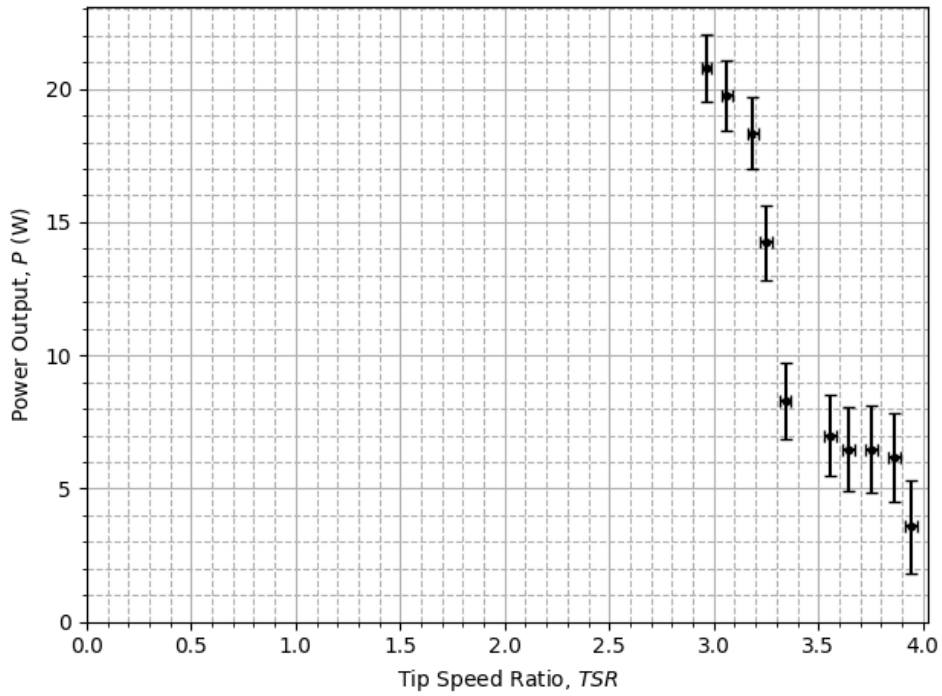

(a) Power

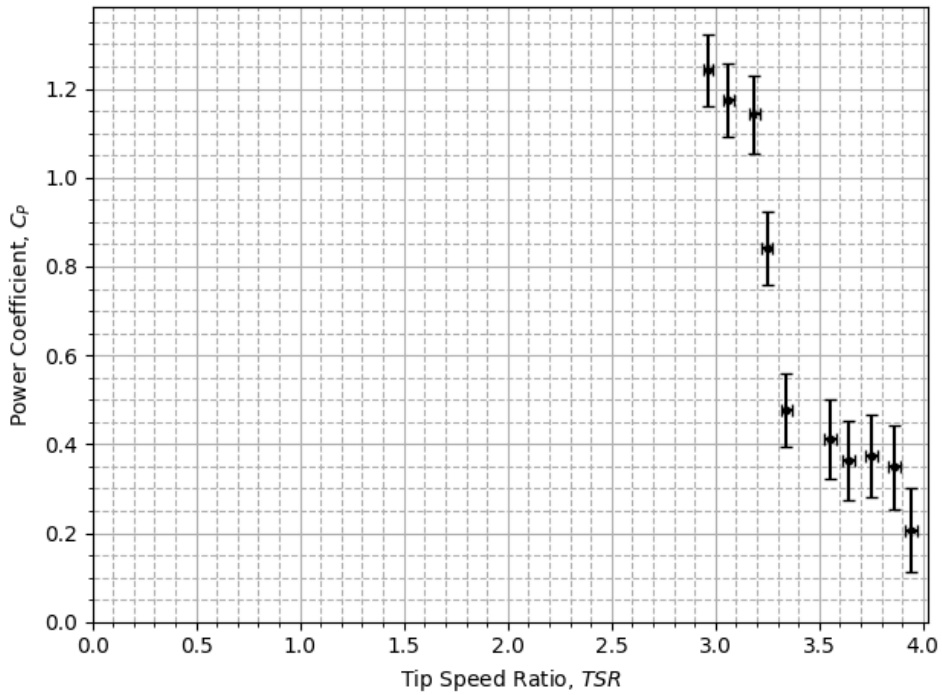

(b) Power Coefficient

Figure G.10: Power and power coefficient curves of the baseline blades in the wind tunnel at a motor frequency of 32.5 Hz using steady state torque measurements.

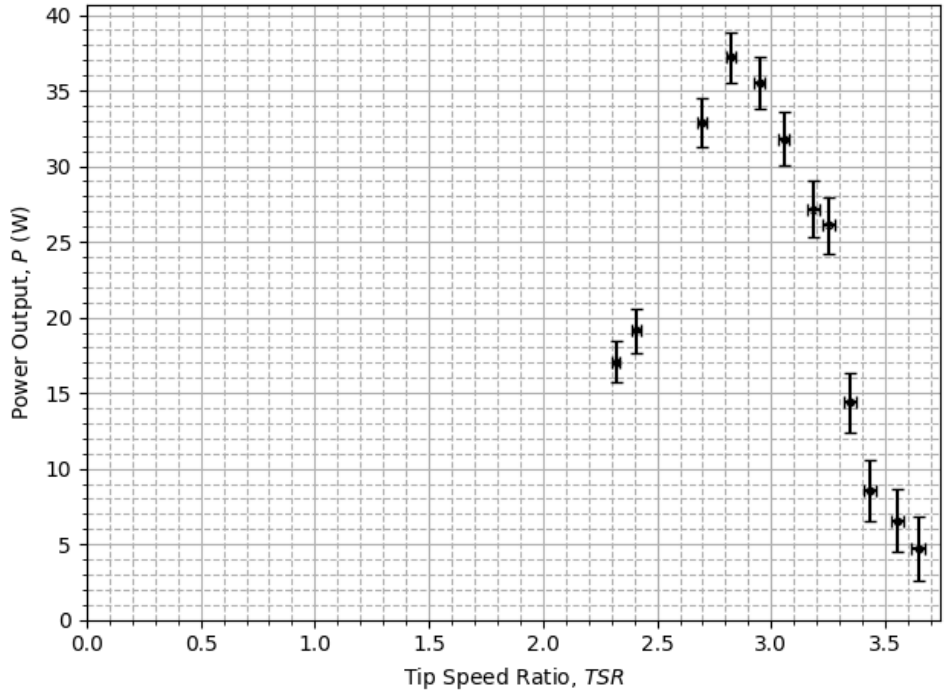

(a) Power

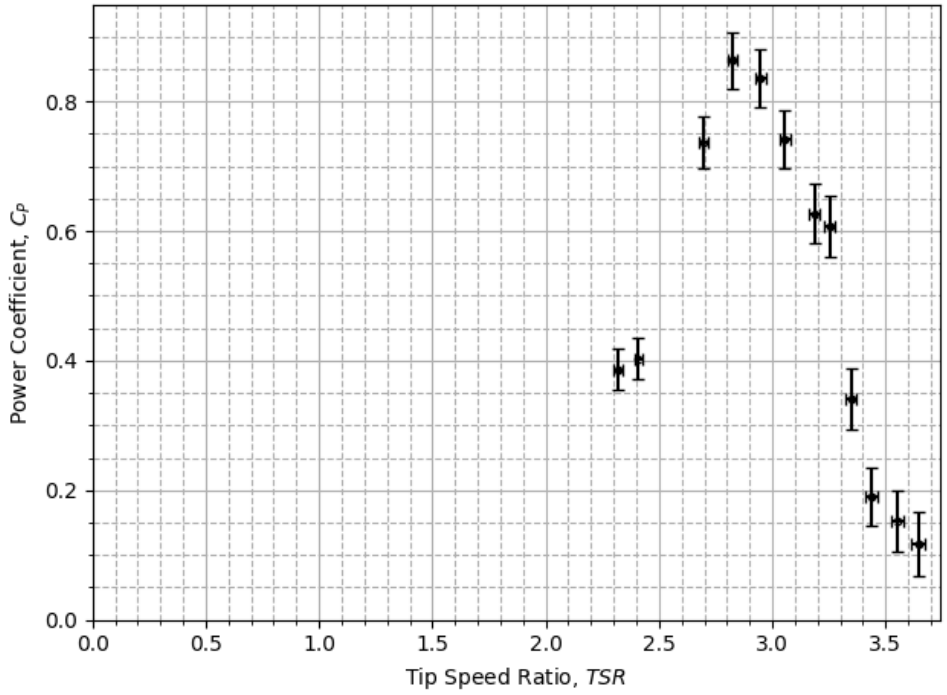

(b) Power Coefficient

Figure G.11: Power and power coefficient curves of the baseline blades in the wind tunnel at a motor frequency of 40.0 Hz using steady state torque measurements.

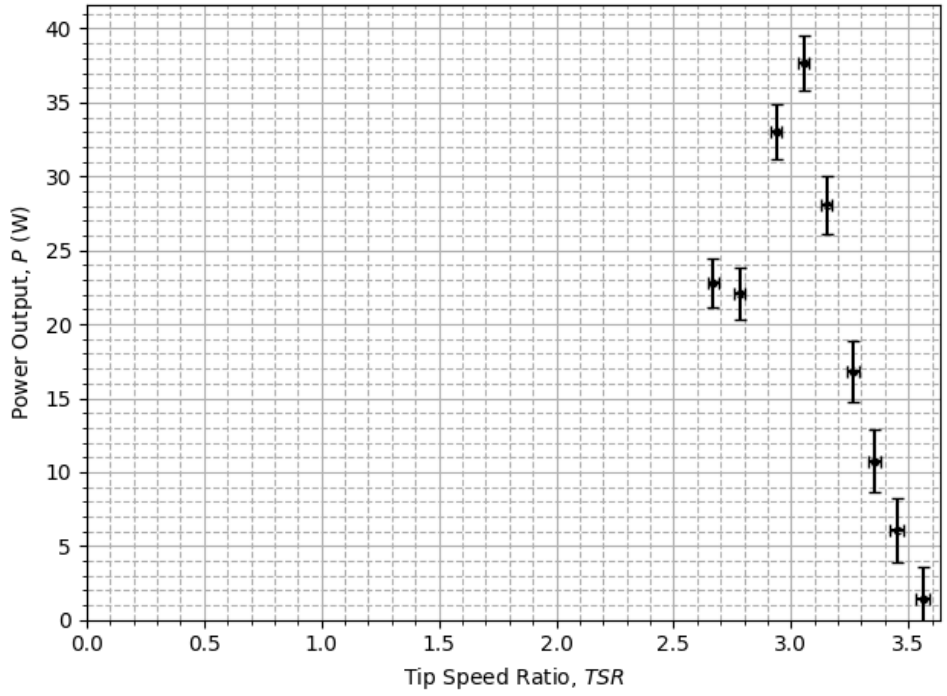

(a) Power

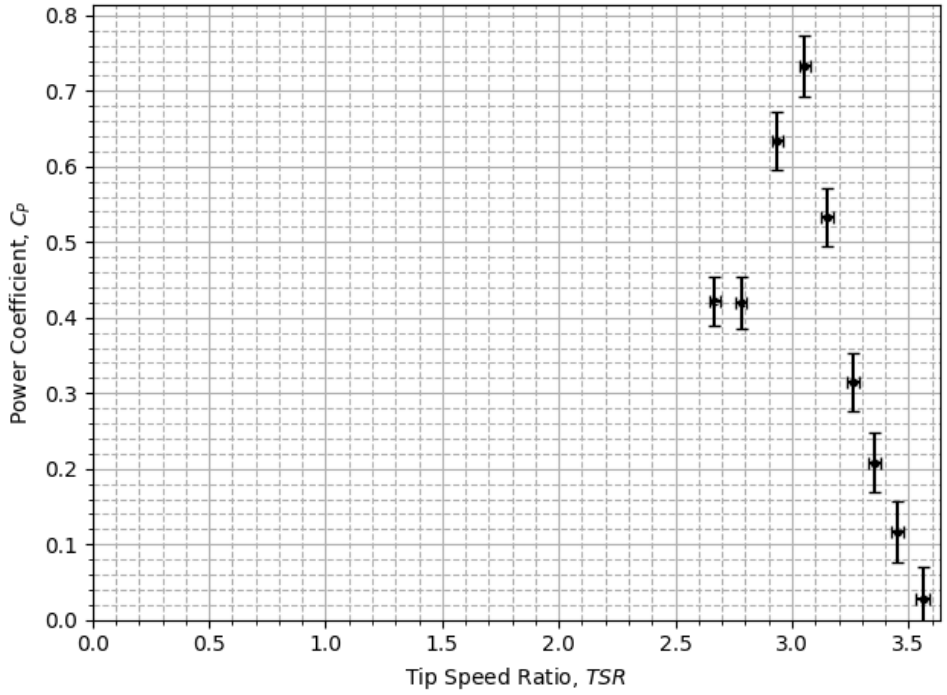

(b) Power Coefficient

Figure G.12: Power and power coefficient curves of the baseline blades in the wind tunnel at a motor frequency of 42.5 Hz using steady state torque measurements.

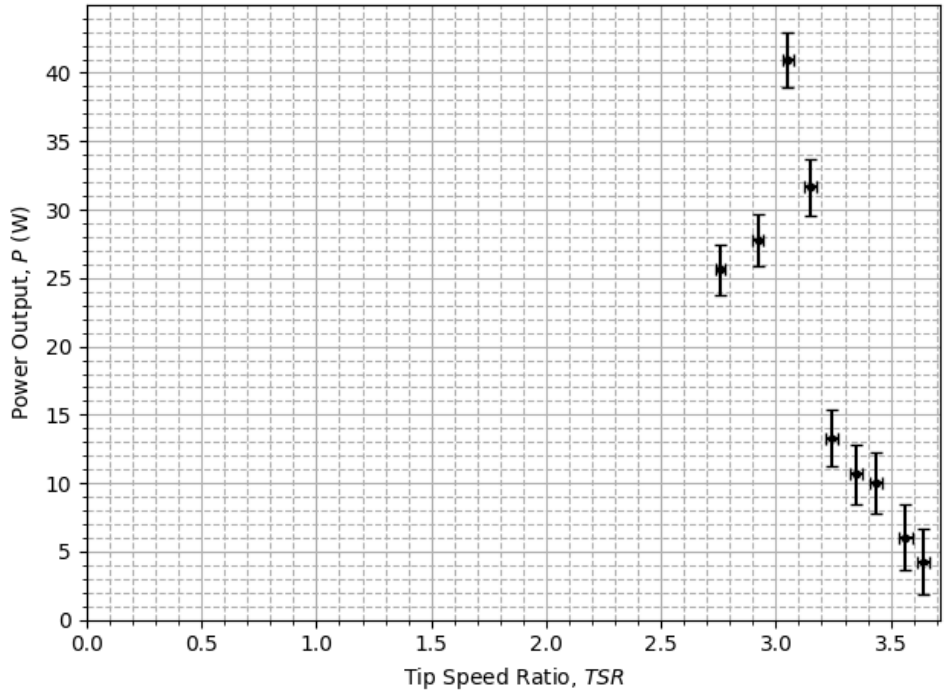

(a) Power

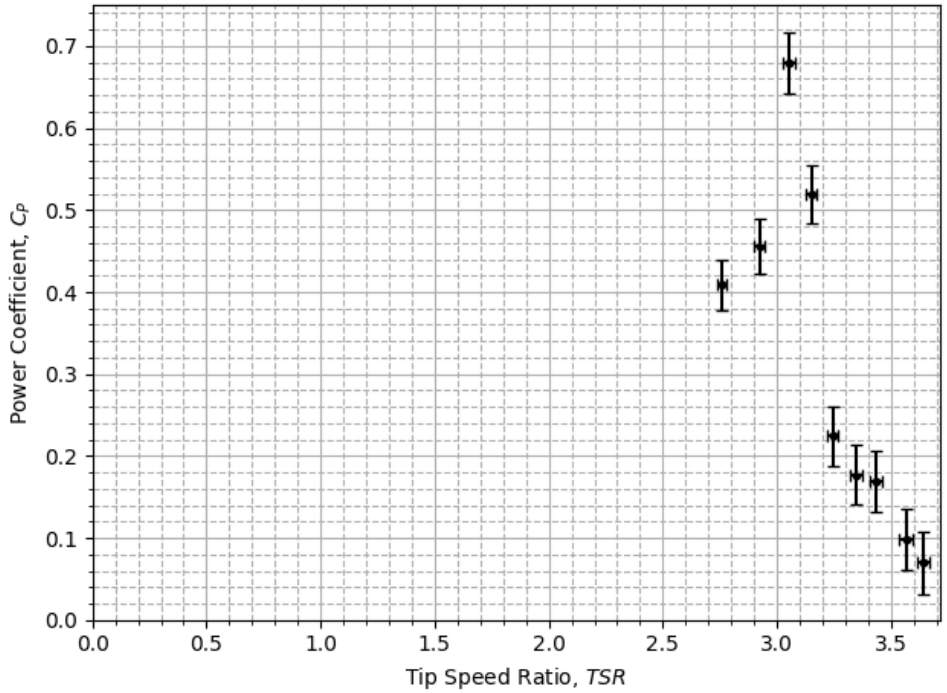

(b) Power Coefficient

Figure G.13: Power and power coefficient curves of the baseline blades in the wind tunnel at a motor frequency of 45.0 Hz using steady state torque measurements.

G.3 Outdoor Startup

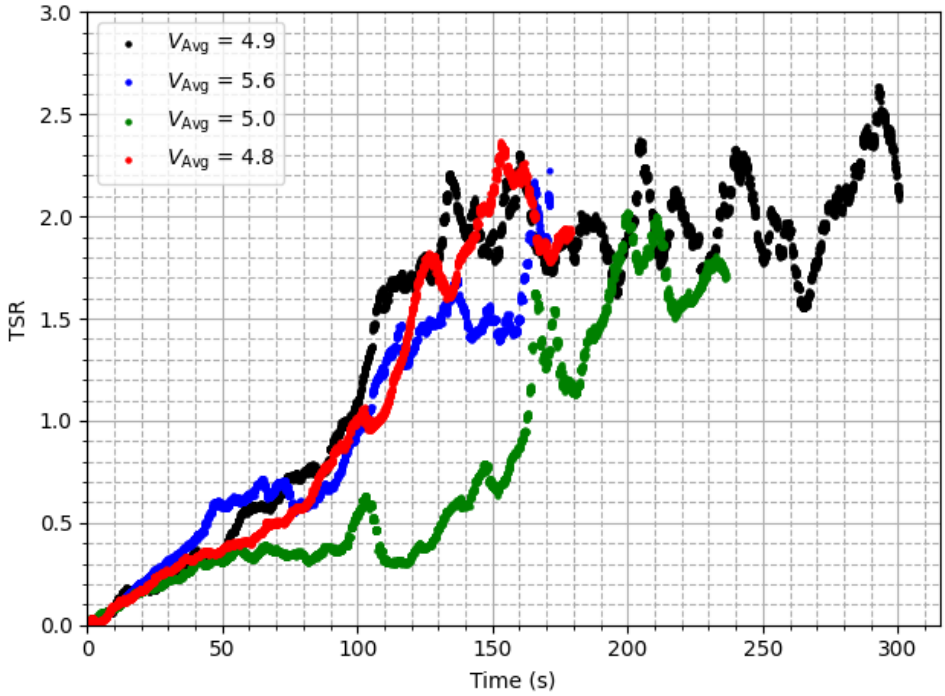

(a) TSR

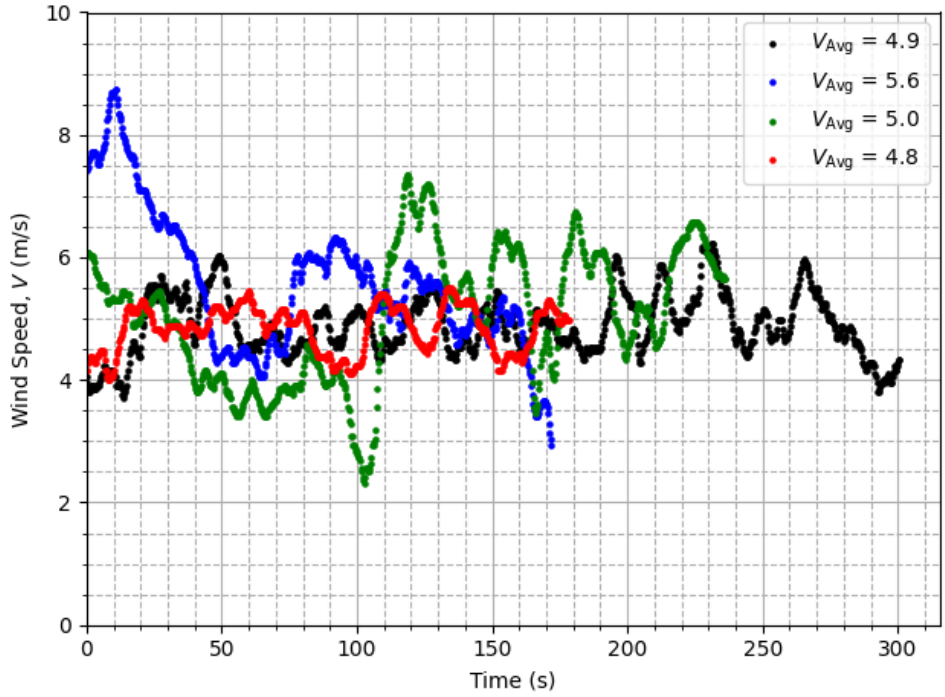

(b) Wind Speed

Figure G.14: Outdoor startup TSR and wind speed of the Baseline blades at varying wind conditions.

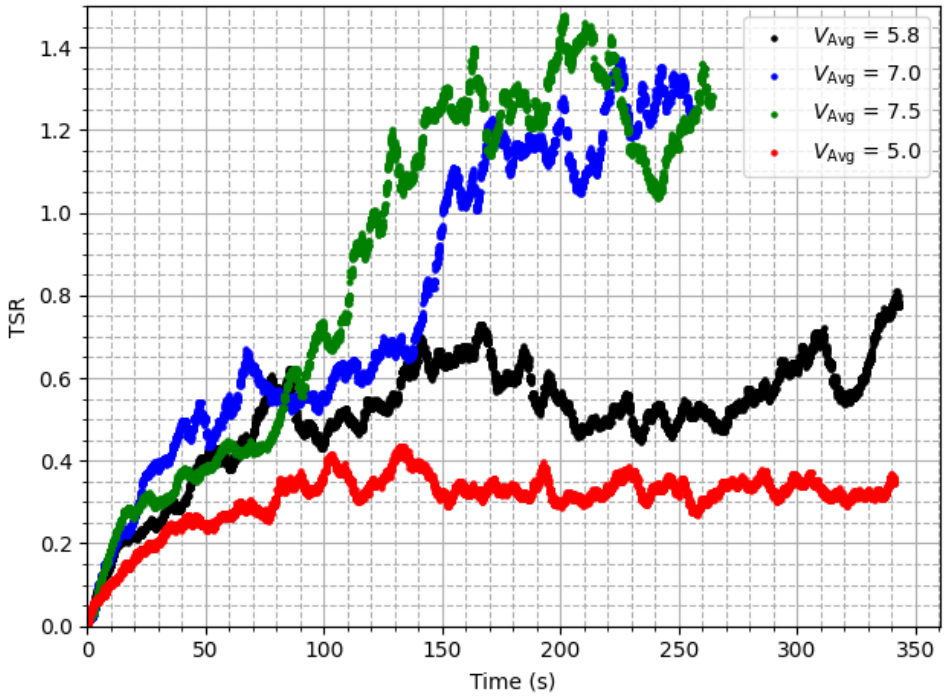

(a) TSR

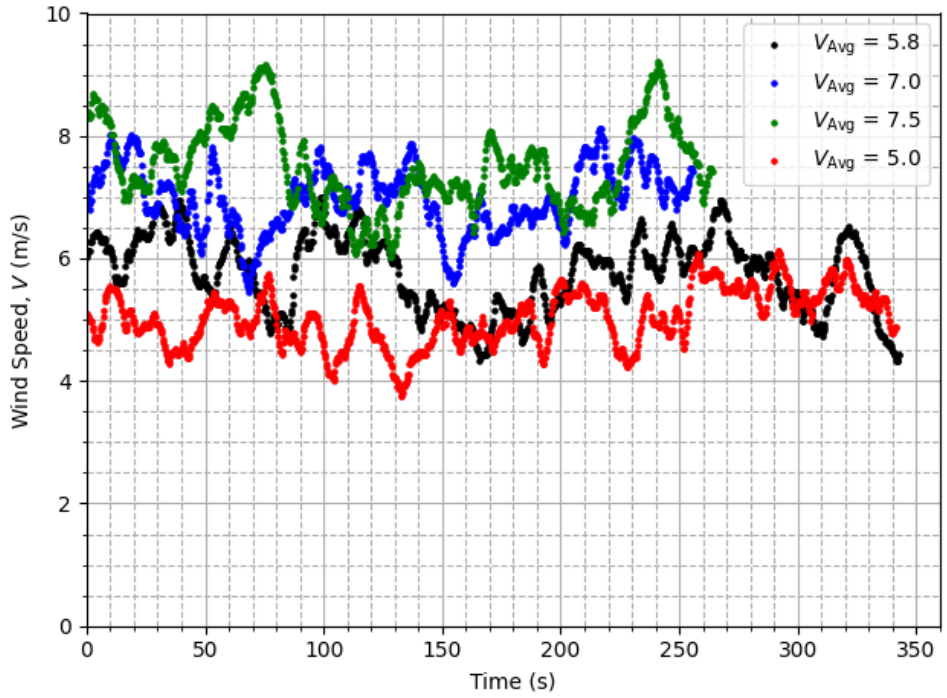

(b) Wind Speed

Figure G.15: Outdoor startup TSR and wind speed of the $A02\lambda09$ blades at varying wind conditions.